Mössbauer Studies on Some Fe-based Multiferroic Materials

By

ALAKA PANDA

PHYS 02 2014 04 003

Indira Gandhi Centre for Atomic Research,

Kalpakkam, India

A thesis submitted to the

Board of Studies in Physical Sciences

In partial fulfilment of requirements

for the Degree of

DOCTOR OF PHILOSOPHY

of

HOMI BHABHA NATIONAL INSTITUTE

July, 2020

Homi Bhabha National Institute[1]

Recommendations of the Viva Voce Committee

As members of the Viva Voce Committee, we certify that we have read the dissertation prepared by Alaka Panda entitled "Mössbauer studies on some Fe based multiferroic materials" and recommend that it may be accepted as fulfilling the thesis requirement for the award of Degree of Doctor of Philosophy.

Chairman – Dr. G. Amarendra G. Amarendra Date Dec 23, 2020

Guide / Convener – Dr. R. Govindaraj R. Govindaraj Date 23-12-2020

Examiner - Prof. A. Srinivasan A. Srini Date 23-12-2020

Member 1- Dr. N. V. Chandrashekar N.V. Chandrashekar Date 23/12/2020

Member 2- Dr. K. Kamruddin Date 23/12/2020

Final approval and acceptance of this thesis is contingent upon the candidate's submission of the final copies of the thesis to HBNI.

I hereby certify that I have read this thesis prepared under my/our direction and recommend that it may be accepted as fulfilling the thesis requirement.

Date: 23/12/2020

Place: IGCAR, Kalpakkam

Signature R. Govindaraj

Guide

---

[1] This page is to be included only for final submission after successful completion of viva voce.

Homi Bhabha National Institute[1]

Recommendations of the Viva Voce Committee

As members of the Viva Voce Committee, we certify that we have read the dissertation prepared by Alaka Panda entitled "Mössbauer studies on some Fe based multiferroic materials" and recommend that it may be accepted as fulfilling the thesis requirement for the award of Degree of Doctor of Philosophy.

Chairman – Dr. G. Amarendra G. Amarendra Date Dec 23, 2020

Guide / Convener – Dr. R. Govindaraj R. Govindaraj Date 23-12-2020

Examiner - Prof. A. Srinivasan A. Srini Date 23-12-2020

Member 1- Dr. N. V. Chandrashekar N. V. Chandra She Date 23/12/2020

Member 2- Dr. K. Kamruddin Date 23/12/2020

Final approval and acceptance of this thesis is contingent upon the candidate's submission of the final copies of the thesis to HBNI.

I hereby certify that I have read this thesis prepared under my/our direction and recommend that it may be accepted as fulfilling the thesis requirement.

Date: 23/12/2020

Place: IGCAR, Kalpakkam

Signature R. Govindaraj

Guide

---

[1] This page is to be included only for final submission after successful completion of viva voce.

DECLARATION FROM GUIDE

I, hereby certify that I have read this dissertation prepared under my direction and recommend that it may be accepted as fulfilling the dissertation requirement.

R. Govindaraj

Dr. R. Govindaraj

Thesis Guide

Date: 23/12/2020

STATEMENT BY AUTHOR

This dissertation has been submitted in partial fulfillment of requirements for an advanced degree at Homi Bhabha National Institute (HBNI) and is deposited in the Library to be made available to borrowers under rules of the HBNI.

Brief quotations from this dissertation are allowable without special permission, provided that accurate acknowledgement of source is made. Requests for permission for extended quotation from or reproduction of this manuscript in whole or in part may be granted by the Competent Authority of HBNI when in his or her judgment the proposed use of the material is in the interests of scholarship. In all other instances, however, permission must be obtained from the author.

Alaka Panda.

Alaka Panda

DECLARATION

I, hereby declare that the investigation presented in the thesis has been carried out by me. The work is original and has not been submitted earlier as a whole or in part for a degree / diploma at this or any other Institution / University.

Alaka Panda.

Alaka Panda

List of Publications arising from the thesis

Journal

1. Formation of bismuth iron oxide based core-shell structures and their dielectric, ferroelectric and magnetic properties. **Alaka Panda**, R. Govindaraj, R. Mythili and G. Amarendra, *J Mater Chem C* 2019, **7**,1280-1291.

   doi: https://doi.org/10.1039/c8tc04908d

2. Complex Dielectric and Impedance Spectroscopic Studies in a Multiferroic Composite of $Bi_2Fe_4O_9$-$BiFeO_3$. **Panda Alaka** and Ramanujan Govindaraj, *Condensed. Matter* 2018, **3**, 44.

   doi: https://doi.org/10.3390/condmat3040044

3. Magnetodielectric coupling in $Bi_2Fe_4O_9$. **Alaka Panda**, R Govindaraj, G Amarendra, *PHYSICA B* 2019, **570**, 206-208.

   doi: https://doi.org/j.physb.2019.06.045

4. Implications of linear correlation between hyperfine parameters in iron oxide nanoparticles. LH Singh, **Alaka Panda**, R Govindaraj, R Mythili, G Amarendra, *Mater. Chem. Phys.* 2018, **214**, 440-448.

   doi: https://doi.org/10.1016/j.matchemphys.2018.04.098

Conferences

1. Magnetodielectric coupling in $Bi_2Fe_4O_9$, **Alaka Panda**, R. Govindaraj and G. Amarendra, International Conference on magnetism and magnetic materials (ICMAGMA) December 09-13, **2018**, NISER Bhubaneswar, Odisha

2. Nanoparticles of $Bi_2Fe_4O_9$ as studied using Mössbauer spectroscopy, **Alaka Panda**, R. Govindaraj and G. Amarendra, ICMAGMA February 01-03, **2017**, Leonia Convention, organized by DMRL Hyderabad.
3. Studies of defects in $Bi_2Fe_4O_9$ using Mössbauer spectroscopy, **Alaka Panda**, R. Govindaraj and G. Amarendra, 2nd International Conference on Condensed Matter and Applied Physics (ICC**)**, Nov 24-25, 2017, Govt. Engineering College, Bikaner, Rajasthan. *AIP Conference Proceedings* 2018, **1953**, 120058.
   doi: http://doi.org/10.1063/1.5033123
4. Magnetic and structural studies in pristine and La doped $BiFeO_3$ using Mössbauer spectroscopy. **Alaka Panda**, R. Govindaraj, K. Vinod, P. Magudapathy, and G. Amarendra, 9th National Conference on Thermophysical Properties (NCTP) November 06-08, 2017, IGCAR, Kalpakkam, Tamil Nadu. *AIP Conference Proceedings* 2018, **1951**, 030020.
   doi: http://doi.org/10.1063/1.5031746
5. Young Materials Researchers' Meet (YMRM), December 10-11**,** 2017 (Workshop), BARC, Mumbai.
6. Nanoparticles of lead hexaferrite as studied using Mössbauer Spectroscopy, **Alaka Panda**, R. Govindaraj, K. Vinod, S. Kalavathi, G. Amarendra, 61st DAE Solid State Physics Symposium (DAE SSPS), December 26-30, 2016, KIIT University, Bhubaneswar, Odisha. *AIP Conference Proceedings* 2017, 1832, 050153.
   doi: http://doi.org/10.1063/1.4980386
7. Mössbauer Spectroscopic Studies in U-Fe and U-Fe-Zr Alloys, **Alaka Panda**, L.H. Singh, S. Rajagopalan, R. Govindaraj, Renjith Ramachandran, S. Kalavathi, G. Amarendra, 60th DAE Solid State Physics Symposium (DAE SSPS), December

21-25, 2015,Amity University, Noida, UP. *AIP Conference Proceedings* 2016, 1731 (1), 140065.

doi: http://doi.org/10.1063/1.4948231

8. Defect-induced magnetism in liquid sodium-exposed stainless steel as studied by Mössbauer and Positron annihilation spectroscopic techniques. **Alaka Panda**, L Herojit Singh, R Govindaraj, S Abhaya, S Rajagopalan, G Venugopal Rao, V Raghunathan, G Amarendra, ICMAGMA, December 02-04, 2015, VIT Vellore, Tamil Nadu.

Peripheral

Defect-induced magnetism in liquid sodium-exposed stainless steel as studied by Mössbauer and Positron annihilation spectroscopic techniques. **Alaka Panda**, L Herojit Singh, R Govindaraj, S Abhaya, R Kumar Yadav, S Rajagopalan, G Venugopal Rao, V Raghunathan, G Amarendra, International Journal of Modern Physics B 2017,31(6), 1750033.

Alaka Panda.

Alaka Panda

This Thesis is

Dedicated to

My Family & Teachers

ACKNOWLEDGMENTS

First and foremost, I would like to express my deepest gratitude to my thesis guide Dr. R. Govindaraj, for his guidance, encouragement and persistent help. I would like to thank my doctoral committee members, Dr. G. Amarendra, Dr. N. V. Chandra Shekar and Dr. M. Kamruddin, for their support and inputs. I would also like to thank my collaborators in IGCAR and IIT Bombay. In addition, special thanks to Dr. R. Mythili for the microscopic measurements and discussions. I acknowledge Dr. K. Vinod, Mr. P. Magudapathy, Dr. T. R Ravindran, Mr. Manoj Kumar for availing the experimental facility. My sincere thanks to Dr. Jayant Kolte and Mr. Manas Ranjan Panda and SAIF facility of IIT Bombay, for dielectric and PE measurements. I am grateful to Dr. S. Rajagopalan, Dr. S R Mohapatra and Dr. Madhusmita Sahoo for all the help and feedback. I am thankful for the efforts given by Shradha and Saikumaran for experimental help. I am grateful to Director IGCAR, Dr. A K Bhaduri, and IGCAR administration for providing the opportunities for research. I would like to thank Dr. Saju, Director MSG. I am thankful to Dr. Lakshmi Narasimhan, Dean of Student Affairs and to Dr. R. Rajaraman, Dean of Physical Sciences for providing a comfortable atmosphere for conducting this research work. I am truly lucky to have Mrs Parvathy and Mr.Ravi in lab and I would like to thank them for helping me in both workfront and otherwise. I would like to thank all the MPS members for their timely help and support. A heartfelt thanks to my friends Arpita, Teena, Sithara, Anuj, Ronit, Jayanthi, Koushika, Ijee, Shraddha, Surojit, Fayaz, Shubhra, Suchana, Chandu, Nilakantha, Bijay, Binay and Alok for their motivation. A big part of the credit goes to all my teachers who always helped me for betterment. A big thanks to the supportive staffs of S K C G college and specially staff of

Dept of Physics for being supportive. I am blessed to have all the attentions and support from baba and bou.

TABLE OF CONTENTS

List of Publications arising from the thesis xi
ACKNOWLEDGMENTS xvii
TABLE OF CONTENTS xix
LIST OF FIGURES xxv
LIST OF TABLES xxxiii

1 Introduction 1

1.1 Preamble 1
1.2 Ferroic Ordering 2

1.2.1 Ferroelectricity 2
1.2.2 Magnetism 5

1.3 Multiferroicity 9

1.3.1 Origin and Types 9

1.4 Brief Review of Ferroelectric and Magnetic Properties of Bismuth Iron oxide Based Multiferroics 14

1.4.1 $BiFeO_3$: Type I Multiferroic 14

1.4.1.1 Ferroelectricity in $BiFeO_3$ 15
1.4.1.2 Magnetism in $BiFeO_3$ 16

1.4.2 $Bi_2Fe_4O_9$: Type II Multiferroic 17

1.4.2.1 Ferroelectricity in $Bi_2Fe_4O_9$ 18
1.4.2.2 Magnetism in $Bi_2Fe_4O_9$ 19

1.5 Mössbauer Spectroscopy for Local Structure and Magnetic Property Studies 21

1.5.1 Basic Methodology of Mössbauer Spectroscopy 22

1.5.1.1 Isomer Shift due to Electric Monopole Interaction 24
1.5.1.2 Magnetic Hyperfine Field due to Magnetic Interaction 26
1.5.1.3 Quadrupole Splitting due to Electric Quadrupole Interaction 28

1.6 Simulation of Mössbauer Spectra in $BiFeO_3$ and $Bi_2Fe_4O_9$ 31

1.7 Motivation of the Thesis 34
1.8 Organization of the Thesis 34

2 Experimental details 37

2.1 Synthesis Routes 37

2.1.1 Bulk Bismuth Ferrite Preparation through Solid-state Route 37
2.1.2 Preparation of Nanoparticles of Bismuth Ferrite using Sol-gel Method 38

2.2 Bulk Structural, Electrical and Magnetic Characterization .. 41

2.2.1 Crystal Structure Studies 42
2.2.2 Microstructural Analysis 43
2.2.3 Electric Property Studies 44

2.2.3.1 Dielectric Studies 44
2.2.3.2 Ferroelectric Studies 45

2.2.4 Magnetic Properties using Bulk Magnetization Studies 47

2.3 Mössbauer Spectroscopy for Local Structure and Magnetic Properties 48

2.3.1 Methodology and Mössbauer Spectrometer 48

2.3.1.1 Mössbauer Source and Absorber 52
2.3.1.2 Mössbauer Drive System 53
2.3.1.3 Mössbauer Spectrum in α–Fe and Calibration of the Velocity Transducer 54

2.3.2 Deduction of Hyperfine Parameters of some Reference Samples 56

3 Structural, magnetic, ferroelectric and magnetoelectric coupling effects in nano-$BiFeO_3$ 59

Graphical abstract: 59

3.1 Introduction 60
3.2 Synthesis of Nanoparticles of $BiFeO_3$Via Sol-gel Route 61
3.3 Multifunctional Properties of Nanoparticles of $BiFeO_3$ 63

3.3.1 Structural Analysis 64

3.3.1.1 XRD Studies 64
3.3.1.2 Raman Studies 70

3.3.2 Bulk Magnetization Studies 74
3.3.3 Ferroelectric Properties 82
3.3.4 Effect of Magnetic Field on the Ferroelectricity 84
3.3.5 Discussion of Mössbauer Results 86

3.4 Conclusion 90

4 Effect of substitution on the multiferroic properties of $BiFeO_3$ 93

Graphical Abstract- 93

4.1 Introduction 94
4.2 Synthesis of substituted Bulk $BiFeO_3$ Particles using Solid-state Route 99
4.3 Local Structural, Magnetic, Ferroelectric and Magnetoelectric Properties of La substituted $BiFeO_3$ 101

4.3.1 Structural Studies 101

4.3.1.1 X–ray Diffraction Studies 102

4.3.2 Bulk Magnetic Property Studies 104
4.3.3 Ferroelectric and Magnetoelectric Studies 108
4.3.4 Discussion of Mössbauer Spectroscopy Results on La substituted $BiFeO_3$ 111

4.4 Influence due to Ca Substitution at Bi sites and Co-substitution of (Bi,Fe) sites by (Ca, Mn) on Structural, Magnetic and Magnetoelectric Properties of $BiFeO_3$ 115

4.4.1 Structure Analysis 115

4.4.1.1 XRD Studies 116
4.4.1.2 Raman spectroscopic Studies 118

4.4.2 Magnetic studies 122
4.4.3 Ferroelectric and Magnetoelectric Studies 129
4.4.4 Mössbauer Studies 132

4.5 Comparative Studies of Solid-state and Sol-gel Prepared Ca substituted $BiFeO_3$ 136

  4.5.1 Structural Studies 137
  4.5.2 Ferroelectric Studies 138
  4.5.3 Discussion of Mössbauer Results 139

4.6 Conclusion 142

5 Role of Defects on the Multiferroic Properties in $Bi_2Fe_4O_9$ 143

Graphical Abstract– 143

5.1 Introduction 144
5.2 Synthesis of Bulk $Bi_2Fe_4O_9$ using Solid-state Route 144
5.3 Structural and Micro–structural Studies 146

  5.3.1 X–Ray Diffraction Studies 146
  5.3.2 Microscopic Image Analysis 149

5.4 Bulk Magnetization Study 150

  5.4.1 Field Dependent Magnetic Studies 150
  5.4.2 DC Magnetization Studies 152
  5.4.3 AC Susceptibility Studies 153

5.5 Ferroelectric Properties 154
5.6 Discussion on the Results of Mössbauer Studies 156
5.7 Magnetoelectric Coupling 158
5.8 Magnetodielectric Coupling 160
5.9 Conclusion 162

6 Understanding of the Formation of Bismuth Iron Oxide Phases by Thermomechanical Route 163

Graphical Abstract 163

6.1 Introduction 164
6.2 Synthesis of Bismuth Iron Oxides using Ball Milling Route 169

6.3 Identification of Phases, Local Structure and Magnetic Studies using Mössbauer Spectroscopy 170

6.3.1 Structural Characterization 170
6.3.2 Local structure and magnetic studies using Mössbauer spectroscopy 173
6.3.3 Results of Microscopy Studies 164

6.4 Proposed model for the formation of Bismuth Iron Oxide Core-shell Structures 179
6.5 Dielectric, Ferroelectric and Magnetic Properties of $Bi_2Fe_4O_9$–$BiFeO_3$ Core-shell Particles 183

6.5.1 Bulk Magnetic and Ferroelectric Properties 183

6.5.1.1 Magnetization Studies 184
6.5.1.2 Ferroelectric Studies 187

6.5.2 Dielectric Spectroscopic Studies 188

6.6 Conclusions 191

7 Conclusions and Future Prospects 193

7.1 Conclusions 193
7.2 Future Prospects 194

References 197

LIST OF FIGURES

Figure 1.1 Representative PE loop of ferroelectric (hysteretic, red) and paraelectric (reversible path, blue) materials with the ferroelectric parameters. 4

Figure 1.2 Spin alignment corresponding to ferromagnetic, antiferromagnetic and ferrimagnetic structure. 7

Figure 1.3 M H loop showing the magnetic parameters (A), the MH loop of soft (B) and hard ferromagnets (C). 8

Figure 1.4 Typical variation of susceptibility with temperature for ferromagnetic, antiferromagnetically ordered materials. The Néel and Curie temperature for antiferromagnetic and ferromagnetic materials are also marked. 8

Figure 1.5 Classification of multiferroics and shown are the subclass of multiferroics. 11

Figure 1.6 The spin cycloid overriding on the crystal lattice, the spin perpendicular (A) and parallel (B) with respect to the lattice. 12

Figure 1.7 The spherical cycloid (A)and conical cycloid structure (B) with spin orientation. 12

Figure 1.8 Magnetostriction leading to multiferroic properties in Ca_3CoMnO_6 and frustrated magnetism of electronic origin leading to multiferroism. 13

Figure 1.9 Composite multiferroics and their classifications based on origin. 13

Figure 1.10 Unit cell of $BiFeO_3$ showing Fe sites of different distortion with polarization direction along [111] (top) and incommensurate spin cycloid causing AFM order (bottom). 17

Figure 1.11 Unit cell of $Bi_2Fe_4O_9$ depicting the octahedral and tetrahedral Fe sites arrangement (A) and spin frustration exhibited by tetrahedral Fe1 and octahedral Fe2 ions in $Bi_2Fe_4O_9$ (violet bubble represents Bi atom) (B). 18

Figure 1.12 Schematic illustrating Mössbauer effect. 23

Figure 1.13 Nuclear energy levels of a source and an absorber. 24

Figure 1.14 Mössbauer spectrum obtained in a sample in which ^{57}Fe exposed to only monopole interaction. 26

Figure 1.15 Mössbauer spectrum obtained for magnetically ordered material (left) and the energy transition corresponding to the peak of Mössbauer spectrum (right). 28

Figure 1.16 Schematic of hyperfine interaction induced shift /splittings in Mössbauer spectra. 30

Figure 1.17 (left) presents simulated Mössbauer spectra of two octahedral Fe sites along with the resultant spectra of $BiFeO_3$ and (right) the unit cell of $BiFeO_3$ showing presence of the corresponding octahedral sites. 33

Figure 1.18 (left) presents simulated Mössbauer spectra of equidistributed octahedral and tetrahedral Fe sites along with the resultant spectra of $Bi_2Fe_4O_9$ and (right) the unit cell of $Bi_2Fe_4O_9$ showing presence of the corresponding sites as well as bond angles between octahedral and tetrahedral sites. 34

Figure 2.1 Basic steps involved in solid-state route (A), sol-gel method (B), structure of citric acid (C). 42

Figure 2.2 Schematics and image formation in scanning electron microscope (SEM) and transmission electron microscope (TEM) [84]. 45

Figure 2.3 Broadband dielectric set up used for room temperzture (left)and under magnetic field (right). 47

Figure 2.4 PE loop set up for measuring the magnetic response of electric polarization. 47

Figure 2.5 Vibrating Sample magnetometer. 49

Figure 2.6 Schematic displaying the basic principle of Mössbauer spectroscopy. 50

Figure 2.7 Block diagram of Mössbauer spectrometer. 51

Figure 2.8 Photograph of Mössbauer spectrometer showing the NIM bin in which the modules corresponding to waveform generator, Mössbauer drive unit, High voltage power supply and linear amplifiers are housed. Inset shows the vibration free platform in which the shielded source mounted transducer, sample and proportional counter are mounted tightly. 52

Figure 2.9 Decay scheme for a ^{57}Co source leading to 14.41 keV gamma-ray emission. 54

Figure 2.10 Pulse height spectrum obtained with ^{57}Co source in a gas filled proportional counter and shown are the peaks corresponding to the gamma energies of ^{57}Fe (6.4 keV, 14.4 keV and 21 keV) (inset shows channel number varies linearly with energy. 55

Figure 2.11 Mössbauer spectrum with a six line pattern for α -Fe powder with corresponding cubic unit cell [86] and deduced hyperfine parameters of the only sextet present in the case (right inset). 56

Figure 2.12 Variation of velocity with respect to channel number for resonant absorption as deduced from Mössbauer spectrum of α -Fe [86]. 57

Figure 2.13 (A) Mössbauer spectra for sodium nitroprusside which is noncubic and nonmagnetic hence showing doublet (right inset presents structure of sodium nitroprusside) and (B) Mössbauer spectra sextet corresponding to α-Fe_2O_3(right inset unit cell of α-Fe_2O_3). 58

Figure 3.1 Steps followed the preparation of nanoparticles of $BiFeO_3$ (EG –Ethylene Glycol, CA-Citric Acid and DI- Deionised Water). 63

Figure 3.2 XRD patterns and the respective fullprof refined pattern corresponding to precursor (a) and annealed at 873 K for 3 h (b) nano $BiFeO_3$ prepared though citrate sol-gel (right inset presents zoomed in most intense peaks of (a) and (b) respectively). The obtained patterns are compared with the standard $BiFeO_3$ stick pattern. 68

Figure 3.4 Lattice parameters (inset volume variation) variation with respect to the precursor, calcined samples at 723 K and 873 K showing monotonous decrease in lattice parameter and volume. 69

Figure 3.3 Schematic 3.3 (A) represents the unit cell of $BiFeO_3$ while the schematics (B) and (C) represent the polyhedral units of Fe and Bi. Fe–O–Fe bond angle and Fe–O and Bi–O bond lengths are shown as deduced from the Rietveld refinement of the XRD patterns. 70

Figure 3.5 Room temperature Raman spectra corresponding to the citric acid assisted as prepared (A) annealed (B) nano $BiFeO_3$ (inset high wavenumber modes corresponding to overtones). 73

Figure 3.6 Raman studies of BFO-T showing broadened modes and lesser modes are signature of nanosized particle distribution (inset corresponding XRD pattern representative of single-phase formation). 74

Figure 3.7 ZFC FC curves obtained in BiFeO3 prepared using citric acid with an applied magnetic field of 0.1 T (A) with precursor and (B) annealed at 873 K. 77

Figure 3.8 ZFC FC with applied magnetic field of 0.1 T results corresponding to BFO T annealed at 823 K for 2 h. 78

Figure 3.9 MH loop of precursor (A) and sintered at 873 K (B) of BFO-C. 80

Figure 3.10 A B K plot of precursor (A) and annealed (B) nano-$BiFeO_3$ describing the ferromagnetic behavior by means of convex curves. 81

Figure 3.11 (A) Hysteresis loop of BFO-T depicting the antiferromagnetic behaviour with central finite area region corresponding to the core shell type signature with FM shell and (B) A B K plot confirming the concave shaped antiferromagnetic behavior. 82

Figure 3.12 Ferroelectric hysteresis loop of BFO-C annealed at 873 K (A) presenting lossy nature and that of BFO-T annealed at 823 K (B) presenting well groomed loop. 85

Figure 3.13 Change in ferroelectric parameters in PE loop in annealed BFO-C in presence of magnetic field of 0.1 T at 300 K. 87

Figure 3.14 Mössbauer spectra obtained at room temperature in $BiFeO_3$ prepared using Citric acid in the precursor and subsequent to annealing at different temperatures and time duration as mentioned inside each slot of the graph (a-d) as well as tartaric acid assisted nano-$BiFeO_3$ (e). 90

Figure 3.15 Demonstration of core-shell and possible spin arrangements of BFO-C and BFO-T as predicted based on the results of Mössbauer studies. 93

Figure 4.1 Tolerance variation w r t substitution to study the stabilization of the phase. 102

Figure 4.2 Steps involved in solid state preparation of substituted and cosubstituted system. 103

Figure 4.3 XRD pattern corresponding to 20 % La substituted BiFeO3 heat treated at 1073 K 48 h and 1123 K 12 h and 6 h ((a) & (b)) and 10 % La substituted $BiFeO_3$ sintered at 1073 K 48 h and 1123 K 6 h (c) showing the presence of impurity phases such as $Bi_{25}FeO_{40}$ and $Bi_2Fe_4O_9$ in a small concentration in the case of 10 % substituted sample prominently (marked by * and #) and the results are compared with standard stick pattern of Rhombohedral $BiFeO_3$. 105

Figure 4.4 Field dependent magnetization studies of BLFO1 and BLFO2 heat treated at 1073 K 48 h and 1123 K 6 h ((A)&(C)) ZFC FC variation for BLFO1 and BLFO2 ((B)&(D)) showing AFM and Weak FM nature respectively with overlapped ZFC FC in former and bifurcated region in the later. 107

Figure 4.5 A-B-K plot showing concavity for BLFO1 (A) and convex behaviour for a range lower magnetic field and concavity of higher applied field in BLFO2 (B) depicting the AFM predominance and coexisting AFM and weak FM in BLFO1 and BLFO2. 108

Figure 4.6 Ferroelectric hysteresis loop of BLFO1 (A) and BFLO2 ((B) & (C)) studied in presence of magnetic field. The substantial switching behavior is a consequence of strong magnetoelectric coupling with the dominance of ferroelectricity as deduced from the suppressed nonlinearity, where nonlinearity represents the antiferroelectricity induced due to La presence. 111

Figure 4.7 Variation of ferroelectric parameters Pr and Ec with respect to applied magnetic field. Both the polarization and coercive electric field are found to be much higher in BLFO2 then in BLFO1. 113

Figure 4.8 Mössbauer spectrum as obtained in La substituted $BiFeO_3$ at 300 K (a) BLFO1-6h sintered at 1073 K 48 h and 1123 K 6 h (b) BLFO2-6h sintered at 1073 K for 48 h and 1123 K for 6 h and (c) BLFO2-12h sintered at 1073 K 48 h and 1123 K 12 h. 116

Figure 4.9 (A) XRD pattern corresponding to different substitutent is given (zoomed in portion of most intense planes) (B) describes the shifting of the most intense peaks upon substitution. 121

Figure 4.10 (top) Raman mode variation upon substituting with substantially observed mode softening and hardening (bottom) depicts the variation of A_g modes with substitution. 125

Figure 4.11 M-H plot corresponding to BCFO1 and BCFO2 at 5 K and 300 K describing coexisting magnetic features in both the cases. ((A) & (C)) and corresponding ZFC FC plot representing irreversible magnetization at low temperature upto 220 K ((B) & (D)). 130

Figure 4.12 M-H plot corresponding to BCFMO1 and BCFMO2 at 5 K and 300 K describing coexisting magnetic features in both the cases. Interestingly saturation is attained at room temperature in preence of magnetic Mn ion ((A) & (C)) and ZFC FC plot showing bifurcation below 100 K and hump at 50 K ((B) & (D)). 131

Figure 4.13 χ^{-1}vs T plot for BCFO ((A) & (B)) and BCFMO ((C) & (D)) is presented. A linear fitting of the data is used to deduce the magnetic parameters Curie-Weiss temperature and effective magnetic moment. 132

Figure 4.14 Room temperature PE loop corresponding to Ca and Ca, Mn cosubstituted $BiFeO_3$ In comparison to lossy nature of BCFMO1 a well developed loop is obtained for BCFMO2. 135

Figure 4.15 Magnetoelectric coupling studies in BCFO which shows switching behavior in BCFO1 while unresponsive in case of BCFO2 for applied magnetic field of ± 0.1 Tesla with substantial increase in polarization. 135

Figure 4.16 Room temperatureMössbauer spectra corresponding to substituted and co-substituted $BiFeO_3$ 140

Figure 4.17 Comparative XRD pattern for BCFO prepared using solid-state (annealed 1073 K for 12 h and 1123 K 6 h) and sol-gel route (annealed at 873 K). The shift of most intense peak is shown. 143

Figure 4.18 PE loop for BCFO prepared using sol-gel route and annealed at 873 K for 2 h (A) And the corresponding measured magnetoelectric coupling is presented (B). 145

Figure 4.19 Mössbauer spectra obtained in BCFO prepared through solid state reaction methods (a) and sol gel route (precursor (b) and 873 K 2 h (c)). 146

Figure 5.1 Steps involved in the synthesis of $Bi_2Fe_4O_9$ using solid–state route (SSR). 151

Figure 5.2 Fullprof refined XRD pattern corresponding to as prepared sintered at 973 K for 144 h (a) followed by sintering at 923 K for 24 h (b) and compared with standard stick pattern of $Bi_2Fe_4O_9$ (right inset (c) & (d) zoomed in most intense peaks). 154

Figure 5.3 Unit cell of $Bi_2Fe_4O_9$ as generated using VESTA software and the Fe site in octahedral and tetrahedral environment is presented. 154

Figure 5.4 SEM image of as prepared (A) and sintered (B) $Bi_2Fe_4O_9$ with scaling of 100 nm. 155

Figure 5.5 M–H loop (A) and corresponding A–B–K plot (B) of $Bi_2Fe_4O_9$ sintered at 923 K. 157

Figure 5.6 ZFC FC plot of as prepared under different applied field (A) and (B) sintered at 923 K for 24 h. 159

Figure 5.7 Frequency dependent real and imaginary part of ac susceptibility measurement w r t T for sintered $Bi_2Fe_4O_9$ showing shift of relaxation peak.160

Figure 5.8 Room temperature polarization Vs electric field loop for the $Bi_2Fe_4O_9$ sintered at 923 K. 161

Figure 5.9 Room temperature MS of as prepared (a) and sintered at 923 K for 24 h (b) $Bi_2Fe_4O_9$. 163

Figure 5.10 Exhibition of magnetoelectric switching in electric field in magnetic environment when magnetic field is applied. The zoomed in region (inset) implicates the change. 165

Figure 5.11 Variation of the percentage of the magnetodielectric coupling upon the application of magnetic field at different frequencies in $Bi_2Fe_4O_9$ SSR sintered at 923 K for 24 h (a) 10 kHz and (b) 100 kHz. 167

Figure 6.1 Patterns corresponding to treatment (a) S_0– ball-milled α-Fe_2O_3 and α Bi_2O_3 (b), (c) S_1 and S_2 while (d) S_3 (e) S_4 (* and # indicates the presence of $Bi_{25}FeO_{40}$ and $BiFeO_3$ respectively). 173

Figure 6.2 Mössbauer spectra obtained at room temperature on (a) $BMFe_2O_3$ (b) S_0 (as ball-milled mixture of Bi_2O_3 and Fe_2O_3), (c) and (d) corresponding to treatments S_1 and S_2 respectively, (e) treatment S_3 with addition of bismuth oxide to as ball-milled powder and subjected to annealing and (f) refers to $Bi_2Fe_4O_9$ prepared through solid-state route (S_4). 178

Figure 6.3 Variation of relative fractions of Fe associated with α-Fe_2O_3 (f_1), $BiFeO_3$(f_2) and $Bi_2Fe_4O_9$ (f_3) with different annealing treatments of ball-milled sample.179

Figure 6.4 SEM images of ball milled Bi_2O_3 and Fe_2O_3 subjected to annealing treatments S_1 and S_2 showing (A) fine particles and (B) coarse particles respectively. 181

Figure 6.5 (A) TEM micrograph of S_2 , Magnified view of region marked in (B) showing the presence of core-double shell structures, where the core is identified to be $Bi_2Fe_4O_9$ as confirmed by the FFT pattern from this region in (C) and two distinct amorphous shell structures around the core. 183

Figure 6.6 (A) HREM image of sample S_2 from another region, (B) FFT from region marked in (A) confirming the presence of $Bi_2Fe_4O_9$/ $BiFeO_3$ and $Bi_{25}FeO_{40}$, (C) Inverse FFT from reflections of $Bi_2Fe_4O_9$/ $BiFeO_3$ (D) Inverse FFT from $(0\bar{1}1)$ and (420) reflections present adjacent to $Bi_2Fe_4O_9BiFeO_3$. 184

Figure 6.7 Schematic of the formation of $Bi_2Fe_4O_9$ core with shell of off stoichiometric bismuth iron oxide ($BiFeO_{3-x}$) and iron oxide (Fe_2O_3). Step I involves the occurrence of nanoparticles of α-Fe_2O_3 and Bi_2O_3. II step of reaction indicates the formation of $Bi_2Fe_4O_9$ core with a shell of bismuth oxide due to ball milling followed by annealing treatments. These particles while coming in to contact with α-Fe_2O_3 leading to the next step due to annealing. Step–III leads to the formation of $Bi_2Fe_4O_9$– $BiFeO_{3-x}$ – $Bi_{25}FeO_{40}$ core-double shell structure as shown in an enlarged manner. Analogously in certain cases $Bi_2Fe_4O_9$ crystalline core is observed with shells that are of amorphous nature and could be considered as composites. 187

Figure 6.8 Variation of magnetization with temperature as obtained in samples S_1 and S_2 as referred to in the text (A) and M–H loop of S_2 at 298 K (B). 192

Figure 6.9 P–E loop as obtained in $Bi_2Fe_4O_9$ through solid state reaction (B) and in ball milled sample S_2 (A). 193

Figure 6.10 (A) Temperature dependence of (a) dielectric permittivity Corresponding variations marked inside rectangular panels are magnified and shown in insets as (i) and (ii) respectively. 6.10 (B) shows the core-shell structured particle having dielectric constants ε_C and ε_s for core and shell respectively. 197

LIST OF TABLES

Table 1.1 Various allowed transition and its relative intensity. 28

Table 1.2 Brief description of hyperfine interactions and the details of the deduced solid state parameters using Mössbauer spectroscopy. 31

Table 3.1 Rietveld refinement parameters of precursor and annealed nano-$BiFeO_3$. 70

Table 3.2 Raman modes in the present study and a comparison with literature. 75

Table 3.3 Magnetic parameter of as prepared and sintered at 873 K with citric acid (CA) and tartaric acid (TA) at 5 K and 300 K. 83

Table 3.4 Room temperature Mössbauer parameters of precursor, annealed BFO-C and BFO-T. 91

Table 4.1 Literature review on La substituted $BiFeO_3$, Ca substitution and co substitution. 97

Table 4.2 Magnetic parameters of BLFO2. 110

Table 4.3 Hyperfine parameters deduced from deconvoluted spectra of BLFO1 and BLFO2 from fig 4.8. 117

Table 4.4 Frequencies of Raman modes (in cm^{-1}) corresponding to BCFO and BCFMO as obtained in this thesis work [147]. 123

Table 4.5 Magnetic parameters obtained from MH loop. 128

Table 4.6 Blocking (T_b) and irreversibility temperature (T_{irr}) and Weiss constant calculated from χ^{-1} vs T plot. 129

Table 4.7 Mössbauer parameters as obtained in BCFO and BCFMO. 138

Table 4.8 Comparative room temperature MS parameter for BCFO prepared using solid-state and sol-gel routes. 146

Table 5.1 Bond length and bong angles as deduced from refinement for as prepared (973 K for 144 h) and sintered (973 K for 144 h and 923 K for 24 h) $Bi_2Fe_4O_9$. 153

Table 5.2 Weight percentage of the standard, as prepared and the sintered sample as obtained from EDAX analysis. 156

Table 5.3 Magnetization parameters i.e. M_r, M_s and H_c for the sintered $Bi_2Fe_4O_9$. 157

Table 5.4 Mössbauer parameters corresponding to as prepared and sintered $Bi_2Fe_4O_9$. 163

Table 6.1 Details of the different treatments adopted in the study. 173

Table 6.2 Phase identification through XRD analysis after different heat treatments. 174

Table 6.3 Hyperfine parameters obtained through Mössbauer spectroscopy of samples subjected to different annealing treatments. 180

Table 6.4 Analysis of FFT pattern in Figure 6.6. 183

7 Conclusions and Future Prospects

7.1 Conclusions

This thesis extensively addresses the aspects related to the manifestation of defects on the ferroelectric and magnetic properties of bismuth iron based multiferroic oxides such as $BiFeO_3$ and $Bi_2Fe_4O_9$. Importantly this thesis work elucidates the atomic scale understanding of the effect of particle size (nano and bulk), substitution at Bi and Fe sites on the bulk magnetic and ferroelectric properties of $BiFeO_3$ by means of Mössbauer studies and thereby providing the comprehension of the observed bulk ferroelectric and magnetic properties.Effect of ferroelectric distortion in these systems on the Fe–O–Fe based superexchange interaction and hence the magnetic properties and local structure of FeO_6 octahedra are studied extensively using ^{57}Fe based Mössbauer spectroscopy.

Atomic scale understanding of the weak ferromagnetic properties of nanoparticles of $BiFeO_3$ has been deduced. Nanoparticles of $BiFeO_3$ have been prepared by means of sol-gel method using citric acid as a fuel and are studied for the size effect on multiferroic properties and compared with that of the nanoparticles of $BiFeO_3$ prepared using same method but with tartaric acid as a fuel. Presence of weak ferromagnetic and AFM/PM like phases have been deduced using magnetization results. Based on the results of Mössbauer studies the occurrence of $BIFeO_3$ nanoparticles in core-shellconfiguration with antiferromagnetically ordered core and a weak ferromagnetic shell has been proposed. Based on this configuration the observed bulk magnetic/ ferroelectric properties could be explained.

Effect of substitution of lower sized Ca^{2+} at Bi^{3+} sites in $BiFeO_3$ is understood to resultin strain leading to an appreciable modification of magnetic properties resulting in the occurrence of weak ferromagnetic ordered zones in the dominantly antiferromagnetically ordered matrix leading to an appreciable magnetoelectric coupling effects. Consistently in addition two distinct Fe sites associated with FeO_6octahedra experiencing antiferromagnetic interactions, the Mössbauer spectrum could be deconvlouted in to an additional sixline pattern implying the presence of a weak ferromagnetic ordered zones. In case of 20 % Lasubstituted sample in addition to the effect of strain, the occurrence of oxygen vacancies as deduced by Mössbauer studies are understood to be contributing to the weak ferromagnetic ordering and hence an appreciable magneto-ferroelectric coupling effects.

Effect of annealing treatments on the most stable $Bi_2Fe_4O_9$ phase has been studied. While the magnetization results show the occurrence of weak ferromagnetic ordering, defect associated component could be deduced using Mössbauer Spectroscopy providing an understanding of the observed weak ferromagnetic component. This results in a defect induced magnetoelectric coupling effects as observed in $Bi_2Fe_4O_9$ at room temperature, which otherwise exhibits AFM ordering with Néel temperature of 250 K and the Curie temperature of 260 K.

Microscopic understanding of the formation of the core-shell structure having core as as$Bi_2Fe_4O_9$ and having $BiFeO_3$–$Bi_{25}FeO_{40}$ has been studied in a detailed manner using Mössbauer spectroscopy.

7.2 Future Prospects

Based on the results obtained in the present thesis work it is proposed to study the effect of suitable substitutions of cations at both the Bi ad Fe sites to obtain ferromagnetically ordered zones leading to a significant coupling between ferroelectric and magnetic properties in $BiFeO_3$. In addition the influence of defects incorporated in a controlled manner due to additional substitution / selective annealing treatments could be studied in $BiFeO_3$aiming at the enhancement of the coupling effects while retaining the stability of the phases leading to the realization of magnetic and ferroelectric based memory devices.

Based on the results obtained in the present thesis work it is deduced that the defects in $Bi_2Fe_4O_9$ lead to a significant magnetoelectric coupling effects at room temperature in

$Bi_2Fe_4O_9$. Based on this result it is proposed to study the effect of defects in the composite system of $Bi_2Fe_4O_9$–$BiFeO_3$ system aiming at significantly improving the magnetoelectric coupling effects.

Also it is proposed to study the memory effect of the application of high value of electric field / magnetic field on the magnetic / ferroelectric properties of these systems. These studies will be carried out by means of exposing the samples to high electric / magnetic field and subsequently the magnetization / ferroelectric studies will be carried out to look for the memory effects towards realizing memory devices.

In general perovskite based oxides are mostly used for a number of magnetic and ferroelectric applications. Multifunctional system could be realized with the complex of $BiFeO_3$ with the chosen perovskite system depending upon the concerned multifunctional application.

Homi Bhabha National Institute

1. **Name of the Constituent Institution: IGCAR**
2. **Nam of the Student: Ms.Alaka Panda**
3. **Enrolment No.: PHYS 02 2014 04 003**
4. **Title of the Thesis: Mössbauer Studies on Some Fe-based Multiferroic Materials**
5. **Name of the Board of Studies : Physical Sciences**

Abstract

This thesis deals with the studies of the multiferroic properties of Bismuth iron based type I and type IIoxides such as $BiFeO_3$ and $Bi_2Fe_4O_9$. $BiFeO_3$exhibits antiferromagnetic and ferroelectricordering with the Neel and Curie temperatures at 643 K and 1103 K respectively. G-type AFM ordering due to Dzyaloshinskii-Moriya interaction is compensated by the presence of spin cycloid of wavelength 62 nm resulting in net zero magnetic moment. Further the ferroelectricity is originated from the off-centric arrangement along (111) direction resulted from stereochemically active $6s^2$ lone pair of Bi. The observed magneto electric coupling is weak as the magnetic and ferroelectric origins are different.There are challenges involved in observing multiferroicity in $BiFeO_3$ due to prevalent impurity phase presence as well as low resistance of the product. By properly controlling the synthesis parameters these shortcomings can be overcome. In order to order study the effect of size on the multiferroic properties nanoparticles of $BiFeO_3$ has been prepared using sol-gel route at low temperatures far below the temperature of formation of $BiFeO_3$through solid state route. Further suitable substitution of ions like isovalentLa^{3+}, divalent Ca^{2+} at Bi sites and Mn^{3+} at Fe sites are carried out following solid-state route aimed at enhancing multiferroic properties in addition to stabilizing $BiFeO_3$ phase. Another system of study in this thesis is $Bi_2Fe_4O_9$which is a type II multiferroic with transition temperatures close to room temperature i.e magnetic Neel transition at 250 K and ferroelectric Curie transition at 260 K. In $Bi_2Fe_4O_9$ the magnetic and ferroelectric properties are coupled by means of frustrated magnetic spin structure leading to off-centrosymmetric ferroelectric ordering with comparatively large value of magnetodielectric coupling. In addition, an attempt is made in understanding the growth of different phases in Bi_2O_3-Fe_2O_3 phase diagram by means of HRTEM and Mossbauer analysis supported by XRD results.

Suitable synthesis methods in preparing pristine phases are employed for detailed studies which is generally a challenge especially in case of $BiFeO_3$. Sol-gel auto-combustion route for nanoparticle $BiFeO_3$ preparation and solid-state route for substituted $BiFeO_3$ as well as bulk $Bi_2Fe_4O_9$ followed by heat treatment is

found to be effective towards achieving the goal. Different characterization techniques for phase identification, magnetic, ferroelectric as well as coupling are used. For structural characterization X-ray Diffraction techniques and supporting Raman spectroscopic measurements and microscopic measurements are carried out. The magnetic and ferroelectric properties are carried out using vibrating sample magnetometer (VSM) and ferroelectric PE loop tracer respectively. An arrangement is made to observed the PE under the application of magnetic to observe the coupling between magnetic and ferroelectric properties. Dielectric measurements are also carried out to look for possible magnetodielectric coupling. Mössbauer spectroscopic studies helped in understanding obtained bulk magnetic and ferroelectric properties at the atomic scale by means of probing the Fe sites in the studied systems.

Nano-particles of $BiFeO_3$ are prepared using sol gel method with different chelating agents resulting in different complex formation mechanisms hence causing size differences. Structural property studies discusses the presence of distortion and thus the consequences of these observations upon multiferroic properties are studied. These nanoparticles are deduced to be occurring in core-shell configuration with core and shell exhibiting antiferromagnetic and weak ferromagnetic ordering respectively based on the results of Mössbauer studies.Magnetic properties are found to be originated from the anioic defects and 62 nm spin cycloid anomaly causing soft ferromagnetism and leaky loop in citrate assisted $BiFeO_3$ while size effect dominated coexisting weak FM shell and AFM core with well developed PE loop for tartarate based $BiFeO_3$. An appreciable switching is observed implying exhibition of magnetoelectric coupling in the nano-$BiFeO_3$.

Isovalent La at Bi sites and co-substituted aliovalentCa in place of Bi and Mn at Fe sites are prepared via solid-state route and its structural magnetic,ferroelectric properties are studied. The structural transition is observed with respect the substitution concentration. The structural transition and distortion are found to result in complex and interesting magnetic properties. Ferroelectric properties are studied in all the cases and magnetoelectric coupling are observed. 20% La doped $BiFeO_3$ due to the presence of defects and structural transition and in 20% Ca and 5% Mn co-substituted $BiFeO_3$ due to J-T distortion ofMn and altered magnetic exchange interaction are observed to have substantial magnetoelectric electric coupling as deduced from Mössbauer spectroscopy.

The mechanism of the growth of Bismuth iron oxide phases is proposed based on the results of Mössbauer spectroscopy along with that of TEM studies. $BiFeO_3$-$Bi_2Fe_4O_9$ composite system as obtained using thermo mechanical treatment of the oxides of Bi and Fe , is found to exhibit significant magnetoelectric coupling as well giant dielectric behavior providing scope for device applications.

1 Introduction

1.1 Preamble

Materials exhibiting more than one ferroic order such as ferromagnetic, ferroelectric and/or ferroelastic are called as multiferroic materials [1–4]. This thesis extensively addresses several aspects of bismuth iron oxide based multiferroic materials exhibiting quite interesting ferroelectric and magnetic properties. Ferroelectric and ferromagnetic orderings are mutually exclusive. While confining to perovskite based (ABO_3) oxides it can be observed that the systems containing the transition metal atom B with partially filled d shells exhibit magnetic ordering (e.g. Ca**Ru**O_3, Ca**Mn**O_3, Sr**Ru**O_3) while the presence of transition metal atoms B with empty d orbitals are required for the system to exhibit ferroelectricity (e.g Ba**Ti**O_3, PbZr**Ti**O_3). $BiFeO_3$ exhibits ferroelectric ordering as contributed by $6s^2$ lone pair electrons of Bi along with antiferromagnetic ordering as contributed by Fe atoms due to Fe–O–Fe based superexchange interactions. As the ferroelectric and antiferromagnetic ordering are due to different elements such as Bi and Fe, respectively, magnetoelectric coupling in $BiFeO_3$ has been reported to be quite small [5]. Hence, it is interesting to probe the effect of size of the particles, substitution at Bi and Fe sites, and defects on the modification of magnetic properties resulting in weak ferromagnetic ordering, which could eventually lead to an enhanced magnetoelectric coupling. In the case of $Bi_2Fe_4O_9$, another multiferroic system chosen for the studies in this thesis, magnetic properties are understood to result in ferroelectric properties in which the coupling between the ferroelectric and antiferromagnetic (AFM) properties is quite significant.

Ferroelectricity in bismuth iron oxide based multiferroic materials results in significantly distorted Fe–oxide polyhedra. Importantly the distortion of polyhedra made of Fe and O would result in changes in Fe–O–Fe bond angle and hence the superexchange interaction which primarily dictates the magnetic interactions. Hence by means of probing the local structure and magnetic properties at Fe sites and thereby correlating these results with that of the bulk structural, magnetic and ferroelectric properties of the system might help us to obtain a more detailed understanding of the multiferroic properties of these systems. Therefore, ^{57}Fe based Mössbauer spectroscopy is extensively used along with other bulk structural, magnetic and ferroelectric studies in this thesis work to understand the local structure and magnetic properties in terms of hyperfine parameters deduced at Fe sites in bismuth iron oxides. This is motivated at providing an atomic scale understanding of the observed bulk ferroelectric and magnetic behavior in different systems of bismuth iron oxides of interest.

1.2 Ferroic Ordering

Multiferroic ordering is termed to properties of materials which displays one or more ferric phases such as antiferro/ferro magnetic, ferroelectric and ferroelastic domains wherein the individual domains which can be reoriented by applied electric field, magnetic field, electric stress field or combinations of these fields. In this section we will discuss about two such properties i.e., ferroelectricity and ferromagnetic ordering in detail, which carries importance in applications. Ferroelectricity and ferromagnetism though have different origin and carriers as well as parameters but phenomenologically analogous to each other.

1.2.1 Ferroelectricity

Ferroelectricity is the property by virtue of which the material possesses polarization with respect to externally applied electric field and also retains it when the field is removed in the realizable range of temperature and pressure. Ferroelectric materials possess piezoelectric as well as pyroelectric behavior. The memory effect deteriorates with increase in temperature and beyond a temperature T_C known as Curie temperature, a transition from polar ferroelectric to nonpolar paraelectric phase arises. Hence in the absence of electric field the material possesses two or more stable and metastable phases canceling the net polarization and in presence of applied electric field these polarization switches along the applied field producing net polarization along the easy direction resulting a hysteresis loop. At the paraelectric phase the material behaves as a normal dielectric material and exhibit linear P vs E relationship. Valasek *et al.* discovered the ferroelectricity in Rochelle salt and he claimed that the origin of such property was due to the hydrogen bonding in that salt [6]. A typical ferroelectric loop is presented in Figure 1.1. The various other materials, which were reported to exhibit polarization, are $BaTiO_3$, perovskites oxides, tungsten bronze structure, tantalates, phosphates, bismuth oxide layered structures, ceramic polymer composites, organic polymers like PVDF, compounds containing hydrogen bonded radicals like KH_2PO_4 (KDP), Rochelle salt [7–9]. Initially d^0-ness of the transition metal atom B in ABO_3 perovskite was considered as a basic criterion for material to possess ferroelectricity. However, a detailed analysis proved that d^0-ness is a necessary condition for ferroelectricity. Perovskites like $BiFeO_3$, $BiMnO_3$ and $PbTiO_3$ exhibit ferroelectricity due to the lone pair activity of Bi and Pb ion. There are two microscopic models to understand the ferroelectric phenomena. The first one is order-disorder type and the other one is displacive type [10].

In order-disorder type ferroelectrics, the dipoles exist within the structure in paraelectric state above T_C, but thermally disordered between two or more states hence resulting in zero value of average polarization e.g. KDP. It is tetragonal paraelectric above the ferroelectric Curie temperature (T_C) of 123 K and orthorhombic ferroelectric below T_C. The tetrahedral PO_4 groups are linked by corner shared hydrogen bonding. Below T_C the proton sitting in the double potential well are localized between the two minima of the wells. This distorts the PO_4 tetrahedra. The Phosphorous (P) and Potassium (K) ions are displaced relative to oxygen polyhedra resulting in a net polarization. Other example of ferroelectric material of this kind is $NaNO_2$ in which NO^{2-} is ordered below 436 K.

In displacive type model of ferroelectrics, no dipoles are present above T_C and in paraelectric phase but dipoles appear leading from the cooperative movement of ions. This is termed as softening of zone centre optical phonons. The frequency of optical phonon mode with zero wave vectors goes to zero at T_C. It involves the displacement of cations in opposite direction to the displacement of anions in the structure. As the frequency goes to zero, the dipolar displacement results in ferroelectricity [10]. Example of a material exhibiting such phenomena is $BaTiO_3$. The explanation of ferroelctricity in $BaTiO_3$ is as follows. $BaTiO_3$ unit cell is of ABO_3 type in which Ti ion is at the centre of oxygen octahedra. The adjacent electron cloud of Ti and O forms a covalent bond giving rise to off centrosymmetry of Ti site ion giving displacive type ferroelectricity.

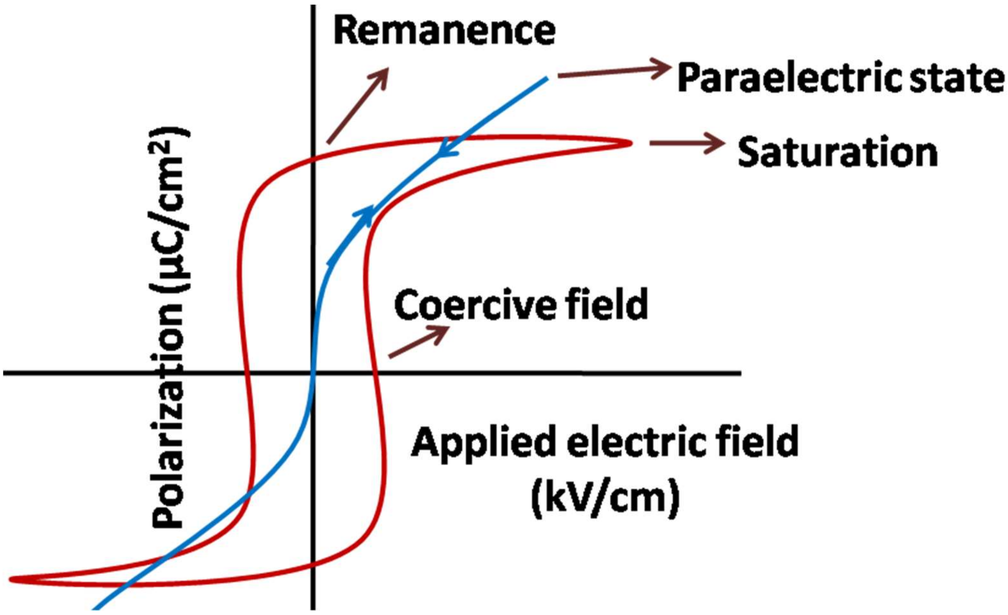

Figure 1.1 Representative PE loop of ferroelectric (hysteretic, red) and paraelectric (reversible path, blue) materials with the ferroelectric parameters.

Antiferroelectricity results from ordered array of ions and electrons of electric dipoles while neighboring dipoles are oriented in opposite directions. The antiferroelectric sublattices are interpenetrated and net spontaneous polarization is zero. This is in contrast to ferroelectric materials in which the dipoles are oriented in the same direction as reported in [11]. The antiferroelectricity phenomenon depends upon temperature, pressure, external electric field and preparation routes. Above Curie temperature (T_C) the hysteretic behavior of ferroelectric and double loop shaped PE disappears leaving a traceable reversible variation of P vs E resulting in paraelectric behavior.

1.2.2 Magnetism

Magnetism is the property of materials in which the spin alignment causes spontaneous magnetization in magnetic materials. The first known magnetic material to humanity is the loadstone or magnetite or Fe_3O_4 [12]. The magnetic ordering depends on the magnetic moment of each transition metal atom or ion and the exchange interaction between them. Based on this, magnetically ordered materials are divided into ferromagnetic, antiferromagnetic and ferrimagnetic. These materials are capable of exhibiting magnetic hysteresis under different circumstances of spin alignment of electrons as shown in Figure 1.2. In the case of ferromagnetic materials the exchange interaction of spins occurs through the unbalanced electron spins of the d-shell electrons. The oppositely aligned spin moments get cancelled completely giving a net zero magnetic moment in antiferromagnetic materials. Ferrimagnetism is a special condition of antiferromagnetism in which the oppositely aligned magnetic spins have unequal magnitude hence giving nonzero magnetic moment. In these above cases the magnetic behavior is controlled by temperature and governed by Curie-Weiss law. According to which the magnetic properties are lost beyond the Curie (Néel) temperature for ferromagnetic (antiferromagnetic/ferrimagnetic) materials. A brief discussion is provided below.

(a) Ferromagnetic Material

Ferromagnetic materials are considered to be composed of magnetic domains wherein the moments are aligned in a specific orientation in each domain as compared to that of the neighbouring domains. When the applied magnetic field increases these neighbouring domains align along the applied magnetic field the magnetization increases till saturation i.e., till all the domains align along the applied field. However when the applied field decreases, the magnetization decreases differing from the earlier path i.e., it does not reverse back the same way when the field was increased. As a result a remanent magnetization prevails in the absence of applied field. And an additional field, known as coercive field, is required to remove the remanence completely. Examples of such materials are Fe, Ni and Co. Depending upon the remanence and coercive field the ferromagnetic materials are classified as soft or hard ferromagnetic materials. Ferromagnetism strongly depends upon the temperature. With increase in temperature the randomisation of moments due to thermal energy dominate over the atomic phenomena of domain alignment. Hence the spins become paramagnetically ordered above after a certain temperature known as the ferromagnetic Curie temperature.

(b) Antiferromagnetic Materials

In Antiferromagnetic material, the neighbouring moments of the magnetic sublattice are aligned oppositely with equal magnitude and thus the net magnetic moment becomes zero. The spins become paramagnetically ordered above a certain temperature known as Néel temperature. Further, such type of material can exhibit weak ferromagnetism or ferrimagnetism under certain conditions such as surface effects or size effects or spin canting. Antiferromagnetic ordering in such materials are driven by Dzyaloshinskii-Moriya type of exchange interaction [13].

(c) Ferrimagnetic Materials

The special case of antiferromagnetism is ferrimagnetic in which the neighbouring spins though aligned in opposite direction lead to net magnetic moment arising from unequal magnitude of spins on the application of external magnetic field.

The spin alignment and the field dependent magnetization of different type of magnetically ordered materials are presented in Figure 1.2 and Figure 1.3. Further the temperature dependence of susceptibility (χ = M/H) for different type of magnetically ordered materials are shown in the Figure 1.4.

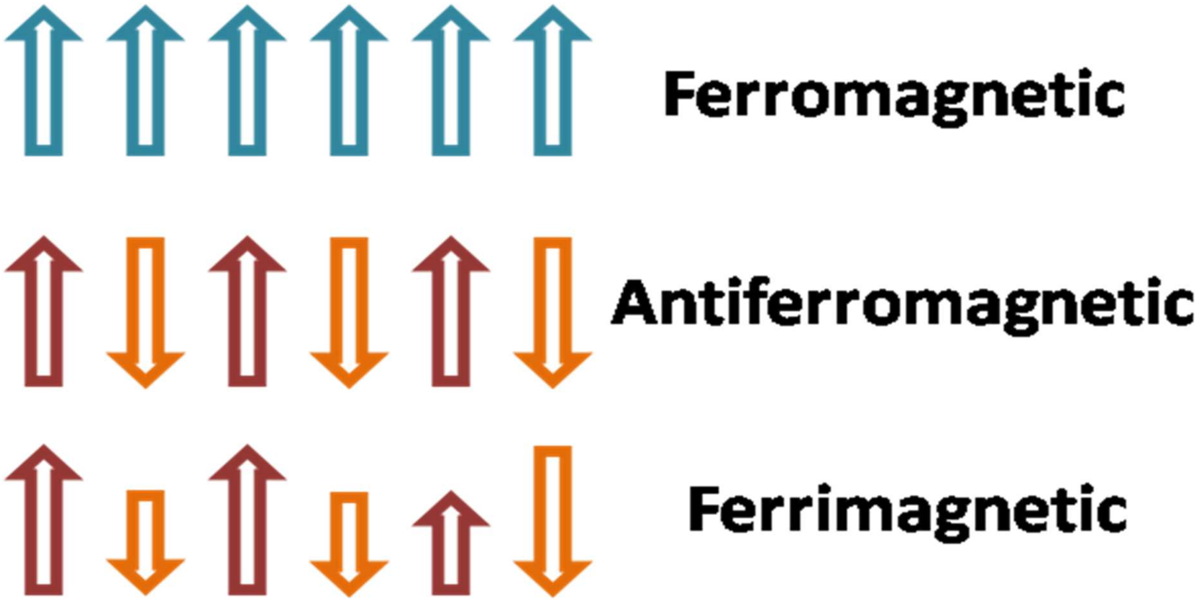

Figure 1.2 Spin alignment corresponding to ferromagnetic, antiferromagnetic and ferrimagnetic structure.

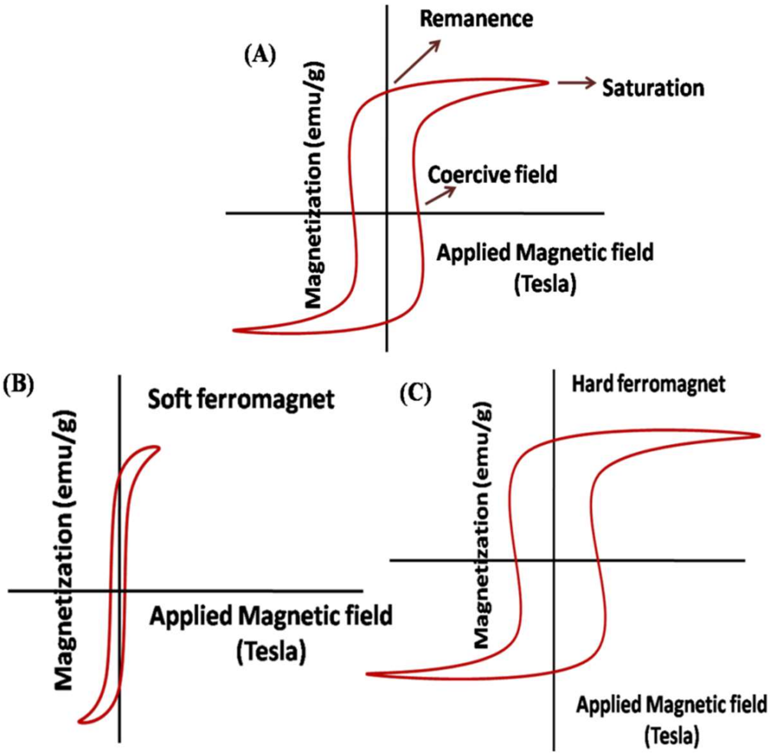

Figure 1.3 M H loop showing the magnetic parameters (A), the MH loop of soft (B) and hard ferromagnets (C).

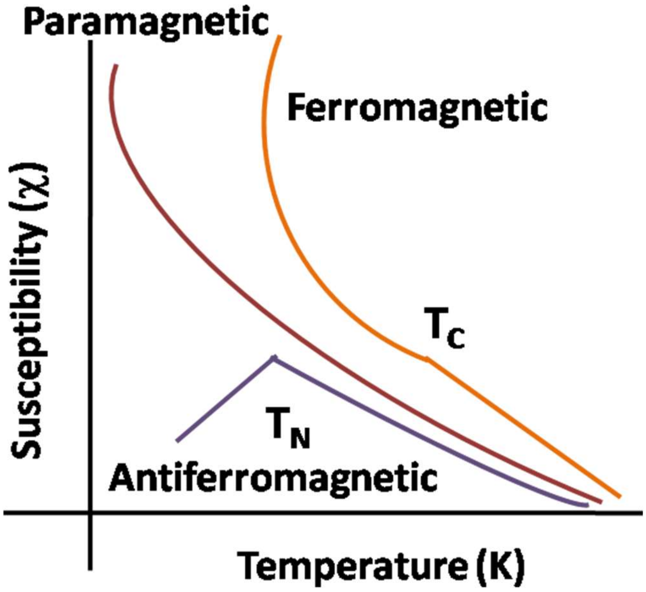

Figure 1.4 Typical variation of susceptibility with temperature for ferromagnetic, antiferromagnetically ordered materials. The Néel and Curie temperature for antiferromagnetic and ferromagnetic materials are also marked.

1.3 Multiferroicity

Materials with more than one ferroic order are termed as multiferroics. This term was first coined by Schmid [14]. However the possibility of the existence of such physical phenomenon of magnetoelectric effect was theoretically proposed by Landau and Lifshitz [15]. Almost after a decade, the experimental observations were made by Astrov and Ascher [16–18] towards the existence of such materials. The multiferroic materials are broadly divided into two groups: ferroelectric multiferroic and magnetic multiferroic. These groups are further branched into subgroups based on the origin of multiferroicity as schematically shown in Figure 1.5. Type I group is known as ferroelectric multiferroic in which the sources of magnetic and ferroelectricity are different e.g. $BiFeO_3$, $BiMnO_3$. The second type categorised as type II belonging to materials in which specific magnetic ordering leads ferroelectricity. These materials are expected to display optimal magnetoelectric coupling.

As there is a scarcity of single phase multiferroics, extensive research have also been carried out towards obtaining composite multiferroic based on multiphase materials, nanostructures, heterostructures and heterostructured multilayer thin-films [19,20].

1.3.1 Origin and Types

Based on the source of the contribution to magnetoelectric coupling the whole family of multiferroic materials are divided into two broad classes. In type I based multiferroic material the source of magnetic and ferroelectric is of different origin and in type II with the origin of ferroelectricity lying on type of magnetic structure. The former type shows weak coupling and known as ferroelectric multiferroic whereas the later with the coupled the origin exhibits comparatively stronger magnetoelectric coupling and known as magnetic multiferroic.

The schematic of broad classifications as well as subclasses are presented in Figure 1.5. Type I ferroelectric multiferroic is subdivided on the basis of origin of ferroelectricity such as lone pair associated, charge order related or geometric multiferroic. In these classes of multiferroics the ferroelectric origin governs the multiferroicity while the magnetism is originated from the magnetic ions at a different site. Such materials exhibit high transition temperatures and hence multiferroic at room temperature. The magnetic domains in ferroelectrically ordered regions lead to the magnetoelectric coupling. The first subclass of lone pair associated multiferroic consists of cations with stereochemically active lone pairs (e.g. Bi^{3+}, Pb^{4+}) contributing to ferroelectricity by the displacing cations with respect to the bigger oxygen octahedron. The magnetic ions (e.g. Fe^{3+}, Mn^{4+}) contribute to magnetic nature. Examples of materials having this origin are $BiFeO_3$, $BiMnO_3$. The second subclass with charge order related ferroelectric multiferroic exhibits charge ordering to break inversion symmetry hence inducing ferroelectricity and the magnetic ion comprehending for magnetic properties makes the system multiferroic. A first such mechanism was presented in 2004 [21]. An example of it is H_2 where charge ordering induces multiferroicity. Geometric multiferroic is a secondary phenomenon involving rotation and tilting of octahedra responsible for ferroelectricity. Such phenomenon is basically experienced in hexagonal perovskites $RMnO_3$where R are rare earth ions. The five fold Mn^{3+} is surrounded by oxygen trigonal bipyramids forming a layered structure of Mn between oxygen tetrahedra. This induces distortion of varying R–O bonds and causes distortion. This changes the local environment which is responsible for formation and stability of the crystal structure [22]. Such phenomenon is called as pseudo Jahn-Tellar effect or second order Jahn-Tellar effect [23].

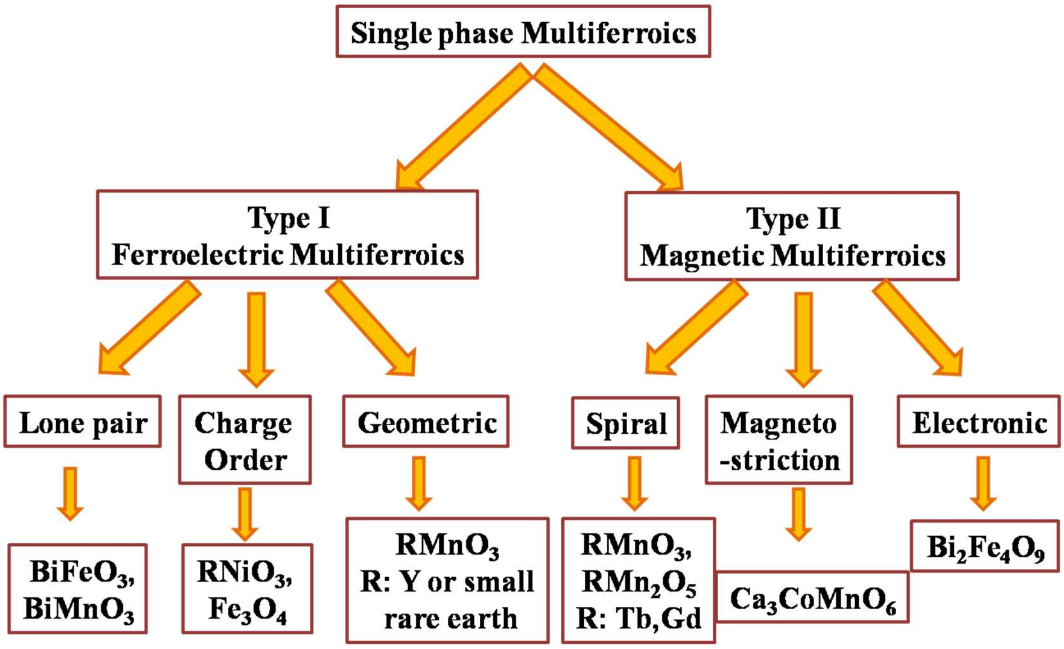

Figure 1.5 Classification of multiferroics and shown are the subclass of multiferroics.

The type II class of magnetic multiferroic is divided into spiral magnetic structure leading to ferroelectricity and hence multiferroicity or mechanism such as magnetostriction and electronic origin leading to magnetic properties. This particular type magnetic structure breaks inversion symmetry leading to ferroelctricity in the first subclass of magnetic multiferroic. There are various types of spiral structures e.g. cycloids, conical, spherical (Figure 1.6 andFigure 1.7). In general, the spin wave cycloids are incommensurate with underlying crystal lattice. The polarization is produced by cycloidal structure wherein polarization of consecutive bonds adds, produce net ferroelectric and multiferroic behavior. The total polarization of the cycloid lies in the plane of rotating spin and perpendicular to the spiral axis. The mechanism of ferroelectric and multiferroic in the most common case of cycloidal structure is explained by Dzyaloshinskii-Moriya effect [13]. The second class under type IIis magnetostriction, which depends on superexchange interaction. The ions shift in magnetically ordered phase and cause electric polarization. Examples of such material are $TbMn_2O_5$, Ca_3CoMnO_6 (cf. Figure 1.8(A)) [24,25]. In these cases collinear structure can also exhibit multiferroicity and expected to show large polarization values. Frustrated magnetic system exhibits multiferroicity by following electronic mechanism. In this type, charge redistribution occurs leading to dipole moment orientation as shown in Figure 1.8(B), e.g. in $Bi_2Fe_4O_9$.

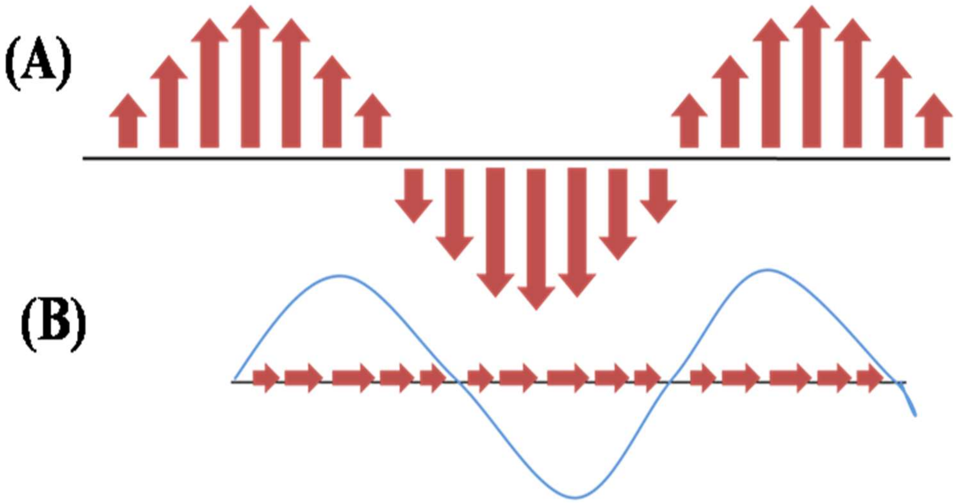

Figure 1.6 The spin cycloid overriding on the crystal lattice, the spin perpendicular (A) and parallel (B) with respect to the lattice.

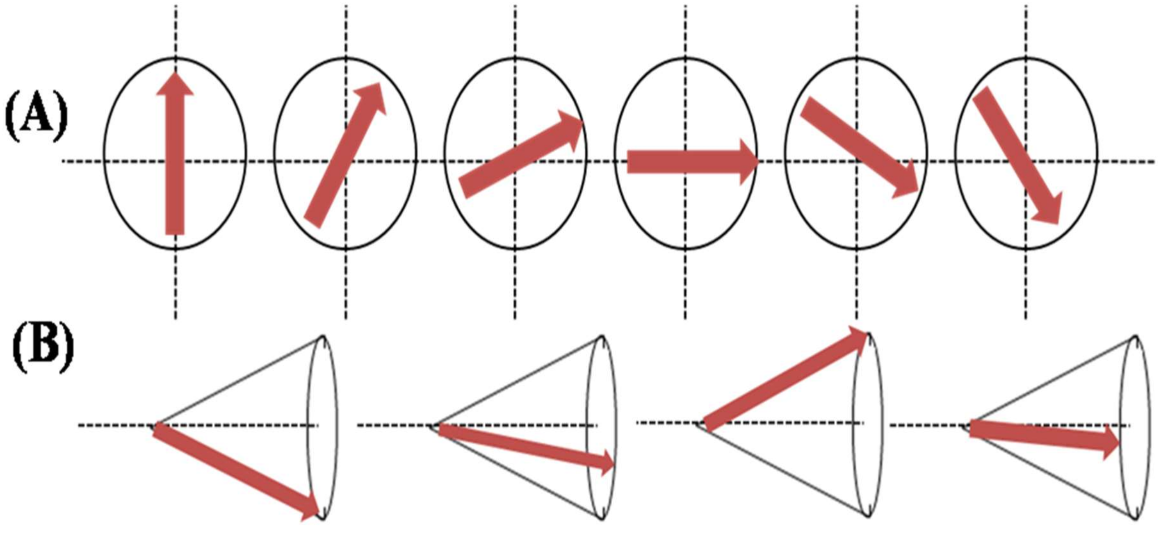

Figure 1.7 The spherical cycloid (A) and conical cycloid structure (B) with spin orientation.

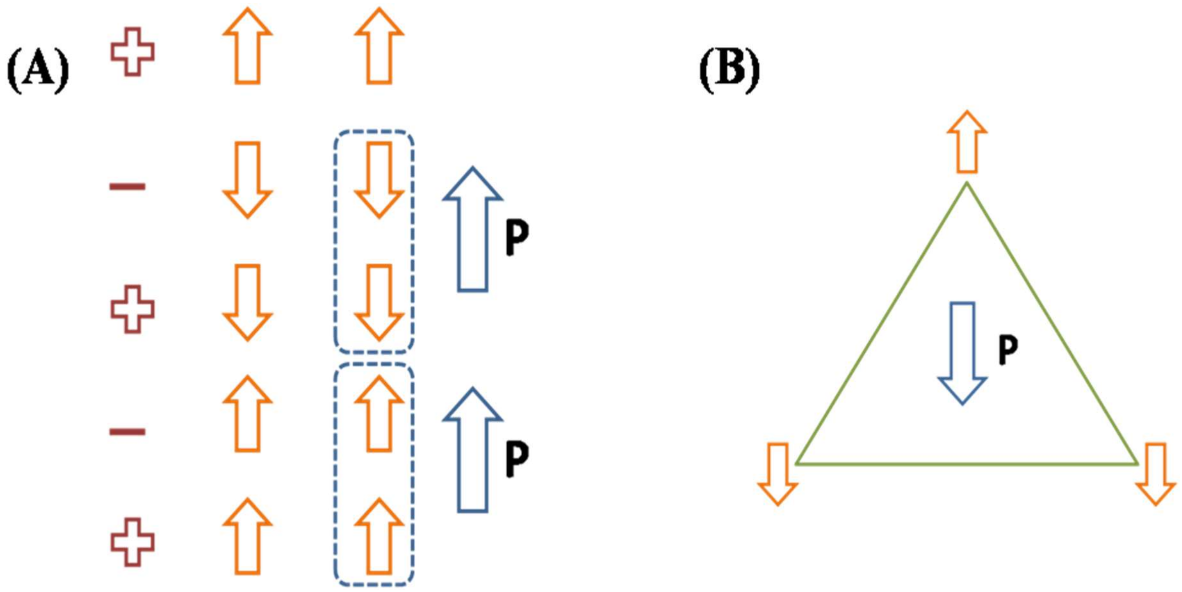

Figure 1.8 Magnetostriction leading to multiferroic properties in Ca_3CoMnO_6 and frustrated magnetism of electronic origin leading to multiferroism.

In spite of these characteristic origins, it is cumbersome to get multiferroic of appreciable ordering parameter values and coupling and thus composites of different structure are studied. The divisions of classes are presented Figure 1.9.

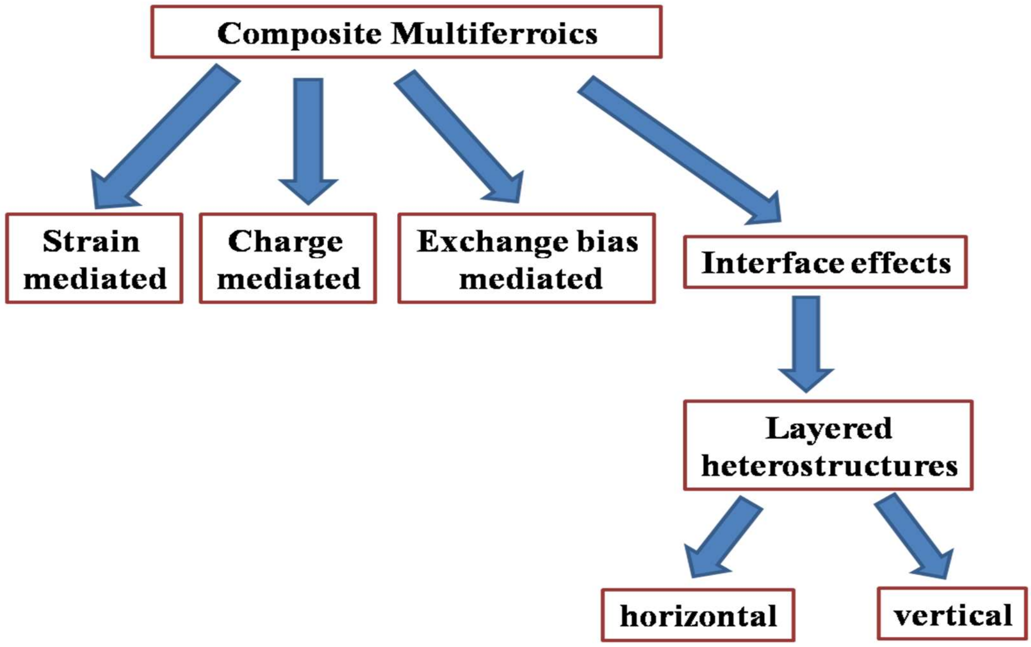

Figure 1.9 Composite multiferroics and their classifications based on origin.

1.4 Brief Review of Ferroelectric and Magnetic Properties of Bismuth Iron oxide Based Multiferroics

Even though a wide number of materials e.g fluorides, borides and manganites exhibit multiferroism but hardly a few are suitable for different applications because the transition of ferroelectric to paraelectric, AFM/FM to PM temperature lies lower than room temperature (RT) and hence a low value of coupling coefficient. In order to explore the applicability, the transition temperature should be close to RT and the coupling coefficient should be enhanced appreciably. Further, Fe based multiferroic is unusual because of the presence of d electrons in Fe which is complementary to the existence of ferroelectricity and tends to inhibit multiferroism. So far, out of the well studied materials $BiFeO_3$ finds importance in research because the (AFM-PM and ferroelectric-paraelectric) transition occurs well above 300 K, so that it exhibits multiferroic properties at room temperature. The magnetic transition from antiferromagnetic to paramagnetic occurs at 643 K whereas ferroelectric to paraelectric at 1103 K [26,27]. From the Fe rich end of the Bi_2O_3–Fe_2O_3 phase diagram, in addition to $BiFeO_3$, i.e. $Bi_2Fe_4O_9$ also has the potential of a type II multiferroic material. The magnetic and electric transition temperature are observed to be at 250 K, 260 K respectively [28,29]. The applicability of these multiferroic materials are reported in [30–32]. Properties of both these materials were studied in detail starting from structure, magnetic, ferroelectric, dielectric as well as magnetoelectric properties. The following section discusses briefly the magnetic and ferroelectric properties so far known.

1.4.1 $BiFeO_3$: Type I Multiferroic

$BiFeO_3$ is an equilibrium compound in the respective phase diagram of bismuth and iron oxides. It has a distorted rhombohedral structure of space group *R3c* with lattice parameter a=b=5.576 Å, c=13.867 Å and $\alpha=\beta=90°$, $\gamma=120°$ [33] consisting of six formula units per hexagonal unit cell. This distorted structure is analogous to the pseudocubic structure with lattice parameters a= 3.958 Å and $\alpha=90°$ [34] and contains two formula units. The unit cell of $BiFeO_3$ is shown in Figure 1.10. $BiFeO_3$ exhibits rhombohedral (*R3c*) α-phase at room temperature which undergoes structural transition to orthorhombic *Pbnm* β-phase at 825 °C [35] and further to γ-phase which is cubic metallic $Pm\bar{3}m$ at 1204 °C [36] satisfying the maximal subgroup criterion [37,38]. Being type I, the multiferroicity comes from two different sites; ferroelectricity comes from $6s^2$ lone pair electrons of Bi and magnetism arises due to Fe atoms.

1.4.1.1 Ferroelectricity in $BiFeO_3$

$BiFeO_3$ has three-fold rotational symmetry along c-axis and each fold has two possible directions of spin rotation. There are three equivalent propagation vectors for cycloidal arrangement with $Q_1[110]$,$Q_2[\bar{2}10]$ and $Q_3[1\bar{2}0]$ related to the magnetic structure due to DM interaction [39]. The possible direction related to spin chiral vector e_1 parallel to $[\bar{1}10]$ produces clockwise rotation and that of e_2 parallel to $[1\bar{1}0]$ produces anticlockwise direction as viewed from hhl plane [40]. The clockwise spin rotation gives induced polarization due to the inverse DM effect. The additional electric polarization observed is given by $\Delta P= A\ e \times Q$, where A is the material specific coefficient, e is the spin rotation of the chiral vector and Q is propagation vector of chiral magnetic structure [41]. Based on the symmetry of $BiFeO_3$ above T_N, ΔP should be parallel to the total polarization direction along the c axis. The ΔP is equally valid for the other two Q vectors [40]. Thus the polarization in $BiFeO_3$ is due to antiphase rotations of FeO_6 octahedra along the $[111]_c$ or $[001]_h$ axis by 13.8° with Fe displacing around the same axis away from the oxygen octahedra. Single crystal $BiFeO_3$ is reported to exhibit ferroelectricity in the order of 6 $\mu C/cm^2$ [42,43]. However, the thin films of the same exhibits two orders of magnitude higher than that of bulk due to strain enhancement [44,45]. Abinitio calculations of predicted high polarization values for bulk $BiFeO_3$ [5,45,46]. But the bulk form exhibits smaller experimental value because of the leakage due to conductive nature and high coercivity to attain the polarization state of $BiFeO_3$ [47].

1.4.1.2 Magnetism in $BiFeO_3$

The magnetic behavior in $BiFeO_3$ originates from the Fe site with Fe moments ordered in antiferromagnetic manner showing G type AFM behavior each having spin of Fe^{3+} is surrounded by six numbers of Fe^{3+}whose spins are aligned antiparallel. There are two distinct sites of Fe with differing distortions which could be studied by Mössbauer spectroscopy. Due to Dzyaloshinskii-Moriya (DM) interaction the unequally balanced spins result in canting which is superimposed upon a incommensurate spin cycloid of wavelength approximately 62 nm and cancels out the possible net magnetic moment [37]. Thus net magnetic moment of the bulk $BiFeO_3$ equates to zero. The spin cycloids propagate along the <111> direction for single crystal monodomain $BiFeO_3$ suggesting the magnetic symmetry lowering [43]. In thin film form as well, the magnetic structure varies because of surface strain effects [48]. Though in thin film form the polarization value is comparatively higher but in bulk and nanoform the coupling is expected to be higher as the spin cycloid is absent in the later case [49]. It has been reported that nanostructure as well as thin films provide better multiferroicity by modifying the ordering e.g. nanostructure form of $BiFeO_3$ exhibits ferromagnetic behaviour while in thin film form it shows strain mediated enlarged polarizations [2,50]. Further heterostructures as well as self assembled layers find wide range of applications because of their better properties [3,32].

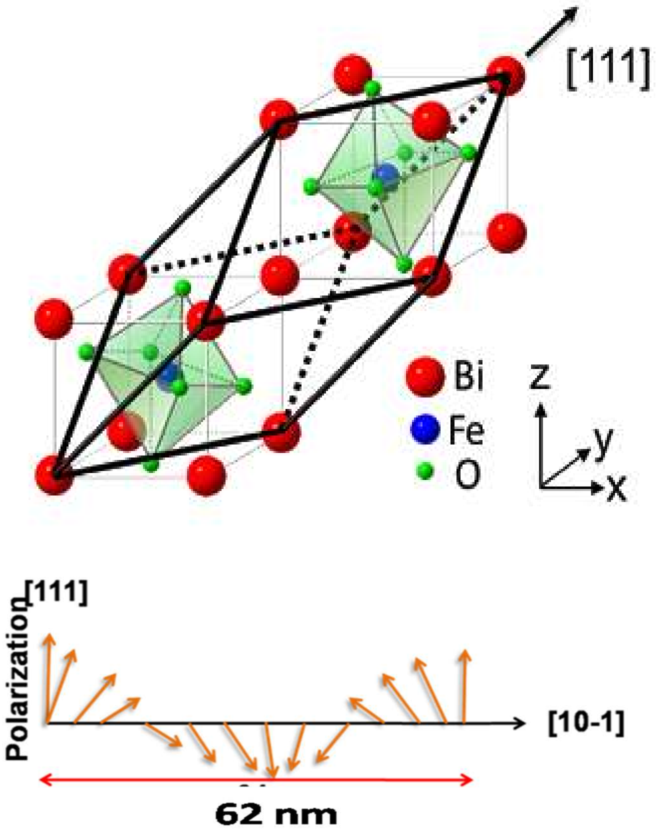

Figure 1.10 Unit cell of $BiFeO_3$ showing Fe sites of different distortion with polarization direction along [111] (top) and incommensurate spin cycloid causing AFM order (bottom).

Another bismuth iron oxide based multiferroic system which has been studied in this thesis is $Bi_2Fe_4O_9$. The role of defects in modifying the multiferroic properties of $Bi_2Fe_4O_9$ has been studied in a detailed manner.

1.4.2 $Bi_2Fe_4O_9$: Type II Multiferroic

$Bi_2Fe_4O_9$ is a generally formed as mullite phase during the preparation of $BiFeO_3$ at high temperature and found in Fe rich regions of the Bi_2O_3–Fe_2O_3 phase diagram. It is studied to have promising applications as photocatalysts and gas sensors in addition, claimed to be multiferroics. $Bi_2Fe_4O_9$ belongs to type II group of multiferroics with transition temperature T_C~260 K and T_N ~ 250 K [28,29]. Type II $Bi_2Fe_4O_9$ exhibits orthorhombic D_{2h}-*Pbam* structure with unit cell parameters a=7.95 Å b= 8.44 Å c= 6.01 Å and α=β=γ= 90° as reported in [51]. The Fe occupies equally at two sites by tetrahedral and octahedral sites of the unit cell. The octahedral Fe units are aligned along the c axis and connected through the corner sharing tetrahedral Fe units. The Bi surrounded by eight O^{2-} ions is sandwiched between the FeO_6 octahedral unit with orthogonal shorter BiO_3 and longer BiO_5 [52]. Being type II multiferroic, $Bi_2Fe_4O_9$ exhibits strong magnetoelectric coupling at room temperature.

1.4.2.1 Ferroelectricity in $Bi_2Fe_4O_9$

In addition to the frustrated magnetic behaviour of $Bi_2Fe_4O_9$ the Cairo pentagonal lattice structure also results in interesting ferroelectric behaviour leading from the spin frustration. Presence of stereochemically active $6s^2$ lone pair of Bi in $Bi_2Fe_4O_9$ contributes to ferroelectricity. The hybridization between s-orbital of Bi and p-orbital of oxygen leads to a non-centrosymmetric distortion which might be attributed to the ferroelectricity in $Bi_2Fe_4O_9$ [28,52–59].

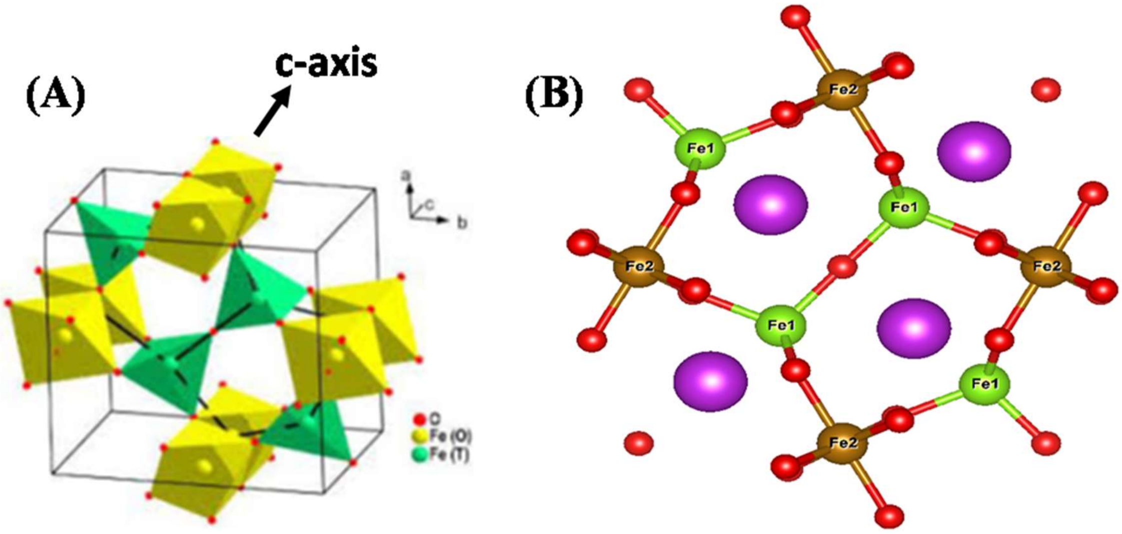

Figure 1.11 Unit cell of $Bi_2Fe_4O_9$ depicting the octahedral and tetrahedral Fe sites arrangement (A) and spin frustration exhibited by tetrahedral Fe1 and octahedral Fe2 ions in $Bi_2Fe_4O_9$ (violet bubble represents Bi atom) (B).

1.4.2.2 Magnetism in $Bi_2Fe_4O_9$

$Bi_2Fe_4O_9$ exhibits pseudo-planar *Pc2/m* magnetic structure [61] with bismuth planes sandwiched between Fe planes containing tetrahedral and octahedral units where the octahedra Fe units form chains along the c-axis and the corners shared by the tetrahedral units, with rich magnetic properties [61,62]. Bi is surrounded by eight O^{2-} ions with mutually orthogonal shorter BiO_3 and longer BiO_5 units [64]. The octahedral and tetrahedral Fe sites are equally distributed in the unit cell with a lower packing density than that of corresponding closed packed structures [51]. The tetrahedral Fe sites are antiferromagnetically ordered among themselves and with that of octahedral sites whereas the octahedral sites are ferromagnetically ordered [55,60]. There is a competitive exchange interaction between the FeO_6 octahedra with FeO_4 tetrahedra inducing geometric spin frustration and antiferromagnetic order in $Bi_2Fe_4O_9$ [28,60]. The weak ferromagnetism in $Bi_2Fe_4O_9$ is attributable to the uncompensated spin surfaces and spin canting [28,64].

Summarising in both $BiFeO_3$ and $Bi_2Fe_4O_9$, the ferroelectricity is seen to be arising due to the $6s^2$ lone pair electrons of the Bi atoms. This results in hybridization between the empty 6p orbital of Bi and 2p orbital O causing off-centering of cations towards the neighbouring anions. For example in the case of $BiFeO_3$ it is seen that the ferroelectricity leads to the distortion of the FeO_6 octahedra. This would result in the variation of local structure around Fe atoms. This can be probed effectively by any technique like EXAFS which is capable of resolving short range structural informations like coordination numbers, bonding and bond lengths. The above ferroelectricity induced distortion of the FeO_6 octahedra would also lead to the variation of Fe–O–Fe bond angle, thus affecting the super exchange interaction. Hence, the local magnetic properties like magnetic moments at Fe atoms would be different. Similarly in the case of $Bi_2Fe_4O_9$ there is a strong coupling effect between the ferroelectricity, which is contributed mainly by the lone pair $6s^2$ electrons which get significantly modified by the frustration of spins at the Cairo pentagonal lattice, and the magnetic properties. Hence, by means of probing both the local structure and magnetic fields at the Fe sites a number of important issues related to the bulk multiferroic properties of bismuth iron oxide can be understood using hyperfine interaction based techniques.

Thus in this thesis, ^{57}Fe Mössbauer spectroscopy, a hyperfine interaction based technique is employed to deduce the local structure and hyperfine fields at Fe sites to provide a deeper understanding of some of the important issues such as the role of defects if any in $BiFeO_3$ nanoparticles and of cationic substitution in bulk $BiFeO_3$ for the multiferroic properties of these systems. The defects induced modifications in the local structure of $Bi_2Fe_4O_9$ are studied using Mössbauer spectroscopy in this thesis. Bulk structural studies are carried out using X-ray diffraction and Raman spectroscopy. While the ferroelectric properties of the systems of interest are studied using P–E loop measurements, bulk magnetic properties of bismuth iron based oxides are studied by deducing magnetization. These studies will provide an atomic scale understanding of the bulk structural and magnetic properties of the systems of interest of the present thesis namely bismuth iron oxides produced and/or subjected to different treatments, by means of looking for a correlation if any exists between the local structure and magnetic fields at Fe sites as deduced by Mössbauer spectroscopy with the bulk properties of these bismuth iron oxides. In the following the basic principle and the deduction of hyperfine parameters using ^{57}Fe based Mössbauer spectroscopy are briefly discussed emphasizing with respect to bismuth ferrites. The Interaction between the nuclear moments with the electromagnetic fields at the sites of probe nuclei is called as the hyperfine interaction. Details regarding the hyperfine interactions and the basics of obtaining the related solid state hyperfine parameters using Mössbauer spectroscopy are discussed in the following.

1.5 Mössbauer Spectroscopy for Local Structure and Magnetic Property Studies

Mössbauer spectroscopy is a hyperfine interaction based technique based on which the local structure and magnetic fields at the sites of probe atoms could be studied and thereby the solids of interest can be studied at atomic scale. Interaction between nuclear moments at the isomeric state of the probe nucleus with electromagnetic fields at their sites of their occupation in any matrix of interest is called as hyperfine interaction consisting mainly of electric monopole interaction, magnetic dipole interaction and electric quadrupole interaction. Electric monopole interaction is due to the interaction between nuclear and electronic charges which result in a shift of nuclear energy levels. Magnetic dipole interaction occurs due to the interaction between the nuclear dipole moment at the isomeric state with magnetic field at the site of the probe atom in a magnetically ordered solid. Quadrupole interaction is between nuclear quadrupole moment at the isomeric state of the probe nucleus with electric field gradient at the site of occupancy of the probe atom in the solid. This interaction exists in defect free non-cubic solid or in solid with defects. Probe atoms located at nearby defects experience non-cubic symmetry and hence experience quadrupole splitting. Hyperfine interaction, results in shift and/or splitting of nuclear energy levels thereby resulting in removal of (2I+1) fold degeneracy of isomeric state of spin I. Also the hyperfine interaction results in precession of nuclear spin. Strength of hyperfine interaction can be deduced either by measuring the spin precession frequency or by measuring shift and /or splitting of nuclear levels which will be typically of the order of a few micro eV. Hyperfine interaction technique such as time differential perturbed angular correlation (TDPAC) spectroscopy is used for measuring the spin precession frequency. The shift and / or splitting of nuclear levels quantifying the magnitude of hyperfine interaction can be measured directly by Mössbauer spectroscopy. These techniques are used for characterizing local structure and magnetic properties at an atomic scale around the probe atoms. In this thesis, ^{57}Fe based

Mössbauer spectroscopy is extensively used for characterizing the local structure and magnetic properties of bismuth iron oxide based ferroelectric materials. In the following, each hyperfine parameters and the basic principle of Mössbauer spectroscopy for deducing hyperfine splitting of the order of micro-electronvolt (μeV), thereby the characterization of the local structure and magnetic properties are discussed.

Hyperfine Interaction:

The interaction between nuclear moments at the isomeric state of the resonant nucleus with electromagnetic field at the nucleus results in the shift and/or splitting of nuclear levels leading to the removal of (2I+1) degeneracy of the isomeric state with spin I. The three main hyperfine interactions corresponding to the nuclear moments determining the nuclear levels:

a) Electric monopole interaction (e0) – isomer shift.

b) Magnetic dipole interaction (m 1) – nuclear Zeeman effect.

c) Electric quadrupole interaction (e2) – quadrupole splitting

1.5.1 Basic Methodology of Mössbauer Spectroscopy

Mössbauer spectroscopy is based on the Mössbauer effect which is defined as the recoilless emission and absorption of gamma rays by probe nuclei in a solid matrix. Mössbauer effect is schematically shown in Figure 1.12. In the following it is discussed as to how this effect is utilized to measure directly the hyperfine interactions induced shift and/or splitting of nuclear levels and thereby use it as a powerful tool for the studies of local structure and magnetic properties of the systems of interest.

Considering a radioactive source in which the source atoms are introduced in a solid matrix and subjected to a Doppler velocity shift + v with respect to a fixed solid matrix in which the absorber atoms (which can resonantly absorb the gamma ray of interest as emitted by the source concerned) are introduced. These two matrices (or samples) will simply be referred henceforth as source and absorber respectively. Because of the Mössbauer effect there is resonance absorption of gamma ray by the absorber atoms which are in the ground state.

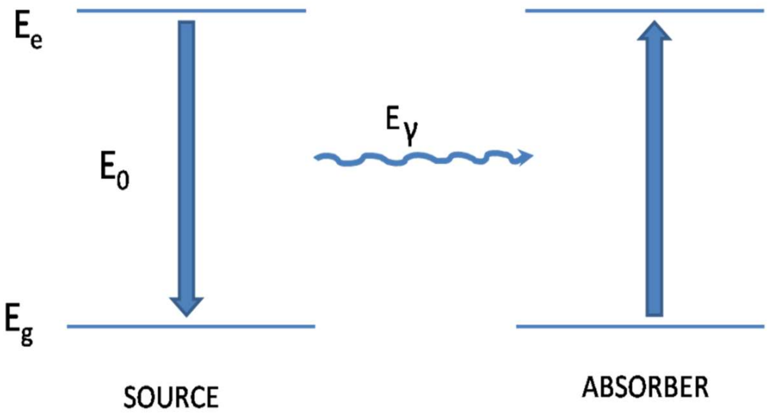

Figure 1.12 Schematic illustrating Mössbauer effect.

In view of the sharpness of the zero phonon emission line (10^{-7} eV), limited only by the lifetime of the excited state, it was immediately realized that this resonance phenomenon could be used as a probe to study the magnetic and quadrupole interaction of the nuclear moments with the surrounding electrons of the matrix of interest. Among others, Mössbauer probes such as ^{57}Fe, ^{119}Sn and ^{61}Ni are commonly used [65–67]. ^{57}Fe Mössbauer spectroscopy is quite commonly used due to the reasonably low gamma energy which in turn reduces the recoil of nuclei, longer half life time of the gamma source and the high abundance of Fe and its compound. Application of Mössbauer spectroscopy in probing solid state materials brings out a very good understanding of the local structure, electronic and magnetic properties, relaxation phenomena and lattice dynamics [68–71]. Review articles and books describing instrumentation and applications can be found [72–74] elsewhere. Interaction between nuclear moments at the isomeric state of resonant absorber atoms with electromagnetic fields results in a shift and splitting of nuclear energy levels. By means of Doppler shifting of the source γ-rays energy the resonant absorption is measured as a function of the relative velocity of the source with respect to the absorber in a Mössbauer measurement. Different terms of hyperfine interaction and the deduced solid state parameters have been explained in the following.

1.5.1.1 Isomer Shift due to Electric Monopole Interaction

The nuclear energy levels respond to the change in the s-electron density which arises due to change in valence electrons via shielding effect resulting to an altered Coulombic interaction which manifests itself as a shift in the nuclear levels as shown in Figure 1.13. The term “isomer shift” has been uniformly adopted because the effect depends on the difference in the nuclear radii of the ground (R_{gd}) and isomeric, excited (R_{ex}) states. The term “chemical shift” has also been used. The effect is properly considered as a part of electric hyperfine interaction and called as the “electric monopole interaction” in analogy with the electric quadrupole splitting.

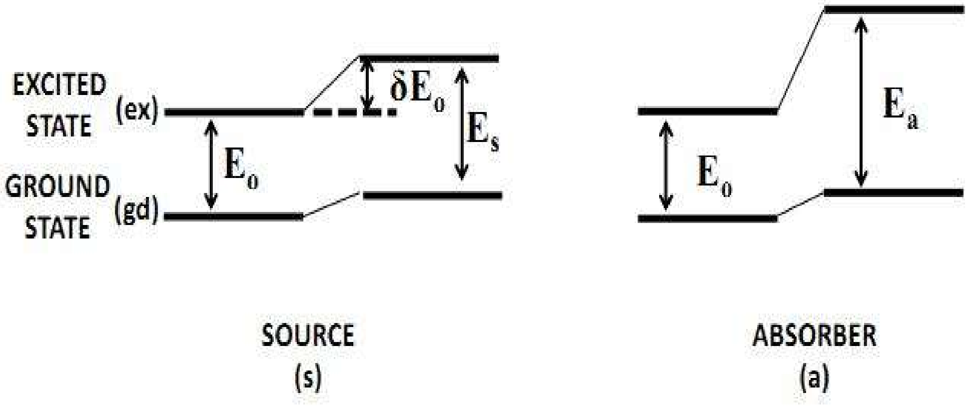

Figure 1.13 Nuclear energy levels of a source and an absorber.

The change in the energy of the gamma ray due to the nuclear electrostatic interaction can be expressed as:

$$\delta E = \delta E_{ex} - \delta E_{gd} = \frac{2\pi}{5} Ze^2 |\psi(0)|^2 (R_{ex}^2 - R_{gd}^2) \qquad 1.1$$

Where, $-e|\psi(0)|^2$ is the electronic charge density

The gamma ray energy of a recoilless free emission and absorption is given by:

$$E_s = E_o + \frac{2\pi}{5} Ze^2 |\psi_s(0)|^2 (R_{ex}^2 - R_{gd}^2) \qquad 1.2$$

and,
$$E_a = E_o + \frac{2\pi}{5} Ze^2|\psi_a(0)|^2(R_{ex}^2 - R_{gd}^2) \tag{1.3}$$

Therefore, Isomer shift (IS) $= Ea - Es$

$$= \frac{2\pi}{5} Ze^2|\psi_a(0)|^2(R_{ex}^2 - R_{gd}^2) \tag{1.4}$$

The simplified formula for chemical isomer shift is given as

$$\delta_c = \Delta E_{IS}\left(\frac{c}{E_0}\right) = \alpha\,\Delta|\psi(0)|^2 \tag{1.5}$$

where ΔE_{IS} is the difference between the median transition energies of the absorber (E_A) and the source $\Delta E_{IS}\left(\frac{c}{E_0}\right)$ is the Doppler conversion factor from energy to speed. $\Delta|\psi\ (0)|^2$ is the difference between the electron densities at two identical nuclei, one of which is embedded in the source material, while the other in the absorber material. Among others the parameter α comprises of many factors including the relative difference between the radius of source and absorber atoms.

The second order Doppler shift (SOD) is added to the isomer shift and the sum is referred to as centroid shift. The crystal vibrations are temperature dependent and based on the Debye model of vibrations of atoms the second order Doppler shift could be derived based on the Debye model as

$$SOD = -2.19 \times 10^{-3}\left(\frac{T^4}{\theta_D^3}\right)\int_0^{\theta_D} \frac{x^3}{e^x - 1}dx \tag{1.6}$$

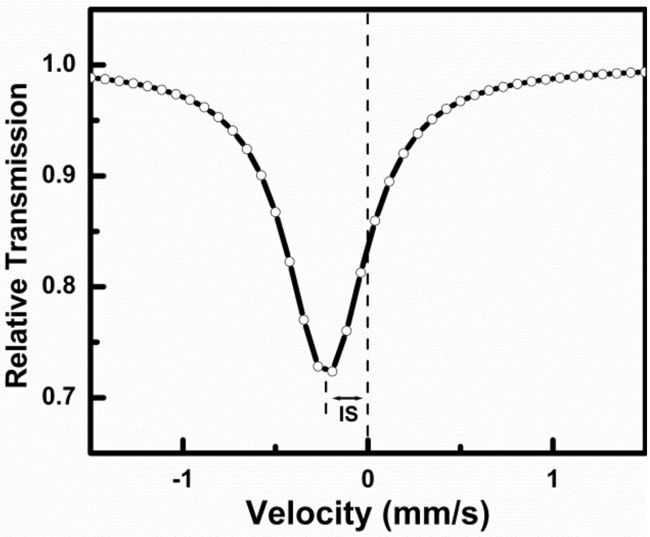

Figure 1.14 Mössbauer spectrum obtained in a sample in which ^{57}Fe exposed to only monopole interaction.

Hence the SOD at high temperature is almost dependent of the Debye temperature of the crystal. Hence SOD will be contributing mainly at the low temperatures. Hence at room temperature the centroid shift is almost same as isomer shift (cf. Figure 1.14).

1.5.1.2 Magnetic Hyperfine Field due to Magnetic Interaction

The magnetic hyperfine structure arises from the interaction of the magnetic dipole moment **μ** at the isomeric state with the magnetic field, **H**, due to the atom's own electrons. The eigenvalues of the Hamiltonian of the interaction or the energy levels obtained are

$$E_m = -\mu \frac{Hm_I}{I} = -g\mu_n H m_I , \quad m_I = I, I-1, \dots, -I \qquad 1.7$$

Splitting due to magnetic hyperfine interaction is hence given as

$$\Delta_m = \Delta E_m \left(\frac{c}{E_0}\right) = -g_I \mu_N B_{eff} \left(\frac{c}{E_0}\right), \qquad 1.8$$

where ΔE_m is the energy splitting due to magnetic interaction. g_I is a nuclear factor depends on the nuclear spin I of the nucleus, m_I is the magnetic quantum number and μ_N is the nuclear magneton. Effective magnetic field at the site of a resonant absorber is essentially due to the combination of different mechanisms such as Fermi contact interaction, orbital and dipolar interactions. Fermi contact field (H^c) arises from a net spin-up or spin-down s-electron density at the nucleus as a consequence of spin polarization of inner filled s-shells by spin-polarized partially filled outer shells. Hyperfine field H^L is due to orbital motion of valence electrons with the orbital momentum quantum number L. Spin dipolar field H^d is understood to arise from the total electron spin of the atom under consideration. All contributions add up to the total effective magnetic field $H_{eff} = H^c + H^L + H^d$.

The allowed gamma transitions between the equally spaced sublevels of the excited state and those of the ground state in the case of pure magnetic interaction between nuclear magnetic moment with effective magnetic field are given by the selection rules for magnetic dipole transitions: $\Delta I = 1$, $\Delta m_I = 0, \pm 1$. Therefore for ^{57}Fe having ground state I = 1/2 and excited state I = 3/2, exhibit 6 allowed transition as shown in Figure 1.15

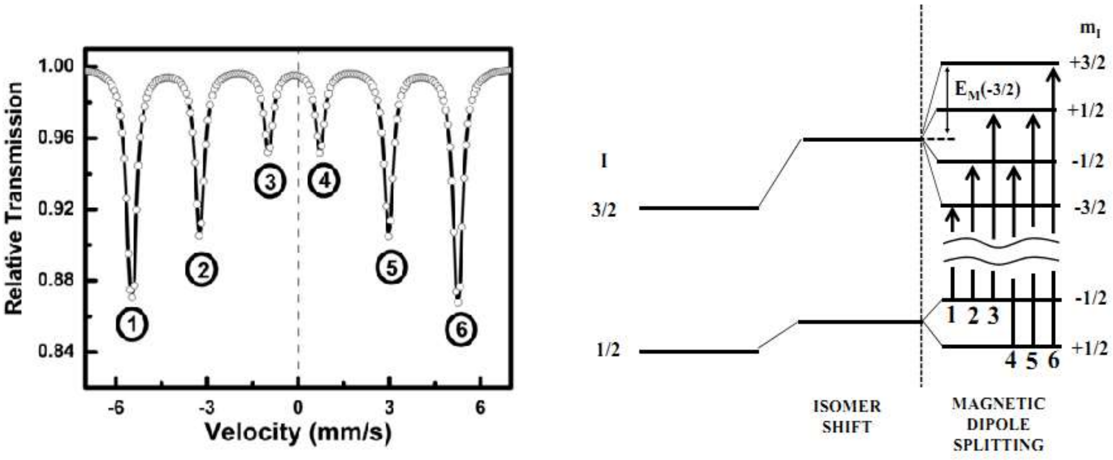

Figure 1.15 Mössbauer spectrum obtained for a magnetically ordered material (left) and the energy transition corresponding to the peak of Mössbauer spectrum (right).

In a Mössbauer spectrum of a magnetically ordered absorber usually observes a resonance sextet, the centroid of the spectrum may be shifted from zero velocity by electric monopole interaction yielding the isomer shift parameter δ. The peak position assigned to the peaks of Mössbauer spectrum (Figure 1.14(left)) refer to those of the γ-ray transitions between the sublevels of the excited state and the ground state (right). The relative intensities of the various allowed transitions as determined by the squares of the Clebsch-Gordan coefficients are given in Table 1.1.

Table 1.1 Various allowed transition and its relative intensity.

Transitions	Δm	Total	Angular dependence
3/2 → 1/2 -3/2 → -1/2	1 +1	3	$\frac{9}{4}(1+\cos^2\theta)$
1/2 → 1/2 -1/2 → -1/2	0 0	2	$3\sin^2\theta$
-1/2 → 1/2 1/2 → -1/2	+1 -1	1	$\frac{3}{4}(1+\cos^2\theta)$

For isotropic orientation of magnetic spins with respect to the direction of the γ-ray propagation the relative intensities are 3:2:1:1:2:3. The separation between the lines 2 and 4 (3 and 5) refers to the magnetic dipole splitting of the ground state. The separation between lines 5 and 6 (1 and 2, 2 and 3, 4 and 5) refers to the magnetic dipole splitting of the excited I = 3/2 state. The magnetic hyperfine splitting can be utilized to determine the effective magnetic field, magnitude and direction acting at the nucleus.

1.5.1.3 Quadrupole Splitting due to Electric Quadrupole Interaction

Interaction between nuclear quadrupole moment with the electric field gradient at the site of absorber atoms results in quadrupole splitting of isomeric state. The electric field gradient can be qualitatively understood to be due to valence electronic term V_{zz}^{elect} resulting from inequivalent electronic properties of five 3d orbitals of Fe and V_{zz}^{latt} which is due to non-cubic symmetry of the absorber. The V_{zz}^{latt} could arise either due to point defects associated with the absorber atoms or the non-cubic symmetry of the matrix or due to the quadrupole interaction the isomeric state with spin I=3/2 is split into $\pm 3/2$ and $\pm 1/2$ while there is no splitting of ground state spin with I= $\pm 1/2$ (Figure 1.16). Resonant absorption of 14.4 keV rays by absorber atoms results in a doublet in a Mössbauer spectrum as shown in Figure 1.16.

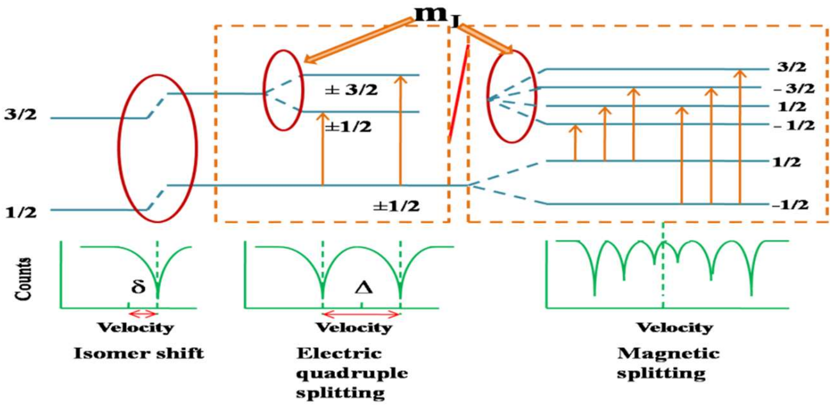

Figure 1.16 Schematic of hyperfine interaction induced shift /splitting in Mössbauer spectra.

The quadrupole splitting is given as

$$\Delta = \Delta E_Q\left(\frac{c}{E_0}\right) = \frac{1}{2}\left(\frac{c}{E_0}\right) eQV_{zz}\left(1+\frac{\eta^2}{3}\right)^{\frac{1}{2}}, \qquad 1.9$$

where V_{zz} is the principal component of EFG tensor, Q is the quadrupole moment and η is the asymmetry parameter given as $(V_{xx}-V_{yy})/V_{zz}$.

Magnetic dipole interaction and electric quadrupole interaction may be simultaneously present in certain cases. The perturbations are treated depending on their relative strengths. In the case of relatively weak quadrupole interaction the nuclear sublevels $|I, m_I>$ arising from magnetic dipole splitting are additionally shifted by the quadrupole interaction energies $E_Q(I, m_I)$; as a result, the sublevels of the excited I = 3/2 state are no longer equally spaced. The shifts by E_Q are upwards or downwards depending on the direction of the EFG. This enables one to determine the sign of the quadrupole splitting parameter ΔE_Q. Having discussed the basics of Mössbauer spectroscopy, the reported results the local structure and hyperfine fields at iron sites in bismuth ferrites are elucidated in the following.

Table 1.2 Brief description of hyperfine interactions and the details of the deduced solid state parameters using Mössbauer spectroscopy.

Hyperfine Interaction	Brief definition	Conditions to be satisfied with respect to	Resultant effect and the nature of the Mössbauer spectrum	Details of solid state parameters that are obtained

		nuclear and solid state parameters		
Electric monopole interaction	Interaction between nuclear charge and electronic charge. Source atoms ^{57}Co and absorber atoms^{57}Fe are different. The Coulombic interactions affects the ground and excited state of these atoms differently leading to a energy difference that is not the same	$R_{exc} \neq R_{gnd}$ $Abs^2 (\Psi_{exc}) \neq Abs^2(\Psi_{gnd})$	Shift in the ground and excited state nuclear levels Singlet with the centroid shifted from the origin	Oxidation state of absorber atoms,
Magnetic dipole interaction	Interaction between nuclear dipole moment with the magnetic field at the site of the nucleus	$I \geq \frac{1}{2}$,magnetic dipole moment $\mu > 0$ Matrix is magnetically ordered $B \neq 0$	Complete removal of (2I+1) fold degeneracy ➔ Splitting of ground in to 2 states and excited state in to 4 states. Transition between these states with selection rule $\Delta m_I = 0, \pm 1$ result in a six lined spectrum	Hyperfine field at the sites ofFe atom. Magnetic properties of systems of interest can be investigated
Electric quadrupole interaction	Interaction between nuclear quadrupole moment and the electric field gradient (EFG) at the site of the nucleus	$I \geq$,quadrupole moment $Q > 0$ Non-cubic charge symmetry at the site of the nucleus	Partial removal of degeneracy w. r t abs(m_I) of the nuclear levels. Excited state (I=3/2) splits in to two lines and there is no splitting of ground state with I=1/2. Transition results in a doublet	Electric field gradient at the site of the nucleus. Local structural and lattice / charge type of defects related aspects can be studied

1.6 Simulation of Mössbauer Spectra in $BiFeO_3$ and $Bi_2Fe_4O_9$

It is discussed earlier that the rhombohedral distortion along (111) as induced by ferroelectricity results in two FeO_6 octahedra being subjected to different degree of distortion. It is interesting and important to find out whether the Mössbauer study would be able to distinguish in terms of different values of hyperfine parameters as experienced by the Fe atoms associated with these two sites of the Fe–O_6 octahedra. Based on the reported results of Mössbauer spectroscopy it is understood that the octahedral distortion as experienced by two Fe atoms are different. This leads to the quadrupole splitting associated with these two sites are different quantifying different degree of octahedral distortion. This in turn also results in a slightly differing values of Fe–O–Fe based super exchange interaction resulting in two different values of hyperfine fields associated with the FeO_6 octahedra. The values of isomer shift associated with these two octahedral sites remains same as 0.3 mm/s implying that the valence of Fe atoms remains as +3. The simulated resolved spectra corresponding to two different sites and the resultant Mössbauer spectrum simulated in $BiFeO_3$ is shown in the Figure 1.17.

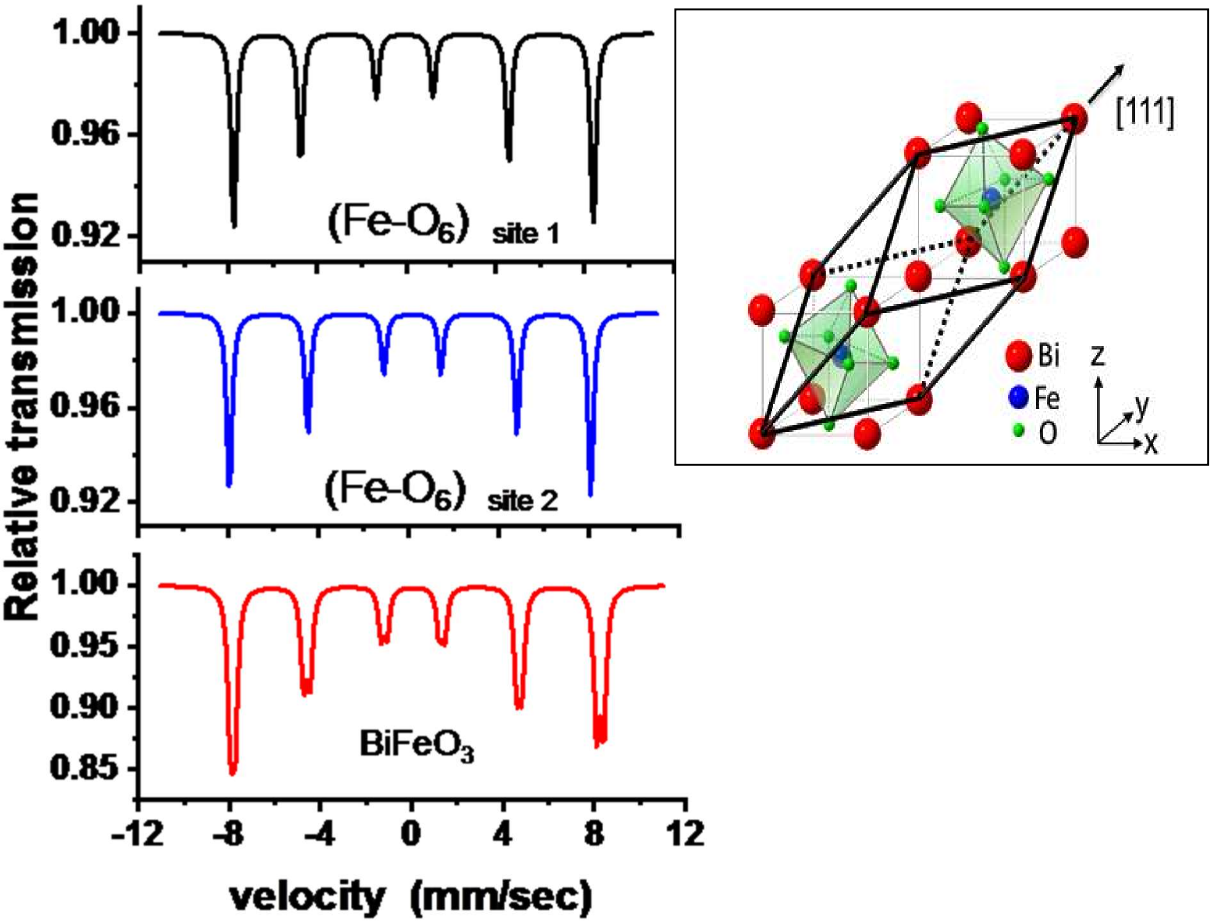

Figure 1.17 (left) presents simulated Mössbauer spectra of two octahedral Fe sites along with the resultant spectra of $BiFeO_3$ and (right) the unit cell of $BiFeO_3$ showing presence of the corresponding octahedral sites.

$Bi_2Fe_4O_9$ is paramagnetic at room temperature. In contrast to two octahedral Fe sites associated with $BiFeO_3$, the Fe sites of $Bi_2Fe_4O_9$, Fe sites are equally associated with octahedra and tetrahedra as can be seen in the Figure 1.18. Simulation of the resultant doublet is shown. Fe sites experiencing lower value of isomer shift close to 0.24 mm/s and high value of quadrupole splitting close to 0.92 to 1 mm/s is attributed Fe–O_4 tetrahedral sites. Fe atoms occupying octahedral sites experience Isomer shift close to 0.34 mm/s and a quadrupole splitting close to 0.35 mm/s.These sites are less distorted and the s-electron density is lower than that of other sites and hence experiencing a slightly higher value of isomer shift. Fe atoms associated with these two sites might be of +3 valence states.

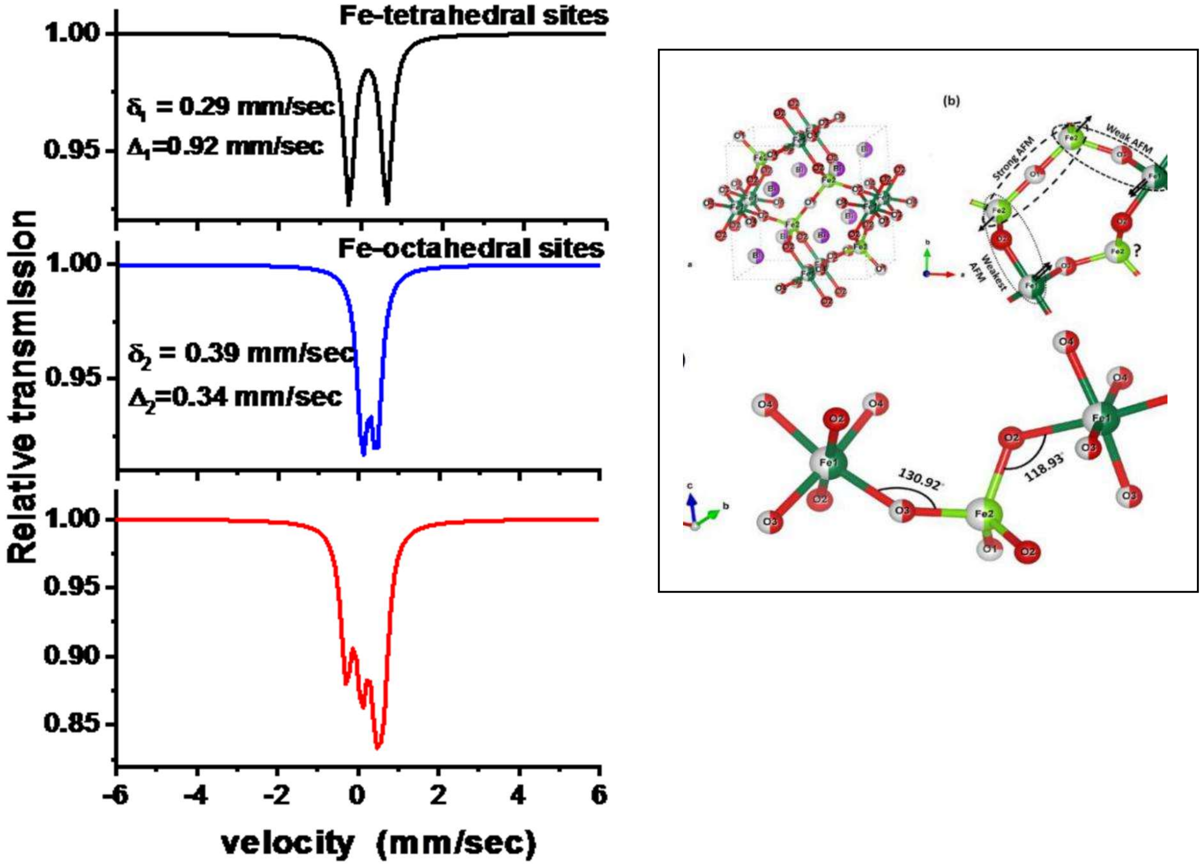

Figure 1.18 (left) presents simulated Mössbauer spectra of equidistributed octahedral and tetrahedral Fe sites along with the resultant spectra of $Bi_2Fe_4O_9$ and (right) the unit cell of $Bi_2Fe_4O_9$ showing presence of the corresponding sites as well as bond angles between octahedral and tetrahedral sites.

Following are some of the important issues related to bismuth ferrite which need to be addressed and understood in a more detailed manner.

1) Effect of ferroelectric properties on the antiferromagnetic ordering

2) Influence of size of the particles on ferroelectric and hence antiferromagnetic properties.

3) Influence of substitution at Bi sites on ferroelectric and any correlation of the same on the magnetic properties

4) The effect of simultaneous substitution at Bi and Fe sites on the multiferroic properties of $BiFeO_3$

5) Are there any other phases of iron oxides coexisting in a very small concentration less than 5% in $BiFeO_3$, which could not be deduced using XRD but can affect the effective magnetic property of such system.

Mössbauer spectroscopy could be effectively utilized along with other structural and magnetic characterization techniques to address the above issues as explained in detail as follows.

1.7 Motivation of the Thesis

This thesis is motivated to provide an understanding of the bulk structural, magnetic and ferroelectric properties of $BiFeO_3$ and attempts to comprehend the observed magnetic and ferroelectric properties and their coupling in terms of correlation of these bulk properties with hyperfine parameters as deduced using Mössbauer spectroscopy. This in turn could enable us to provide an atomic scale understanding of the observed bulk magnetic and ferroelectric properties in nano sized and substituted $BiFeO_3$.

Further in the case of $Bi_2Fe_4O_9$ the distortion of octahedral and tetrahedral Fe sites plays a crucial role in controlling the magnetic properties and hence ferroelectricity. $Bi_2Fe_4O_9$ is of a type II multiferroic wherein the magnetic frustration leads to the occurrence of ferroelectricity with the expected strong coupling between ferroelectricity and magnetic ordering. Mössbauer spectroscopy is utilized significantly for the studies of the changes in the local structure around the Fe sites due to defects and its manifestation or influence on the bulk ferroelectric and magnetic properties in $Bi_2Fe_4O_9$.

1.8 Organization of the Thesis

The chapters of the thesis are structured as follows. **Chapter 1** illustrates the basics of ferroic ordering with brief discussions on ferroelectricity and magnetism and multiferroic properties. Literature results on the ferroelectric, magnetic properties of $BiFeO_3$ and $Bi_2Fe_4O_9$ are briefly reviewed. Basic methodology of Mössbauer spectroscopy and the significance of hyperfine parameters have been elucidated. Various synthesis methods employed and characterization techniques used for studying different problems of interest in bismuth iron oxides are discussed in **chapter 2**. The effect of size of the particles of $BiFeO_3$ on the structural and magnetic properties has been elucidated in a detailed manner in **chapter 3**. In **chapter 4**, the influence of substitution at Bi site and the effect of simultaneous substitution of suitable cations at both Bi and Fe sites on the structural, magnetic and ferroelectric properties have been discussed. **Chapter 5** deals with the role of defects on the multiferroic properties of $Bi_2Fe_4O_9$ as well as on the magnetoelectric and magnetodielectric coupling. **Chapter 6** aims at understanding the basic mechanism of the formation of bismuth iron oxides through thermo-mechanical methods based on the results mainly obtained using Mössbauer spectroscopy and microscopic studies. Summary of the important findings of the thesis are highlighted in **Chapter 7** along with the possible future directions as driven by the results obtained in this thesis.

2 Experimental details

In this chapter the methods of preparation and tools for characterization of different phases of bismuth iron oxides are discussed in detail. The bulk solid state synthesis as well as the preparation of the nanoparticles of bismuth iron oxides (type-I $BiFeO_3$ and type- II $Bi_2Fe_4O_9$) using sol gel route are discussed in an elaborated manner. The structural analysis of these multiferroics were performed by XRD and Raman spectroscopy. The microstructural analysis SEM and TEM are employed. The VSM is used for bulk magnetic studies, while, dielectric studies and ferroelectric loop tracer are used for electric transport and coupling property studies respectively. Mössbauer spectroscopy has been extensively used in the thesis for the structural and magnetic properties as deduced at Fe sites by means of looking for a possible correlation, if any, of the hyperfine parameters with that in the bulk magnetic and ferroelectric properties of the systems under study.

2.1 Synthesis Routes

In this section the two well adopted synthesis techniques viz. Solid-state route and wet chemical citrate based sol-gel auto combustion method, which we have used in our work for the synthesis of bulk and nanoparticles of $BiFeO_3$, respectively, is discussed in detail.

2.1.1 Bulk Bismuth Ferrite Preparation through Solid-state Route

The solid-state reaction method is a well established technique for the preparation of a number of inorganic materials, mixed oxides, sulphides and nitrides to name a few [76]. The feasibility and the rate of a solid state reaction mainly dependent on the reaction condition, structural properties of the reactants, surface area of the solid particles and change in the thermodynamic free energy associated with the reaction. It is a simple method of preparation arising from thermally induced solid-state reaction without any other element involved, the steps involved are shown in Figure 2.1(A). In this process the starting materials are mixed thoroughly in agate mortar or ball milling to initiate the defects at the interfaces to reduce the particle sizes so as to allow the diffusion by reducing the diffusion path length between the cations and anions. The next step is the pelletization of thoroughly mixed powder which further ensures that the numbers of crystallites are in close proximity for reaction to occur. The heating of the pellets is done at any suitable temperature following Tammann's rule [77]. According to this rule the temperature of heat treatment should be two third of the melting temperature of the constituting materials in the mixture which exhibits the lower melting point. As the constituents in the pellet do not react at RT, hence, to provide an activation energy to initiate the reaction, the pellet is subject to a high temperature [77].The nucleation occurs at the interface followed by formation of the product layer at the interface. Diffusion occurs at these contact surfaces following the Fick's 1st law of diffusion as given by eq. 2.1 [78]. The diffusion flux J is given by

$$J = -D\frac{dC}{dx}, \qquad 2.1$$

where flux J is proportional to diffusivity D and negative concentration gradient.

The complete reaction occurs depending upon the interaction between the reactants which takes from hours to weeks. Hence intermittent grinding comes handy in long annealing hours as it creates fresh surfaces to come in contact and fastens the reaction and attains completion. The process of mixing, pelletizing and annealing continues until the final required product is formed.

2.1.2 Preparation of Nanoparticles of Bismuth Ferrite using Sol-gel Method

Solid state reaction leading to the correct resultant product phase depends upon many factors mainly including purity of the reactant phases, homogeneous mixing of the reactant phases, starting mixtures and mainly the comparative vapour pressures of each of the phases of the reactants. Also limited by the mass transport, as the reaction occurs due to the surface interaction of adjacent materials any inhibition in diffusion will block the reaction giving rise to unreacted materials in the product. Further, as this route involves higher temperatures, there is a difficulty in controlling the size and morphology of the particles [79]. Therefore, wet chemical routes are preferable. In this section we will discuss the sol gel preparation route in detail and its advantages over solid-state techniques.

Sol gel techniques find wide adoptability in the preparation of ceramic oxides and covers various aspects in the goal of preparation of nanoparticles and thin films as well [80]. The traditional sol gel synthesis of metal oxides is actually broad. The basic steps involved are shown in Figure 2.1(B). As this method involves the formation of intermittent metal alkoxide and hence poses a serious drawback on the formation of metal oxide [79]. Hence it is modified by the hydrolysis reactions in aqueous metal salts in which by incorporating small organic molecules thus facilitating H^+ formation in a continuous manner according to eq. 2.2.

$$[M - OH]^{z+} \leftrightarrow [M - OH]^{(z-1)+} + H^+ \leftrightarrow [M = O]^{(z-2)+} + H^+ \qquad 2.2$$

This depends on the pH as well as the deprotonation of hydrolysis by weakening of O–H bond in water [79]**.**Further there are cases when the aqueous solution is stable enough to form gel and in such situations addition of a chelating agent as complexant and fuel come handy. Here we will narrow down our discussion to citrate sol gel method where the citric acid ($C_6H_8O_7$) is used as complexant. Citric acid is weak triprotic acid with three carboxylic groups and one hydroxyl group connected by means of five carbon chains (ref Figure 2.1(C)). The dissociation reaction in citric acid is shown by eq. 2.3 [79].

$$\begin{gathered} H_3cit \leftrightarrow H_2cit^- + H^+ \qquad 2.3 \\ H_2cit^- \leftrightarrow Hcit^{2-} + H^+ \\ Hcit^{2-} \leftrightarrow cit^{3-} + H^+ \end{gathered}$$

Citric acid is cheap and readily available and an efficient chelating agent that produces viscous gel on heating of aqueous metal salts. The final metal citrate is obtained with pyrolysis in air. It forms metal citrate complex whose heat of combustion occurs at around 300–400 °C [79].At this temperature the organic components evolve out of the system. Instead of routine aqueous solutions, specific nitrate salts are preferred because the nitrate salts act as oxidant and citric acid behaves as organic fuel encompassing the combustion [81].This is also experimentally observed as seen by a sharp feature in TGDTA and a rapid loss of mass in TGA analysis and a corresponding exothermic peak in DTA implying that the combustion is self propagating [82].

The citrate sol gel reaction is as follows. In the beginning the equimolar metal nitrates are allowed to mix in the solvent along with citric acid thus forming a clear aqueous solution of metal citrates. After removal of the water content from the solution and on giving appropriate thermal treatment a viscous gel is formed. Organic matrix formation confirms the uniform growth and nucleation and hence the grain thus formed will be in the order of nanometer (nanoparticles). This gel is then heated up around 300-400 °C to facilitate the auto-combustion reactions and thus forming a fluffy ash or glassy solid depending on the system. In certain cases the final outcome is a spongy like material due to organic components evolving during reaction as gases in abundant quantity [83]. These precursors are calcined for the formation of required crystallized phase.

The advantage of citrate sol gel route is that this method ensures homogeneity in complex ternary and quaternary oxides. Maintenance of the homogeneity at the precursor stage favours lowering of the temperature of crystallinity [83]. In special cases wherein the crystallinity arrives at later stage after the combustion, the homogeneous precursor ensures stability till the final product. For example in $Y_3Al_5O_{12}$ and YAG, the intermediate phases disturb the nucleation and the growth of the required phase giving rise to inhomogeneity and irregular grains in the final product, whereas the formation of such intermediate phases are inhibited in the sol gel auto-combustion method [84].

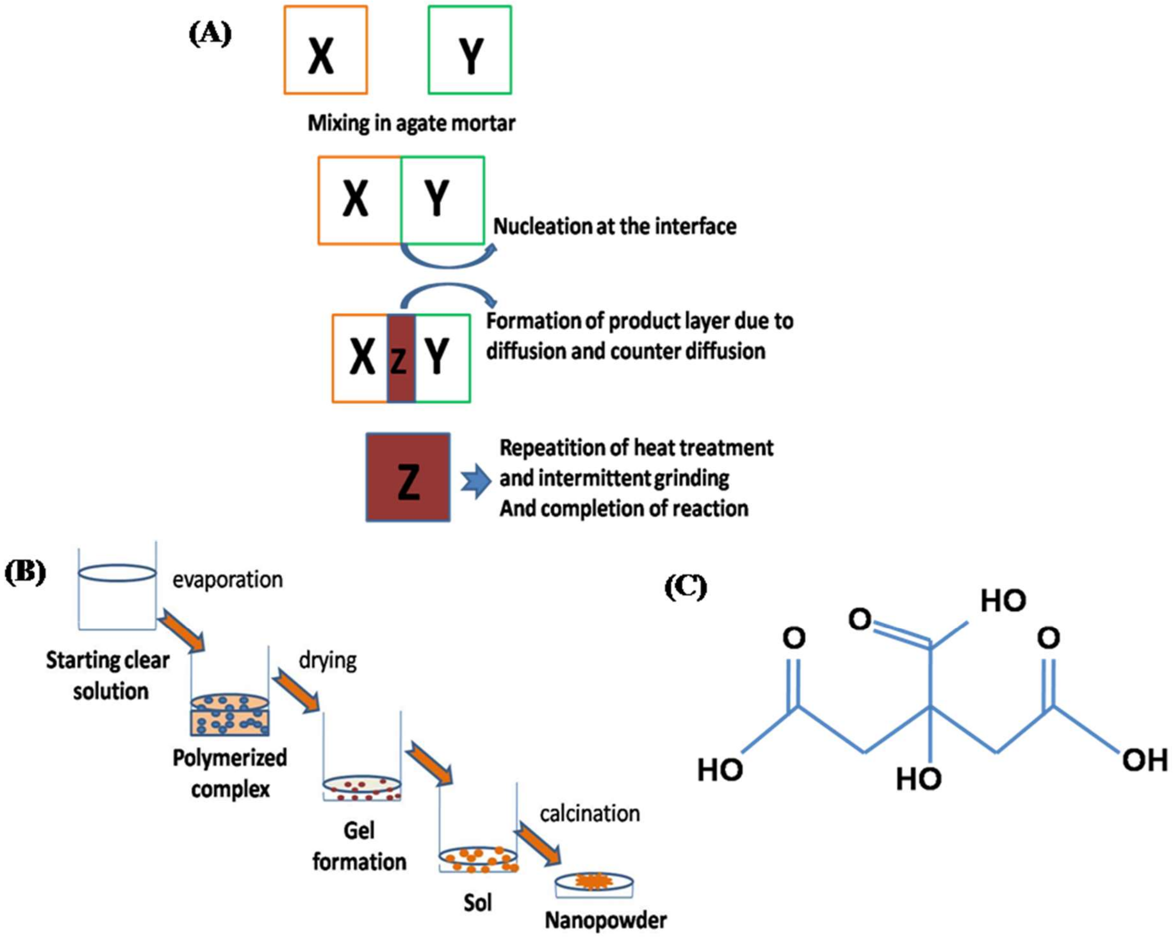

Figure 2.1 Basic steps involved in solid-state route (A), sol-gel method (B), structure of citric acid (C).

2.2 Bulk Structural, Electrical and Magnetic Characterization

The structural and microstructural studies are being carried out using XRD and Raman spectroscopy, and SEM and TEM techniques respectively. To establish the multiferroic behavior, the evidences from both direct and indirect coupling of electric properties are studied using PE loop tracer and dielectric measurements with and without magnetic field. The bulk magnetic characterization is taken using vibrating sample magnetometer. The atomic level hyperfine parameters and hence magnetic properties are carried out using Mössbauer spectroscopic technique. The details of these techniques are discussed in the following.

2.2.1 Crystal Structure Studies

X-ray diffraction is a useful technique for the identification and characterization of crystalline and amorphous materials based on the principles of Braggs law

$$n\lambda = 2d\sin\theta \,, \qquad 2.4$$

where λ is the wavelength of the incident wave from a monochromatic source, d is the interplanar spacing and θ is the scattering angle. Constructive and destructive interference occurs when monochromatic beam of incident beam falls on the target material depending upon the regular and irregular arrangement in the structure of the material.

An inel 2000 based X ray diffractometer with Cu k_α-source of wavelength 1.54 Å in Bragg Brentano geometry was employed for the structural identification. The diffractometer was calibrated with the Si (111) plane. A Si-based sample powder of approximately 100 mg was spread evenly so as to form a smooth surface is used in this diffractometer.

The obtained XRD patterns are refined using Fullprof software and the unit cells after refinement were generated using VESTA software. Rietveld refinement developed by Hugo Rietveld was used to deconvolute the different aspects of XRD / neutron diffraction pattern. The unit cell dimensions, atomic position i.e height, width and position can be obtained from the pattern profile fitting. Rietveld refinement involves non linear least square fitting approach that correlates the theoretically calculated profile to that of experimentally observed one [85]. The principle is to minimize the function M defined as eq. 2.5

$$M = \sum_i Wi \left\{ y_i^{obs} - \frac{y_i^{calc}}{c} \right\}^2 , \qquad 2.5$$

where W_i is the statistical weight and c is overall scale factor such that $y^{obs} = y^{calc}$.

Raman scattering has been used to understand the modes corresponding to the vibration of molecules. Raman scattering is a weak inelastic scattering based on the interaction of incident light with the molecules of the system of interest. This interaction leads to the distortion of the electron cloud resulting in the formation of unstable virtual state and soon after photons are released with energy equivalent to the energy difference as scattered light. There is a change of polarizability due to this process. Each peak in a Raman spectrum corresponds to a specific lattice vibration acting as a molecular fingerprint of the target material under study. A Renishaw Raman spectrometer using Ar ion laser of wavelength 514 nm is used. Si is used as a reference sample. A 5 mg sample, in powdered form, was spread over a quartz glass plate thus forming a smooth surface was used for Raman measurements.

2.2.2 Microstructural Analysis

Scanning electron microscope (SEM) and Transmission electron microscope (TEM) are used to study the microstructure of the samples. The schematic of the microscopes are shown in Figure 2.2. In SEM technique the electron of energy ranging from 0.2 to 40 keV was used. The sample surface is scanned by the incoming electron beam, which interacts with the atoms in the sample producing voltage signal. This voltage signal is amplified and contains various information on topography and composition of the sample investigated. As the electron beam is narrow, SEM image with have a large depth of field, and therefore, a better 3D surface image for structural analysis can be obtained. Since the samples studied are insulators or non conducting, the samples are spin coated with gold over a copper tape. It takes only a short time almost of the order of nanosecond to acquire an SEM image, which can effectively be zoomed up to a fraction of nm.

TEM is a microscopy method in which an electron beam is transmitted through a sample to form a high resolution image. In a TEM microscope, the sample is located in the middle of the column. The electrons pass through the target sample as well as a series of electron lenses below the sample (intermediate and projector lenses). An image is directly shown on a fluorescent screen or via a charge-coupled device (CCD) camera, onto a PC screen.

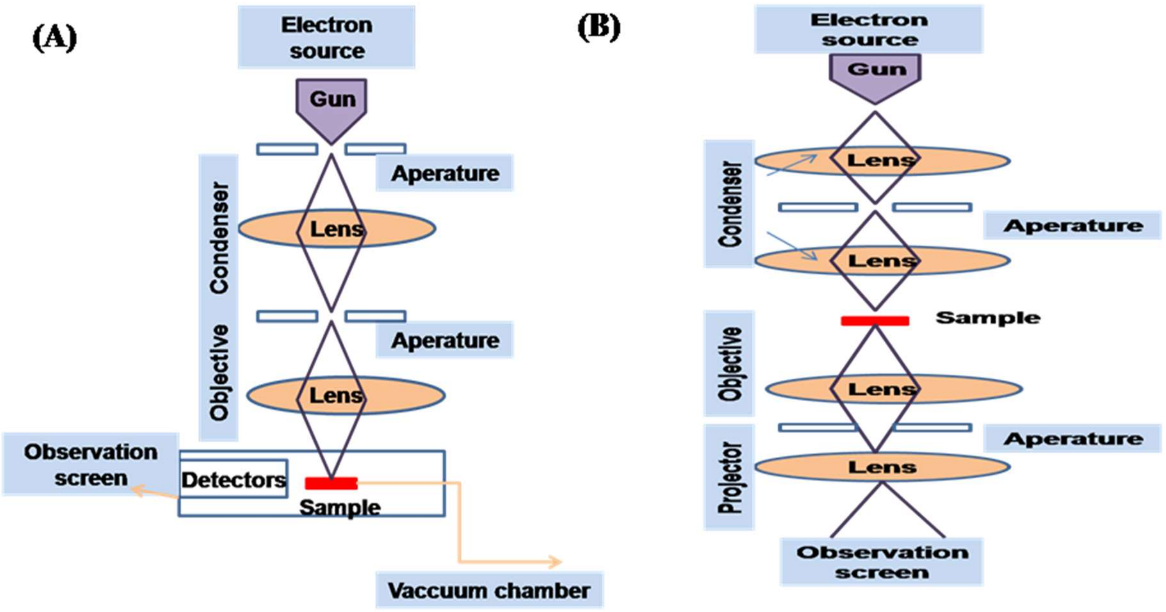

Figure 2.2 Schematics of scanning electron microscope (SEM) and transmission electron microscope (TEM) [86].

2.2.3 Electric Property Studies

2.2.3.1 Dielectric Studies

‘In dielectric spectroscopy (DS),the interaction of the electric dipole moment of the sample with an external applied electric field of fixed or changing frequency is studied. The response of the sample to such external fields is known as its permittivity. DS gives insight of the electric and dielectric properties in the bulk and interfacial regions of the solid samples (cf. Figure 2.3**)**. The parameters obtained are useful in analyzing energy storage and dissipation properties. The different types of relaxation phenomenon involve mechanisms in different frequency ranges are electronic, dipole, atomic and ionic polarizations. A broad band dielectric spectrometer was used to study the dielectric properties of the samples in different temperature and frequency range. Further the dielectric properties of these samples were also studied under the application of magnetic field which in turn leads to the understanding of the magnetodielectric coupling in these systems.

2.2.3.2 Ferroelectric Studies

The direct coupling can be observed from the behavior of the ferroelectric domains in response to the magnetic field. Similar to magnetic hysteresis loop, the loop corresponding to the variation of polarization with applied electric field is observed and this is called ferroelectric loop (cf. Figure 2.4). Materials exhibiting stable loop behavior are suitable for ferroelectric memory devices. A ferroelectric PE loop tracer is used to study the polarization of the samples. The sample in the form of pellet can be considered as parallel plate capacitor to which the Ag electrode is attached to the top and bottom flat surface. Marine India based PE loop tracer was used for the measurement and it has a set up to apply external magnetic field. This arrangement provides an extra control to investigate the coupling.

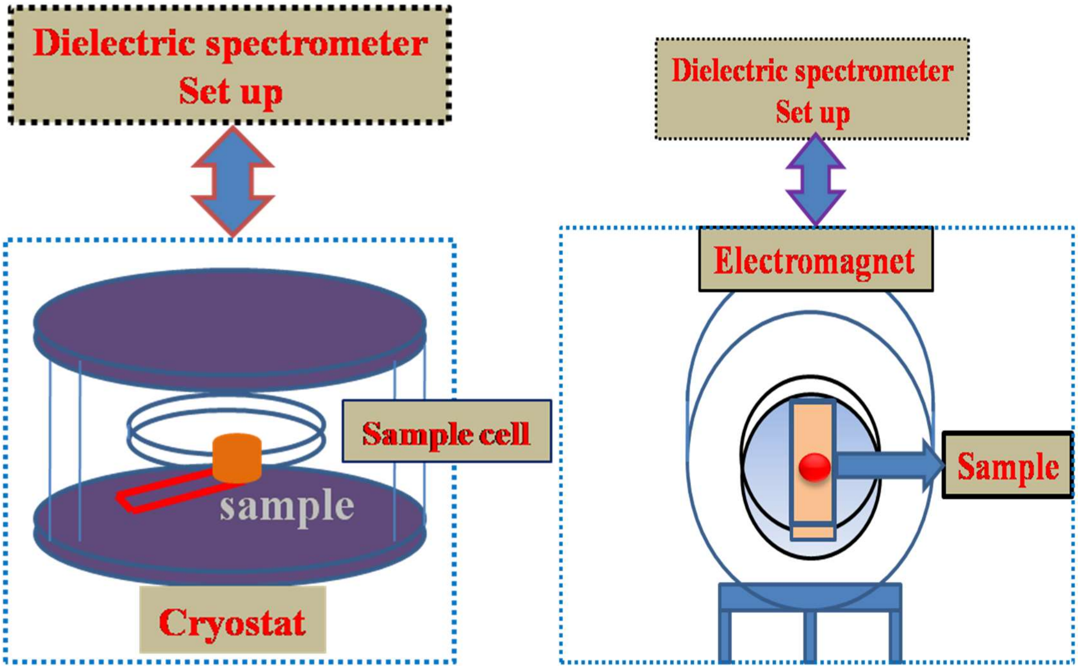

Figure 2.3 Schematic of broadband dielectric set up used for studying samples at room temperature (left) and under magnetic field (right).

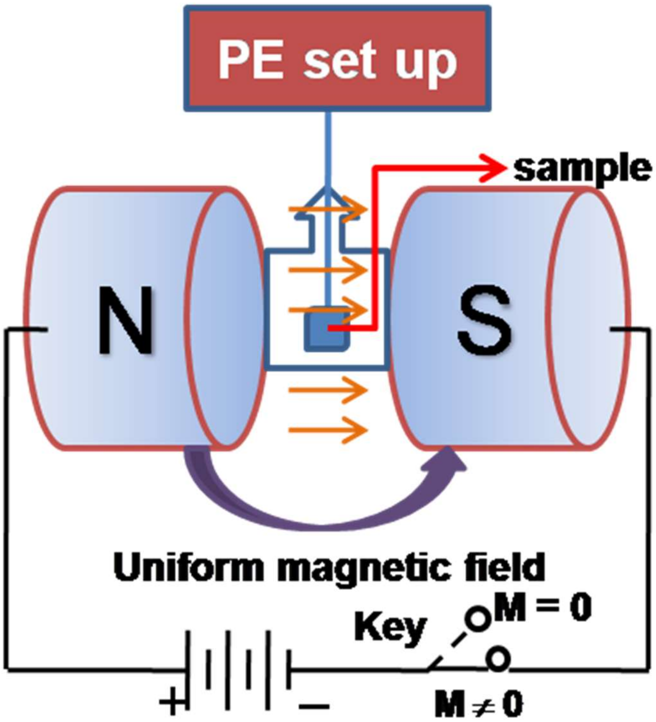

Figure 2.4 PE loop set up for measuring the magnetic response of electric polarization.

2.2.4 Magnetic Properties using Bulk Magnetization Studies

The magnetic properties provide an insight of the structure of the metallic and nonmetallic solids. A vibrating sample magnetometer (VSM) is used for understanding the bulk magnetic properties. It measures the magnetic moment. When sample is placed in between strong magnetic poles, a uniform magnetic field and a magnetic dipole moment is produced around the sample (ref Figure 2.5). Upon experiencing sinusoidal magnetic field, the sample induces an electric signal depending on the sensitivity of the suitably located stationary pick-up coil. This signal is proportional to magnetic moment, vibration amplitude and frequency. A hysteresis curve can be drawn between the produced magnetic moment and the applied magnetic field which gives information on memory and energy loss. Thermomagnetic measurements are performed with zero field cooled conditions wherein the variation in magnetic moment with respect to temperature is obtained. In zero field cooled condition a measurement was taken by lowering the temperature from room temperature to 5

K without external magnetic field and subsequently from room temperature to 5 K with small external field. This type of measurement is useful in deducing the magnetic transition temperatures, blocking and spin glass behaviour in samples [87].

A UK based 16 T vibrating sample magnetometer (VSM) is used for investigating the bulk magnetic properties. A 30–40 mg sample was taken for the measurement, placed on the sample holder using cotton wools so as to avoid any additional vibration within the sample and its holder. The field dependent measurements were taken with an external magnetic field under various required temperatures till saturation whereas the temperature dependent measurements were taken with small external magnetic field for resolving the intrinsic thermal response of the sample.

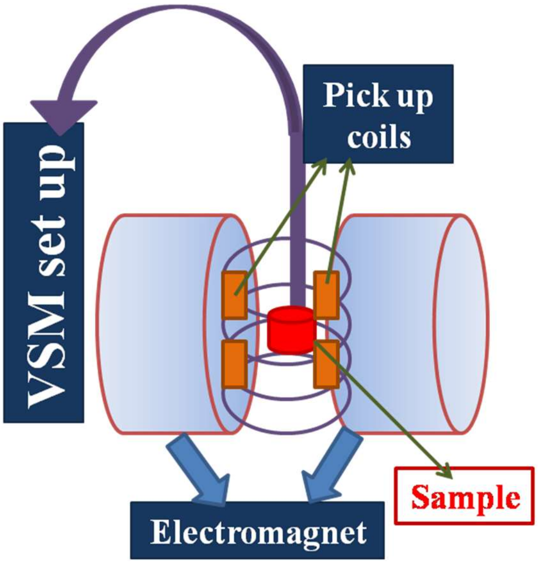

Figure 2.5 Schematic of the Vibrating Sample magnetometer.

2.3 Mössbauer Spectroscopy for Local Structure and Magnetic Properties

2.3.1 Methodology and Mössbauer Spectrometer

Mössbauer spectroscopy is based on the Mössbauer effect which is defined as the recoilless emission and absorption of gamma rays by probe nuclei introduced in a solid matrix. Having discussed the Mössbauer effect, it remains to be explained as to how the Mössbauer effect is to be utilized to measure the hyperfine interaction induced shift and /or splitting of nuclear energy levels. This is done by modulating the energy of the gamma ray as emitted by the source by means of subjecting the source to Doppler shift by means of velocity v with respect to the absorber and thereby scanning the velocity range to deduct for the effect of resonant absorption. This is schematically shown in the Figure 2.6.

Energy of the gamma ray as emitted by the source subjected to Doppler velocity shift +v with respect to fixed absorber is given by

$$E_\gamma = E_0\left(1 \pm \frac{v}{c}\right), \tag{2.6}$$

where ± sign of velocity is determined by the source moving towards the absorber or away from the absorber respectively.

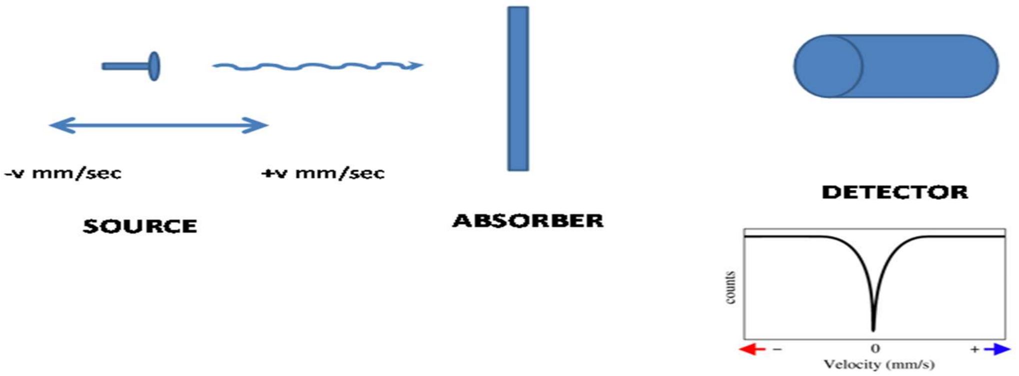

Figure 2.6 Schematic displaying the basic principle of Mössbauer spectroscopy.

Hence the change in gamma ray energy caused due to Doppler shift is given by $\Delta E = E_0 \frac{v}{c}$. Thus by fine tuning the velocity for occurrence of resonance absorption of gamma ray, hyperfine level shifting or splitting could be effectively measured from experiment.

Basic instrumentation for Mössbauer spectroscopy requires a thorough discussion on absorption spectrum linewidth. The natural linewidth of an absorption line is determined by the Heisenberg uncertainty relation $\Delta E.\Delta\tau \geq \hbar$. The spectral line has a Lorentzian shape centred on E_0 , the intensity I_0 and with full width at half maximum (Γ) is given by

$$I(E) = \frac{I_0 \left(\frac{\Gamma}{2}\right)^2}{\left[(E - E_0)^2 + \frac{\Gamma^2}{4}\right]} \qquad 2.7$$

Block diagram of a Mössbauer spectrometer is shown in Figure 2.7. The spectrometer mainly consists of a Mössbauer drive unit, detector set for 14.4 keV gamma ray, which is energized by a high voltage bias supply, preamplifier, amplifier and a multichannel analyzer operated in Multi Channel Scaling mode. Mössbauer source is mounted on a drive which could be moved with a continuously varying velocity between zero and a preset value v. The slope of the v–t waveform i.e. acceleration is constant referred to as constant acceleration mode as shown as inset in Figure 2.7. The velocity changes from -v to +v in a half cycle (T/2 seconds).

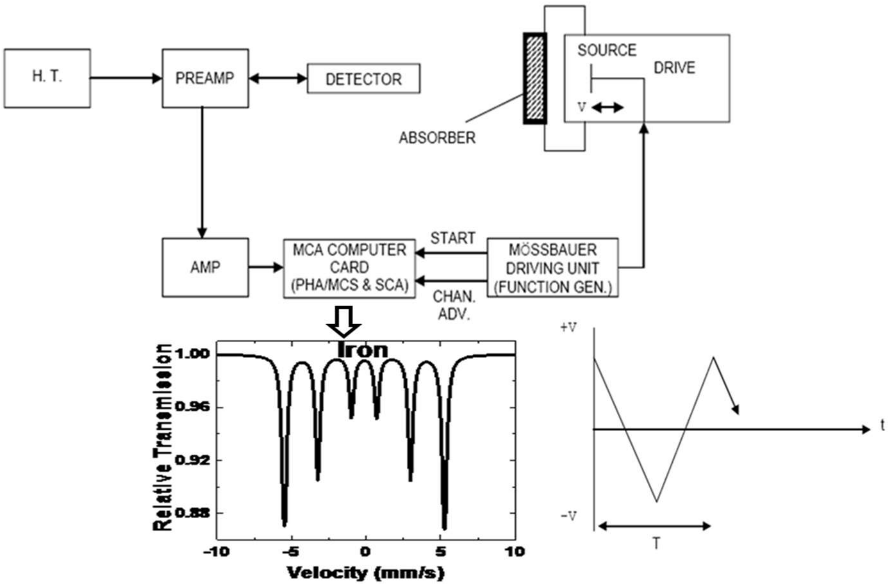

Figure 2.7 Block diagram of Mössbauer spectrometer.

The analogue output from the function generator is applied to power amplifier, which drives the source. The output from the function generator is applied to the multichannel analyzer (MCA) to provide synchronization and channel incrementing in multichannel scaling (MCS). Correspondence between the channel numbers and the velocity of the drive is established through Doppler equation. The source velocity is controlled by a transducer in a constant acceleration mode. A waveform generator sends a reference waveform (either triangular or sine) to the drive amplifier through a digital to analog converter. This signal is sent to the vibrator where it is converted to a mechanical oscillation of the drive shaft and source. Feedback signal is provided by a small coil within the vibrator to correct any deviations from the reference waveform. Gas filled proportional counter is used a detector of gamma rays.

From the detector pulse after amplification, 14.4 keV γ photons have been selected using energy discrimination by single channel analyzer. The digital logic pulses from single channel analyzer are fed as input to MCA and counted at different Doppler velocity. Thus a Mössbauer spectrum in terms of the intensity of the transmitted gamma rays through an absorber versus the velocity of the source i.e., Doppler shifted gamma energy is obtained.

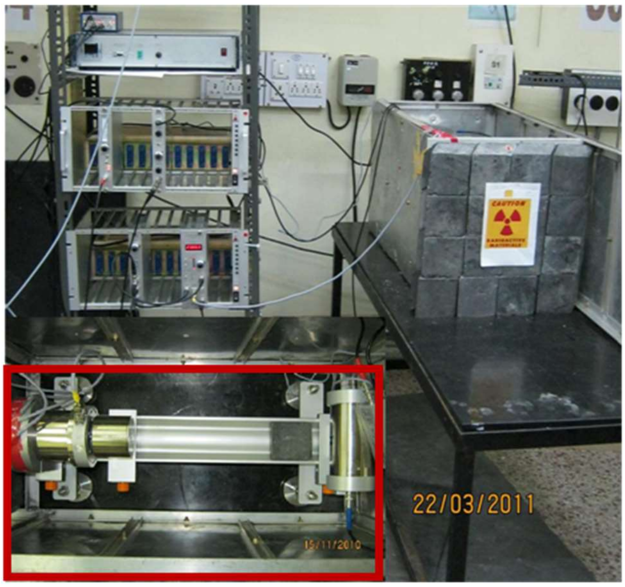

Figure 2.8 Photograph of Mössbauer spectrometer showing the NIM bin in which the modules corresponding to waveform generator, Mössbauer drive unit, High voltage power supply and linear amplifiers are housed. Inset shows the vibration free platform in which the shielded source mounted transducer, sample and proportional counter are mounted rigidly.

The detector counts and source velocity are synchronized using a microprocessor system. The counts are accumulated in 1024 channels for one complete cycle, which contain two complete spectra viz., one for positive and another for negative acceleration of the source. As the acceleration is constant the time interval is equal for all velocity channels, hence each channel records for the same amount of time. During analysis the full spectrum acquired over positive and negative acceleration of source is folded around a centre point to obtain a single spectrum. This increases the statistics of the data.

2.3.1.1 Mössbauer Source and Absorber

The source used in ^{57}Fe Mössbauer spectroscopy was ^{57}Co dispersed in Rh matrix. The decay scheme of ^{57}Co isotope is shown in Figure 2.9. The half-life of ^{57}Co is 271.7 days and decays by electron capture to I = 5/2 excited state of ^{57}Fe. This is followed by a subsequent de excitation to I = 3/2 level, which is the isomeric state of interest for the Mössbauer effect. The excited state is characterized by a mean lifetime of 10^{-7} seconds and decays to ground state I = ½. The excited state I=3/2 is characterized by magnetic and quadrupole moments as 0.153 nm and 0.29 barn respectively. While the ground state with I=1/2 is characterized by magnetic and quadrupole moments as 0.093 nm and 0 barn respectively. Based on the half-life of the 14.41 keV excited state (i.e.) 97.8 ns, the natural linewidth is deduced to be around 0.097 mm/s. The linewidth of a resonant emission and absorption event is thus 0.194 mm/s in ideal conditions [88].

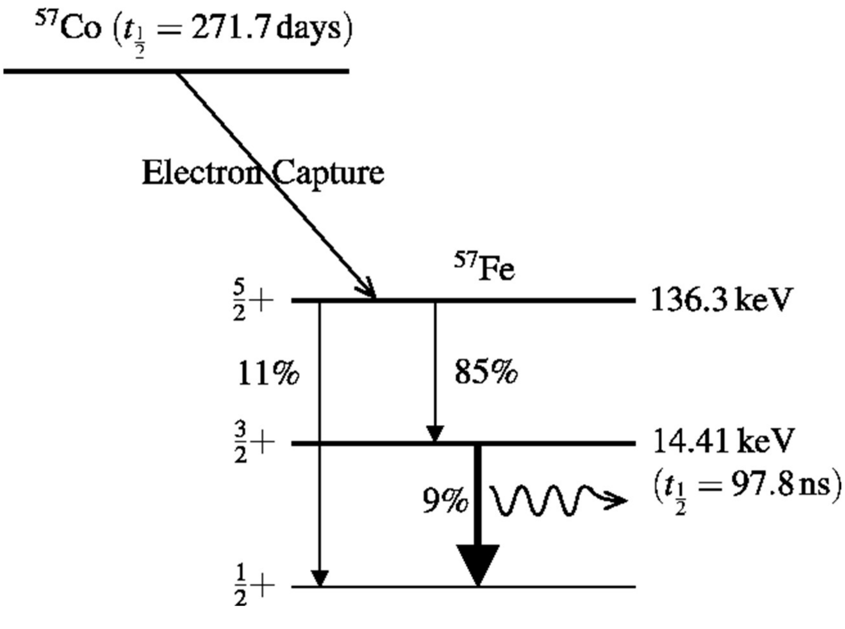

Figure 2.9 Decay scheme of ^{57}Co source leading to 14.41 keV gamma-ray emission.

^{57}Co atoms diffused rhodium foil which provides a non-magnetic and cubic matrix is used as a Mössbauer source. Thus the ^{57}Co atoms occupying substitutional and defect free sites in Rh matrix provides a solid environment with a high recoil-free fraction produce mono-energetic gamma-rays. The specific activity of the source is 50 mCi.

Bismuth iron oxide powder samples weighing roughly to 30–40 mg are mixed with boron nitride and pressurized in a pressure cell. Thus pellets of the samples are prepared. The resonance absorption is maximum for an optimal thickness of the absorber leading to a minimum linewidth. A linewidth of 0.28 mm/s is obtained with a 10 μm thick α-Fe absorber. This is covered with a thin Al foil while carrying out measurements below 300 K.

2.3.1.2 Mössbauer Drive System

The drive system mainly consists of a Mössbauer drive unit and a velocity transducer. It provides a precise motion of the γ-source for the measurement of the Mössbauer effect. The drive unit feeds the velocity transducer with an electronically controlled voltage. The waveform for the source motion is given by the reference signal of the function generator. Drive unit and the transducer form a feedback system which minimizes the deviation of the actual source motion from its correct value. The drive system is suitable for desired waveform; however the best results are yielded with a sinusoidal waveform. Amplitudes of the waveform of the drive unit and the error signal are observed to be around 3 V and0.25 mV respectively indicating that the signal / noise ratio is of the order of 10^4.

A proportional counter filled with a gas consisting of 90% of Ar and 10% of Methane is used for detecting gamma photons. Detector is energized by a bias of 1700 V to obtain the pulse. This is amplified and the output of the amplifier is fed to CMCA. Complete pulse height spectrum as obtained in the gas filled proportional counter is shown in Figure 2.10. By means of a single channel analyser 14.4 keV gamma photons are selectively processed and counted in the measurements.

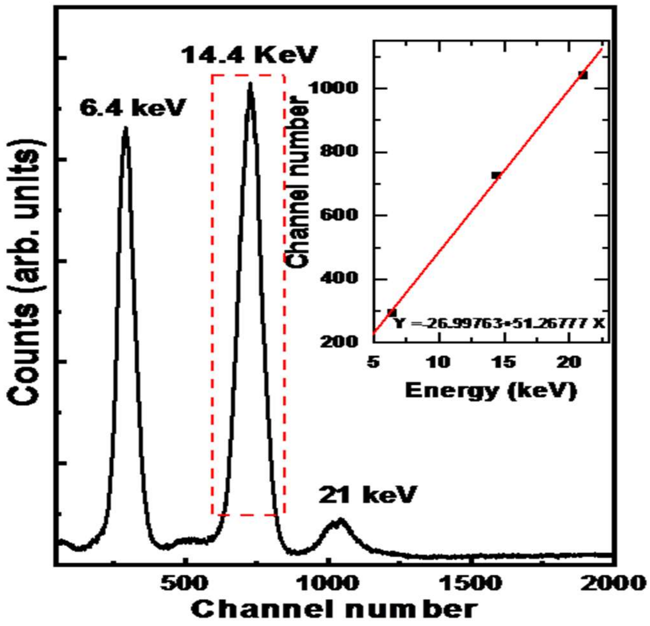

Figure 2.10 Pulse height spectrum obtained with ^{57}Co source in a gas filled proportional counter with the peaks corresponding to the gamma energies of ^{57}Fe (6.4 keV, 14.4 keV and 21 keV). The inset shows channel number varies linearly with energy.

2.3.1.3 Mössbauer Spectrum in α–Fe and Calibration of the Velocity Transducer

Mössbauer spectra are calibrated with respect to calibration parameters such as velocity scale, centre point of the spectrum and the linearity of the velocity/time profile of the oscillation are compared to a standard reference of α-Fe foil at room temperature. α-Fe is bcc and ferromagnetically ordered at room temperature. Due to the presence of magnetic interactions the ground state and first excited state spins undergo splitting leading to six possible transitions corresponding to six values of the velocities at which resonance absorption occurs leading to a six line pattern or sextet as shown in Figure 2.11.Mössbauer spectra are fitted using WinNormus software. Best fit to the spectrum is obtained with reference to Lorentzian peak profile shape including position, linewidth and intensity.

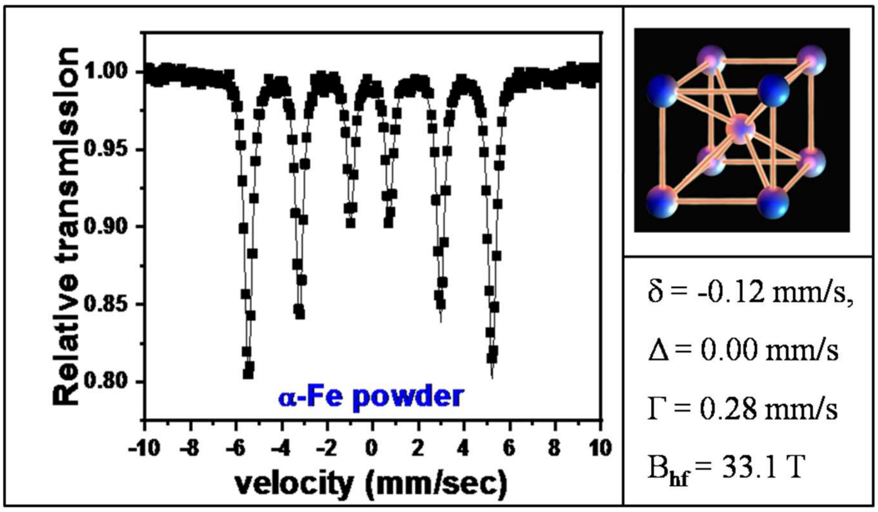

Figure 2.11 Mössbauer spectrum with a six line pattern for α-Fe powder with corresponding cubic unit cell [88] and deduced hyperfine parameters of the only sextet present in the case (right inset).

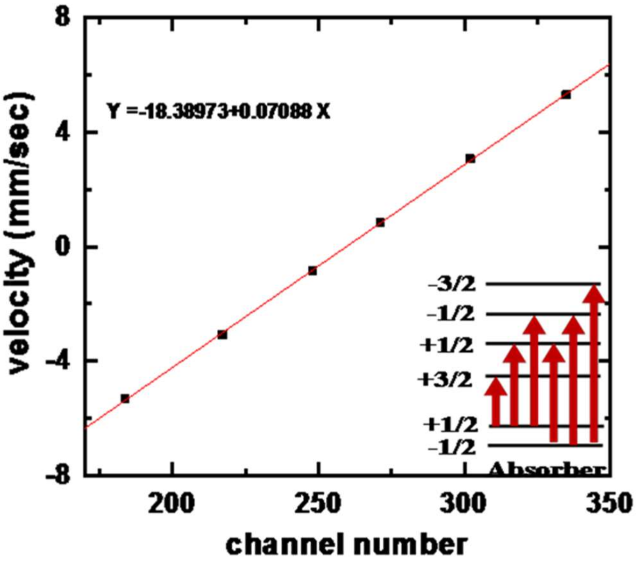

Figure 2.12 Variation of velocity with respect to channel number for resonant absorption as deduced from Mössbauer spectrum of α -Fe foil [88].

The program follows nonlinear optimization with best χ^2 fitting model for obtaining optimum values of hyperfine parameters (δ, Δ and B_{hf}). $0.9 \leq \chi^2 \leq 1.5$ fitting were considered as best fit.

The velocity scale is calibrated using the well defined line positions of the sextet from α–Fe, which occur at ± 5.312 mm/s, ± 3.076 mm/s, ± 0.840 mm/s [89]. The peak channels corresponding to the above line positions of sextets of α-Fe in terms of velocities are obtained and are shown in Figure 2.12. The centre of this α-Fe at room temperature is taken as the reference point (0.0 mm/s) for isomer shift values of sample spectra. The values of isomer shifts presented in this thesis henceforth are given with respect to that of α- Fe absorber at 300 K.

2.3.2 Deduction of Hyperfine Parameters of some Reference Samples

Sodium nitroprusside exhibits orthorhombic crystal structure with space group *D2h 12-Pnnm*. As the system is non-cubic and not magnetically ordered the resultant Mössbauer spectrum is a doublet as shown in Figure 2.13 (A).The Mössbauer spectrum could be fitted with the parameters such as the isomer shift = -0.28 mm/s and a quadrupole splitting of 2.17 mm/s. A huge value of Electric field gradient at Fe sites originates from unbalanced d-electron density. A large value of the total s-electron density at ^{57}Fe nucleus as implied by the value of isomer shift is quantitatively related to the effective 3d electron population and to the partial occupation of4s orbitals. As a reference system, Mössbauer results have also been obtained in α-Fe_2O_3 which has a rhombohedral structure, same as that of one of the main systems of the study in this thesis namely $BiFeO_3$. This has a space group of *D3d6* and having the lattice parameters as a=5.4243 Å and alpha= 55° 17’. This system exhibits a weak ferromagnetic ordering above 260 K and the spins lie in (111) plane. The Mössbauer spectrum as obtained in α-Fe_2O_3 is shown in Figure 2.13(B). The resultant hyperfine parameters are such as isomer shift =0.3 mm/s, quadrupole splitting = -0.21 mm/s and the hyperfine field = 51.1 Tesla.

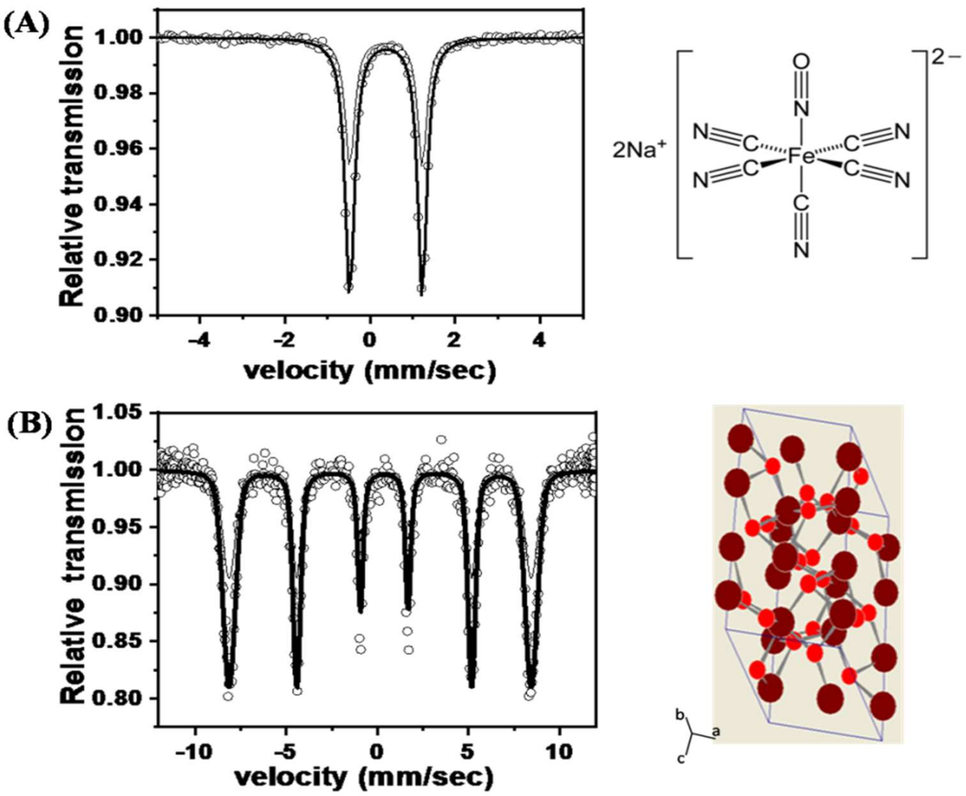

Figure 2.13 (A) Mössbauer spectra of sodium nitroprusside which is noncubic and nonmagnetic hence showing doublet (right presents structure of sodium nitroprusside) and (B) Mössbauer spectrum of α-Fe_2O_3 (right unit cell of α-Fe_2O_3).

Summarizing in this thesis all the systems of interest to be studied are characterized for their bulk structural properties using XRD along with Raman spectroscopy studies for addressing local structural aspects with respect to frequencies corresponding to modes associated with Bi and Fe. Magnetization and ferroelectric studies have been carried out followed by magnetoelectric coupling studies based on P–E loop studies on the samples of interest under different values of magnetic field. Mössbauer studies have been extensively used to understand the local structure and magnetic properties of nano and bulk of the bismuth ferrite samples thereby addressing the observed bulk magnetic and ferroelectric behavior if any in terms of atomic scale properties as derived using hyperfine parameters at Fe sites.

3 Structural, magnetic, ferroelectric and magnetoelectric coupling effects in nano-$BiFeO_3$

Graphical abstract:

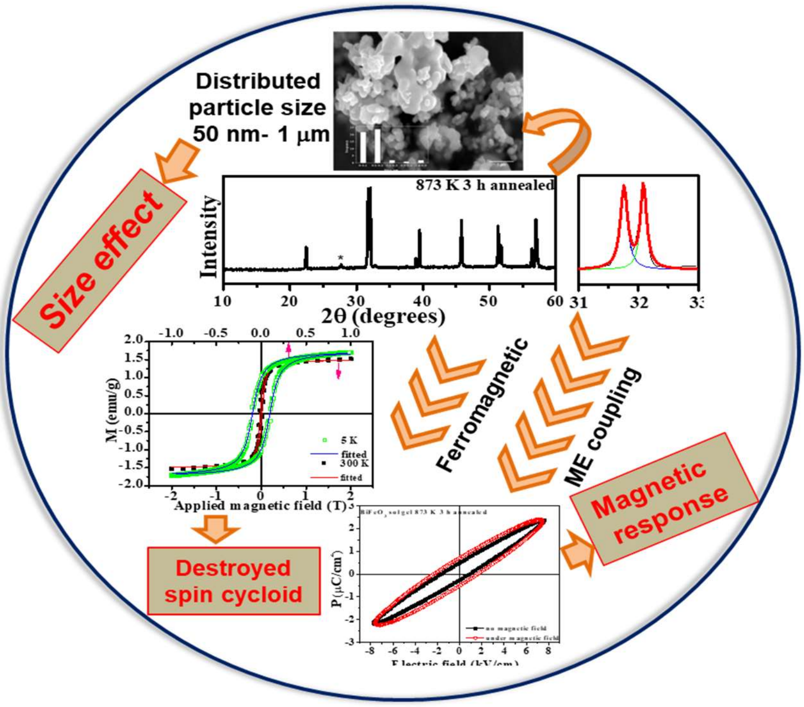

Schematic elucidates the main results of this chapter in terms of multiferroic properties of $BiFeO_3$ nanoparticles

Abstract:

Nanoparticles of $BiFeO_3$ are observed to exhibit weak ferromagnetic and ferroelectric properties and hence resulting in a significant magnetoelectric coupling. Presence of lattice distortion as well as the vacancy kind of defects are deduced be present in the nanoparticles of $BiFeO_3$ using Mössbauer studies, thus providing a good understanding of the observed multiferroic properties of nano $BiFeO_3$ and substantial magnetoelectric coupling.

3.1 Introduction

Single-phase $BiFeO_3$ is of technological importance in photocatalysts, sensors, actuators, spintronics applications [3,30,44,89]. Till date various methods are employed in the preparation of $BiFeO_3$ in single phase [90–93]. Especially bulk $BiFeO_3$ prepared through solid-state route involving high reaction temperature(800–810 °C) results in parasitic phases in addition to the dominantly present $BiFeO_3$ and exhibits antiferromagnetic and leaky ferroelectric behavior because of leakage due to Fe^{3+}/Fe^{2+} hopping and influenced in the presence of the parasitic phases [34,94]. The magnetic and ferroelectric properties of bulk $BiFeO_3$ though devoid of any impurity phase are not promising for the multifunctional device applications because of a low value of magnetoelectric coupling [50]. Instead nanoparticles of $BiFeO_3$ are reported to exhibit weak FM behavior instead of AFM, due to the breaking up of spin cycloid of wavelength ~62 nm as well as unequal compensation of surface spins due to canting [95,96]. Such canting effect is conventional for nano-antiferromagnetic systems. In nanoparticles however the density plays a crucial role in exhibition of ferroelectric properties. Hence nanoparticles of multiferroic systems are technologically superior over bulk as both the ferromagnetic as well as ferroelectric properties are altered positively in the case of single-phase nanoparticles and are significantly important in realizing miniaturized devices [31,97].In addition nano-$BiFeO_3$ is devoid of any impurity phase due to a low temperature of reaction of the phases and hence its consequences on properties. Crystallite size distribution as well as intrinsic defects control the multiferroic properties of $BiFeO_3$ to a large extent especially while the size of $BiFeO_3$ becomes close ~62 nm , the spin cycloid period [96].The magnetic properties of nano particles of $BiFeO_3$ about the mean size of 62 nm or lesser are observed to exhibit larger magnetization values arriving from new origin in addition to the contributions from change in domain structure and uncompensated surface spin effects of the smaller sized particles as discussed by Huang *et al.* [96]. The additional anomaly and the new origin are not explained and needs to be explained.

This chapter aims at studying the nature of magnetic ordering in nano-$BiFeO_3$ and the magnetoelectric coupling. Especially the role of defects if there is any leading to modification of magnetic properties in $BiFeO_3$ and hence resulting in the modification of the magnetoelectric coupling effects are also addressed.

In this chapter we have followed sol-gel auto combustion technique for the preparation of nanoparticles of $BiFeO_3$ with different fuels and succeeded in achieving pure phase similar to the reported results [33,98]. Structures are discussed using XRD, Raman spectroscopy while magnetic and multiferroic properties are addressed using magnetization and ferroelectric studies. Mössbauer spectroscopy is extensively used to provide the atomic level understanding of the magnetoelectric coupling properties. The chapter also discusses the intrinsic magnetic, ferroelectricity as well as possible magnetoelectric behavior exhibited by the prepared samples.

3.2 Synthesis of Nanoparticles of $BiFeO_3$Via Sol-gel Route

Step by step processes taken for the preparation of citrate-based sol-gel $BiFeO_3$ is given in Figure 3.1 following the route given by Popa *et al.* [99]. The salt of nitrates of Bismuth and iron in 1:1 molar ratio and that of citric acid in the ratio 1:1 with metal ions are taken. It acts as a chelating agent as well as a complexant because it interacts with metal ions uniformly throughout, giving them proximity for the reaction [33]. Ethylene glycol is used as solvent and along with citric acid as a chelating agent using the sol-gel method as mentioned above, a clear Bismuth nitrate solution to stabilize Bi ions is obtained which otherwise requires strong acids like HNO_3 [99].The reactant salts are uniformly dissolved in the solvent using magnetic stirrer to form a clear solution in a manner given in schematics in Figure 3.1.

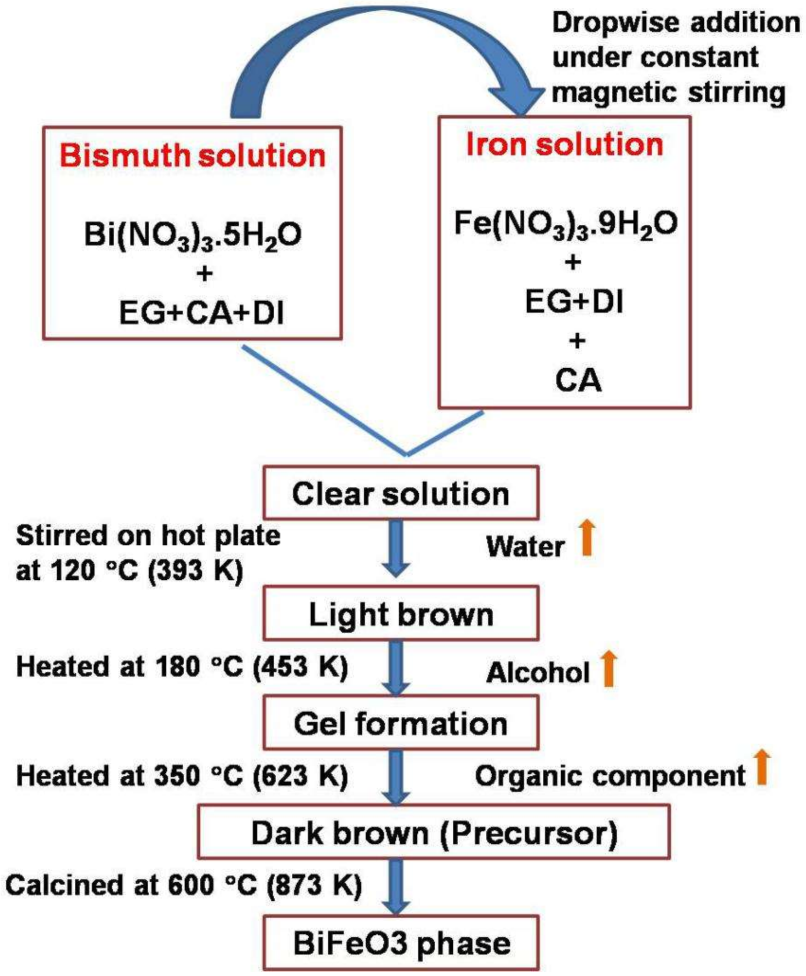

Figure 3.1 Steps followed for the preparation of nanoparticles of $BiFeO_3$ (EG –Ethylene Glycol, CA-Citric Acid and DI- Deionised Water).

The solution is dried at 393 K for ~12 h for evaporation of water. After reduction of the solution to almost half in comparison to the starting solution, the temperature is raised to 453 K at which point the colour of the solution got changed to light brown. Gel is formed after alcohol evaporation starting from 403 K onwards. The dark brown precursor powder is formed after combustion at 623 K with the evolution of gases of organic constituents. The precursor is further calcined at 873 K to form the $BiFeO_3$ phase.

Fuel and chelating agents are important in controlling shape and size of the particles. TG-DTA studies provide an understanding of the role of different fuel and optimum annealing temperature for preparation of nano-$BiFeO_3$ using sol-gel route by reviewing the decomposition temperature regions. TG-DTA studies in $BiFeO_3$ prepared through sol-gel route using citric acid as a fuel, the major weight loss is caused by decomposition process only. The crystallization temperature was earlier reported to be 623 K [33]. Whereas TG-DTA studies shows that the major weight loss of the dried gel occurs due to decomposition of chelate complex and crystallization of phase happens around 723K [33].

In spite of the advantages over using citric acid in preparation of pure $BiFeO_3$, there are shortcomings in terms of the occurrence of impurity phases due to the dimeric nature of complex [99,100].On the other hand it has been reported that the tartaric acid while used as fuel result in formation of polynuclear complexes with molecular level mixing of metal ions resulting in the formation of phase pure $BiFeO_3$.Because of the presence of two carboxylate and two hydroxalate groups in proper orientation in tartaric acid while used as a fuel result in hetero-metallic poly-nuclear complexes on solution where reacting metal atoms comes in close proximity. Thus the poly-nuclear complex which contains Bi and Fe atoms decomposes in presence of nitric acid giving $BiFeO_3$ particles of comparatively lesser size distribution in this case. Henceforth the $BiFeO_3$ samples prepared using citric and tartaric acid as fuels respectively in the sol-gel method as discussed will be termed as BFO-C and BFO-T respectively.

3.3 Multifunctional Properties of Nanoparticles of $BiFeO_3$

To give an insight to the multiferroic properties it is essential to understand the bulk structural, magnetic and ferroelectric properties and further the coupling effects as exhibited by $BiFeO_3$ prepared in this case using the sol-gel route.XRD and Raman studies are carried out for understanding the structural aspects while the magnetic and ferroelectric properties of the systems are investigated using the magnetization and the electric polarization studies. These are carried out using VSM and PE loop tracer respectively. Magnetoelectric coupling are characterized through PE loop response to magnetic field. A Mössbauer study is effectively used to understand the defect contribution to the magnetic and multiferroic properties.

3.3.1 Structural Analysis

Multiferroic and other physical properties of materials are closely related to its structure. Hence it is important to understand and throw light on the structural properties of the prepared samples to assign the phase purity as well as to correlate the properties. For this purpose, we have carried out the XRD and Raman studies of the prepared samples.

3.3.1.1 XRD Studies

To give an insight to the crystal structure, Rietveld refined X-ray diffraction pattern corresponding to the precursor as well as optimized annealing (873 K for 3 h) of BFO-C is shown in Figure 3.2. The obtained pattern is compared with standard ICDD-71-2494 [102] and observed to fit well with distorted rhombohedral space group *R3c*. Within instrumental accuracy, we could obtain almost phase pure $BiFeO_3$ in the optimally annealed sample. The zoomed-in region in the right inset in Figure 3.2 corresponds to the evolution of most intense planes and fitted with two Gaussian peaks as shown. Well resolved most intense (104) and (110) planes signify good crystallinity of the observed phase with annealing. The crystallite size for precursor and annealed $BiFeO_3$ are found to be of ~ 66 nm, 88 nm on an average as calculated using Debye Scherrer formula [103] from the fitted peaks as follows.

$$D = \frac{0.89\lambda}{\beta cos\theta}, \qquad 3.1$$

where λ is the wavelength of the X-ray source, β full width at half maximum and θ is Bragg angle in radian. These peaks are observed to be shifted minutely towards higher 2θ implying structural distortion in terms of decrease in lattice parameter as well as the volume which is discussed with deduced refined parameters. The lattice parameter values obtained for the nano-$BiFeO_3$ is close to that of 62 nm and 83 nm particles as obtained by Huang *et al.* [96]. A comparative studies on solid state and sol gel prepared $BiFeO_3$ with particle size ~90 nm and ~60 nm by Suresh *et al.* [104] discussed the slight difference in lattice parameter as the optimized heat treatments does not change the structure model and hence the lattice parameter and bond lengths but rather suppress the formation of impurities.

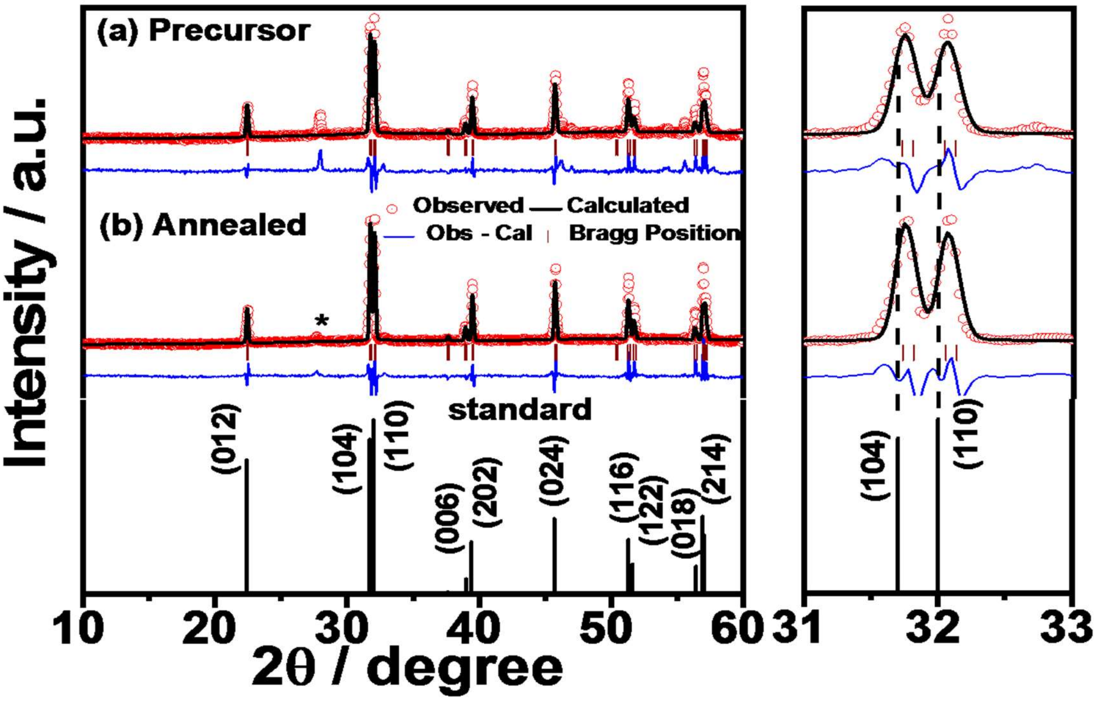

Figure 3.2 XRD patterns and the respective Fullprof refined pattern corresponding to precursor (a) and annealed at 873 K for 3 h (b) nano $BiFeO_3$ prepared though citrate sol-gel (right inset presents zoomed in most intense peaks of (a) and (b) respectively). The obtained patterns are compared with the standard $BiFeO_3$ stick pattern.

The fitting was obtained using Fullprof suit software till acceptable χ^2 values are obtained with the exclusion of region of $Bi_{25}FeO_{40}$. The unit cell generated using VESTA software is also shown in Figure 3.3. It is observed that with increasing annealing temperature the lattice parameters a and c as well as volume decreases (cf. Figure 3.4). This can be ascribed to the presence of defects i.e. oxygen vacancy types and /or the suppressed parasitic phase contracting the unit cell volume. Thus FeO_6 octahedra have to tilt to get accommodated in a comparatively smaller unit cell. Both the A and B site cations (Bi and Fe) show displacement from their assigned higher symmetry (000) position along z-axis which is possible because of the resettlement of Bi ions which is a consequence of the variation of lattice sites to minimize the distortion. Further these displacements, as well as the tilting angle of octahedral, are important parameters that directly correlate crystal structure with the multiferroic properties [105]. The above observation and interpretation go hand in hand with the conclusion drawn from the tolerance calculation as discussed below.

The tolerance factor of $BiFeO_3$ can be calculated using the Goldman- Schmidt tolerance factor formula [106]

$$t = \frac{1}{\sqrt{2}}\left(\frac{r_{Bi}+r_O}{r_{Fe}+r_O}\right), \qquad 3.2$$

where r_{Bi}, r_{Fe}, r_O are the Shannon radii of Bi^{3+}, Fe^{3+} and O^{2-} respectively. The value of t is found 0.88 which should be 1 for an ideal perovskite. The $t<1$ value implies that there exists strain in Fe–O as well as Bi–O bonds leading to distortion in $BiFeO_3$ structure which causes the FeO_6 octahedra to tilt along [111] direction to attain minimal overall strain in the unit cell. Hence the bond lengths as well as the bond angles changes. The Bi–O and Fe–O bond lengths for perovskite type $BiFeO_3$ and $LaFeO_3$ should be 2 Å and the Fe–O–Fe bond angle 180° [107]. Bi–O bond distance is observed to increase to 2.523 and 2.31 Å as compared to standard. This type of cationic displacement gives rise to ferroelectric behavior in $BiFeO_3$ [107].There are six Fe–O bond lengths out of which three bond lengths are reduced (from 1.98 to 1.86 Å) and the other three are increased (from 2.12 to 2.15 Å) due to rotation of FeO_6 octahedra. The variation of Fe site bond length is compensated by buckling of FeO_6 octahedra which is responsible for distortion in the system. Maximum AFM superexchange interaction occurs for Fe–O–Fe bond angle to be 180°. The buckling of octahedral also leads to the deviation in Fe–O–Fe bond angle from ideal 180°. It is well known that Fe–O–Fe bond angle is a deciding factor in determining as well as modifying the magnetic behavior in the system [107]. As the magnetic behavior proportional to cos(Fe–O–Fe) bond angle, the reduction in this angle can drastically vary the magnetic behavior [108]. The refined parameters are tabulated (cf. Table 3.1).

Table 3.1 Rietveld refinement parameters of precursor and annealed nano-$BiFeO_3$.

Sample → Properties ↓		Precursor			873 K for 3 h annealed		
Structural		a= b=5.58157 Å c=13.8719 Å			a= b= 5.58057 Å c=13.87050 Å		
Atomic	Atom	x	y	**z**	x	y	**Z**
	Bi	0	0	0.00086	0	0	0.00029
	Fe	0	0	0.21419	0	0	0.21355
	O	0.434	-0.025	0.95855	0.4317	-0.026	0.95882
Bond length (Å)		Bi–O = 2.56 , 2.46 Fe–O = 2.15, 1.86			Bi–O = 2.58, 2.47 Fe–O = 2.14, 1.86		
Bond angle (degrees)		Fe–O–Fe = 162 Bi–O–Fe = 80 Bi–O–Bi = 104			Fe–O–Fe = 163 Bi–O–Fe =79 Bi–O–Bi =103		
Volume (Å^3)		374.265			374.093		
χ^2		7.2			6.3		

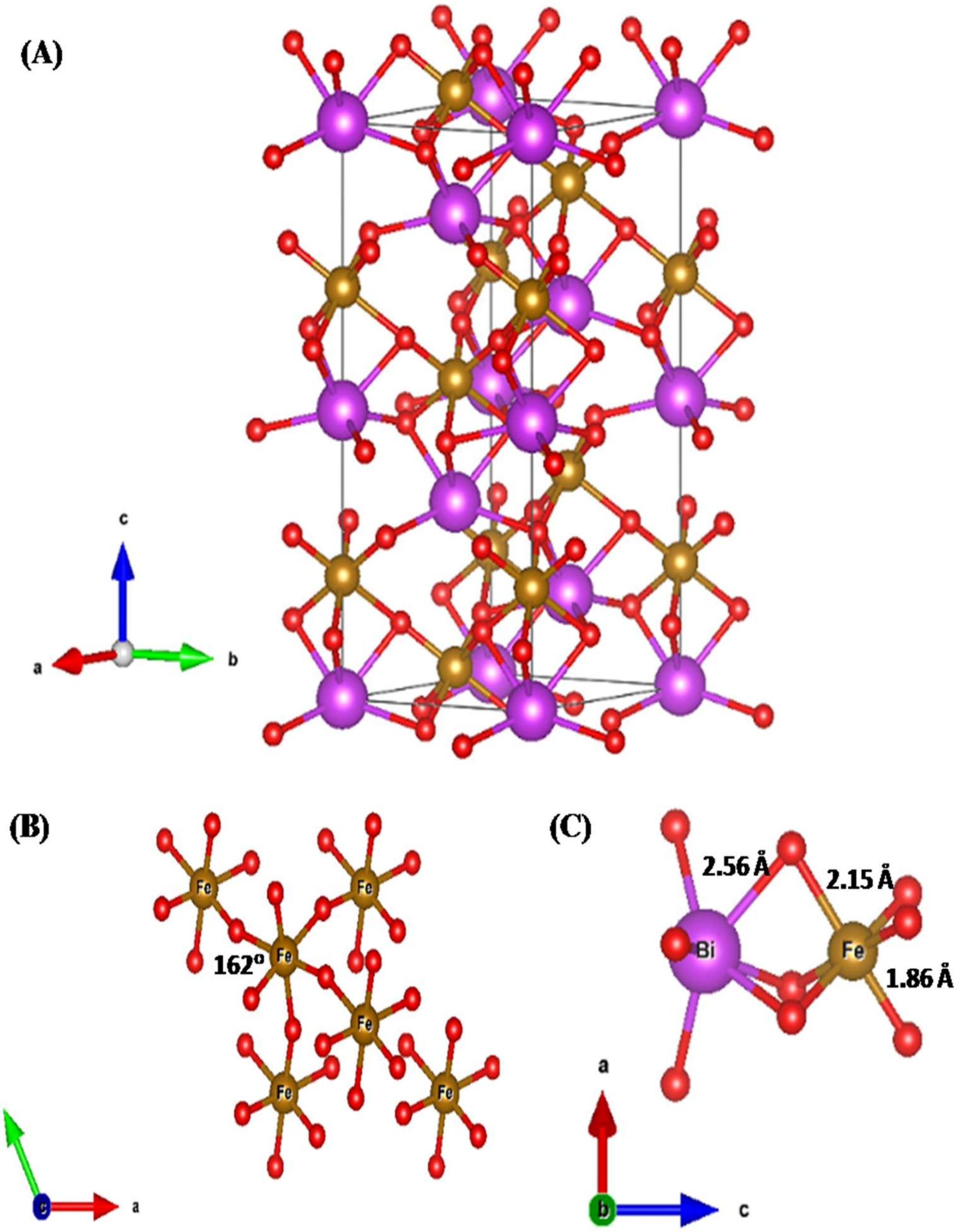

Figure 3.3 Schematic 3.3 (A) represents the unit cell of $BiFeO_3$ while the schematics (B) and (C) represent the polyhedral units of Fe and Bi. Fe–O–Fe bond angle and Fe–O and Bi–O bond lengths are shown as deduced from the Rietveld refinement of the XRD patterns.

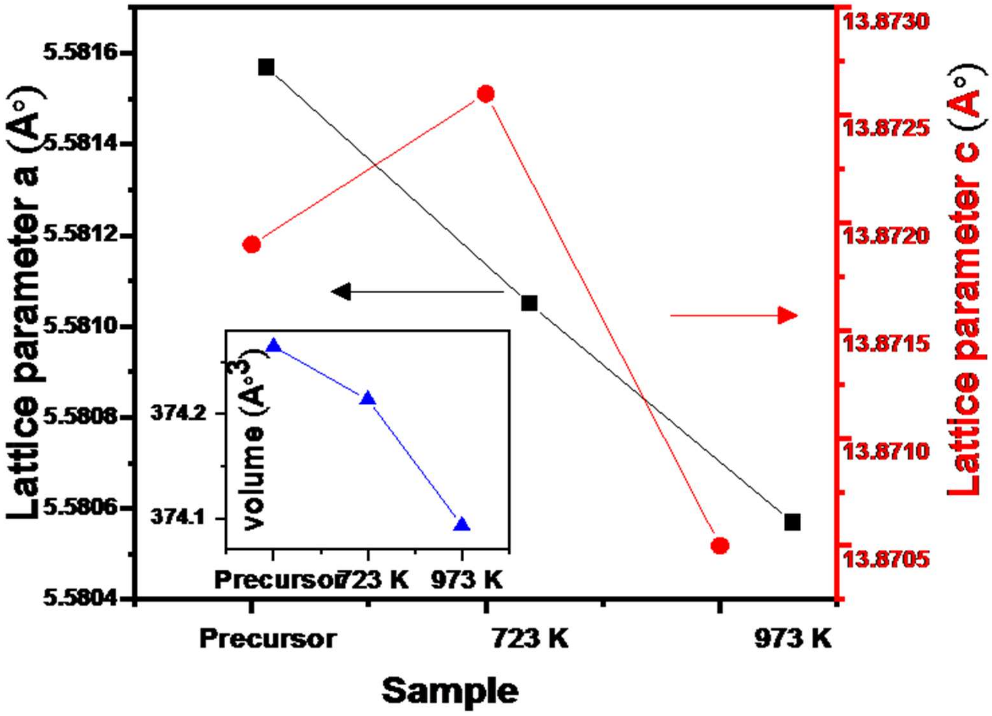

Figure 3.4 Lattice parameters (inset volume variation) variation with respect to the precursor, calcined samples at 723 K and 873 K showing monotonous decrease in lattice parameter and volume.

The * marked peaks in Figure 3.2 correspond to the Bi rich $Bi_{25}FeO_{40}$ phase whose occurrence is expected from the Bi_2O_3–Fe_2O_3 phase diagram [38] in this mentioned temperature region as well as per reported TG-DTA analysis [33]. The fraction of the Bi rich $Bi_{25}FeO_{40}$ phase suppressed appreciably as seen from XRD with respect to annealing of the precursor at 873 K i.e. in the temperature zone of crystallization of $BiFeO_3$. The presence of the $Bi_{25}FeO_{40}$ phase being paramagnetic at room temperature does not affect the magnetic properties of $BiFeO_3$. Again the magnetoelectric property is related to the degree of octahedral distortion and hence can be correlated with structural variations [109]. The decrease in the fraction of impurities with calcinations indicates the effect of temperature on phase stabilization of $BiFeO_3$. The obtained crystallite size for precursor and annealed nano-$BiFeO_3$ are close to spin cycloid wavelength 62 nm has a substantial effect on the magnetic properties of $BiFeO_3$ [96].

The XRD pattern analysis followed by the Rietveld refinement of the data result in the understanding of the buckling of octahedra, as well as shrinking of the volume of the unit cell. The value of the calculated distortion implies the reduction in impurities and the possible presence of oxygen deficiency. Furthermore, the bond angles and bond lengths which are closely related to multiferroic and magnetic properties are found to be altered as concluded from the above analysis and will be explained later.

3.3.1.2 Raman Studies

Raman spectroscopy is a complementary technique supportive for XRD observations, providing additional informations on microscopic phases present as well as possible presence of spin phonon coupling, thus we have carried out the structural understanding through Raman studies as well. The modes of single-phase $BiFeO_3$ are obtained for both precursor and optimally annealed sample are shown in Figure 3.5. The observed modes at around 134, 168, 214, 469 cm^{-1} correspond to A_1 and that around 261,344,532,601 cm^{-1} are assigned to E modes [109–111]. The low wavenumber modes up to 200 cm^{-1} is related to Bi-O modes and modes beyond 200 cm^{-1} are related to complex modes corresponding to Fe-O and oxygen related modes [112]. Depending upon the synthesis processes the oxygen stoichiometry varies and hence the properties. The modes at 134 cm^{-1} is related to magneto-electric coupling [113] A comparative studies of the observed modes in the present case is presented in Table 3.2 along with the literature report. The differences in observed modes and the absence of certain modes are related to the sample preparation techniques [110].The additional modes corresponding to the Bi rich phase $Bi_{25}FeO_{40}$ in precursor are observed prominently at 518 cm^{-1} and the two phonon modes at 1300 and 1500 cm^{-1}[114] which are suppressed in the annealed sample also observed in XRD as discussed previously. The Bi–O mode softening in $BiFeO_3$ is observed which also explains the increase in Bi–O bond length and the corresponding consequences that are also evidenced from crystal structure as comprehended from XRD studies. Further, the sharpened modes in the annealed sample compared to precursor implicate the better crystallinity as well as the agglomeration of crystallites upon heat treatment.

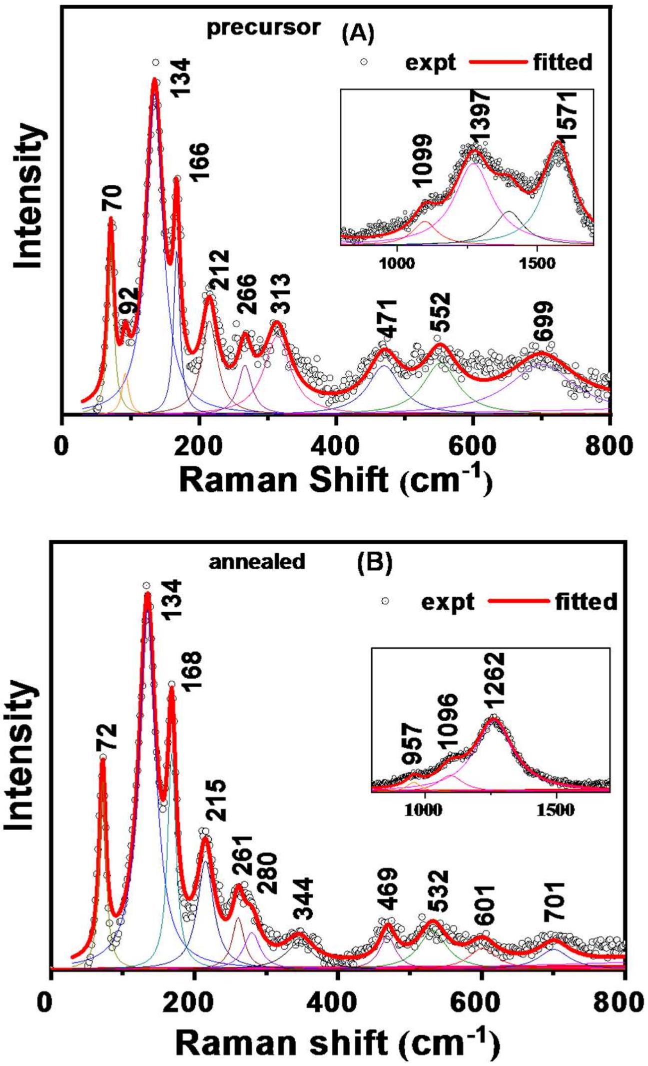

Figure 3.5 Room temperature Raman spectra corresponding to the citric acid assisted as prepared (A) annealed (B) nano $BiFeO_3$ (inset high wavenumber modes corresponding to overtones).

The high wavenumber modes (800–1300 cm^{-1}) arise from either electronic Raman scattering or high order phonon overtones (cf Figure 3.5 inset). From first principle calculations, these modes are attributed to the two phonon modes [113].

For ferroelectric materials these modes are, in general, weak however enhancement occurs for semiconductors when the bandgap energy of the material matches with the excitation energy. Yang *et al.* reported a similar phenomenon in $BiFeO_3$ and reported the mode around 1250 cm^{-1} to enhance when 532 nm wavelength is used which is close to the bandgap energy of 2 – 2.5 eV reported for $BiFeO_3$ [102]. The mechanism involved in $BiFeO_3$ is different from ferroelectric materials as the magnetic ions are also contributed in the scattering signifying spin-phonon coupling [113]. Specific to the observations here the two phonon modes are hence related to magnetic structure and the prominent contribution in this case indicates the resonant enhancement in absorption edge of $BiFeO_3$ [115].

Nanoparticles of $BiFeO_3$ was prepared using tartaric acid as fuel instead of citric acid as the later resulted in small fraction of $Bi_{25}FeO_{40}$ phase. The reaction involved in tartaric acid result in enhanced reactions between Bi and Fe and smaller crystallites.

The XRD pattern Figure 3.6 (inset) and Raman spectrum as obtained in BFO-T are shown in Figure 3.6. The XRD pattern matches completely with the *R3c* distorted rhombohedral structure. None of the peaks corresponding to any impurity phase is observed signifying the purity of the prepared sample. The peak positions coincide with the intensity ratio corresponding to that of the standard sample. The exact coincidence of most intense peak in BFO-T compared to that of precursor and annealed BFO-C suggests the absence of additional distortion in unit cell of BFO-T unlike BFO-C. The mean crystallite size was obtained to be 24 nm as calculated using Scherrer equation given in eq 3.1. Raman spectra with broad and relatively fewer number of modes confirm the nano-size distribution of the particles in tartaric acid assisted nano $BiFeO_3$ in comparison to that of citric acid assisted $BiFeO_3$ which is relatively larger (~66 nm and 88 nm for precursor and annealed one respectively). The obtained Raman modes for BFO-C are similar to that of the bulk while

BFO-T with ~25 nm has broadened modes as compared to that of bulk and also compared in the Table 3.2.

Table 3.2 Raman modes in the present study and a comparison with literature.

BFO-C precursor	BFO-C sintered	BFO T	Singh *et al.*	Yang *et al.*	
134	134	132	136	137	A_1 modes
166	168	168	168	172	
212	215	214	211	217	
471	469	469	425	470	
266	261			262	
	280		275	275	E modes
313	344	322	335	307, 345	
			365	369	
			456	429	
552	532		549	521	
	601	601	597	613	
699	701				
70	72				
92					

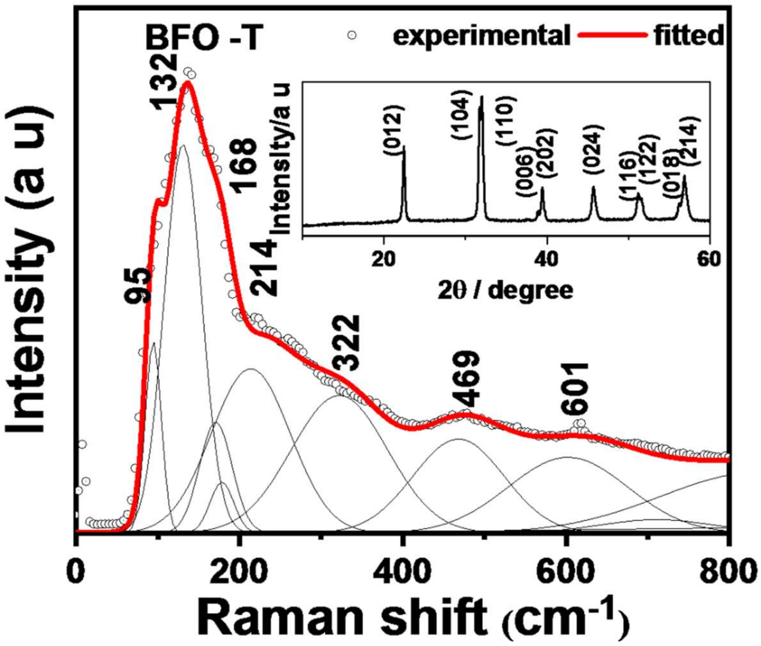

Figure 3.6 Raman studies of BFO-T showing broadened modes and lesser modes are

signature of nanosized particle distribution (inset corresponding XRD pattern representative of single-phase formation).

Hence the obtained crystallites in both citrate and tartarate based samples were studied further to establish the multiferroic properties.

3.3.2 Bulk Magnetization Studies

Bulk magnetization studies are important towards exploring the applications of the material in magnetic storage devices. Polycrystalline $BiFeO_3$ experiences antiferromagnetic behavior up to ~643 K (T_N) [26]. It has been reported that the nanoparticles of $BiFeO_3$ exhibit weak ferromagnetic behavior due to suppression of ~62 nm spin cycloid arrangement, uncompensated surface spins due to size effect [95] which is observed to be ~66 and 88 nm for precursor and annealed $BiFeO_3$ respectively. Inculcating the approximate crystallite size close to the spin cycloid wavelength of 62 nm, enhanced range of magnetization is observed which is ascribed to be of additional origin as depicted by Huang *et al.* [96]. Such additional contribution is discussed here to be originated from redistribution of cationic defect sites and will be discussed in later with reference to Mössbauer studies [116].

The Temperature dependent magnetization of the precursor as well as 873 K annealed $BiFeO_3$, is presented in Figure 3.7. The ZFC FC plots show bifurcated regions below room temperature up to 5 K implying the presence of coexisting AFM and FM components as partial antiferromagnetism still exists even when rotational distortion of FeO_6 octahedra occurs and also that the Néel temperature lies well above our measurement range [26]. Further $BiFeO_3$ prepared with tartaric acid as fuel (cf. Figure 3.8) shows competing interaction between AF and weak FM and hence a blocking temperature around 80 K is observed. For tartaric acid assisted $BiFeO_3$, almost linear behavior of ZFC plot up to room temperature implies strong inter-particle correlation in addition to the superparamagnetic isolated effect in all the cases [117,118]. No cusp at 50 K corresponding to spin glass or antiferromagnetic domain pinning effect as discussed by Huang *et al.* [96] is observed in the present study.

Saturated M–H loop is observed for both the samples at 5 K as well as at room temperature and is presented in Figure 3.9. The feature implicates soft ferromagnetic type behavior as exhibited by the samples prepared through the citrate route. The loop area decreases with increasing temperature which is indicative of the agglomeration of particles [119]. But the finite loop area at room temperature implies the presence of ferromagnetic behavior even at room temperature. This result is commensurate with the results deduced based on XRD and SEM, showing the mean crystallite size in BFO-C is close to the spin cycloid period of 62 nm. $BiFeO_3$ particles of size close to or lesser than the spin cycloid assigned to size effect reported by Park *et al.* thus, breaking AFM order to exhibit weak FM behavior [119].

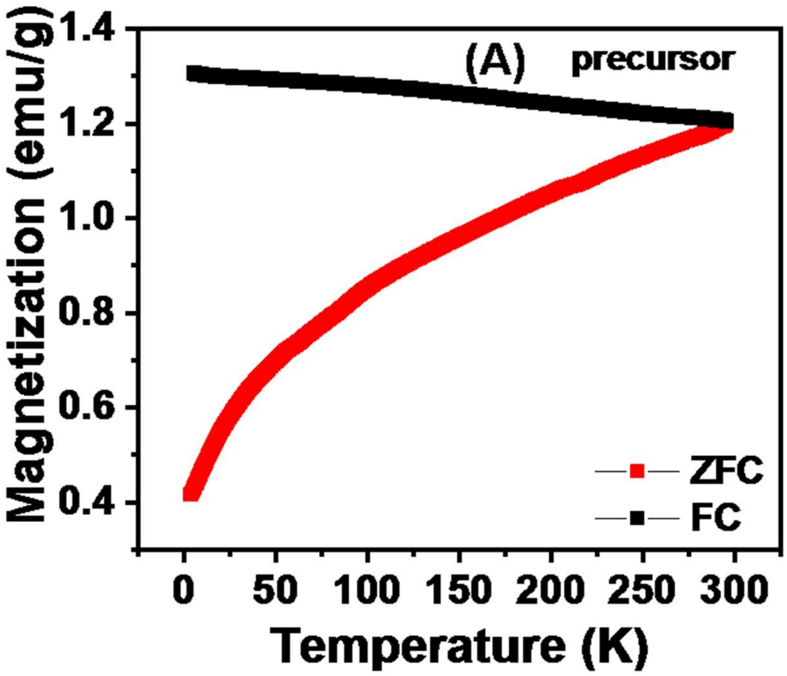

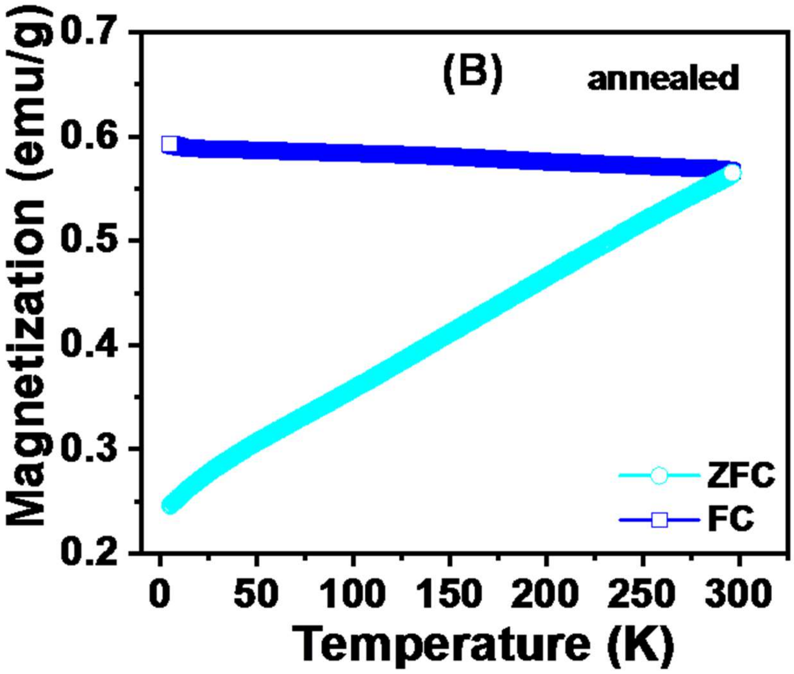

Figure 3.7 ZFC FC curves obtained in $BiFeO_3$ prepared using citric acid with an applied magnetic field of 0.1 T(A) with precursor and (B) annealed at 873 K.

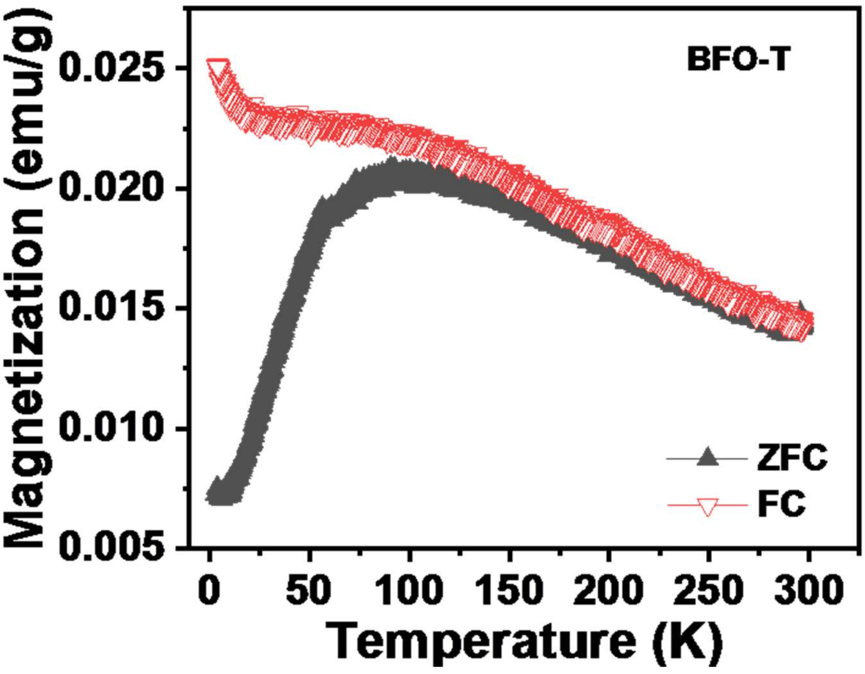

Figure 3.8 ZFC FC with applied magnetic field of 0.1 T results corresponding to BFO T annealed at 823 K for 2 h.

Additionally due to the presence of distortion and hence change in Fe–O–Fe bond angle leads to soft ferromagnetic interaction in precursor. Furthermore precursor BFO-C with smaller crystallites (~ 66 nm), close to spin cycloid wavelength of 62 nm as described by Huang *et al.* possesses larger magnetization (cf. Table 3.3) due to the additional contribution from Bi/Fe site defect distributions as compared to annealed $BiFeO_3$. The magnetization parameter M_r, M_s and H_c values are deduced to be 1.89 emu/g , 3.28 emu/g and 1030 Oe for precursor and 0.96 emu/g, 1.67 emu/g and 1050 Oe for the annealed sample at 5 K respectively (cf. Table 3.3) which closely matches with reported values of Co, Cr and Sm substituted $BiFeO_3$ and larger in comparison to that reported by Huang *et al.* Suresh *et al.*, Park *et al.* with similar crystallite sizes [95,103,118]. The room temperature magnetization values (M_r) decreases by 10 times as compared to that obtained at 5 K which can be ascribed to the agglomeration due to annealing and hence the absence of enhanced magnetization of 62 nm anomalous contribution. Thus the magnetically phase pure $BiFeO_3$ exhibits enhanced magnetization values with almost zero contribution from the impurity phase. The impurities being paramagnetic, as well as present negligibly at room temperature, marked as * in XRD.

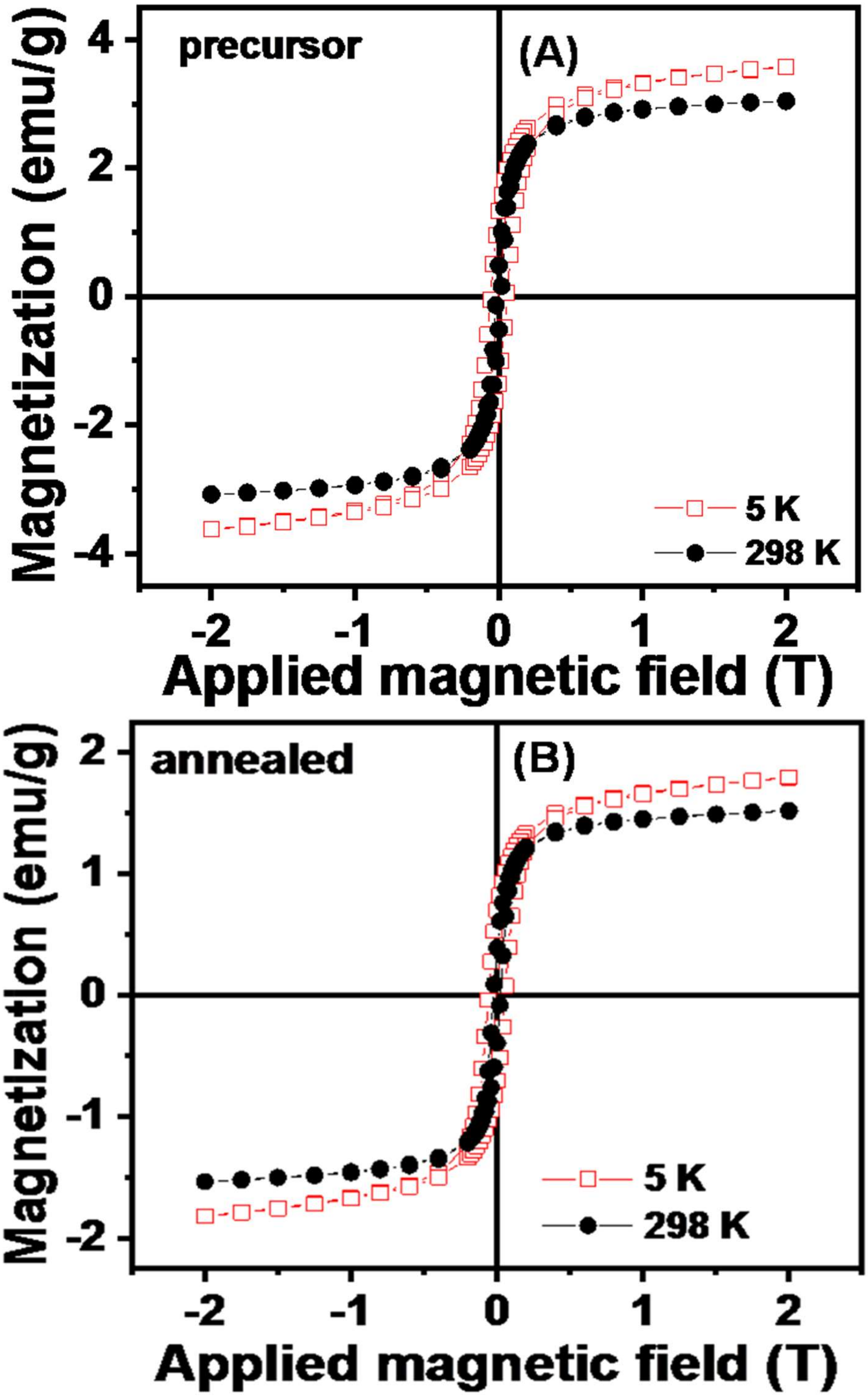

Figure 3.9M-H loop of precursor (A) and sintered at 873 K(B) of BFO-C.

Thus, the enhancement of magnetization can be attributed to the breakdown of a spin cycloid (~62 nm), uncompensated surface spin effects ,contribution from size effect as well as distortion and defect site distributions leading to soft ferromagnetic behavior of the sample [96]. Nanoparticles of $BiFeO_3$ prepared using tartaric acid (cf. Figure 3.11(A)) however show unsaturated finite MH loop indicative of competing for AFM and FM interaction in the form of AFM core and weak FM shell due to size effect. This is due to uncompensated surface spins arising from the nano-size of the particles. This sort of core-shell structure in the AFM system is widely studied in the literature [118,119].

The A-B-K plot is shown in Figure 3.10. The convex surface further strongly indicates the soft ferromagnetic behavior and the y-intercept give the saturation magnetization value in citrate $BiFeO_3$ nanoparticles. The decrease in intercept value with temperature implies the ferromagnetic contribution is suppressed due to the agglomeration of particles with annealing. For both the sample throughout the Temperature range no concave surface is observed which symbolizes the sample to be ferromagnetic rather than antiferromagnetic contradictory to bulk $BiFeO_3$ further supporting the presence of contribution from the distortion observed. While the sample with tartaric acid as fuel (cf. Figure 3.11(B)) is AFM throughout implying the AFM dominance for all the applied field and is contributed from size effect only.

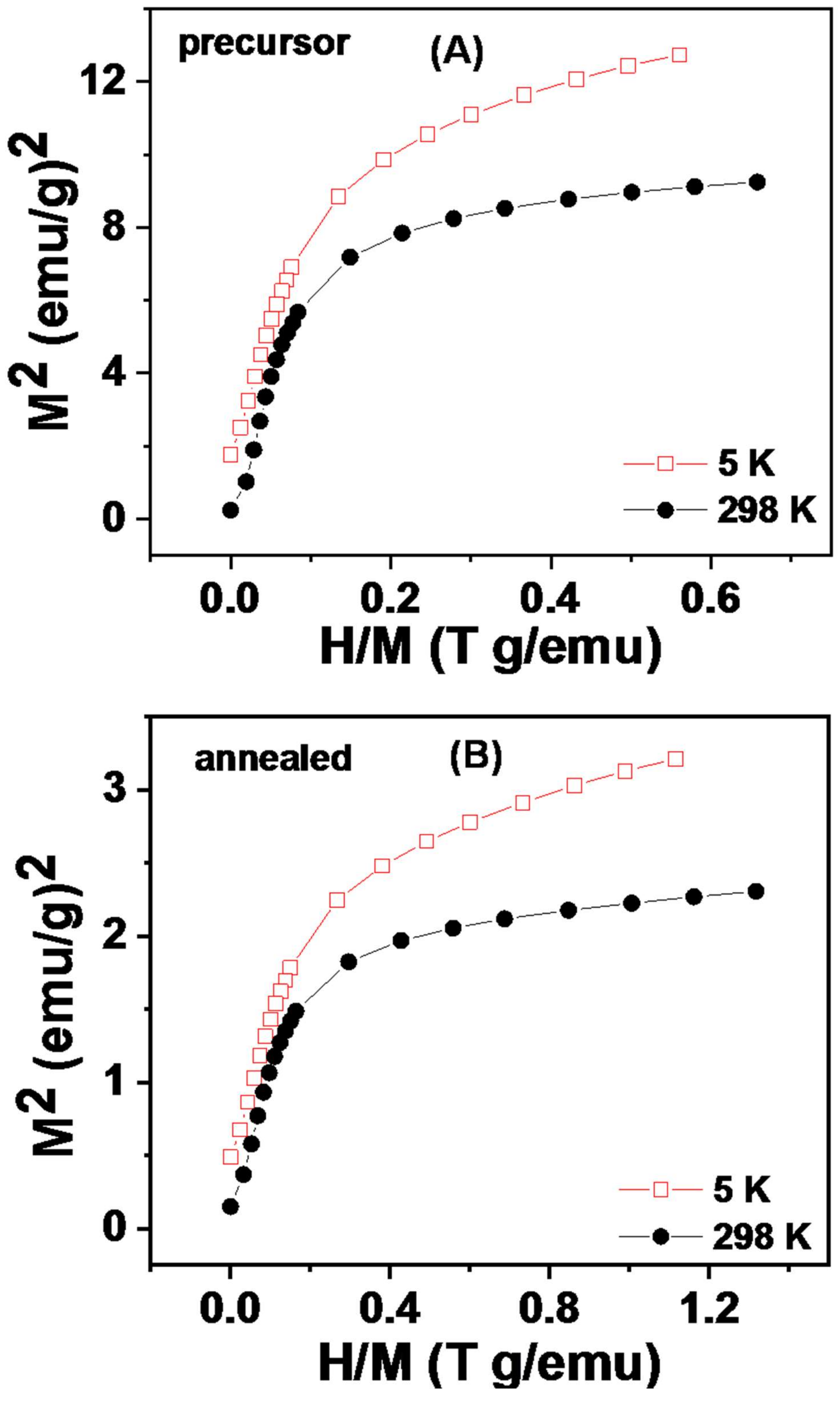

Figure 3.10 A B K plot of precursor (A) and annealed (B) nano-$BiFeO_3$ describing the ferromagnetic behavior by means of convex curves.

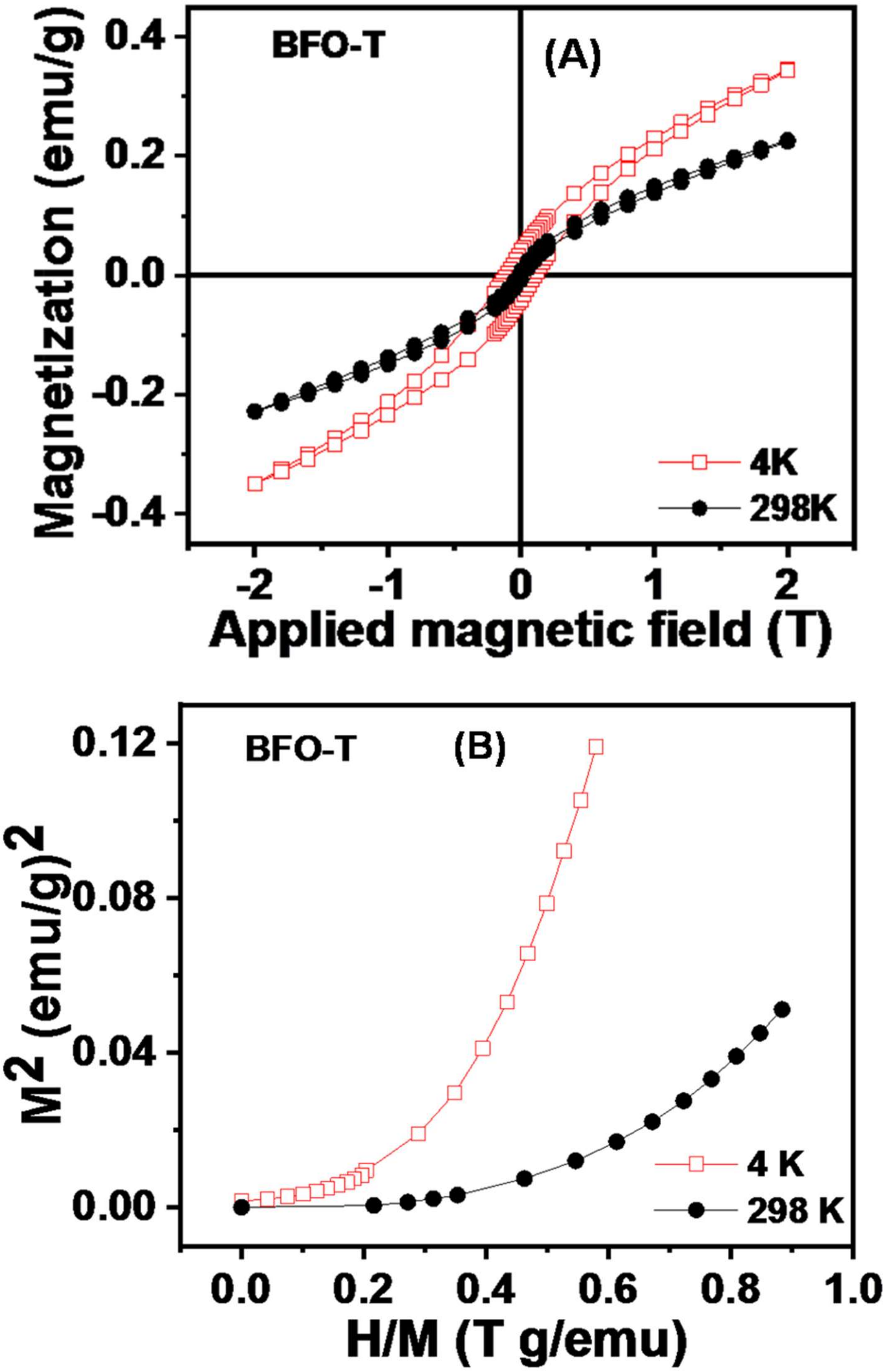

Figure 3.11(A) Hysteresis loop of BFO-T depicting the antiferromagnetic behaviour with central finite area region corresponding to the core shell type signature with FM shell and (B) A B K plot confirming the concave shaped antiferromagnetic behavior.

Table 3.3Magnetic parameter of as prepared and sintered at 873 K with citric acid (CA) and tartaric acid (TA) at 5 K and 300 K.

Sample	T (K)	Mr (emu/g)	Hc (T)	Ms (emu/g)	Mr/Ms
$BiFeO_3$	5	1.89	0.103	3.28	0.58
Precursor (CA)	298	0.49	0.0154	3.05	0.16
$BiFeO_3$ 873 K	5	0.96	0.105	1.67	0.57
3 h annealed (CA)	298	0.39	0.024	1.51	0.26
$BiFeO_3$ 773 K 2 h	5	0.04	0.104		
(TA)	298	0.007	0.0195		

The sample is understood to be nano-sized exhibiting ferromagnetic behavior throughout the temperature range of measurement. Magnetization studies using VSM suggests the appearance of weak ferromagnetic behavior to be due to size effect. The grain size distribution as obtained from SEM averaging out to be 1 micron as deduced from XRD further clarifies the above statement. The obtained distorted Fe–O–Fe bond angle as deduced from the refinement is a plausible cause of such magnetic behavior.

3.3.3 Ferroelectric Properties

Ferroelectric properties of the samples prepared using citric acid and tartaric acid as fuels are carried out. The closed PE loops with finite area imply the presence of ferroelectricity in $BiFeO_3$ at room temperature (cf. Figure 3.12). The ferroelectric Curie temperature is very high around 1143 K [108] which is outside the measurement limit of our instrument so the ferroelectric to paraelectric transition could not be confirmed through PE loop tracer. The citric acid-based sample demonstrates a round-shaped PE loop. This can be ascribed to the presence of distortion as deduced from XRD in nanoparticles of $BiFeO_3$ prepared using citric acid. The unsaturated PE loop with rounded corners can be ascribed to conducting paths in the sample and similar to results obtained by Sharma *et al.*[121].

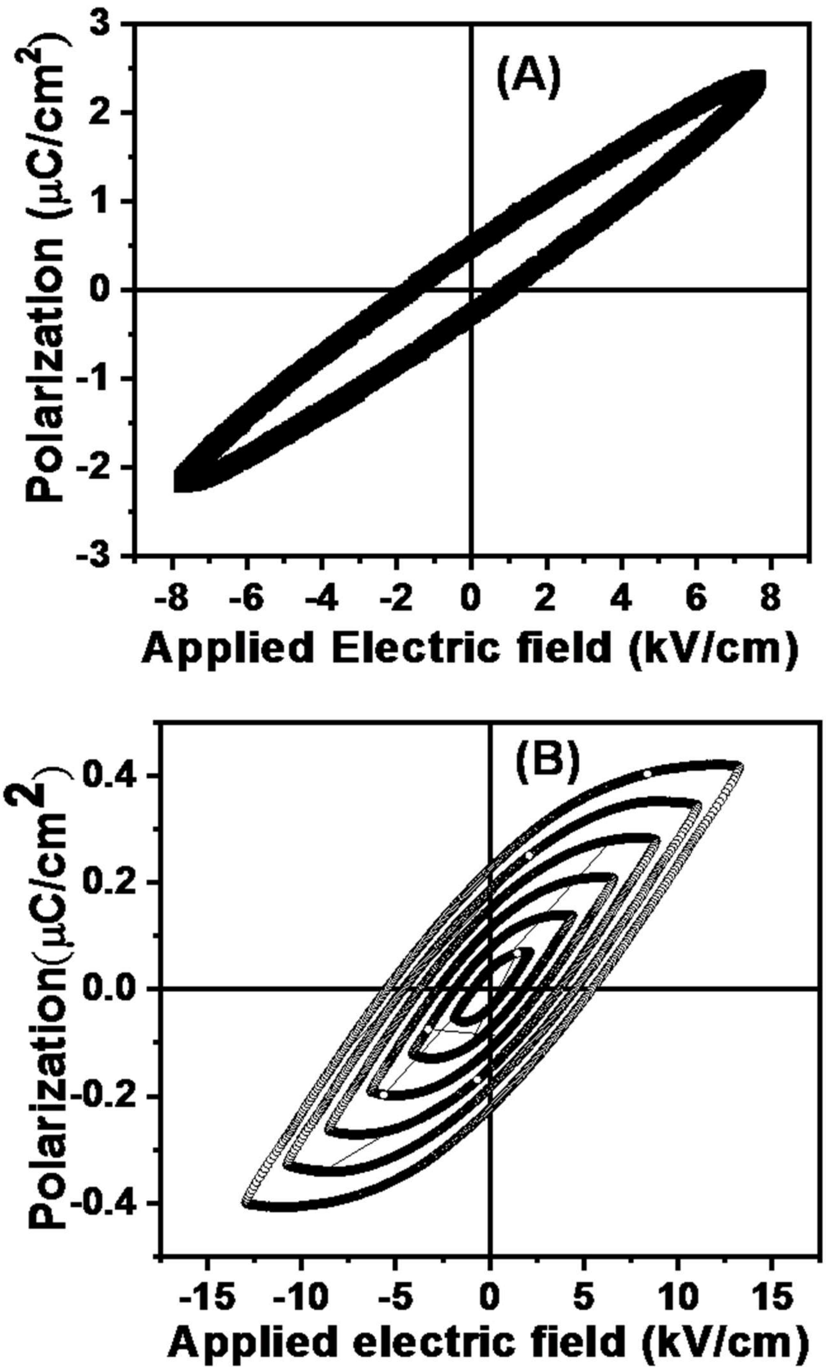

Figure 3.12 Ferroelectric hysteresis loop of BFO-C annealed at 873 K (A) presenting lossy nature and that of BFO-T annealed at 823 K (B) presenting well groomed loop.

$BiFeO_3$ sample prepared using tartaric acid shows however a well developed PE loop implying the ferroelectric nature of the sample. The increase in the applied electric field improves the polarization and intrinsic signature of the ferroelectricity. Whereas the leaky loop in case of citrate samples prohibits the application of the larger electric field with similar values of polarization. The obtained polarization values are 0.4 μC/cm^{2}and 0.3 μC/cm^2 for tartarate and citrate-based $BiFeO_3$ respectively and appreciably closer to the reported literature for polycrystalline $BiFeO_3$ [122]. The polarization value close to ~60 μC/cm^2 could be attained for thin films [108] and in substituted $BiFeO_3$ accompanied by appreciable values of remanent polarization [122,123]. The higher value of polarization in thin film of $BiFeO_3$ than the bulk counterpart can be ascribed to the strain at the interface or probable structural transition to polar structures [122]. In the substituted $BiFeO_3$ sample, the phase stabilization and improved density of the sample due to the presence of substituent ions at volatile Bi site cause for the increased P_r value [123].

3.3.4 Effect of Magnetic Field on the Ferroelectricity

The ferroelectric loop measured with and without the magnetic field is shown in Figure 3.13. In both cases, the PE loop could be observed indicative of the ferroelectric nature. The interesting point observed here is the variation in ferroelectric parameters such as P_r and E_c with the application of the magnetic field. The variation in P_r and E_c in presence of magnetic field is observed to decrease by 39 and 62 % respectively with response to absence of magnetic field. Further the ferroelectric parameters response to change in the range of applied magnetic field from negative to positive which is possibly leading from the switching behavior of ferroelectric domains under applied magnetic field [125]. This provides the direct evidence of significant magnetoelectric behavior observed in the sample.

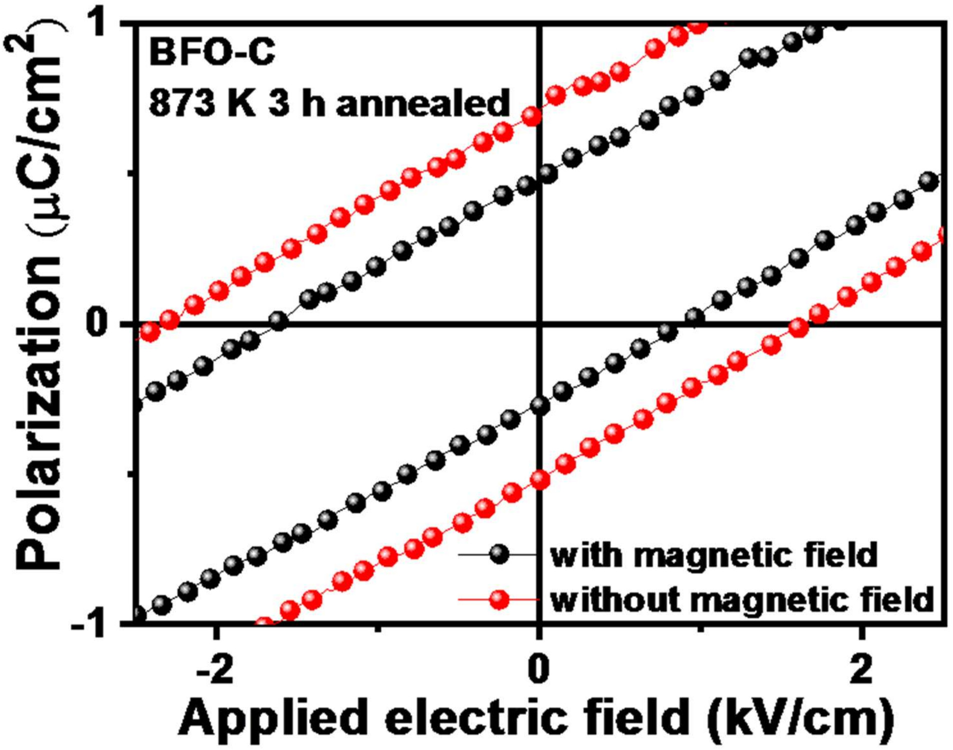

Figure 3.13 Change in ferroelectric parameters in PE loop in annealed BFO-C in presence of magnetic field of 0.1 T at 300 K.

The citrate sample exhibiting soft ferromagnetic behavior is studied further to give an insight to its magnetoelectric coupling. The sample interestingly shows reduced loop area under the applied magnetic field of 0.1 T. This is direct evidence of sample exhibiting multiferroicity in terms of magnetic properties through magnetoelectric coupling. The coupling can be understood as follows. Soft ferromagnetic behavior leads to increased distortion leading to buckling of Fe–O–Fe bond angle and hence indirectly altering the Bi related octahedral displacement which is the origin of ferroelectricity [124,125]. Similar behavior is observed at low temperatures for type II multiferroics. Hence the direct evidence of multiferroicity in the case of nano-$BiFeO_3$ is established in this chapter.

3.3.5 Discussion of Mössbauer Results

Mössbauer spectra obtained at 300 K in $BiFeO_3$ prepared using sol-gel method are shown in Figure 3.14 corresponding to precursor and subjected to different annealing treatments. The results of hyperfine parameters corresponding to the analysis of these spectra are shown in Table 3.4. In $BiFeO_3$ precursor sample the XRD results show the significant presence of $BiFeO_3$ along with the occurrence of impurity phase such as $Bi_{25}FeO_{40}$. The concentration of the impurity phase is observed to decrease sharply with annealing treatments. Mössbauer spectrum as obtained in precursor sample could be deconvoluted into four six line components and two double line components with the corresponding fractions of absorber atoms experiencing magnetic and pure electric quadrupole interactions respectively. Two doublets are attributed to Fe atoms associated with $Bi_{25}FeO_{40}$ phase. Also fractions experiencing hyperfine field of 44 T with high quadrupole splitting is interpreted to be associated with off stoichiometric $Bi_xFe_yO_3$ with $x>1$ and $y>1$. Fraction of Fe atoms associated with these sites are exposed to FeO_6 octahedral distortions significantly larger than that of $BiFeO_3$ phase hence resulting in lower hyperfine field and much larger quadrupole splitting as compared to stoichiometric $BiFeO_3$ phase. Remaining three fractions 1, 2 and 6 are associated with $BiFeO_3$. Among these the values of hyperfine parameters corresponding to fraction 1 and 6 are similar while that of 2 corresponds to high quadrupole interaction. The fractions 1 and 6 represent low quadrupole site fraction with absorber while experiencing hyperfine field of 48.7 and 50.9 Tesla.

In the precursor the two doublets are associated to that of Fe atom associated with $Bi_{25}FeO_{40}$. M–H loop shows weak ferromagnetic behaviour which is understood to be due to nanosized nature of the particles. In 873 K annealed sample defects at the shell such as oxygen, Bi vacancies corresponding to $Bi_{25}FeO_{40}$ phase contributes for weak ferromagnetism. In the precursor sample, oxygen vacancies associated with $BiFeO_3$ phase and Bi vacancies result in local distortion leading to high quadrupole splitting and low hyperfine field. In 873 K annealed sample the hyperfine parameters corresponding to $BiFeO_3$ quite close to the reported values.

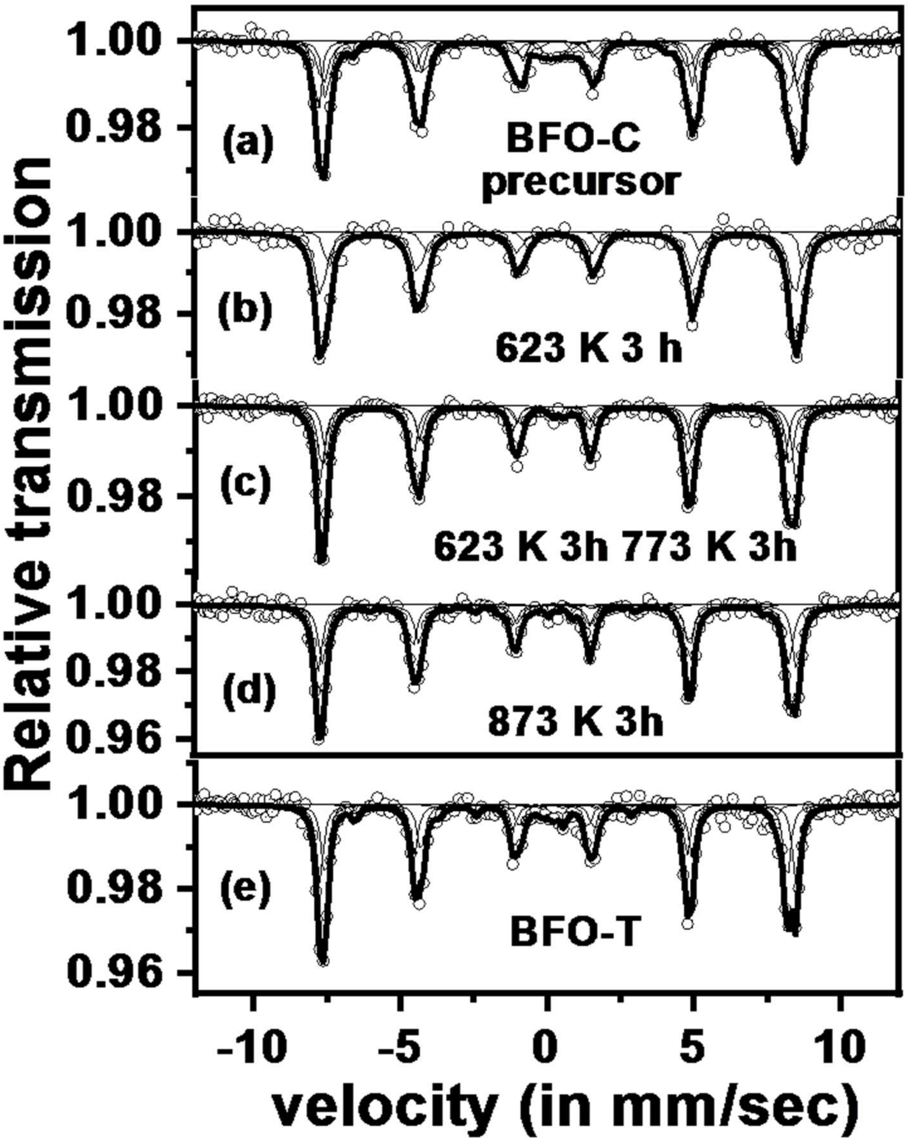

Figure 3.14Mössbauer spectra obtained at room temperature in $BiFeO_3$ prepared using Citric acid in the precursor and subsequent to annealing at different temperatures and time duration as mentioned inside each slot of the graph (a-d) as well as tartaric acid assisted nano-$BiFeO_3$ (e).

Table 3.4 Room temperature Mössbauer parameters of precursor, annealed BFO-C and BFO-T.

Sample	i	δ_i (mm/s)	Δ_i (mm/s)	B_{hf}(Tesla)	Rel Area (%) f_i
$BiFeO_3$	1	0.48±0.01	-0.03±0.02	48.7±0.1	26
Precursor	2	0.40±0.01	0.30±0.06	50.0±0.1	41

	3	0.43±0.09	1.17±0.13	0	02
	4	0.36±0.03	-0.45±0.07	0	03
	5	0.31±0.08	0.65±0.15	44.2±0.5	04
	6	0.50±0.02	0.01±0.02	50.9±0.1	24
623 K 3h	1	0.42±0.01	0.09±0.01	50.0±0.1	83
	2	0.71±0.01	0.08±0.02	50.1±0.1	17
623 K 3 h 723 K 3 h	1	0.39±0.01	-0.09±0.01	49.5±0.1	51
	2	0.40±0.01	0.36±0.01	49.8±0.1	42
	4	0.51±0.04	0.39±0.08	0	02
	5	1.08±0.14	0.90±0.27	34.3±1.0	05
873 K 3h	1	0.41±0.00	0.05±0.01	49.2±0.1	47
	2	0.38±0.01	0.22±0.01	50.5±0.1	46
	3	0.59±0.06	0.81±0.14	0	02
	5	0.76±0.08	0.10±0.17	41.5±0.6	02
	6	0.26±0.06	0.34±0.13	17.0±0.5	03
$BiFeO_3$ Tartaric acid 500C 2h	1	0.39±0.01	-0.10±0.01	49.4±0.1	44
	2	0.41±0.01	0.33±0.01	49.8±0.1	43
	3	0.28±0.33	0.76±0.53	0	01
	4	0.46±0.05	0.35±0.24	0	02
	5	0.68±0.04	0.17±0.09	44.6±0.3	06
	6	0.39±0.07	-0.07±0.14	16.4±0.6	04

Similarly in the case of $BiFeO_3$ prepared through tartaric acid as fuel also exhibits the presence of oxygen vacancies as can be deduced using Mössbauer results. As these are nanoparticles the oxygen vacancies are quite likely to occur at the shell of particles. Hence it is deduced that these particles might be occurring in core-shell structure schematically shown as below with shell of the particles are associated with offstoichiometric $BiFeO_3$.

Annealing at 873 K has resulted in increase in grain size commensurately having both oxygen and Bi vacancies. Fraction associated with Bi vacancies experience low hyperfine field caused by low interaction of superexchange interaction. Thus the magnetic interaction gets altered as compared between $BiFeO_3$ precursor and well annealed samples. These particles are largely AFM as comprehended by core corresponding to $BiFeO_3$ and in the shell due to off-stoichiometric $BiFeO_3$. In the case of BFO-T, the magnetization values are much smaller close to one tenth that of BFO-C. M–H loop close to few Tesla clearly and consistently display AFM nature of the sample. Lesser the percentage of oxygen vacancies associated fraction magnetization values is smaller but this system would be dominantly ferroelectric than that of BFO-C. Hence a well saturated PE loop could be obtained with BFO-T than that of BFO-C.

On the other hand the presence of appreciable fraction of defects such as oxygen vacancies in BFO-C lead to weak ferromagnetism whiles the system shows lesser ferroelectric than that of BFO-T. BFO-C is observed to exhibit magnetic field dependent value of P–E loop and hence magnetoelectric coupling. Thus the observed weak ferromagnetic and magnetoelectric coupling is comprehended due to defects at the shell of $BiFeO_3$.

Commensurate to the observation that BFO-T is more weakly ferromagnetic than that of BFO-C, it is elucidated from the results of PE studies that BFO-T is more strongly ferroelectric than that of BFO-C. Hence in both BFO-C and BFO-T core are AFM ordered while the shell are weakly ferromagnetically ordered. While comparing the magnetization results it is observed that the value of magnetization is lesser in the case of BFO-T as compared to BFO-C. Concomitantly BFO-T is observed to exhibit stronger ferroelectric behavior with well developed PE loop as compared to that of BFO-C. Though the core-shell structures (cf. Figure 3.15) are almost similar in both the cases, the difference in observed in the bulk magnetic and ferroelectric behavior is understood due to spatial distribution of the particles. In the case of BFO-T the particles are more closely spaced than that of BFO-C. Because of more dominant AFM interaction in case of BFO-T as particles are more densely formed, the magnetization in BFO-T is much smaller as compared to BFO-C. Using the same analogy due to much closer packed nature of BFO-T as compared to BFO-C, though the cationic and anionic vacancies are present commonly in both the cases, the difference is observed in magnetic and ferroelectric behavior in BFO-C and BFO-T.

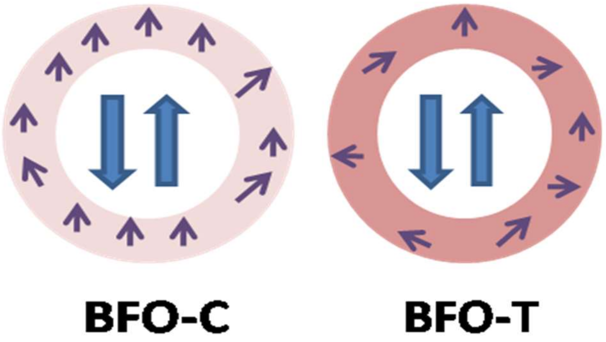

Figure 3.15 Demonstration of core-shell and possible spin arrangements of BFO-C and BFO-T as predicted based on the results of Mössbauer studies.

3.4 Conclusion

Prepared nanoparticles using sol gel route with citric acid and tartaric acid is studied extensively. The effect of fuel and size distribution on multiferroic properties of nanoparticles of $BiFeO_3$ is explored. Smaller size distribution is obtained for BFO-T in comparison to BFO-C due to the proximity of reactants cations in the earlier case. Further BFO-C precursor is observed to have size distribution close to spin cycloid wavelength exhibiting interesting properties. Distortion and Bi/Fe site redistribution is deduced for BFO-C from XRD pattern analysis while that is relatively absent in BFO-T. Raman studies of tartarate assisted $BiFeO_3$ possesses lesser number of broadened modes in comparison to BFO-C resulting from the nano-sized particle distribution. Magnetic property is observed to enhance and depending upon fuel and size distribution. Magnetization studies imply soft ferromagnetic nature of BFO-C due to distorted structure and in addition interestingly the defect site distribution contributes for the ferromagnetic behavior. Defects such as oxygen vacancies as deduced based on Mössbauer results are understood to be present at the shell of nanoparticles contributing to the weak ferromagnetic behaviour as observed based on magnetization studies. In these nano sized particles it is understood that the core are AFM ordered while the shell exhibits weak FM ordering due to uncompensated surface spins. Ferroelectric properties are sensitive to the presence of conductive paths and also found to be sensitive to size. The bulk magnetic and ferroelectric properties could be explained based on defect sites present and illustrated using Mössbauer spectroscopy. The reason of the exhibition of soft ferromagnetic behavior and leaky loop in the case of citrate sample is ascribed to the presence of oxygen vacancies in BFO-C as deduced using Mössbauer results as discussed above. The exhibition of magnetoelectric coupling in BFO-C is also viewed and understood to be due to defects present in the case of citrate sample as comprehended using Mössbauer studies.

4 Effect of substitution on the multiferroic properties of $BiFeO_3$

Graphical Abstract-

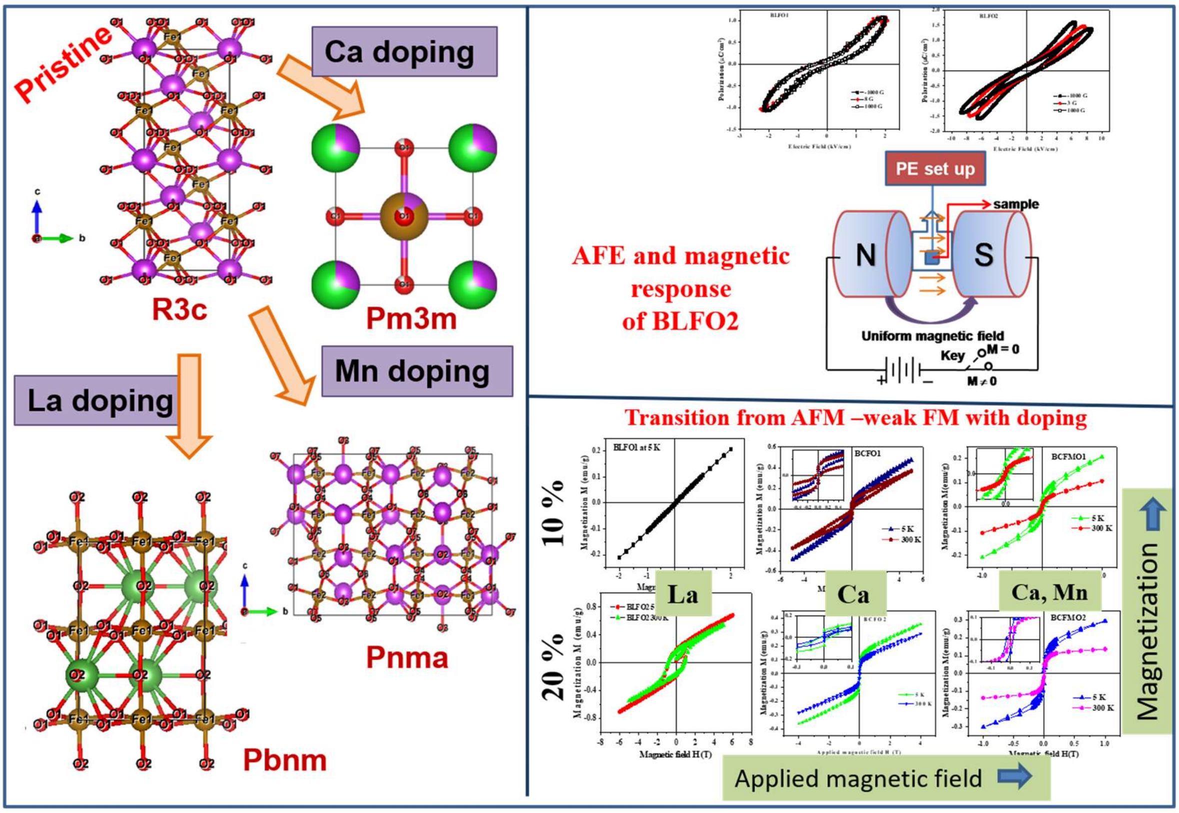

Schematic depicting the phase transition and multiferroic properties in the La, Ca substituted and (Ca,Mn) substituted $BiFeO_3$

Abstract:

Schematic depicts the multiferroic properties of La, Ca and (Ca, Mn) co-substituted at (Bi,Fe) sites in $BiFeO_3$ prepared using solid state synthesis route. The evolution of magnetic properties is discussed with respect to substitution and the ferroelectric properties as well. Atomic level understanding of the distortion and defects are explained with the help of Mössbauer spectroscopy and hence multiferroic properties in this system are also explained. To bring out the understanding of size effects on the multiferroic properties these results are compared with that of the nanoparticles of Ca substituted $BiFeO_3$ prepared using sol-gel route.

4.1 Introduction

$BiFeO_3$ finds extensive applications in arena of electronics and multistage memory devices [31,32,126]. Solid-state route is a standard technique for synthesizing many ceramic oxides [104]. But the solid state route of the preparation of $BiFeO_3$ suffers from serious limitation due to Bi volatility. One of the ways to get rid of this limitation is by means of substituting suitable cations partially at Bi sites. Furthermore substitution also favours the stability of $BiFeO_3$ phase [127–129] with respect to any heat treatments. Enhanced stability of the $BiFeO_3$ phase is attributed to chemical pressure as induced due to substitution of cations at Bi sites. Hence substituting of cations partially at Bi sites results in the stabilization of the $BiFeO_3$ phase. This also provides a wider temperature window for phase formation unlike that of pristine $BiFeO_3$ as deduced in the phase diagram [38].But depending upon the ionic radius and valence of substituent ions as compared to that of Bi^{3+} , the magnetic and electrical properties of the substituted system could get altered [130–132].

Literature results upon the effect of substitution of La, Ca as well as Ca and co-substituted systems on the structural, magnetic and ferroelectric properties are briefly presented in

Table 4.1. While the results on the substituting effects on the magnetic properties and linking with multiferroicity are available, only a few results are available for addressing the effect of substitution at both Bi and Fe sites. Many of these results are interesting but yet to be understood completely. Importantly the multiferroic properties linking the magnetic and ferroelectric properties are not completely understood yet. Hence this chapter intends to throw light on the important effects of substituting at Bi sites and also the effect of simultaneous doing at Bi and Fe sites in $BiFeO_3$.

Table 4.1 Literature review on La substituted $BiFeO_3$, Ca substitution and co substitution.

Substituent	Research highlights	Literature [ref]
La	• Ceramics prepared using solid state route • Structural transition from *R3c* to orthorhombic • Enhanced magnetization • Increased Néel temperature with La concentration	P Suresh *et al*. [134]
La	• Pechini method • *R3c* structure • Improved Ferroelectricity and Ferromagnetism	D S Garcia Zaleta *et al*. [131]
La	• Solid state prepared using high pure oxides • Concentration up to 50 % La is studied to have *R3c* structure • Insulating behaviour with substitution and weak ferromagnetic behaviour	S Jangid *et al*. [135]
La	• Concentration up to 20% caused structural transition from *R3c* to orthorhombic • Weak ferromagnetic behavior ascribed to orthorhombic phase	DV Karpinsky *et al*. [136]
La	• Hydrothermal prepared of preparation up to 30% La substitution • *R3c* structure i.e no structural transition up to 30 % substitution • Increased magnetization value with increase in La substitution	Du *et al*. [130]
La	• Nanoparticles of pristine and substituted $BiFeO_3$ using sol-gel route • Structural transition from *R3c* to orthorhombic	B P Reddy *et al*. [137]
La	• La substituted $BiFeO_3$ revealed the magnetic contribution of cation vacancies with formation of Bi monovacancies and vacancy clusters upon La concentration increasing	W Ge *et al*. [138]
La	• Coprecipitation method used for preparing La substitution up to 30% • Substitution reduced grain size • Leakage current reduced upon increase in substituent concentration • Interfacial polarization at grain boundary is studied	B Yotburut *et al*. [139]
La	• Structure change from *R3c* to orthorhombic with La substitution more than 17 % • Transition magnetic field decreased to produce homogeneous structure and increase in	G Le Bras *et al*.[140]

	magnetocapacitance • Structure change gives enhanced latent magnetization	
La	• Structural transition from $R3c$–$Pm\bar{3}m$ – $Pbnm$	Yao *et al.* [106]
Ca	• Oxygen partial pressure affecting the conductivity • The annealing atmosphere affects the activation energy and conductivity as well • Semiconducting behavior due to mixed valence state	N Maso *et al.* [141]
Ca	• Substitution of Ca similar to inducing hydrostatic pressure • Ca substitution leading to controlled band filling and hence electronic behavior • Creation of pn-junction as well as its destruction and inversion could be controlled • Magnetoelectricity and magnetoelectronics could be merged for application	C H Yang *et al.* [142]
Ca/Ti Ba/Ti	• Ca /Ti and Ba /Ti co substitution is studied • Structure change is observed as $R3c$ –$Pnma$ and $R3c$-$Pm\bar{3}m$ respectively	V A Khomchenko *et al.* [143]
Ca	• Decrease in FeO_6 distortion and increased oxygen vacancies • Controlling structure and magnetic properties with substituent concentration • Increase in a magnetization ascribed to magnetic polarons attached to impurities • Local ferromagnetic ordering is studied	H Xian *et al.* [128]
Ca	• Thin film of Ca substituted $BiFeO_3$ is a better sensor for H_2 gas with sensitivity of 212% for 500 ppm and selectivity at temperature up to 250 °C	Arindam Bala *et al.*[144]
Ca,Sr,Pb	• Effect of Ca, Sr, Pb substitution on leakage properties • Reduction of Fe^{2+} upon substitution	S Chu *et al.*[145]
Ca, Ba	• Fe–O–Fe bond angle variation obtained from refinement and attributed to the magnetic enhancement due to aliovalent substitution	B Ramachandran *et al.* [146]
Ca	• Structure change from $R3c$ to $C222$ • Magnetization increase ascribed to uncompensated spin surface as well as oxygen vacancies	Y N Feng *et al* .[147]
Ca Co Co-substituti	• Ca/ Co co substitution on band gap reduction • $R3c$ to $Pm\bar{4}m$ • Volume decrease and stiffened Bi–O bond	C Quan *et al.* [148]

on	• Suppressed spin cycloid enhancing magnetism	
Co-substitution	• Enhanced magnetization due to destroyed spin cycloid with fine tuned optical properties	R R Awasthi *et al.* [149]
Mn	• Nanofibres of $BiFeO_3$ • Mn substitution of 5% caused large saturation magnetization and double exchange interaction	Bin *et al.* [150]
Mn	• Structural transition to *Pbnm* upon 30% substitution and improved remanence	L Chen *et al.* [151]
Mn	• Thin film shows distorted structure and altered magnetic interaction	Y Zhang *et al.* [129]
Mn	• Induced FM due to JT distortion of MnO_6 and suppressed saturation magnetization with Mn concentration increase in nano-ceramic sol-gel sample	M Abushad *et al.* [152]
Mn	• ME coupling is established through capacitance variation with applied magnetic field • Photo luminescent properties are studied	S Chauhan *et al.* [102]
Mn	• Structural in homogeneity and defect sites of Bi and O lead to charge carrier hopping • FE and magnetic hysteresis are studied • ME coupling is established	B Dhanalakshmi *et al.* [132]
Mn	• Decrease in Curie temp • Reduced particle size and local FM due to Mn substitution to enhanced magnetization	S Basu *et al.* [153]

The structural properties are directly correlated with the magnetic and ferroelectric properties hence the substitution at different sites cause varying bond lengths and bond angles altering overall crystal structure leading to the alteration of multiferroic properties as well [101,130,131]**.** Hence structural stability plays a significant role in controlling the properties. The stability of the perovskite phase is defined in terms of Goldschmidt tolerance factor [106] calculated by using the formula

$$t = \frac{1}{\sqrt{2}}\left(\frac{r_{Bi}+r_O}{r_{Fe}+r_O}\right), \qquad 4.1$$

where r_A, r_B and r_O are the ionic radii of the cations A and B and anion respectively. The Shanon radii for the elements taken are 1.01, 1.00, 1.34, 0.645,0.645 and 1.4 Å for Bi^{3+}, La^{3+}, Ca^{2+}, Fe^{3+}, Mn^{3+} and O^{2-} respectively. The tolerance factor ‘t’ as calculated using the formula and its variation with respect to substitution is shown in Figure 4.1. The value of t varying in the range 0.85 to 1.05 are expected to be stable whereas that below and above arises due to distortion [154]. The t value for La substitution is close to that of pristine $BiFeO_3$.The decreasing value of t with an increase in the La substitution can be ascribed to increased distortion in addition to the stabilized phase formation and hence leading to interesting properties [129,130,154]. Notably, the plot shows that the t value at the lower limit for Ca substitution of 10% and with concentration increasing t values becomes more stabilized implying reduced distortion. Furthermore, the co- substitution of Mn along with Ca has similar value of tolerance factor implying the B site substitution has negligible effect on distortion.

In this chapter the following substituted systems such as $Bi_{1-x}La_xFeO_3$ (x= 0.1, 0.2), $Bi_{1-x}Ca_xFeO_3$ (x= 0.1,0.2) and $Bi_{1-x}Ca_xFe_{1-y}Mn_yO_3$ (x= 0.1,0.2 and y~0.05) are studied for their magnetic and ferroelectric as well as coupling properties.

This chapter is divided into two sections. The first section discusses the effect of the isovalent La substitution up to 20 % at Bi site and the second part probes the effect of co substitution of (Ca, Mn) at (Bi, Fe) sites on the multiferroic properties of this system. The details of structural, bulk magnetic as well as ferroelectric properties of each substituent are discussed. Further the magnetoelectric coupling of the systems is understood by deducing magnetoelectric coupling parameters from the PE experiments under applied magnetic field. A brief study on the size effect in the case Ca substituted $BiFeO_3$ is discussed at the end of the chapter. Mössbauer spectroscopy is effectively used to deduce the hyperfine parameters which correlates the magnetic structure and defect site information and also gives an atomic level picture of the distorted structure and correlates with magnetic properties at an atomic scale.

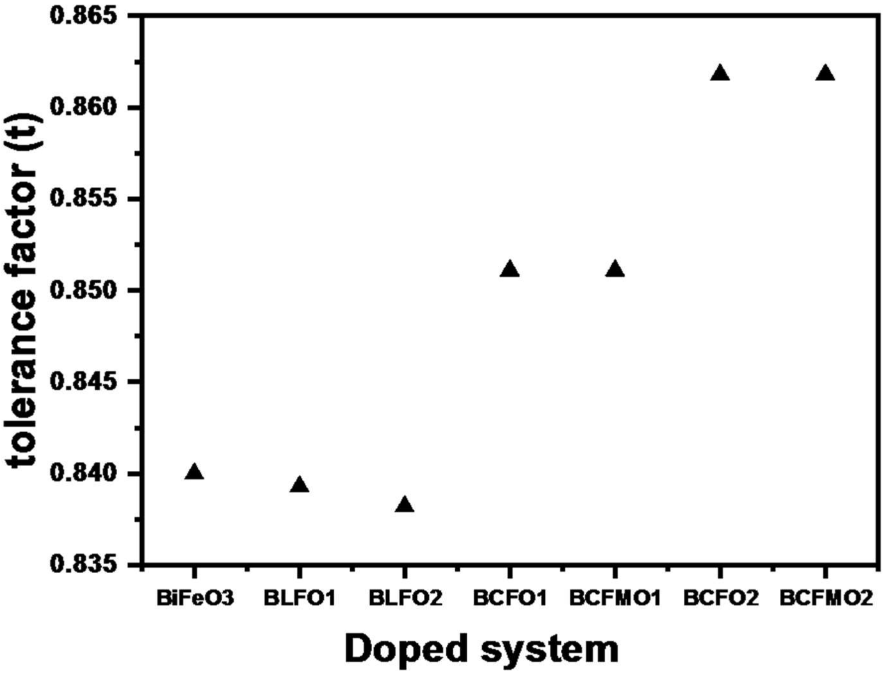

Figure 4.1 Tolerance variation w r t substitution to study the stabilization of the phase.

4.2 Synthesis of substituted Bulk $BiFeO_3$ Particles using Solid-state Route

Bulk $BiFeO_3$ are prepared using the starting oxides. Bi_2O_3, Fe_2O_3, La_2O_3, CaO, MnO of LR grade are taken in required stoichiometric ratio for preparation of $Bi_{1-x}La_xFeO_3$, $Bi_{1-x}Ca_xFeO_3$, $Bi_{1-x}Ca_xFe_{0.95}Mn_{0.05}O_3$ (x=0.1 and 0.2). The oxides are ground thoroughly and pelletized using hydraulic press into 10 mm diameter pellets and sintered at 1073 K 48 h and subsequently 1123 K for 6 h/12h (for La substituted $BiFeO_3$) and 1073 K 48 h (for Ca substituted and Ca, Mn co-substituted $BiFeO_3$) respectively (cf. .Figure 4.2).The synthesis process followed here is similar to literature [156]. Solid-state chemistry involves the diffusion mechanism. The interactions of adjacent particles take place by mass transport and subsequent diffusion of Bi into Fe [157] details of which are discussed in chapter 2. The annealing at 1073 K facilitates the surface interaction forming the intermediate stable Bi rich phase which grows and interacts with Fe_2O_3 in gradual manner and upon heating for sufficiently long time, forms required $BiFeO_3$ phase. Due to defect chemistry and non-stoichiometry arising from Bi volatility causes the appearance of parasitic phases in $BiFeO_3$ [34]. However, substitution helps in the formation of pure $BiFeO_3$ phase. The samples thus prepared henceforth referred to as BLFO1, BLFO2, BCFO1, BCFO2, BCFMO1, BCFMO2 respectively for La substituted, Ca substituted and Ca, Mn co substituted samples with 10 and 20 % concentration of La, Ca substitution and with 5 % Mn in case of co-substitution respectively .Sol-gel method is employed for preparing Ca substituted $BiFeO_3$ using citric acid as fuel and steps similar to that discussed in chapter 3.

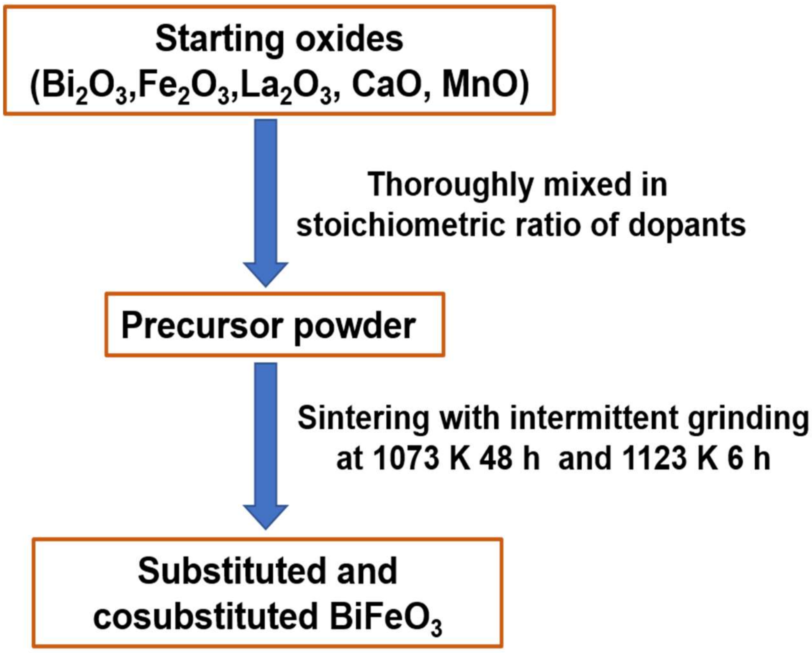

Figure 4.2 Steps involved in solid state preparation of substituted and co substituted system.

The prepared materials are characterized for structure and multiferroic magnetoelectric studies by using suitable techniques.

4.3 Local Structural, Magnetic, Ferroelectric and Magnetoelectric Properties of La Substituted $BiFeO_3$

La is isovalent to Bi. Unlike Bi, La lacks active lone pair. The stability of the structure is affected upon La substitution. However, $BiFeO_3$ structure is stabilized in presence of La. Hence the substitution effect at Bi site by La is important to study the improvised properties. Hence we have carried out the structural and magnetic studies of the bulk La substituted $BiFeO_3$.

4.3.1 Structural Studies

Characteristic feature of distorted *R3c* structure in pristine $BiFeO_3$ modifies in presence of La in the neighbourhood of Bi. XRD is thus used to probe the structural properties when La is substituted.

4.3.1.1 X–ray Diffraction Studies

The XRD pattern of the prepared La substituted $BiFeO_3$ through solid-state route are presented in Figure 4.3 and observed to exhibit $BiFeO_3$ phase predominantly matching well with ICDD 71-2494 [102]. It is observed that the formation of phase pure sample is obtained with higher annealing temperature for a longer time as seen from the progressive steps of annealing leading to standard intensity ratio of the (104) and (110) planes. The crystallization of $BiFeO_3$ phase is improved with annealing at higher temperature for a comparatively longer time of 12 h (cf. Figure 4.3). The concentration of substitution has substantial effect on structural transition as well as on crystallization of *R3c* phase fraction. The *R3c* rhombohedral structure found to be modified with La substitution which is also linked to the distortion with respect to tolerance factor. In 10% La substituted $BiFeO_3$, the most intense peaks as well as planes at (006) are found to change in terms of intensity ratio as compared to the standard. Further with increase in La concentration, these peaks completely merge and facets like (012) and (024) split signifying the structural distortion due to substitution at A site [133,136,139,157]. The splitting and merging of the peaks corresponds to structural transition from *R3c* to *Pbnm* structure with increasing La content similar to that of orthorhombic $LaFeO_3$ [134]. XRD patterns highlighting the variation of most intense peaks are shown as right panels in Figure 4.3. Intensities of peaks and peak positions corresponding to (104) and (110) planes vary with the concentration of La. Intensity of (104) plane, which is a signature of *R3c* structure decreases and that of (110) plane increases with increasing La fraction. This implies that with an increase in La fraction, the *Pbnm* structure grows at the cost of *R3c* phase fraction.

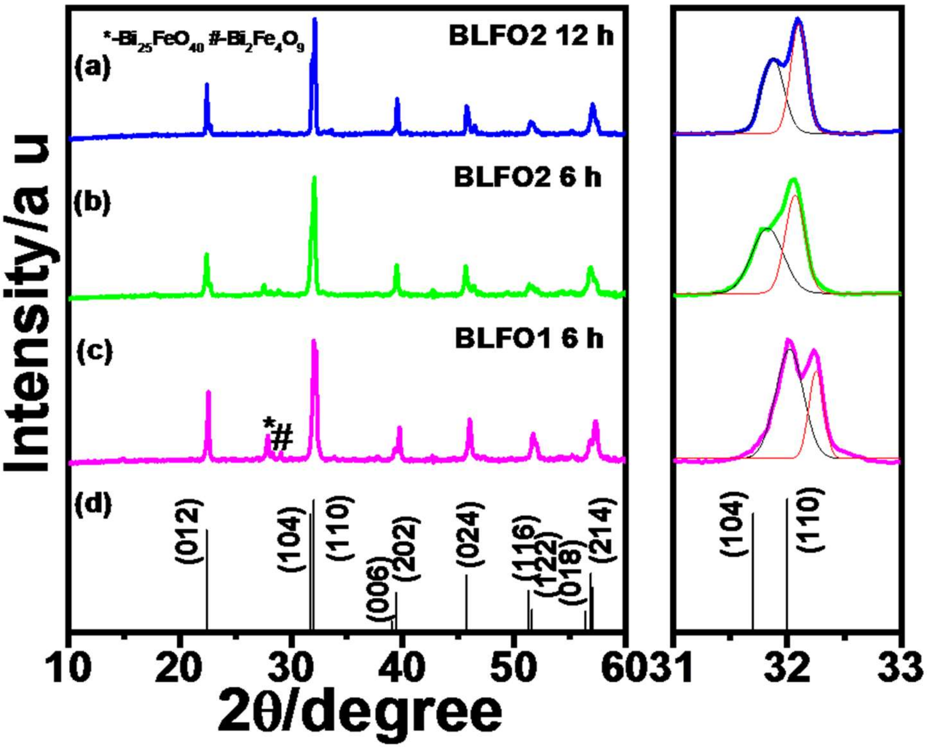

Figure 4.3 XRD pattern corresponding to 20 % La substituted $BiFeO_3$ heat treated at 1073 K 48 h and 1123 K 12 h and 6 h ((a) & (b)) and 10 % La substituted $BiFeO_3$ sintered at 1073 K 48 h and 1123 K 6 h (c) showing the presence of impurity phases such as $Bi_{25}FeO_{40}$ and $Bi_2Fe_4O_9$ in a small concentration in the case of 10 % substituted sample prominently (marked by * and #) and the results are compared with standard stick pattern of Rhombohedral $BiFeO_3$

A close inspection of the variation of the most intense peak with respect to La substitution as compared with respect to standard XRD pattern of pristine $BiFeO_3$ is shown as the right panel of Figure 4.3. The shifting of the planes to higher 2θ is a signature for the presence of distortion. And with increasing concentration of La the peak position shifts further to higher 2θ. This observation is similar to the discussion given with respect to the tolerance factor. The formation of impurities can be related with the formation of $BiFeO_3$ in *R3c* crystallization phase and is evident from X-ray pattern plot.

Presence of La in BiO_6 dodecahedron induces distortion and the substitution of La at Bi sites is expected to result in a reduced ferroelectric properties. However as the ferroelctricity and magnetic properties are mutually exclusive and coexist in this material, hence a decrease in ferroelctricity can in turn may enhance the magnetic properties. In addition the structural transition from *R3c* to *Pbnm* also affects the magnetic properties. Hence the magnetic properties are studied for the prepared La modified $BiFeO_3$ stabilized phase in the subsequent section.

4.3.2 Bulk Magnetic Property Studies

In order to give an insight into the effects induced upon magnetic properties due to isovalent La substitution in $BiFeO_3$ we have carried out both field dependent magnetization M-H loop as well as temperature dependent magnetization ZFC and FC variation on BLFO.

Results of the field dependent magnetization studies of BLFO1 and BLFO2 are shown in Figure 4.4. It is observed that the BLFO1 exhibits AFM linear magnetization with applied magnetic field and an opened up unsaturated loop for BLFO2. The unsaturated finite loop area in case of BLFO2 implies the coexisting weak FM and AFM behaviour [159]. AFM behaviour in case of BLFO1 can be understood as the substitution La fraction is small such that the crystal structure remains as *R3c* resulting in a linear variation of M with H. In case of BLFO2 the combined effect of broken spin cycloid as well as the partial structural transition helps in exhibiting coexisting magnetic behaviour. The presence of the phases is in the form AFM core and weak FM shell resulting from the uncompensated spins at the surface [119].The remanence (M_r) and coercivity (H_c) values of the samples are presented in ABK plot (cf. Figure 4.5) derived from the MH data for the samples further confirms the antiferromagnetic behaviour exhibited by BLFO1 and ferromagnetic behaviour up to applied field of 2 T whereas beyond that AFM behaviour prevails. The linearity in M–H at higher applied magnetic field confirms this fact [165]. The convex curve region decreases with increasing in temperature from 5 K to 300 K which is expected due to randomization of spins with response to thermal energy effects [134].

The magnetization value increases by 1000 times upon the increased substitution of La from 10 to 20%. In a similar manner coercivity enhances from 103 Oe to 8000 Oe upon La substitution. The significant increase in magnetization and coercivity is understood to be due to a combined effect of distortion caused from La replacement as well as partial structural transition. Magnetization at lower applied field of 0.02 to 0.04 T can be ascribed plausibly to the ferromagnetic component [49,132,135] while the linearity at higher applied field is due to dominant antiferromagnetic behaviour. The nonlinear jump of MH loop at magnetization axes is attributed to the nonmagnetic La substitution. Thus the addition of La at A site enhances the magnetic behaviour of $BiFeO_3$ [131].

Temperature dependent magnetization studies shown in Figure 4.4 reveal the effect of La substitution suppressed nonstoichiometry arriving from the Bi volatility as La replaces Bi. BLFO1 exhibits completely overlapped ZFC and FC curve except at the anomaly 50 K. For BLFO2 a bifurcated zone between ZFC FC up to RT with observed 50 K anomaly for ZFC as well as broad anomalies in FC. There is a substantial increase in magnetic moment at low temperature for both ZFC as well as FC. The 10 % La substitution exhibiting *R3c* rhombohedral structure shows antiferromagnetic behaviour due to the compensation of spins following DM interaction with the incommensurate spin cycloid giving rise to zero net magnetic moment hence the ZFC and FC curve overlaps. With concentration of La increasing structural transition leads to suppression of spin cycloid and impediment of the grain size partially as well as distortion and hence anisotropic magnetic behaviour arises. As a result magnetic properties are strongly influenced by the presence of La^{3+} in place of Bi and the ferromagnetism in BLFO2 is a combined effect from partial structural transition as well as distortion and to some extent reduced grain size leading from the lower diffusion rate of La in place of Bi. As the relative fraction of orthorhombic phase increases upon increased substitution of La and hence the homogeneous structure leads to enhancement in magnetic behaviour [134,135]. The ZFC FC measurement is done at higher than 1000 Oe field to get the contribution from the components implying complexity of the magnetic behaviour possibly occurring due to coexisting crystallized phases [134,135]. The splitting attributed to anisotropic magnetic behaviour as reported by Joy *et al.* [160].

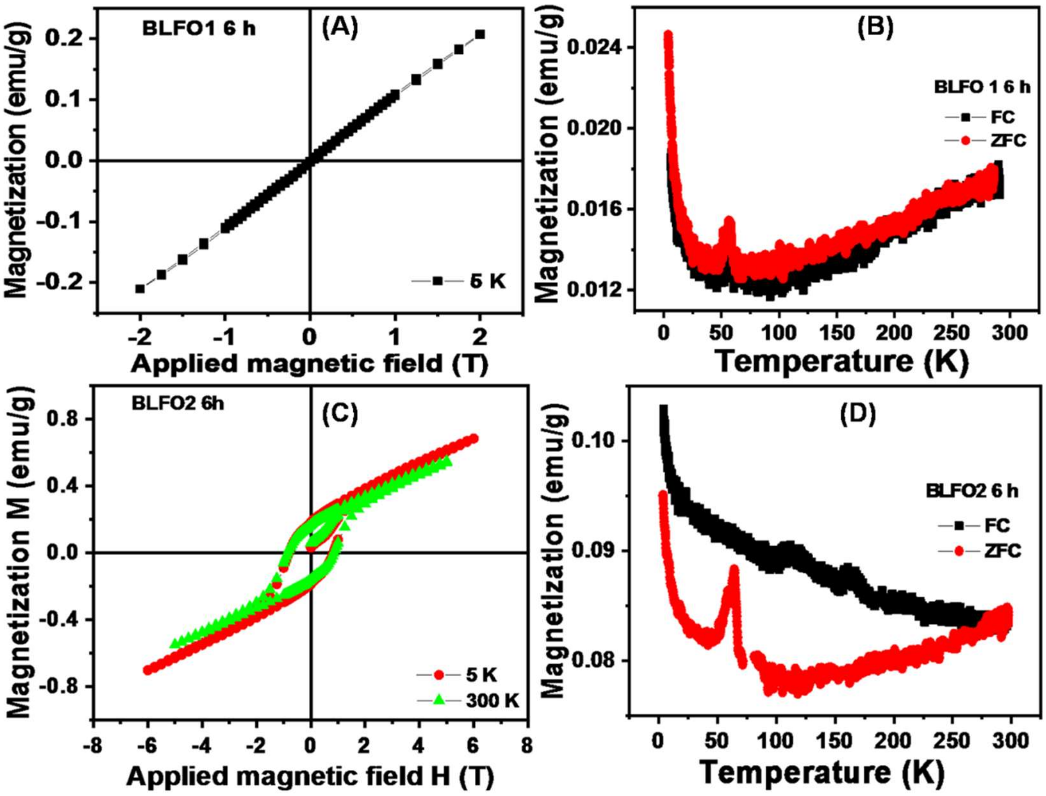

Figure 4.4 Field dependent magnetization studies of BLFO1 and BLFO2 heat treated at 1073 K 48 h and 1123 K 6 h ((A)&(C)) ZFC FC variation for BLFO1 and BLFO2 ((B)&(D)) showing AFM and Weak FM nature respectively with overlapped ZFC FC in former and bifurcated region in the later.

Table 4.2 Magnetic parameters of BLFO2.

Sample	T(K)	Mr(emu/g)	Ms(emu/g)	Mr/Ms	Hc(Tesla)
BLFO2	5	0.1853	0.238	0.778	0.8176

300	0.16305	0.203	0.803	0.85195

The spike around 50–70 K is referred to cluster magnetic pinning effect resulting from the quenching process in Sr Pb substitution $BiFeO_3$ [161] and also observed by several groups [162]. The spike at 50 K also allotted to the spin freezing behaviour by Park *et al.* due to strong inter-particle interaction [119]. Hence we can attribute the peak at 50 K as spin reorientation temperature at low temperature there should be a balance between FM and AFM orderings or electronically phase separated FM and AFM which otherwise leads to magnetic spin glass system [163]. The increase in magnetic moment below 100 K is a signature of weak FM ordering or due to canted AFM ordering [163]. ZFC shows prominent anomalies at 100 K and 150 K apart from the bifurcation at 250 K. Similar anomalies have been reported to be strongly related to magnetoelectric coupling as discussed by Ramachandran [164].

ABK plot (cf. Figure 4.5) derived from the MH data for the samples further confirms the antiferromagnetic behaviour exhibited by BLFO1 and ferromagnetic behaviour up to applied field of 2 T whereas beyond that AFM behaviour prevails. The linearity in M–H at higher applied magnetic field confirms this fact [165]. The convex curve region decreases with increasing in temperature from 5 K to 300 K which is expected due to randomization of spins with response to thermal energy effects [134].

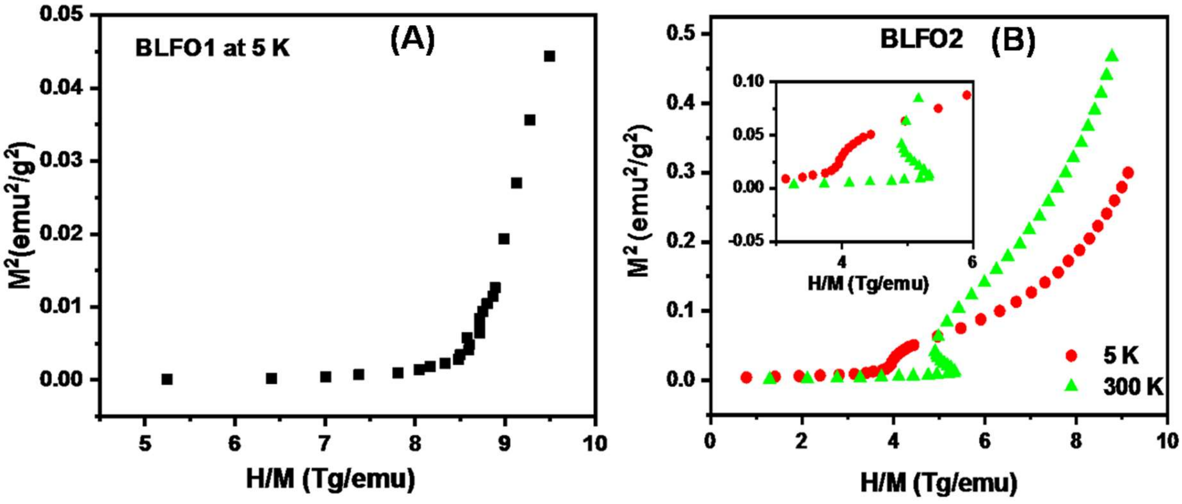

Figure 4.5 A-B-K plot showing concavity for BLFO1 (A) and convex behaviour for a range lower magnetic field and concavity of higher applied field in BLFO2 (B) depicting the AFM predominance and coexisting AFM and weak FM in BLFO1 and BLFO2.

4.3.3 Ferroelectric and Magnetoelectric Studies

In addition to the magnetic studies ferroelectric characterization is explored to understand the effect of distortion and oxygen concentration variation upon ferroelectricity. In addition coupling of the ferroelectric polarization with magnetic field is carried out and discussed.

The ferroelectric PE loops observed for BLFO1 and BLFO2 are shown in Figure 4.6. The observed RT ferroelectric loop implies the existence of ferroelectricity in both the samples and the enhancement with La concentration. The unsaturated loop and the round shaped edges of the loop indicate the leaky behaviour of the samples [130,149,165,166]. The quantitative values are related to higher values as compared to pristine $BiFeO_3$. Further the nonlinearity of the PE loop about the applied electric field is related to the antiferroelectricity induced due to altered ferroelectric domains resulting from La replacing Bi atoms and will be discussed in detail subsequently. This implies an increase in resistivity due to the substitution of La at Bi sites in $BiFeO_3$.

The applied electric field for observing a discrete magnetoelectric switching of ferroelectric domains ranges over a wide applied electric field zone and mostly is high enough to apply within instrument limit. Hence unlike magnetism ferroelectricity is not distinct and has to be understood in an extensive manner following comparative analysis. Hence the relative change in the ferroelectric behaviour makes more sense in understanding magnetoelectricity.

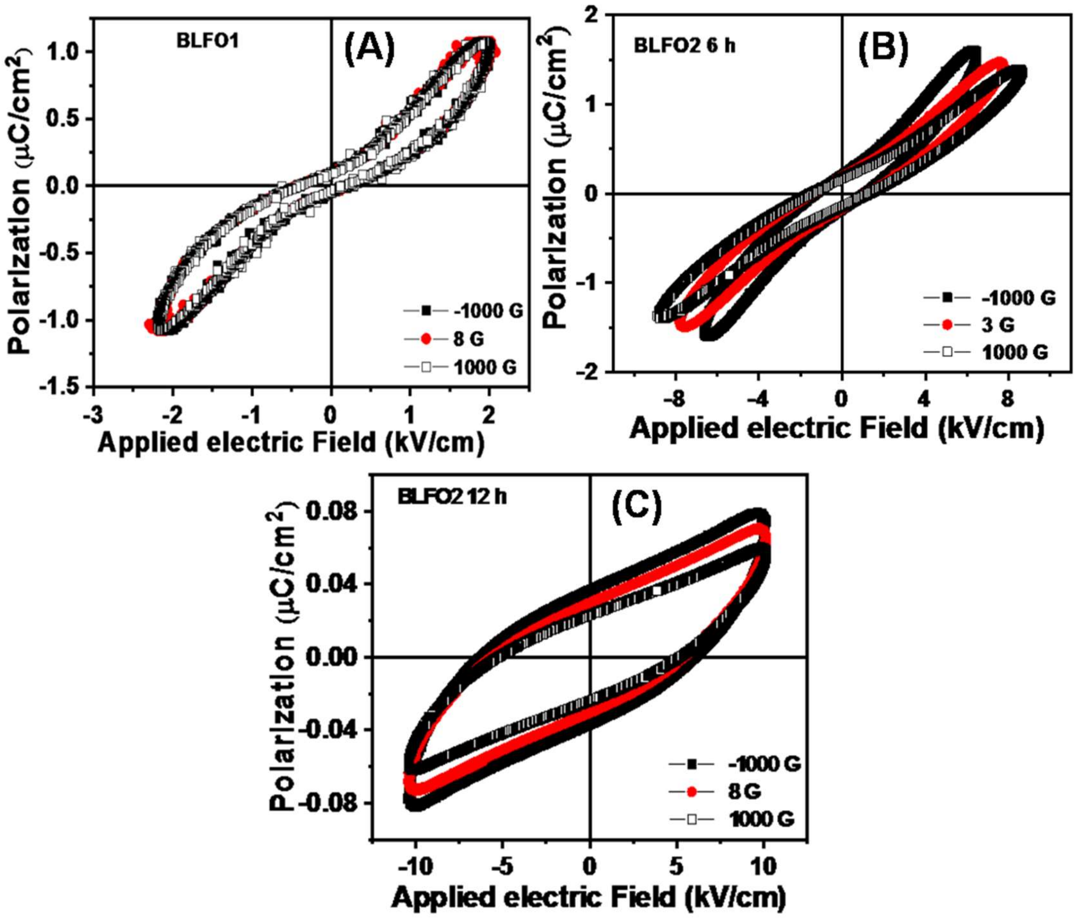

Figure 4.6 Ferroelectric hysteresis loop of BLFO1(A) and BFLO2 ((B) & (C)) studied in presence of magnetic field. The substantial switching behavior is a consequence of strong magnetoelectric coupling with the dominance of ferroelectricity as deduced from the suppressed nonlinearity, where nonlinearity represents the antiferroelectricity induced due to La presence.

The observed variation of PE loops in La substitution $BiFeO_3$ systems under the applied magnetic field are shown in Figure 4.6. The lossy ferroelectric behaviour in BLFO1 exhibiting antiferroelectricity is same even with applied magnetic field. In BLFO2, however, the PE loop nonlinearity is suppressed and ferroelectric behaviour responds to magnetic field. BLFO1 showing AFM behaviour shows negligible response to the magnetic field of 0.1 T whereas with increase in La concentration the response to magnetic field improves. The observed loop for ± 0.1 T shifts to both sides of loop when field is applied from -0.1 to

0.1 Tesla through nearly zero applied magnetic field. This signifies possible switching of ferroelectric order under applied electric field with changing directions of applied magnetic field [125]. The observed phenomenon of response of ferroelectricity to magnetic field is significantly evident, confirming the magnetoelectric coupling.

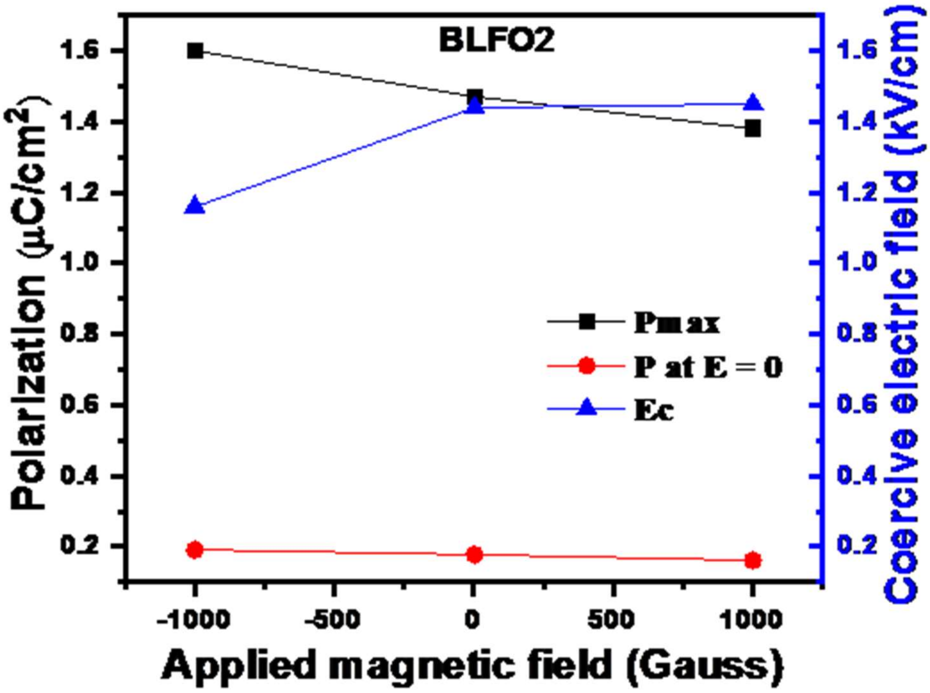

Figure 4.7 Variation of ferroelectric parameters P_r and E_c with respect to applied magnetic field. Both the polarization and coercive electric field are found to be much higher in BLFO2 then in BLFO1.

4.3.4 Discussion of Mössbauer Spectroscopy Results on La substituted $BiFeO_3$

Mössbauer spectra obtained in BLFO1 (prepared through solid state route by means of annealing at 1073 K for 48 h followed by 1123 K for 6 h in air) could be deconvoluted in to four components. Two sextets mainly differ in the values of quadrupole splitting with opposite sign. This is understood to be due to different trigonal distortion of the octahedral environment of both Fe sites resulting in quadrupole splitting of opposite signs. Values of hyperfine field remain almost same close to 50 Tesla. Two doublets differing in the values of isomer shift and quadrupole splitting are attributed to Fe atoms associated with $Bi_{25}FeO_{40}$ and

$Bi_2Fe_4O_9$ phases. Doublet with low isomer shift is associated with high quadrupole splitting. The remaining fraction of Fe atoms is exposed to quadrupole interaction with lower isomer shift and much higher quadrupole splitting as compared to the previous doublet.

BLFO1 is seen to exhibit lower value of magnetization with magnetic field (cf. Figure 4.4) and hence AFM ordering. PE loop studies (cf. Figure 4.6) indicate the ferroelectric nature of BLFO1, it is further observed that the ferroelectricity does not vary with the application of external magnetic field. The observed AFM, ferroelectric and magnetoelectric coupling can be understood based on the results of MS as follows. In the case of BLFO1, based on the values of hyperfine parameters as reported [116] the two sextets are identified to Fe atoms associated with $BiFeO_3$ phases. Based on the values of isomer shifts it could be deduced that the Fe atoms associated with these sites are in Fe^{3+} ionic state. There are no defects associated fractions of Fe atoms viz., presence of Fe^{2+}in the bulk of the La substituted $BiFeO_3$ (BLFO1) pointing out to the presence of oxygen vacancies as seen in the case of the nanoparticles of $BiFeO_3$.

In the case of nanoparticles of $BiFeO_3$ anionic vacancies are observed to be present as discussed in the previous chapter of this thesis based on the Mössbauer results, which are deduced to play an important role for the observed weak ferromagnetic behavior and hence magnetoelectric coupling of $BiFeO_3$. In the case of BLFO1 as discussed above the presence of oxygen vacancies are ruled out. Further there are no additional sextets (as seen in the case of $BiFeO_3$ nanoparticles prepared through sol-gel route) that could be deduced which can be attributed to Fe atoms associated with defects related to $BiFeO_3$. Hence the observed antiferromagnetic behavior of BLFO1 based on the M-H result is consistent with the results obtained using Mössbauer spectroscopy.

Absence of any other sextet that could be attributed to Fe atoms associated with either Bi or oxygen vacancy in 10% La substituted $BiFeO_3$ sample implies that La substitution does not result in formation of any defects associated fractions. This implies that La^{3+} substitutes Bi^{3+} sites without any lattice distortion and further accompanied by the absence of any cationic or anionic defects. Hence the Mössbauer results imply that the 10% La substituted $BiFeO_3$ sample remains strongly antiferromagnetic and there are no defects associated magnetic components are observed what could be attributed to the partial presence of any weak ferromagnetic ordering. Absence of any weak ferromagnetic ordering as deduced in this Mössbauer study is consistent with the observed linear behavior of magnetization with the applied field and the absence of any loop implying the antiferromagnetic ordering. This result also rules out the presence of any magnetoelectric coupling in 10% La substituted $BiFeO_3$ sample as evidenced by the absence of any variation of P–E loop with the applied magnetic field as seen in Figure 4.6.

Weak ferromagnetic ordering in the bulk samples of $BiFeO_3$ substituted with suitable cations at Bi sites could emerge based upon the following viz., 1) suppression of spin cycloid configuration 2) presence of anionic vacancies and/or 3) occurrence of any other impurity phases which are ferromagnetically ordered. Mössbauer results point to the absence of any oxygen vacancies, the presence of any such would lead to the occurrence of some of the iron atoms being in Fe^{2+} state. As all the iron atoms are observed to be in Fe^{3+} as deduced based on the values of isomer shifts of the components, the presence of oxygen vacancies and hence Fe^{3+}–O–Fe^{2+} based double exchange interaction induced magnetic ordering is ruled out. Impurity phases present in the sample were identified to be due only to $Bi_2Fe_4O_9$ and /or $Bi_{25}FeO_{40}$ which are paramagnetic at room temperature.

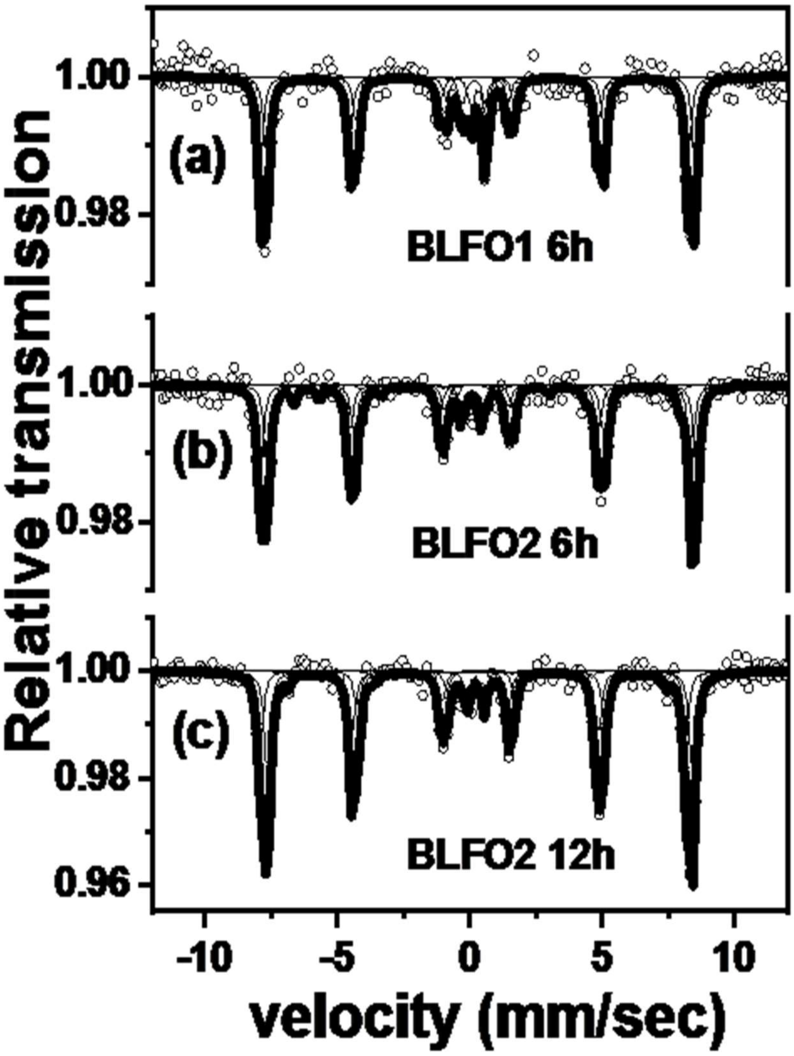

Figure 4.8 Mössbauer spectrum as obtained in La substituted $BiFeO_3$ at 300 K (a) BLFO1-6h sintered at 1073 K 48 h and 1123 K 6 h (b) BLFO2-6h sintered at 1073 K 48 h and 1123 K 6 h and (c) BLFO2-12h sintered at 1073 K 48 h and 1123 K 12 h.

Table 4.3 Hyperfine parameters deduced from deconvoluted spectra of BLFO1 and BLFO2 from Figure 4.8.

Sample	i	δ_i (mm/s)	Δ_i (mm/s)	B_{hf}(Tesla)	Rel Area (%) f_i
BLFO1	1	0.41±0.01	-0.21±0.02	50.1±0.1	41
(1073 K 48 h	2	0.40±0.01	0.24±0.01	50.2±0.1	42
1123 K 6 h)	3	0.41±0.04	0.50±0.07	0	08
	4	0.28±0.02	0.92±0.04	0	09
BLFO2-A	1	0.39±0.01	-0.11±0.01	50.4±0.1	42

(1073 K 48 h	2	0.39±0.01	0.29±0.01	50.3±0.1	41
1123 K 6 h)	4	0.16±0.02	0.75±0.04	0	07
	5	0.51±0.05	0.47±0.09	45.2±0.3	05
	6	0.34±0.04	-0.04±0.09	33.9±0.4	05
BLFO2-B	1	0.39±0.01	-0.25±0.01	49.8±0.1	33
(1073 K 48 h	2	0.40±0.01	0.18±0.01	49.8±0.1	57
1123 K 12 h)	4	0.33±0.02	0.67±0.05	0	06
	5	0.50±0.04	-0.19±0.09	49.4±0.3	04

Therefore, based on the Mössbauer results it is deduced that the observed weak ferromagnetic ordering is deduced to be due to lattice strain induced effects resulting in the partial suppression of spin cycloid. In the following an understanding of the appreciable magnetoelectric coupling effects as observed in BLFO2 which were absent in BLFO1 is provided based on the analysis of Mössbauer results.

Weak ferromagnetic ordering and appreciable magnetoelectric coupling have been observed in the case of BLFO2 as represented in Figure 4.4 and Figure 4.6. In the case of BLFO2 it is already seen that orthorhombic (*Pbnm*) phase in addition to *R3c* phase of bismuth ferrite. Partial presence of *Pbnm* phase of $BiFeO_3$ is likely result in local strain in the lattice resulting in the suppression of spin cycloid which would otherwise be present in *R3c* phase of $BiFeO_3$. This is understood to be main reason for the occurrence of weak ferromagnetic ordering as observed in BLFO2.Another important observation is that both in the case of BLFO2-A and BLFO2-B there occurs a fraction of Fe atoms exposed to magnetic interactions with hyperfine fields 45.2 and 49.4 Tesla component respectively and the value of isomer shift close to 0.5 mm/s in both the cases. This implies the possible presence of Fe^{2+} in BLFO2-A and BLFO2-B samples. This implies that in addition to strain effects the additional presence of oxygen vacancies also might be contributing for the observed weak ferromagnetic ordering. As La^{3+} is of same valence as that of Bi^{3+}, the occurrence of oxygen vacancies in BLFO2-A and BLFO2-B could be understood due to annealing effects.

4.4 Influence due to Ca Substitution at Bi sites and Co-substitution of (Bi, Fe) sites by (Ca, Mn) on Structural, Magnetic and Magnetoelectric Properties of $BiFeO_3$

Aliovalent substitution at Bi^{3+}site has the plausible effect on magnetic properties as elements like divalent Ca^{2+},Ba^{2+} could introduce oxygen vacancies and hence alter the exchange interactions [142,146,167]. Charge defects along with strain arising due to ionic radii difference influences the structural as well as electrical properties. Further it is reported that by substituting isovalent Mn^{3+} at Fe^{3+} site alter the exchange interactions with interesting magnetic properties [101,131,168]. In addition Mn being Jahn-Tellar distorted ion can lead to modified ferroelectric behavior. Hence in this section we will discuss in detail the structural, magnetic, ferroelectric as well as multiferroic properties due to the respective substituents at Bi, Fe sites and also simultaneous substitution at Bi and Fe sites.

4.4.1 Structure Analysis

XRD is used to probe the structural transition when the Bi site is substituted partially by Ca and in addition Fe site is substituted with Mn. Furthermore, the distortions as well as the oxygen related off-stoichiometry are also deduced in the structure analysis. In addition Raman spectroscopic study is carried out to probe the modified phonon-phonon interaction when either A site or both A and B site is substituted. And hence a correlated picture is given to visualize the multiferroic properties further in the subsequent section.

4.4.1.1 XRD Studies

The XRD patterns corresponding to BCFO and BCFMO samples are shown in Figure 4.9(A). It is observed that the split peaks in pristine $BiFeO_3$ merge into single peak (i.e. peaks indexed to (hkl) such as ((104) and (110)), ((006) and (202)) and ((013) and (214)). In addition the peak corresponding to (104) is suppressed and (110) plane is dominating at the cost of (104). As discussed earlier the occurrence of the peak at (hkl) value of (104) signifying *R3c* structure. Its diminishing intensity explains further the structural transition from *R3c* to *C222*. In a similar fashion merging and diminishing intensity of the peaks at (116) and (122) upon Ca substitution fraction can be explained. Another important observation deduced form the XRD is the decreasing relative intensity of (021) in comparison with (110) plane. Above mentioned observations confirm the structural transition from *R3c* to *C222* structure in BCFO and BCFMO due to the substitution of smaller sized Ca at Bi sites. The evolution and intensity variation of most intense peaks with respect to substitution and co-substitution is shown in right inset of Figure 4.9(A). The shift in most intense peaks as well as the variation of lattice parameters is shown in Figure 4.9(B)**.** It is shown that the two peaks corresponding to *R3c* structure of $BiFeO_3$ shifts towards higher 2θ and for higher substitution concentration 20 % Ca the peaks merge into a single one. In addition to Ca substitution when some Fe are replaced by Mn the peak features observed to remain same that without Mn only with subtle additional shift to higher 2θ and attributed to the slight ionic radii mismatch between Fe and Mn. With substitution of Ca, which is smaller in ionic radii and lesser valence than Bi leads to strain induced distortion. No additional peaks are observed implying that Ca and Mn have occupied Bi and Fe respectively without resulting in the formation any impurity phase.

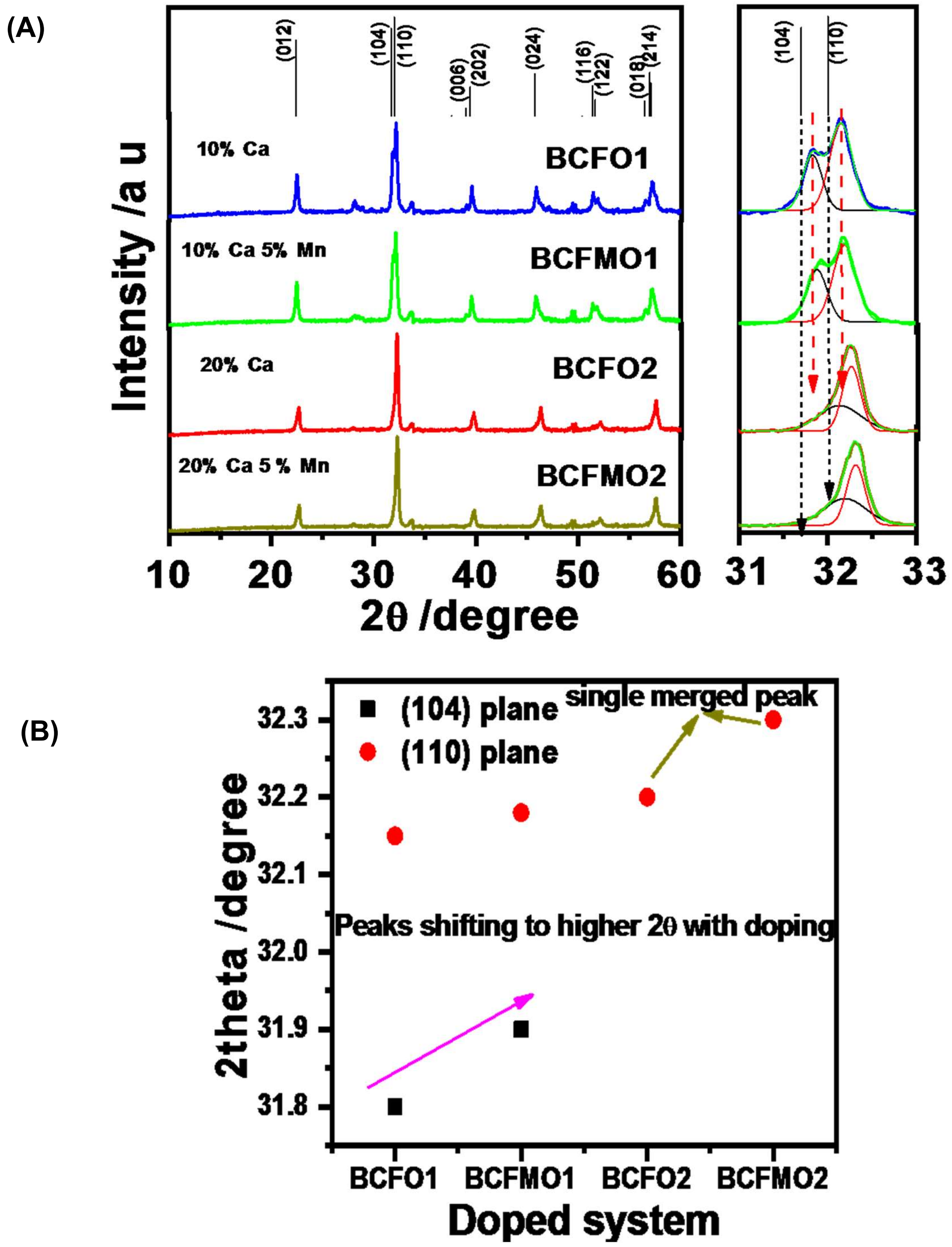

Figure 4.9 (A) XRD pattern corresponding to different substitution is given (zoomed in portion of most intense planes) (B) describes the shifting of the most intense peaks upon substitution.

Partial substitution of different cations at Bi sites, might alter significantly the ferroelectricity as well as magnetism in $BiFeO_3$. Distortion at B sites is expected to play an important role in alteration of multiferroic properties of $BiFeO_3$. Further the substitution of

Ca^{2+} at Bi site causes charge compensation and improves magnetic behavior due to contribution from Fe–O–Fe exchange interaction [107]. Similarly, the co- substitution of Ca at Bi site and Mn at Fe site with Mn being magnetically active as well as Jahn-Tellar ion further improves the magnetic property and contributes to ferroelectricity as well as for the multiferroic $BiFeO_3$ phase. So it is essential to give an insight in to the structural distortion induced effects on the magnetic and ferroelectric properties of these substituted systems.

4.4.1.2 Raman spectroscopic Studies

Raman spectroscopic studies give information on phonon-phonon interactions upon subjected to change in atomic sites and as substitution at cationic sites result in changes in frequencies of different modes and hence give an insight in to substitution induced changes in the properties exhibited by the system. Raman spectra at room temperature for BCFO and BCFMO samples are shown in Figure 4.10 as well as compared with the spectrum obtained in nano-$BiFeO_3$. The modes corresponding to substitution / co- substitution are observed to have larger widths as well as shifting, as compared to pristine one. Ca substituting at Bi site is observed to affect the Bi dominant modes at around 130 and 160 cm^{-1} with shift to lower wave number as compared to 140 and 160 cm^{-1} for pure $BiFeO_3$. This is ascribed to changes brought up by Ca replacing some Bi atoms and being lighter compared to Bi. Modes related to Fe remain almost unaffected and varies slightly in response to the change in environment linked with Bi.

In comparison to pure $BiFeO_3$, 10 % Ca substituted and Ca and Mn co-substituted samples show suppressed high wavenumber Raman modes. Observed modes corresponding to stereochemically active $6s^2$ lone pair of Bi are 71(E(TO_1)),139 (E(TO_2)),172 (A_1(TO_1)) cm^{-1} are observed with decreased intensity implying the substitution of smaller cations(Ca^{2+}) causing softening of Bi–O (bond shortening and lattice distortion) which causes blue shift [106,147]. In addition Ca substitution could introduce oxygen vacancies and affect the ferroelectricity in the system. The changes above 200 cm^{-1} are associated with structural distortion and reduction in FeO_6 octahedral vibration due to substitution [107]. Similar results are also deduced from XRD showing a partial structural transition from rhombohedral to pseudo-cubic causing the change in relative intensity and are seen as merged single peak. It is observed that for 20 % sample the intensity of $A_1(TO_1)$ enhances as compared to $E(TO_1)$ which can be ascribed to the spin dependent scattering mechanism with the magnetic anisotropy [146,167]. A_1 (TO_2) related to soft oxygen mode is seen to be absent in case Mn co- substituted sample. The presence of additional modes and the shifting can further can be related to the strong A site disorder and decreasing rhombohedral distortion due to straightening of Fe–O–Fe bonds due to Ca substitution resulting from maintaining Fe^{3+} oxidation state as well as to balance charge neutrality [147].

It is reported previously that the substitution at B site does not affect the structural change thus the enhancement of 645 cm^{-1} mode is related to increase in intensity of Mn–O bond as compared Fe–O bonds [102]. Similar observation is also seen in Co substituted $BiFeO_3$ reported by Quan *et al.* [148] and Gu *et al.* [138]. Gu *et al* discussed this as distortion of $[(CoFe)^{3+} O_6]$ octahedral Jahn-Tellar distortion due to substitution of Fe^{3+} by Co^{3+} and Mn substitution also discussed in detail [137,147]. It is this distortion of $[(CoFe)^{3+} O_6]$ that might destroy G type AFM spin ordering and induce FM in their studied system. Hence similar scenario can be expected and possible with Mn substitution. Any Change in position or intensity of 140, 171, 599 cm^{-1} are related to changes in FE property [170].

Table 4.4 Frequencies of Raman modes (in cm^{-1}) corresponding to BCFO and BCFMO as obtained in this thesis work [148].

BFO sol-gel	BCFO1	BCFMO1	BCFO2	BCFMO2
		53		56
72	74	71	76	72

134	140	132	125	125
			141	159
168	170	162	171	
215	215	225	222	241
268	232			286
280	273	271	271	
344	290		293	
	325	331		326
	363		363	368
	430	391		
469	476	482	472	479
532	549	540	526	527
601	621	637	624	629
	673		793	
957	965		978	910
1096	1103	1077	1109	1123
1262	1272	1291	1274	1283

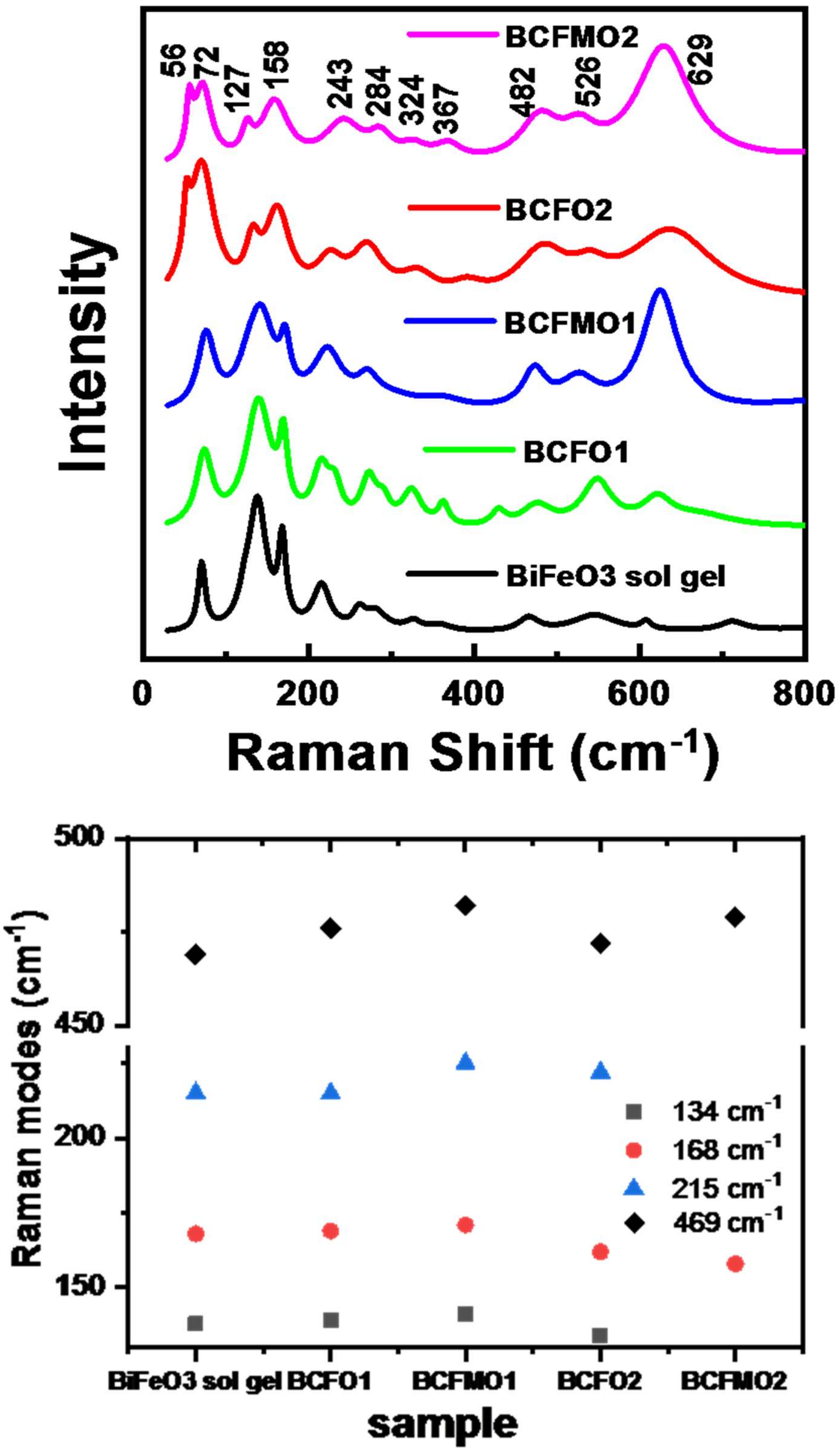

Figure 4.10 (top) Raman mode variation upon substitution with substantially observed mode softening and hardening (bottom) depicts the variation of A_g modes with substitution.

A comparative variation A mode are shown in Figure 4.10(B) describes that the Mn introduction into the lattice bring subtle changes in all the A1 modes to higher wavenumber.

This is indicative of the link of modified Fe site causes changes in modes intrinsically related to Bi.

The two phonon modes are related to strong spin lattice coupling related to octahedral sublattice interaction of B site metal ion. Two phonon modes are assigned to short and long Fe–O bonding respectively (defined as Fe–O_1 short and Fe–O_2 long) O_1 are axial and O_2 are equatorial. Fe–O_2 related to O_h rotation critical to weak FM, 1263 cm^{-1} 2E(LO_9) is highest occurs through super-exchange interaction [112].

4.4.2 Magnetic studies

A brief idea of structure as obtained from XRD describes the distortion and oxygen stoichiometry variation and the variation of Raman modes discusses the substantial effect on Fe related modes. Oxygen concentration significantly alters the exchange interactions responsible for magnetic behaviour. Therefore detailed magnetic property studies are carried out and explained in the following.

Field dependent magnetization MH loop of BCFO and BCFMO are presented in Figure 4.11 and Figure 4.12 ((A) and (C)). Magnetization studies of these samples showed finite hysteresis loops for both 10% and 20% substituted sample. In BCFO the loops corresponding to BCFO1 and BCFO2 show unsaturated loop with finite area. The loop area as well as magnetization increases with increase in temperature for BCFO1 and that of BCFO2 decrease (cf. Table 4.5). Further the magnetization is decreased at higher applied field with increase in temperature from 5 K to room temperature. There exists a portion in the M-H loop showing nonlinear behaviour in these cases. The waist shaped appearance of double loop is attributed to the alteration of Fe–O–Fe interaction due to intervention of nonmagnetic Ca ion of smaller radius into Bi site causing distortion. The enhanced magnetization in the case of BCFO2 as compared to BCFO1 could arise due to strain effects.

In addition if there occurs oxygen vacancies there could be Fe^{2+}–O–Fe^{3+} based exchange interactions.

In case of BCFMO, the loop area is reduced with the reduced value of magnetization. Interestingly in BCFMO2 ferromagnetic/ferrimagnetic behaviour is observed within the limits of applied magnetic field and in BCFO1, the M–H loop tends to show saturation behaviour at higher applied magnetic field at RT. The loop features for both BCFMO1 and BCFMO2 at 5 K is unsaturated and with finite loop area. The decrease in magnetization in BCFMO1 is ascribed to the presence of Ca affecting the magnetic interaction as Mn sites substituting Fe sites are comparatively lesser (5 wt%). However in BCFMO2 the magnetization as well as appreciable loop features is attributed to the altered Fe–O–Fe interaction due to enhanced Ca substitution. This leads to a modified Fe–O–Mn interaction resulting in an enhancement in the magnetic properties. Hence presence of Mn^{3+} causes a complex magnetic scenario and induces a ferromagnetic type interaction at lower applied field due to alteration of exchange interactions. This suggests substitution of Mn at Fe sites induces FM or Ferrimagnetic behaviour. The magnetic parameters are tabulated (cf. Table 4.5).

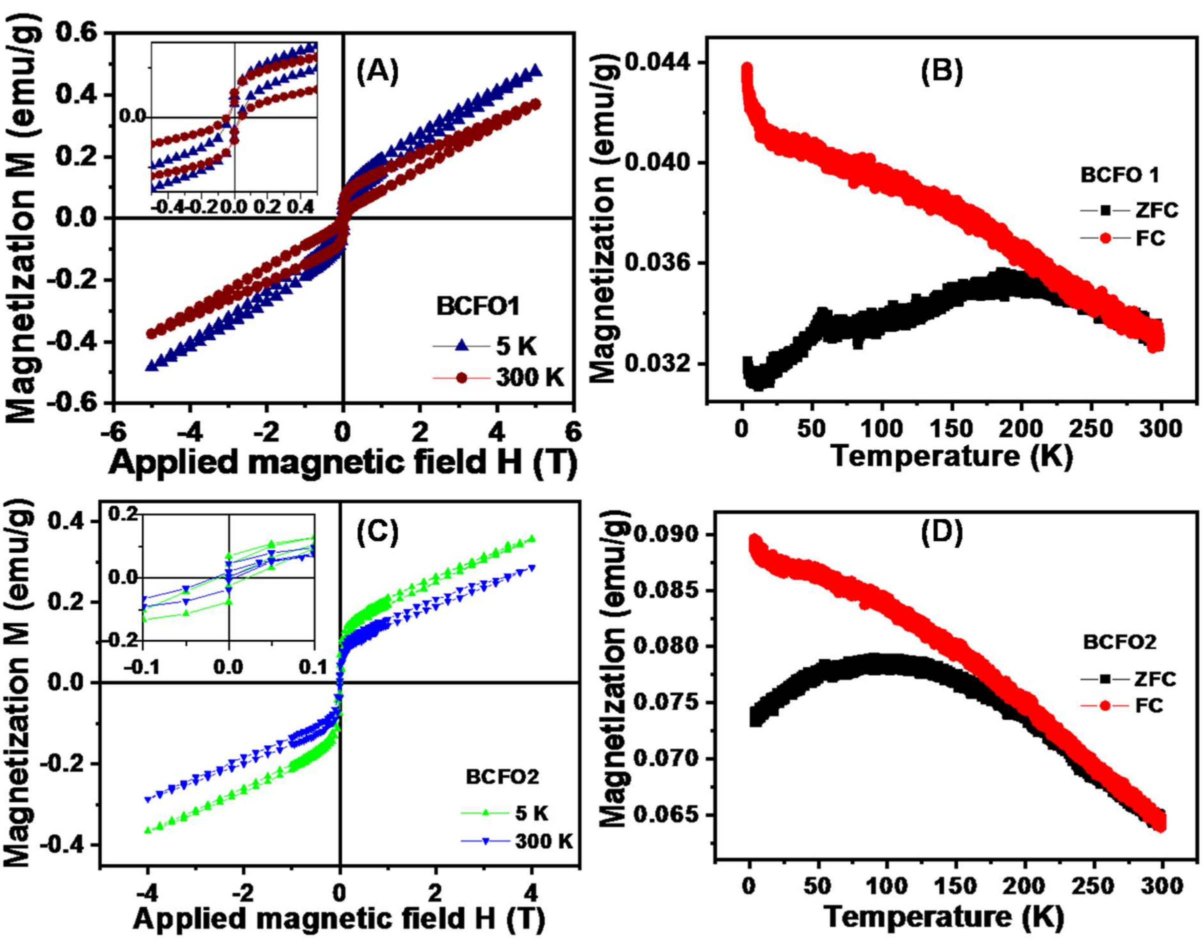

Figure 4.11 M–H plot corresponding to BCFO1 and BCFO2 at 5 K and 300 K describing coexisting magnetic features in both the cases. ((A) & (C)) and corresponding ZFC FC plot representing irreversible magnetization at low temperature up to 220 K ((B) & (D)).

A comparison of BCFO and BCFMO magnetic parameters is discussed as follows. Waist shaped nature of MH loop of BCFMO samples is suppressed or almost absent in cases in comparison with BCFO samples. A soft ferromagnetic behaviour with very less coercivity is observed for BCFMO2 samples at room temperature. This feature is again ascribed to the presence of altered exchange interactions in Mn substituted samples and well correlated with discussed Raman studies.

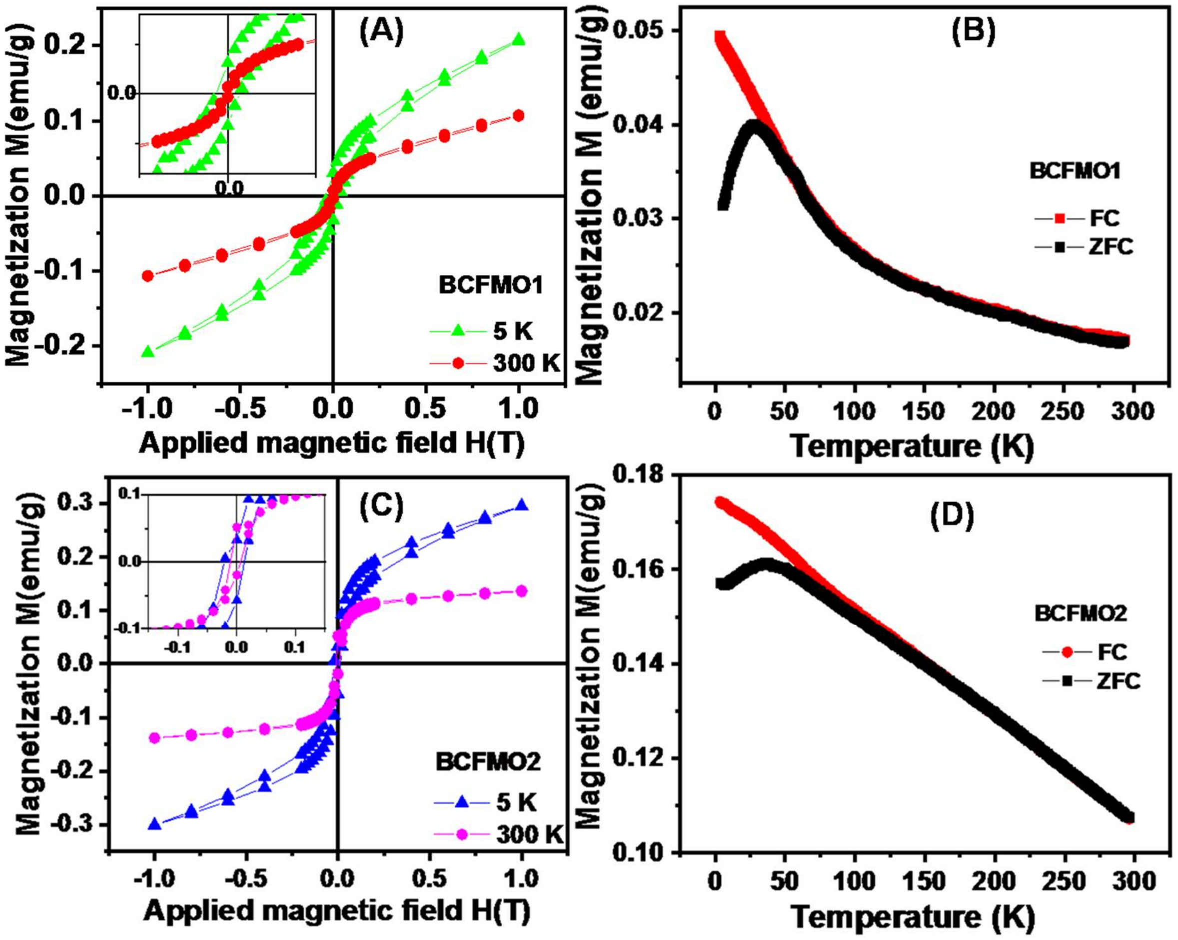

Figure 4.12 M–H plot corresponding to BCFMO1 and BCFMO2 at 5 K and 300 K describing coexisting magnetic features in both the cases. Interestingly saturation is attained at room temperature in presence of magnetic Mn ion ((A) & (C)) and ZFC FC plot showing bifurcation below 100 K and hump at 50 K ((B) & (D)).

A close look at the M–H loops in all the cases is seen to have exchange bias (EB) effect and the exchange bias field is given in Table 4.5. Previously in pristine BFO, exchange bias effect was observed by Bhusan *et al.* [171] and also in case of La and Zr co-substituted $BiFeO_3$ by Das *et al.* [167]. In the later case the occurrence of exchange bias was attributed to the inhomogeneous concentration of substituents along grain boundaries causing AFM inner grain surface and weak FM boundary. Hence in this case the exchange bias effect can also arise due to a similar phenomenon which is enhanced with rise in temperature. The exchange bias effect is observed to be almost absent for Mn substituted samples.

Table 4.5 Magnetic parameters obtained from MH loop.

Sample	Temp (K)	Mr (emu/g)	Hc (T)	EB field (T)
BCFO1	5	0.0434	0.03299	0.00030
BCFO1	300	0.04845	0.04539	0.00164
BCFO2	5	0.05915	0.01685	0.00886
BCFO2	300	0.0243	0.01167	0.01067
BCFMO1	5	0.031	0.033	0.00256
BCFMO1	300	0.036	0.005	0.00366
BCFMO2	5	0.185	0.045	0.00886
BCFMO2	300	0.117	0.054	0.00473

Temperature dependent magnetization studies of BCFO and BCFMO are shown Figure 4.11 and Figure 4.12((B) and (D)).The observations made from the ZFC FC plots of BCFO1 and BCFO2 are (i) bifurcation up to 250 K is observed and enhanced magnetization with substitution (ii) a broad peak centred about 200 K and 150 K is observed respectively for ZFC plot of BCFO1 and BCFO2 (iii) FC curve is observed to increase at lower temperatures and (iv) sharp cusp is observed in both the cases around 57 K but in 10 % substituted one it is prominent. The separation of ZFC FC can be thought of as possible spin glass behaviour of the system which bifurcates upon decreasing temperature [163].The broad peak implies the distribution of relaxation of magnetic moments. The increase in FC magnetization value at low temperatures is a consequence of strong interparticle interaction [167,171].Observation of sharp cusp is related to reasons like superparamagnetic nature or spin glass type behaviour [172]. However as in this case the sharp cusp is temperature independent hence can be attributed to the spin glass type behaviour. Further the suppressed cusp in BCFO2 can be explained as spin glass behaviour is suppressed upon Ca concentration increase and plausibly because of accompanied structural transition in case of BCFO2.

The irreversibility and the blocking temperature for BCFO1 and BCFO2 are obtained from the thermo-magnetic curves and reported in Table 4.6. As can be seen both these parametric temperatures decrease with increased concentration of Ca. Magnetization exhibits a Curie-Weiss behaviour at higher temperatures close to paramagnetic regime. The linear fitting of the plot gives negative and positive θ_p for BCFO1 and BCFO2 respectively. The negative value of θ_p corresponds to the AFM dominance due to Fe^{3+}–O–Fe^{3+} interaction whereas the positive value of θ_p signifies the dominance of FM due to increased oxygen vacancies accompanied by Fe^{2+}–O–Fe^{3+} type exchange interactions.

Table 4.6 Blocking (T_b) and irreversibility temperature (T_{irr}) and Weiss constant calculated from χ^{-1} vs T plot.

Sample	T_{irr} (K)	T_b (K)	θ_p (K)
BCFO1	219	186	-39
BCFO2	203	96	39
BCFMO1	45	28	-140
BCFMO2	131	36	54

In a similar manner the observations made for BCFMO ZFC FC plots are as follows. (i) ZFC and FC plots show irreversibility up to 50 K and 130 K respectively with peak about 28 K and 36 K known as blocking temperature, (ii) almost linear variation of merged ZFC FC above bifurcation region, (iii) FC magnetization increases at low temperature. These features can be explained as follows. Linear variation at high temperature zones and FC magnetization increase at low temperatures can be understood due to strong interparticle magnetic interactions. Mn being magnetically active ion, its substitution in Fe site largely influences the magnetic properties as observed.

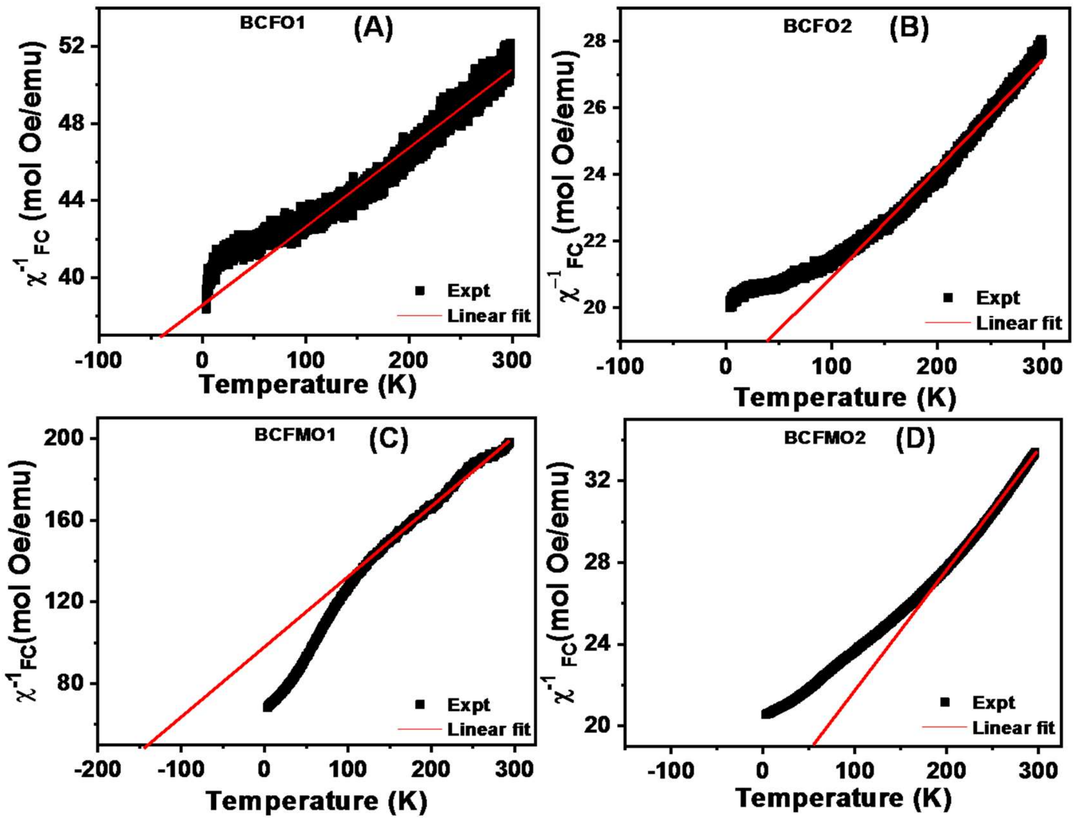

Figure 4.13χ^{-1}vs T plot for BCFO ((A) & (B)) and BCFMO ((C) & (D)) is presented. A linear fitting of the data is used to deduce the magnetic parameters Curie-Weiss temperature and effective magnetic moment.

The χ^{-1}plot against Temperature for FC is fitted linearly are shown in Figure 4.13 and the Curie Weiss temperature is found to be -140 K and 54 K respectively. Hence the substitution of constant fraction of Mn of 5 % in addition to Ca significantly influences the θ_p value. The dominance of AFM is explained based on the results of the field dependent magnetization studies. The presence of altered exchange interactions like Mn^{3+}–O–Mn^{3+} and Fe^{3+}–O–Mn^{3+} due to Mn might play a crucial role in BCFMO2 leading to enhanced magnetization.

From the above discussions it is concluded that the magnetic behaviour in these samples are understood due to the combined effect of the destruction of spin cycloid, strain effects and the possible presence of oxygen vacancies and hence Fe^{2+} as well as substitution of nonmagnetic Ca at Bi site and magnetic Mn at Fe site respectively.

4.4.3 Ferroelectric and Magnetoelectric Studies

Polarization of ferroelectric domains is essential for the investigation of ferroelectricity. As substitution of Ca^{2+} at Bi^{3+} sites is likely to introduce oxygen vacancies, it may affect the ferroelectricity in Ca substituted $BiFeO_3$ samples. However co-substitution of Mn at Fe site has been observed to result in the reduction of the leakage current and also Mn^{3+}being a Jahn-Tellar ion due to strain effect could enhance ferroelectric behaviour as discussed earlier in this chapter. In the case of BCFMO1 a nonlinear central region is observed in P-E loop Figure 4.15 similar to BLFO1 and attributed to the antiferroelectricity while that of BCFMO2 shows well developed PE loop with suppressed nonlinear region. This is understood as follows. Substitution of Ca alters the environment around Bi atoms which are responsible for the ferroelectric behaviour and hence leading to the occurrence of zones having opposing dipoles. This results in the occurrence of the coexisting AFE and FE regions of dipole moments. However with increasing Ca concentration the long range ordering of AFE and FE breaks and FE prevails and hence the nonlinearity is suppressed in BCFMO2 in a similar manner to that of BLFO2. In addition it is observed that BCFMO1 exhibits a high ferroelectric behaviour with the polarization values remaining almost 10 times as that of nano BFO as discussed in chapter 3. This can be understood mainly due to the bulk nature of the samples devoid of defects resulting in the absence of leakage current and also from the presence of Mn ion in case of BCFMO1. Further this enhancement could be linked to ME coupling.

A brief discussion on response of PE loop to the magnetic field is given in order to establish the magnetoelectric coupling. Therefore a magnetic field of 0.1 Tesla is applied and loop is recorded over the field of -0.1 to 0.1 Tesla.

The ferroelectric loop obtained for both the substituent concentration and is observed that the ferroelectric parameters decreases when the same is measured under magnetic field and regains back when subsequently measured with removal of the field. This is a signature of response of ferroelectric remanence under the application of magnetic field and is a direct proof for reversible magnetoelectric coupling.

It is reported that pristine $BiFeO_3$ prepared through solid state route has limited P_r values due to leakage loss and the value is around 0.6 μC/cm^2 for the same [108]. However here with Ca introduction the value enhanced to15 μC/cm^2, is better compared to previously reported values in similar systems [124]. It is to be mentioned that divalent Ca substitution is likely to result in the formation of oxygen vacancies. In addition there is also likely to be strain effects.

Ferroelectric studies in both cases showed quite promising values of polarization as compared to pristine $BiFeO_3$.The ferroelectric loop obtained for both the substitution concentration and is observed that the ferroelectric parameters decreases when the same is measured under magnetic field for BCFMO1 whereas increases for BCFMO2. In addition the ferroelectric parameters increases largely after magnetic field is applied for BCFMO1 and reverse happens for BCFMO2.This also implies that an increase in Ca concentration while maintaining Mn concentration results in large effect on remanence polarization. This is a signature of ferroelectric remanence under application of magnetic field and is a direct proof for the existence of magnetoelectric coupling in this system.

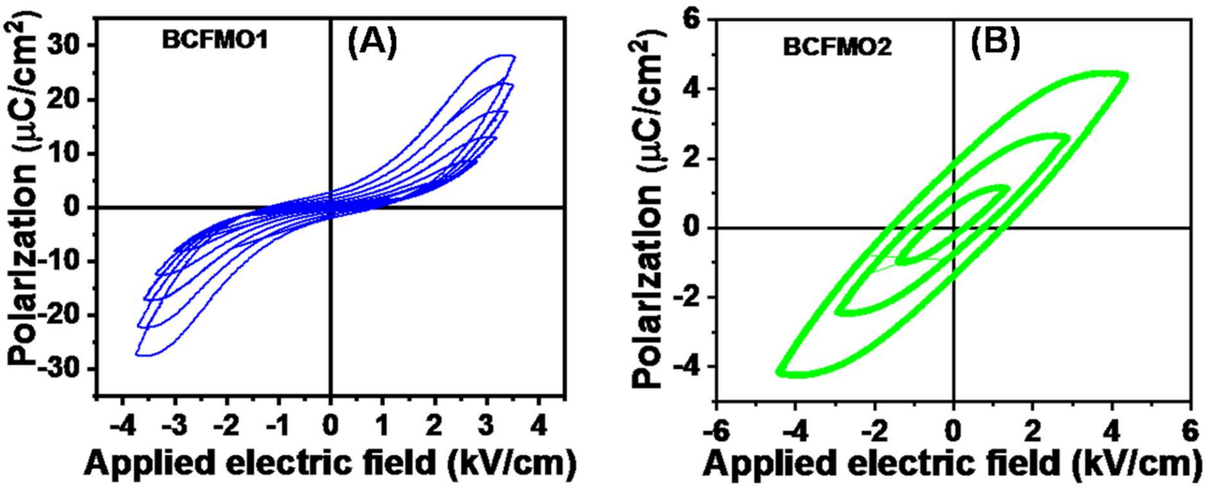

Figure 4.14 Room temperature PE loop corresponding to Ca and Ca, Mn co-substituted $BiFeO_3$ in comparison to lossy nature of BCFMO1 a well-developed loop is obtained for BCFMO2.

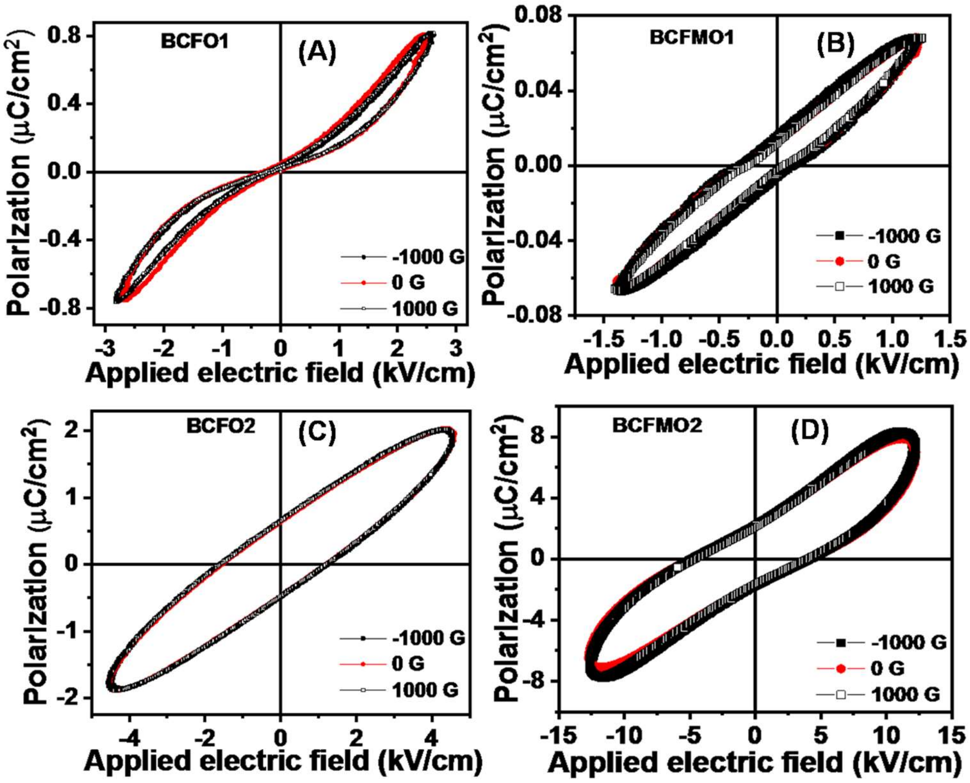

Figure 4.15 Magnetoelectric coupling studies in BCFO which shows switching behavior in BCFO1 while unresponsive in case of BCFO2 for applied magnetic field of ± 0.1 Tesla with substantial increase in polarization.

4.4.4 Mössbauer Studies

Mössbauer spectrum as obtained in BCFO1 could be deconvoluted in to three six line and two double line components. Two fractions of iron atoms adding up to 83 % experiencing hyperfine fields such as 49.6 and 49.7 Tesla with quadrupole splitting of different sign are assigned to iron atoms associated with $BiFeO_3$.The values of isomer shift of each component are close to 0.4 mm/s, implying that the iron atoms associated with these sites are in Fe^{3+} valence state. This important observation implies that these fractions of iron atoms are associated with FeO_6 octahedra of $BiFeO_3$ and devoid of any oxygen vacancies. This implies that Ca substitution at Bi sites does not lead to the formation of oxygen vacancies in the $BiFeO_3$ matrix. About 6 % of Fe atoms experience a hyperfine field of 48 Tesla, which is slightly lesser than the value experienced by Fe atoms associated with FeO_6 of $BiFeO_3$ existing in rhombohedral structures. Also, the magnitude of this fraction matches with that of the percentage of Ca substituted at Bi sites. This fraction is thus understood to have resulted due to Ca substitution. The ionic radius of Ca^{2+} is (1 Å) for a six-fold coordination whiles it is 1.17 Å for Bi^{3+} with a eight fold coordination resulting in a large lattice distortion locally around the sites of substitution of Ca at Bi. This affects the Fe–O_6 octahedra and hence Fe–O–Fe superexchange interaction gets reduced leading to a smaller value of hyperfine field of 48 Tesla. About 11% of the fractions of iron atoms are found to be associated with doublets with the values of quadrupole splitting based on which it could be deduced that these fractions of iron atoms occupy (Fe–O_6) octahedral sites in $Bi_{25}FeO_{40}$ phase.

Mössbauer spectrum as obtained in the case of BCFMO1, i.e the co-substitution of 10% Ca at Bi sites accompanied by 5% of Mn substitution at Fe sites is shown in Figure 4.16. The spectrum could be fitted with four sextets and two doublets resulting in the hyperfine parameters as mentioned in the table. Appreciable changes in the resultant hyperfine parameters as obtained in BCFO1 and BCFMO1 imply the significant effects of co-substitution of Ca and Mn on the resultant local structural and magnetic properties. There is a slight decrease in the hyperfine fields as experienced by fractions of Fe atoms associated with octahedral sites of $BiFeO_3$ phase. The fraction f3 experiencing a hyperfine field of 48 Tesla as seen in the case of BCFO1 is absent in the case of BCFMO1.This is observed to have resulted in two additional sextets, adding up to the fraction f3, experiencing hyperfine fields lower than the value of 48 Tesla, with the associated values of quadrupole splitting are widely different. This is understood to be due to Jahn-Teller distortion due to Mn substitution resulting in differing values of strains leading to the occurrence of additional fractions varying in the values of quadrupole splitting and hyperfine fields.

In the case of BCFO2 the spectrum could be deconvoluted in to four components with a single doublet and three sextets. The fractions of Fe atoms associated with octahedral sites of $BiFeO_3$ have got increased accompanied by the decrease in the area corresponding to the doublet meaning an appreciable reduction in the impurity phase by 10% as corresponding to BCFO1.

In the case of BCFMO1, there is a slight decrease in the fractions, Fraction of iron atoms exposed to 48 Tesla of hyperfine field as seen in BCFO1 is absent in the case of BCFO2 which is understood as follows. Enhanced substitution of Ca up to 20% results in a partial occurrence of orthorhombic phase in addition to the rhombohedral phase of $BiFeO_3$. Fe atoms associated with the orthorhombic phase are likely to be associated with appreciably higher distortion and hence of that of FeO_6 octahedra leading to an enhancement in the value of hyperfine field resulting in an increase in the fractions f1 and f2. About 6% of Fe atoms are exposed to magnetic interaction experiencing a hyperfine field of 46.8 Tesla. This component is understood to be due to Fe atoms associated by 5%, associated with pure $BiFeO_3$ phase as compared to that of BCFO1. This is understood to be due to Jahn-teller distortion due to Mn^{3+} substitution in the system. Also, the Jahn-Teller distortion due to Mn^{3+}

further results in the absence of the fraction of Fe atoms experiencing hyperfine field close to 48 Tesla as seen in sample BCFO1 is absent in BCFMO1 resulting in the occurrence of two fractions of iron atoms experiencing hyperfine fields viz., 42 and 40 Tesla.

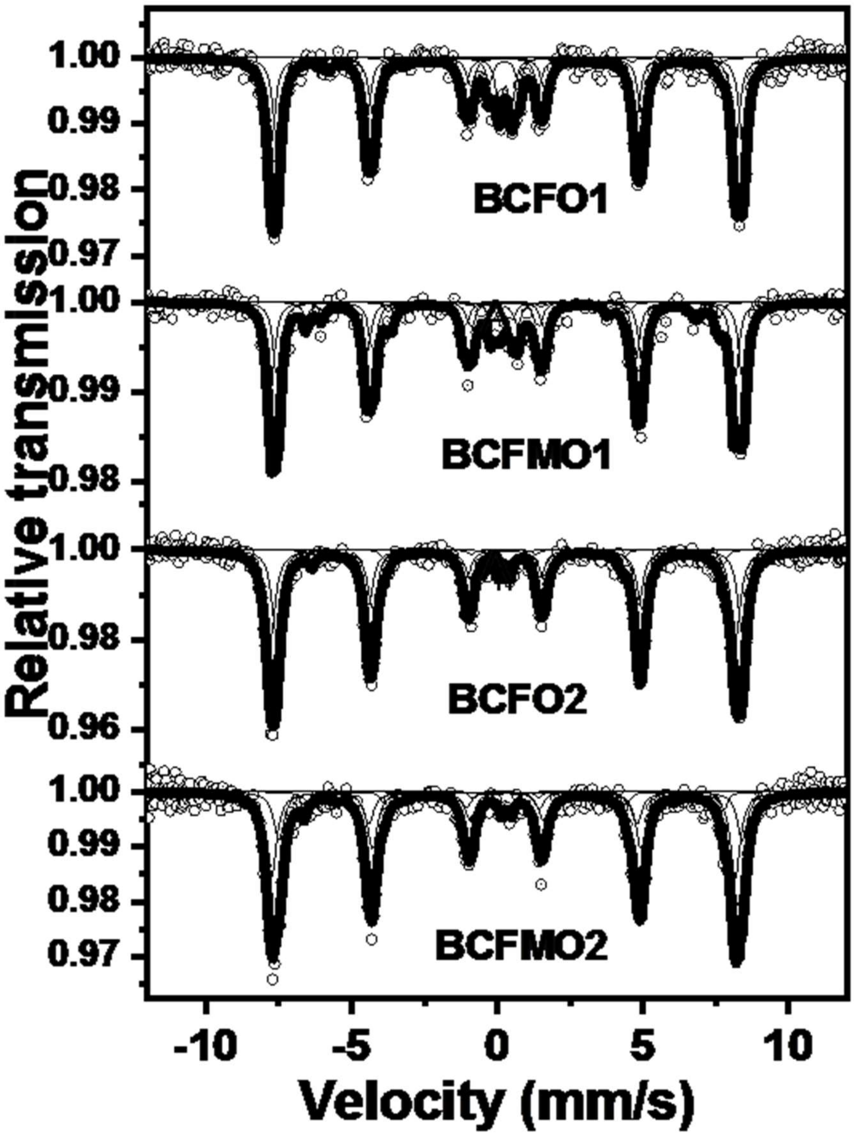

Figure 4.16 Room temperature Mössbauer spectra corresponding to substituted and co-substituted $BiFeO_3$.

Table 4.7 Mössbauer parameters as obtained in BCFO and BCFMO.

Sample	i	δ_i (mm/s)	Δ_i (mm/s)	B_{hf} (Tesla)	Rel Area (%) Fi
BCFO1	1	0.40±0.03	-0.15±0.02	49.6±0.05	43
	2	0.41±0.01	0.28±0.02	49.6± 0.03	40

	3	0.42±0.01	0.08±0.03	48.1±0.52	06
	4	0.40±0.01	0.43±0.03	0	06
	5	0.36±0.01	1.02±0.05	0	05
BCFMO1	1	0.39±0.01	-0.16±0.02	49.4±0.05	39
	2	0.41±0.01	0.29±0.02	49.5±0.05	39
	3	0.58±0.05	0.12±0.09	43.9±0.33	07
	3	0.34±0.01	0.29±0.14	39.8±0.46	05
	4	0.41±0.06	0.39±0.13	0	04
	5	0.37±0.04	0.89±0.12	0	06
BCFO2	1	0.39±0.01	-0.15±0.03	49.5±0.03	45
	2	0.43±0.01	0.16±0.02	49.7±0.03	45
	3	0.37±0.03	0.06±0.02	46.8±0.22	06
	4	0.37±0.03	0.40±0.03	0	04
BCFMO2	1	0.39±0.01	-0.12±0.02	49.8±0.04	31
	2	0.41±0.01	0.28±0.03	49.9±0.06	32
	3	0.38±0.03	0.29±0.06	48.0±0.21	22
	3	0.19±0.03	0.17±0.26	42.0±0.89	04
	3	0.43±0.04	0.07±0.03	45.8±0.04	08
	4	0.41±0.03	0.39±0.05	0	03

Substitution of Ca to 20% at Bi site results in an appreciable increase in the fractions of iron atoms associated with $BiFeO_3$ phase by 7%, at the cost of the impurity phase viz., $Bi_{25}FeO_{40}$, implying that the substitution of Ca leads to a significant improvement in the stability. In the sample BCFMO2, the co-substitution of 20% of Ca at Bi site accompanied by 5% of Mn substitution at Fe sites result in a significant distortion of the lattice due to the combined effects of Jahn-Teller distortion due to Mn substitution and strain effects due to Ca substitution whose ionic radius is lesser than that of Bi. This results in a decrease in the fraction of Fe atoms associated with (f_1+f_2) contributing for both the ferroelectric and magnetic properties. Defects associated fractions of Fe atoms which are understood to occur mainly due to lattice strain caused by Ca substitution along with Jahn Teller distortion are understood to contribute for weak ferromagnetic ordering of the matrix. In the case of BCFO1 and BCFMO1, the values of quadrupole splitting associated with f_1 and f_2 mainly contributing for both the ferroelectric and weak ferromagnetic ordering as observed in these systems are appreciably different in magnitude while the signs are different. This implies that in these two cases the spin at Fe sites associated with FeO_6 are canted leading to the observed weak ferromagnetic ordering. Thus, the observed magneto electric coupling in the samples BCFO1 and BCFMO1 could be understood at atomic scale based on the interpretation of Mössbauer results. In the case of BCFO2 and BCFMO2 the quadrupole splitting associated with f1 and f2 sites are almost of same magnitude but are of opposite sign point to the observed antiferromagnetic ordering of the $BiFeO_3$ phase which can only contribute for both the ferroelectric and magnetic ordering and hence the coupling of these two effects. Hence the absence of magnetoelectric coupling effects in BCFO2 and BCFMO2 is understood based on the Mössbauer results in terms of a strong antiferromagnetic ordering of the $BiFeO_3$ phase.

4.5 Comparative Studies of Solid-state and Sol-gel Prepared Ca Substituted $BiFeO_3$

In order to understand the role of the synthesis methods and consequently the size effect on the structural and magnetic properties of substituted $BiFeO_3$ we have chosen Ca substitution which brings out interesting magnetic properties. An atomic scale understanding of the structural and magnetic properties is provided using Mössbauer spectroscopy.

4.5.1 Structural Studies

Comparative X–ray diffraction pattern of 10% Ca substitution $BiFeO_3$ prepared through sol gel and solid state are shown with respect to the standard in Figure 4.17.The peaks match well with the standard. The planes (104) and (110) show broadening in sol-gel prepared BCFO. In both the cases there is a merging of peaks e.g (006) and (202) as well as splitting e.g (024). The most intense planes are towards higher 2θ in SSR while towards lower 2θ in case of sol gel assisted $BiFeO_3$. The broadening of peaks is implicative of the nano-sized nature of the particles. The calculated size obtained to be ~50 nm obtained using Scherrer formula. The splitting and merging of peaks are attributed to the structural transition from distorted Rhombohedral *R3c* to orthorhombic *C222* structure. The shifting of higher 2θ indicative of the decrease in cell parameter and cell volume in solid state BCFO1 whereas the shifting to lower 2θ in case of sol gel nanoparticles implies the increase in the cell volume.

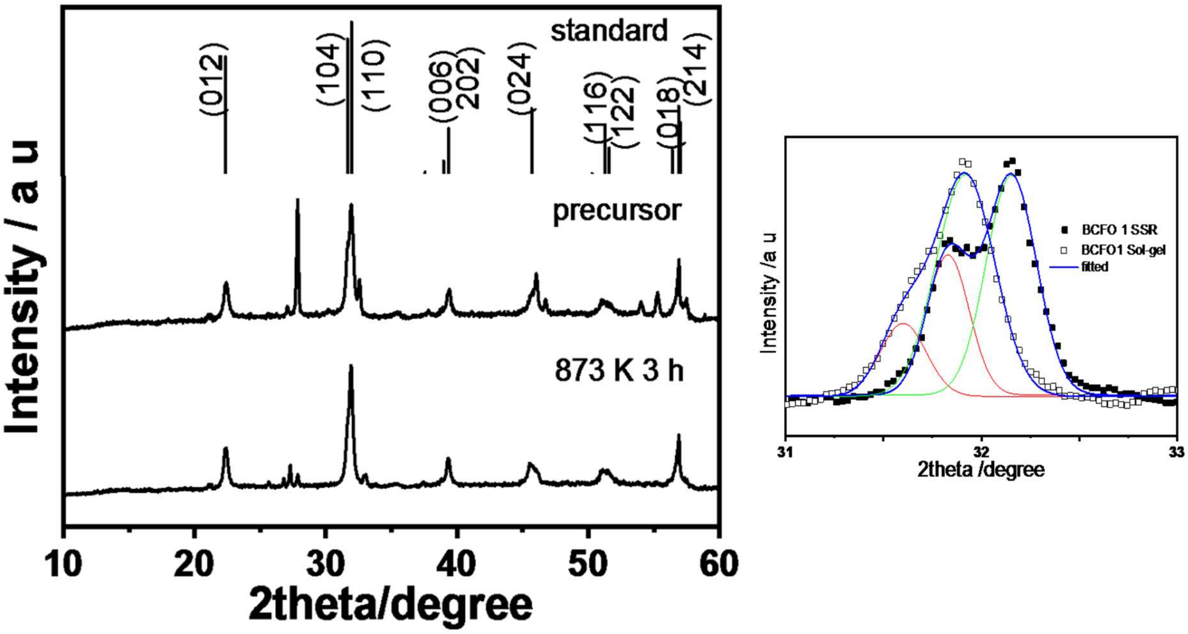

Figure 4.17 Comparative XRD pattern for BCFO prepared using solid-state (annealed 1073 K for 12 h and 1123 K for 6 h) and sol-gel route (annealed at 873 K). The shift of most intense peak is shown (right).

The increase in the volume in the nanoparticles of oxides is caused from the oxygen vacancies thereby reducing the cations and also decreases the bonding forces [172,173]. The other possible explanations for the size dependent lattice expansion could be the finite size contribution to Madelung constant or surface stress [175]. Expansion and compression in these cases can significantly alter the local structure, ferroelectric and magnetic properties [175] and hence Mössbauer studies on BCFO1 prepared though sol-gel and solid-sate are done and discussed subsequently.

4.5.2 Ferroelectric Studies

Polarization variation with response to the applied electric field to understand ferroelectricity and also variation with response to the applied magnetic field to understand the magnetoelectricity is presented in Figure 4.18. BCFO1 prepared using sol-gel route exhibits ferroelectricity.

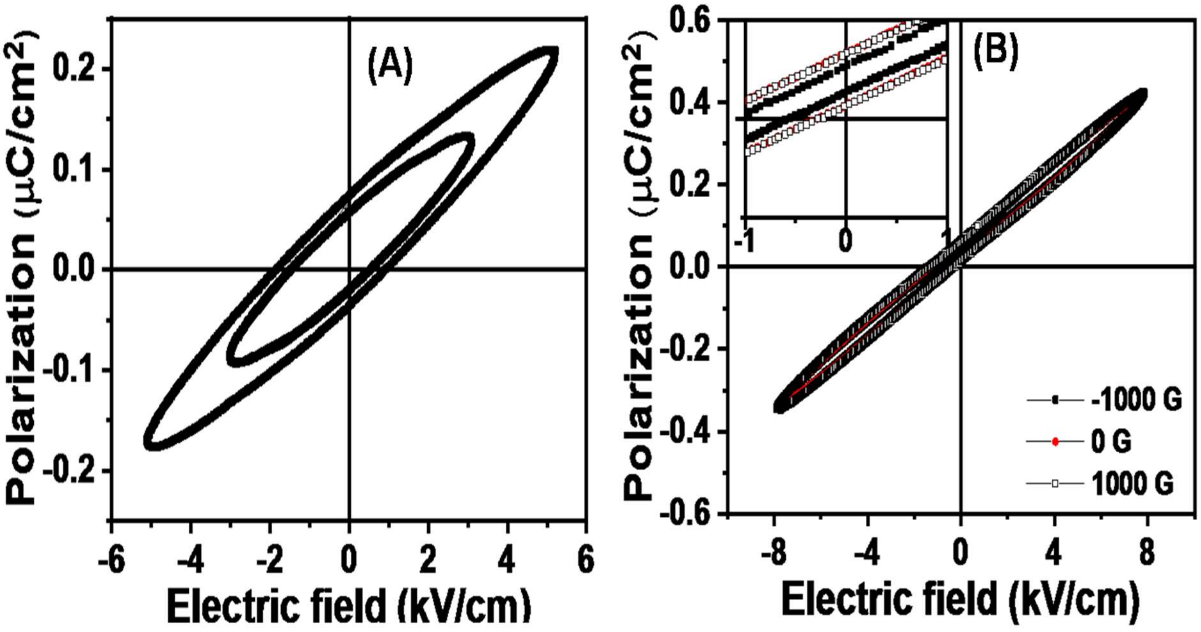

Figure 4.18 PE loop for BCFO prepared using sol-gel route and annealed at 873 K for 3 h (A) and the corresponding measured magnetoelectric coupling is presented (B).

The observed polarization value closely matches with that of the pure $BiFeO_3$. The presence of oxygen vacancies causes leakage behaviour and inhibits the exhibition of large polarization values. The increase in polarization value is observed upon increasing applied electric field. The magnetoelectric studies further shows subtle variation when the field is varied from -0.1 to 0.1 Tesla through nearly zero applied magnetic field. This demonstrates the presence of coupling. This also coincides with the magnetoelectric studies of solid state prepared Ca substituted $BiFeO_3$.

4.5.3 Discussion of Mössbauer Results

Mössbauer results as obtained in BCFO1 sol-gel (cf. Figure 4.19) show that nearly 70% of Fe atoms are associated with the $BiFeO_3$ phase corresponding to significantly strained lattice. This is evidenced by the variation in the values of the magnitudes of the fractions associated with $BiFeO_3$ phase. Two distinct defects associated sites of Fe atoms experiencing magnetic interactions experiencing hyperfine fields of the values 43 and 38 Tesla are seen (cf. Table 4.8). Values of isomer shifts associated with these sites of Fe atoms (around 0.5 mm/s) imply that these iron atoms might be having valence of Fe^{2+}. This indicates the presence of oxygen vacancies in the nanoparticles of Ca substituted $BiFeO_3$. Annealing treatment of sol-gel prepared Ca substituted $BiFeO_3$ at 873 K results in an increase in the fraction of iron atoms associated with the $BiFeO_3$ phase by 10%. Ca substitution induced strain effects leading to the occurrence of two additional fractions of Fe atoms associated with distinct hyperfine fields lesser than that experienced by the fractions f1 and f2. There is a decrease in the fractions of iron atoms associated with the impurity phases. About 6% of Fe atoms are in the Fe^{2+} charge state experiencing a hyperfine field around 46 Tesla.

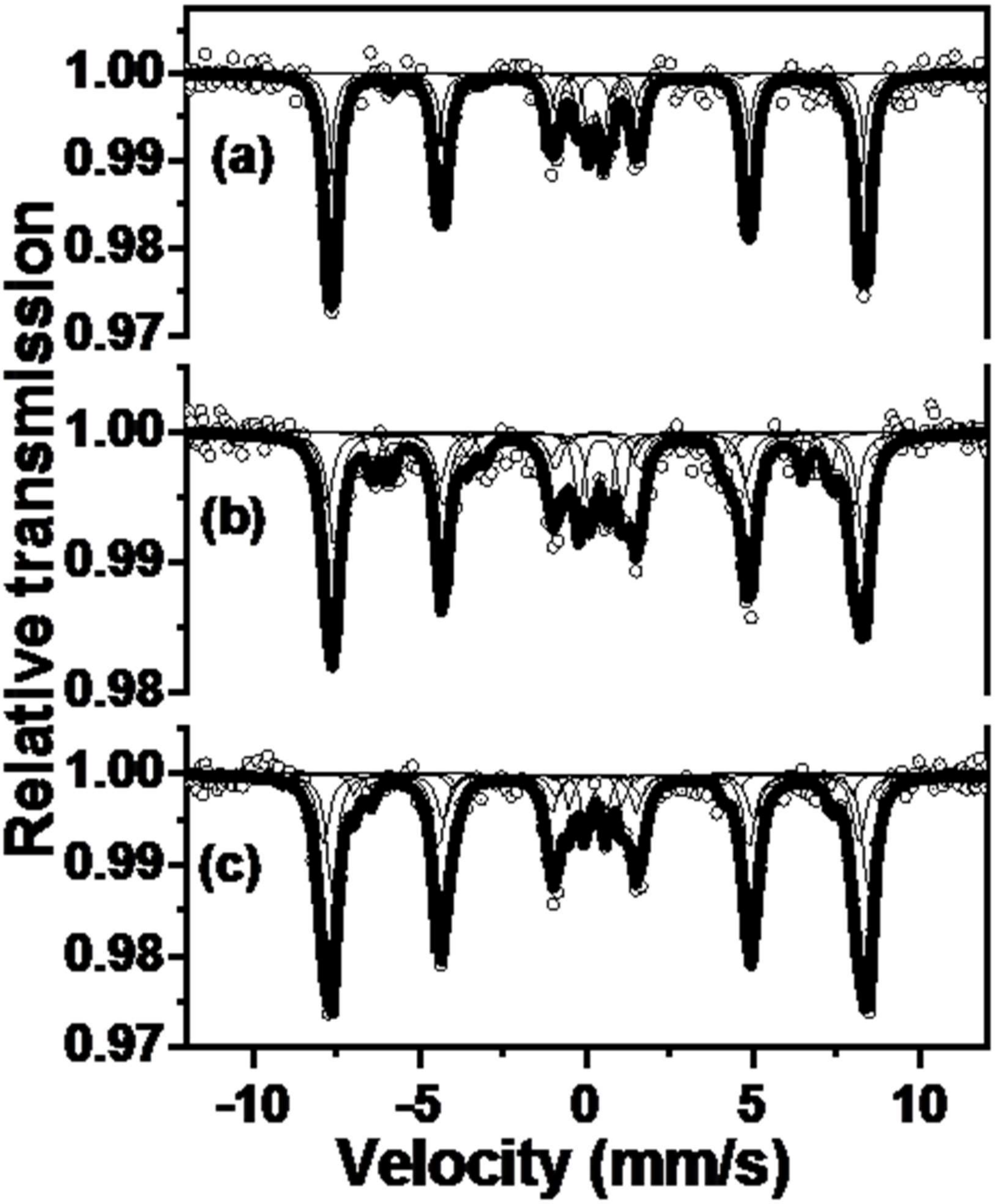

Figure 4.19 Mössbauer spectra obtained in BCFO prepared through solid state reaction methods (a) and sol-gel route (precursor (b) and 873 K for 3 h (c)).

Table 4.8 Comparative room temperature MS parameter for BCFO prepared using solid-state and sol-gel routes.

Sample	i	δ_i(mm/s)	Δ_i(mm/s)	B_{hf}(Tesla)	Rel Area (%) f_i
BCFO1	1	0.27±0.02	-0.06±0.03	49.1±0.09	28
sol-gel	2	0.47±0.02	0.06±0.02	49.3± 0.06	43
Precursor	3	0.55±0.04	0.06±0.07	42.6±0.23	08
	3	0.52±0.03	-0.18±0.07	38.3±0.22	07
	4	0.50±0.02	0.49±0.04	0	07
	5	0.55±0.02	1.30±0.05	0	07
BCFO1	1	0.37±0.01	-0.23±0.03	49.8±0.06	36
sol-gel	2	0.43±0.01	0.19±0.01	49.9±0.04	46
873 K 3 h	3	0.40±0.04	0.33±0.08	42.8±0.29	04
Annealed	3	0.51±0.03	0.22±0.07	46.4±0.27	05
	4	0.37±0.02	0.62±0.04	0	05
	5	0.39±0.03	1.59±0.05	0	04
BCFO1	1	0.40±0.03	-0.15±0.02	49.6±0.05	43
Solid-state	2	0.41±0.01	0.28±0.02	49.6± 0.03	40
Route	3	0.42±0.01	0.08±0.03	48.1±0.52	06
	4	0.40±0.01	0.43±0.03	0	06
	5	0.36±0.01	1.02±0.05	0	05

The observed weak ferromagnetic ordering in the nanoparticles of Ca substituted $BiFeO_3$ as reported in the literature, can be understood based on the presence of strain effects and oxygen vacancies. Appreciable strain effects in $BiFeO_3$ result in the destruction of spin cycloid leading to the occurrence of weak ferromagnetism, while oxygen vacancies lead to double exchange interactions between Fe^{2+}–O–Fe^{3+} resulting in the observed weak ferromagnetic ordering.

4.6 Conclusion

Isovalent La substitution at Bi sites up to 10% in $BiFeO_3$ does not result in any strain effect and is observed to show antiferromagnetic and ferroelectric ordering behavior. On the other hand a weak ferromagnetic ordering accompanied with ferroelectric ordering has been observed in 20% La substituted $BiFeO_3$ samples. These results are comprehended based on the Mössbauer studies which imply that in the case of 20% La substituted $BiFeO_3$ subjected to different annealing treatments (i.e) BLFO2-A and BLFO2-B, it is observed that a small fraction of about 5% of Fe atoms in each of these cases experience isomer shift value close to 0.5 mm/s, implying the presence of oxygen vacancies. Hence the resultant Fe^{3+}–O–Fe^{2+} based double exchange interactions might lead to the occurrence of weak ferromagnetic ordering in these systems. Hence in the case of 20% La substituted $BiFeO_3$ it is understood that both the strain effect and the occurrence of oxygen vacancies contribute for the observed weak ferromagnetic ordering and hence the magnetoelectric coupling. In the case of the bulk of $BiFeO_3$ substitution with Ca, the Mössbauer results do not point to the presence of oxygen vacancies. Hence the observed ferroelectric behaviour accompanied by the weak ferromagnetic ordering in Ca and Ca, Mn co- substituted $BiFeO_3$ are understood due to the strain effects by the substitution of smaller sized Ca^{2+} at Bi^{3+} sites in these samples, whereas in the case of nanoparticles of the Ca substituted $BiFeO_3$ it is comprehended that both the strain and oxygen vacancy type defects contribute for the observed weak ferromagnetism along with the ferroelectric behaviour thus resulting in a strong magnetoelectric coupling.

5 Role of Defects on the Multiferroic Properties in $Bi_2Fe_4O_9$

Graphical Abstract–

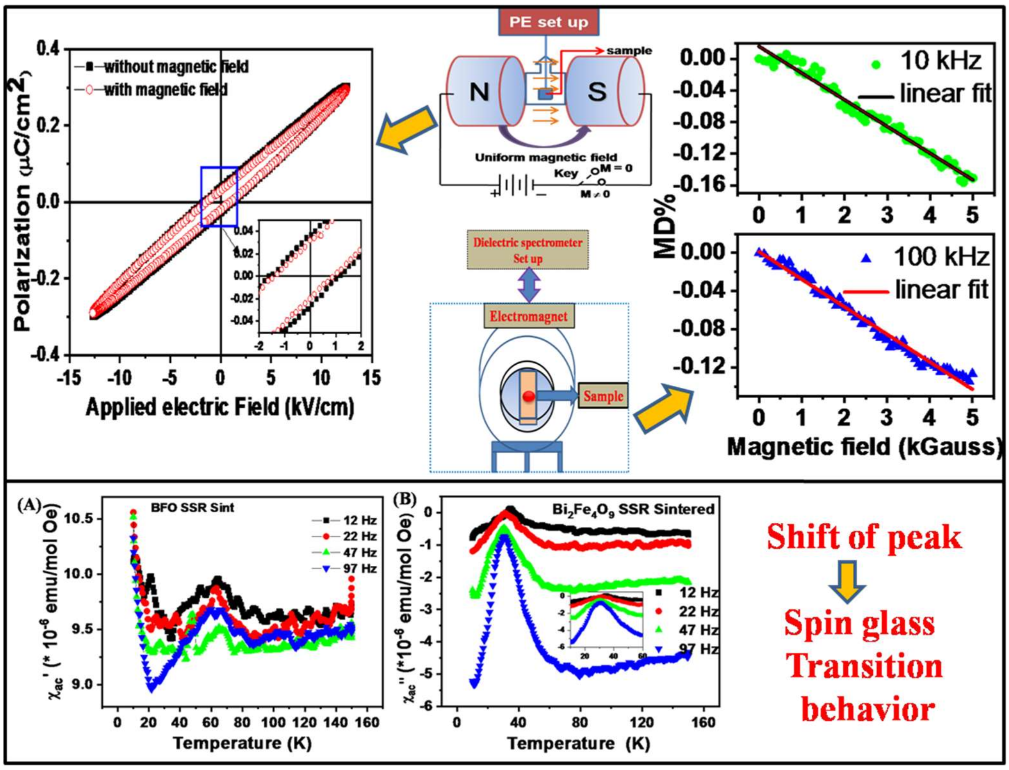

Magnetoelectric and magnetodielectric coupling in $Bi_2Fe_4O_9$ is presented and also the spin glassiness is presented.

Abstract:

Magnetoelectric and magnetodielectric coupling effects as observed in $Bi_2Fe_4O_9$ are reported in this chapter. Interestingly the values of P_r, M_r, and ε' are found to vary with the applied magnetic / electric field (i.e) magnetic properties changed over the applied electric field and vice versa. The spin glass behaviour of $Bi_2Fe_4O_9$ which was speculated in the literature has been observed in this work which is explained based on the results of ac susceptibility measurements. Oxygen vacancies induced variations in magnetic / ferroelectric properties are studied. Atomic scale understanding of the influence of defects on local structural and magnetic properties has been addressed using Mössbauer studies.

5.1 Introduction

$Bi_2Fe_4O_9$ exhibits multiferroic properties having ferroelectric Curie temperature ($T_C \approx 250$ K) and antiferromagnetic Néel temperature ($T_N \approx 260$ K). The coupling between magnetic and ferroelectric properties is significant in this system. $Bi_2Fe_4O_9$ also exhibits magnetodielectric coupling and hence it is a quite important and a highly potential material with respect to several applications in electronics industry [97,175,176]. Besides $Bi_2Fe_4O_9$ is the most stable phase among the bismuth iron oxide phases. Volatile nature of Bi in bismuth iron oxides and hence Bi related defects have been established in the literature [5,177,178] to play an important role in altering the ferroelectric properties in bismuth ferrite. Also partial substitution of other cations at Bi sites (which are responsible for the ferroelectric properties of this system due to lone pair $6s^2$ electrons) in $BiFeO_3$ have also been shown to result in structural transition accompanied by the occurrence of weak ferromagnetic ordering. Hence the magnetic and ferroelectric properties have been shown to get modified in $BiFeO_3$ with the introduction of defects at Bi sites in terms of either vacancies and / or due to substitution. This chapter addresses issues related to Bi related defects in $Bi_2Fe_4O_9$ on its magnetic and ferroelectric properties. Multiferroicity in the form of magnetoelectric and magnetodielectric couplings are discussed in $Bi_2Fe_4O_9$ subjected to different controlled annealing treatments.

5.2 Synthesis of Bulk $Bi_2Fe_4O_9$ using Solid-state Route

$Bi_2Fe_4O_9$ is the most stable phase among the other bismuth iron oxide phases in Bi_2O_3–Fe_2O_3 phase diagram and forms at higher Fe region with 1:2 ratio of Bi_2O_3 and Fe_2O_3. The steps involved in the solid-state route are shown in Figure 5.1. Hence Bi_2O_3 and Fe_2O_3 are taken in the ratio of 1:2 to synthesize bulk $Bi_2Fe_4O_9$. The appropriately weighed oxides are mixed in agate mortar thoroughly in isopropanol for the effective mixing. The prepared mixture is pelletized using a hydraulic press into 10 mm diameter pellets and treated for a long time (144 h at 973 K) with intermittent grindings until the required phase is formed i.e. a complete conversion of starting oxides into the required $Bi_2Fe_4O_9$ phase. XRD is taken at intermediate stages to confirm the phase formation and to ensure completion of reaction. At final stage, the ground bulk $Bi_2Fe_4O_9$ powders were obtained and will be referred hereafter as the 'as prepared' sample. The as prepared $Bi_2Fe_4O_9$ has been subsequently subjected to annealing at a temperature of 923 K for 24 hours and this sample will henceforth be mentioned hereafter as the 'sintered' sample. It can be noted that the sintering temperature of 923 K is lower than the temperature of treatment of the pellet (i.e.) 973 K for the formation of the $Bi_2Fe_4O_9$. The effect of the first step of annealing treatment for the phase formation and the second step of annealing treatment on the multiferroic properties will be investigated using bulk magnetization, ferroelectric studies. In addition the occurrence of defects if any due to these annealing treatments and hence the defects induced changes in the system will also be investigated in a detailed manner using Mössbauer spectroscopy.

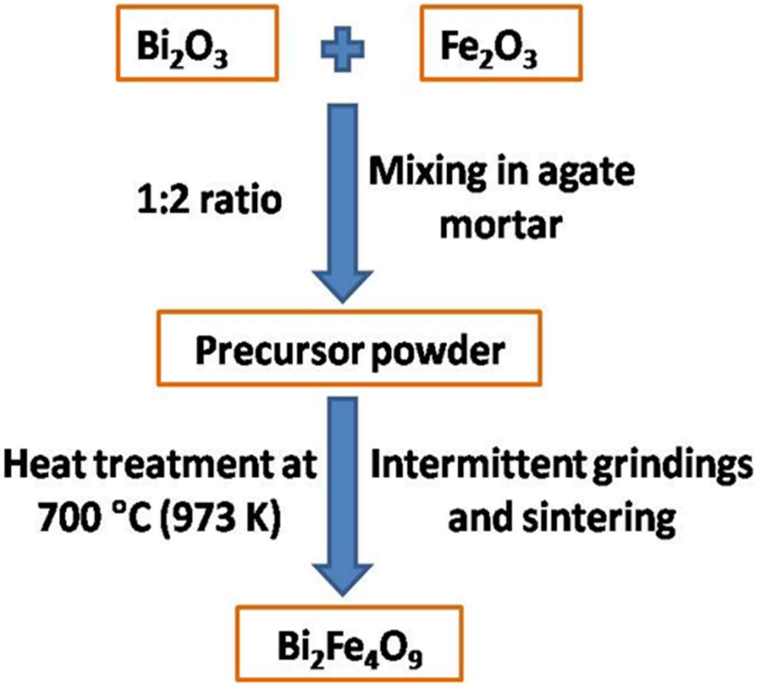

Figure 5.1 Steps involved in the synthesis of $Bi_2Fe_4O_9$ using solid-state route (SSR).

Furthermore, it is essential to establish a correlation between the ferroelectric and magnetic properties of this system in order to explain the multiferroicity.

5.3 Structural and Microstructural Studies

X–ray diffraction is useful to understand the crystal structure, phase evolution and to look for the occurrence of any additional phases due to annealing treatments. In addition microstructural characterizations have been carried out in these samples of $Bi_2Fe_4O_9$. In the following the results of XRD and microscopic studies have been discussed.

5.3.1 X–Ray Diffraction Studies

The experimental X–ray diffraction patterns are Rietveld refined using Fullprof program for the as prepared and sintered $Bi_2Fe_4O_9$ samples and are shown in Figure 5.2. All the peaks could be indexed to the (hkl) values of the $Bi_2Fe_4O_9$ phase both in the as prepared and sintered samples confirming the presence of only the single phase of $Bi_2Fe_4O_9$ matching with standard ICDD–01-08-12982. In the case of the sintered sample selective orientation of certain peaks viz., (001), (002) and (140) could be observed implying the oriented grain growth along (001) (cf. Figure 5.2) [177]. The Rietveld refined structural parameters are provided in the Table 5.1.

The structure refined unit cell of the as prepared $Bi_2Fe_4O_9$ is shown in Figure 5.3.The lattice parameters vary little with sintering while the bond lengths and angles are observed to change relatively. This is because of the redistributed cations reduced anionic defects upon sintering. The two Fe sites denoted as Fe1 and Fe2 corresponding to tetrahedral and octahedral environment respectively are shown (cf. Figure 5.3). In the case of $Bi_2Fe_4O_9$, the FeO_6 octahedra are aligned and connected through FeO_4 tetrahedra whereas BiO units are sandwiched between the octahedral units [180]. The angle between the Fe1 and Fe2 play a crucial role in antiferromagnetic superexchange interaction [181]. The angle Fe1–O2–Fe2 observed here is 120° w r t observed value of 121° by Mohapatra *et al.*[182] and shows weakest superexchange interaction between Fe1 and Fe2 implying the existing weak FM behavior. The angle between tetrahedral Fe1 sites remain close to 108° indicating the strongest antiferromagnetic interaction existing in the system [182].

Table 5.1 Bond length and bong angles as deduced from refinement for as prepared (973 K for 144 h) and sintered (973 K for 144 h and 923 K for 24 h) $Bi_2Fe_4O_9$.

Sample ⟶ **Properties** ↓	**As prepared**	**Sintered**
Crystal structure	a= 7.96b=8.43c=5.99	a= 7.96b=8.43c=5.99
Bond length (Å)	Fe1–O2= 2.106Fe1–O3=1.557 Fe1–O4=1.559 Fe2–O1= 2.19Fe2–O2= 1.935	Fe1–O2= 2.106Fe1–O3=1.584 Fe1–O4=1.526 Fe2–O1= 2.225Fe2–O2= 2.069
Bond angle (degrees)	Fe1–O4–Fe1 = 180 Fe1–O2–Fe2=120 Bi–O2–Fe1 = 126 Bi–O1–Fe2=110 Bi–O2–Fe2=111 Bi–O–Bi = 152	Fe1–O4–Fe1 = 180 Fe1–O2–Fe2=121 Bi–O2–Fe1 = 127 Bi–O1–Fe2=112 Bi–O2–Fe2=117 Bi–O–Bi = 151
Volume (Å^3)	402.194	402.167

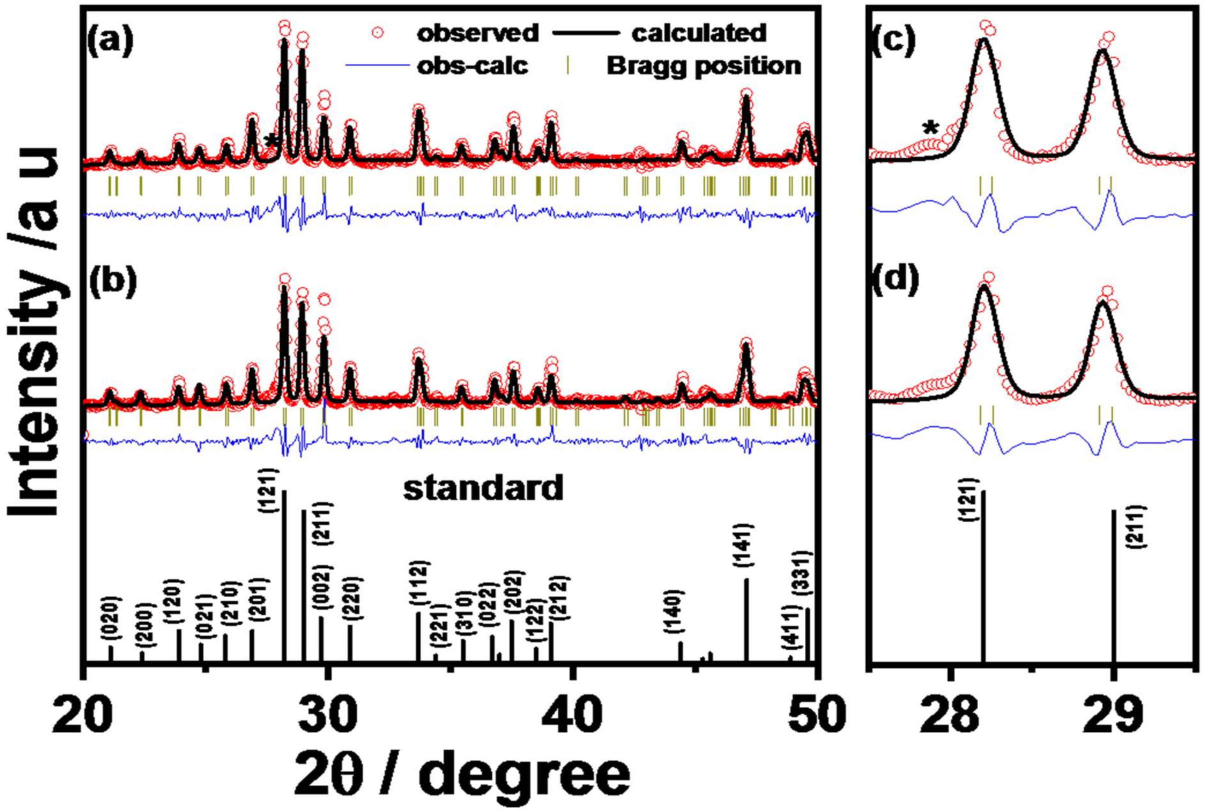

Figure 5.2 Fullprof refined XRD pattern corresponding to as prepared sintered at 973 K for 144 h (a) followed by sintering at 923 K for 24 h (b) and compared with standard stick pattern of $Bi_2Fe_4O_9$ (right inset (c) & (d) zoomed in most intense peaks).

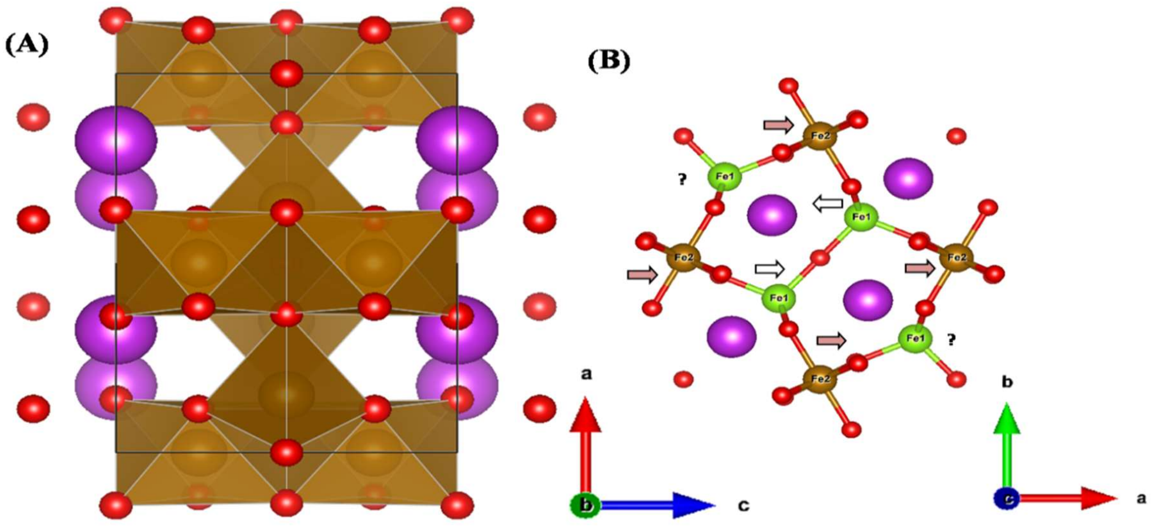

Figure 5.3 Unit cell of $Bi_2Fe_4O_9$ as generated using VESTA software and the Fe site in octahedral and tetrahedral environment is presented.

5.3.2 Microscopic Image Analysis

SEM microscopic studies have been carried out in both the as prepared and sintered $Bi_2Fe_4O_9$ and the respective microscopic images are shown in Figure 5.4.The figure shows almost cube shaped micron sized particles with composition containing higher side of oxygen in the as prepared whereas that of the sintered sample matches well with the standard weight percentage (cf. Table 5.2). Annealing leads to an enhanced crystallinity. This is commensurate with the XRD results in terms of a slight shift in the position of most intense peaks which could be explained due to redistribution of the Bi/Fe cations in the sintered sample. The orientation of particles could be observed from the images wherein the sharp edges of cuboids gradually elongates upon sintering consistent with the results of XRD implying the selective oriented grain growth.

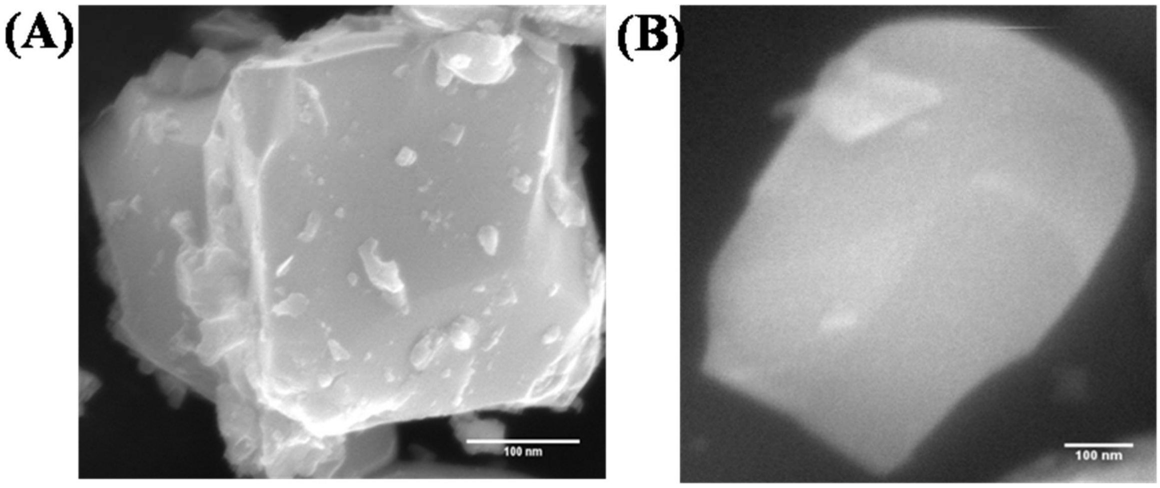

Figure 5.4 SEM image of as prepared (A) and sintered (B) $Bi_2Fe_4O_9$ with scaling of 100 nm.

Table 5.2 Weight percentage of the standard, as prepared and the sintered sample as obtained from EDAX analysis.

Sample →	**Standard**	**As prepared**	**Sintered**
element ↓	**(ICDD–010819282)**		

Bi	53	49.1	53.3
Fe	29	23.7	28.2
O	18	27.2	18.5

5.4 Bulk Magnetization Study

5.4.1 Field Dependent Magnetic Studies

The magnetic structure of the sintered $Bi_2Fe_4O_9$ are investigated by using field dependent magnetization studies over a temperature range from 5 K to room temperature and plots are shown in Figure 5.5(A). Observed hysteresis loop represents the coexisting non linear portion of the curve at the low applied magnetic field region up to 2 T while the magnetization is observed to vary linearly with increasing value of the external magnetic field beyond 2 T. The nonlinear region implies the occurrence of the weak ferromagnetic component and the linear region coincides typically with that of antiferromagnetic behaviour [52,53,62,180–182].With sintering there is a change in canting of Fe1–O–Fe2 angle by the interaction of the external magnetic field resulting in uncompensated surface spins [184]. If there occurs Fe^{2+} in the sample then the double exchange interaction could occur between Fe^{3+}–O–Fe^{2+} neighbouring ions mediated through oxygen forming local ferromagnetic clusters of short range ordering and weak FM is induced, whereas, above T_N the weak ferromagnetism is due to the presence of magnetic polarons. Magnetic polarons (Fe^{2+}–V_o) results from low valence of Fe which are bound to oxygen vacancies and up to a certain concentration of such polarons cause weak ferromagnetism [186]. Further the nonlinearity in magnetization for the values of magnetic field between 2 and -2 Tesla (cf. Figure 5.5 (A)) implies the presence of magnetic interaction at low applied field while the application of higher value of magnetic field causes AFM behaviour which represents the bulk behaviour to dominate over the weak FM contribution. Hence sintered $Bi_2Fe_4O_9$ exhibits weak ferromagnetic behaviour in addition to AFM throughout the measured temperature range of 5 K to 300 K. The variation of magnetization in AFM region is due to temperature effect when the measurement is done from RT to 5 K. The parameters are given in Table 5.3.

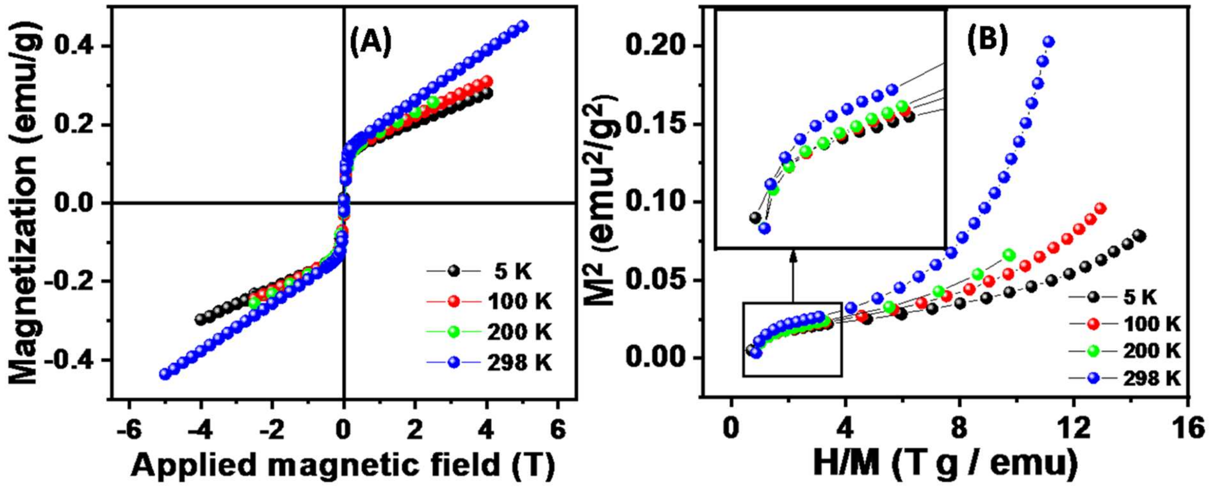

Figure 5.5 M–H loop (A) and corresponding A–B–K plot (B) of $Bi_2Fe_4O_9$ sintered at 923 K.

Table 5.3Magnetization parameters i.e.M_r, M_s and H_c for the sintered $Bi_2Fe_4O_9$**.**

Sample	T (K)	Mr(emu/g)	Ms(emu/g)	Hc(Tesla)
BFO SSR	5	0.00395	0.1358	0.0024
923 Kfor	100	0.00395	0.129	0.0094
24 h	200	0.0147	0.125	0.0138
Sintered	298	0.0145	0.122	0.0071

The Arrot plot (cf. Figure 5.5 (B)) shows correspondence with the M–H loop and is used to obtain the spontaneous magnetization from M–H loop and also expresses the magnetic phase distribution over the bulk. The applied magnetic field region below 2 Tesla shows convex curvature indicative of the occurrence of the weak ferromagnetic behaviour. For the values of magnetic field above 2 Tesla the Arrot plot displays a concave feature confirming the antiferromagnetic behaviour. This further confirms the coexisting weak FM and AFM regions in the sample. The decrease in magnetization in the AFM region with increase in temperature from 5 K to 300 K indicates the temperature induced randomization of spins.

5.4.2 DC Magnetization Studies

Temperature dependent magnetization studies are carried out from 5 K up to RT on the as prepared and sintered $Bi_2Fe_4O_9$ to illustrate the transition temperature and temperature dependent anomalies in the magnetic phase and presented in Figure 5.6. As prepared $Bi_2Fe_4O_9$ show mostly overlapped ZFC FC curves with bifurcation at particular temperatures corresponding to anomalies at 50 K, 130 K and 260 K. There is a decreasing trend in magnetization observed up to around 50 K and sharp increase beyond up to RT. A sharp increase in both ZFC and FC magnetization is seen at low temperature below 30 K. In sintered $Bi_2Fe_4O_9$ bifurcated region up to 250 K is obtained with no anomalies at 50 K or 130 K. The observed features in as prepared sample can be understood as follows. The overlapping ZFC FC is indicative of strong antiferromagnetic interaction in the as prepared $Bi_2Fe_4O_9$. This is expected for $Bi_2Fe_4O_9$ which exhibits spin frustrated AFM behaviour caused from FM ordered O_h sites and AFM ordered tetrahedral sites and antiferromagnetic nature of the octahedral and tetrahedral sites. The increase in magnetization below 30 K is due to the presence of Fe vacancies causing spin compensation and hence resulting sharp increase. The anomaly at 250 K in both the cases is related to the transition from antiferromagnetic to paramagnetic ordering and similar broadness around T_N is discussed elsewhere [28,180,181]. The cusp at around 50 K is spin glassiness and will further be explained subsequently by means of dynamic susceptibility measurements. The anomaly at 130 K is related to the onset of spin reorientation as reported in literature [184].

In case of sintered sample a bifurcation up to 250 K can be explained as weak FM contribution leading exchange interactions and hence irreversibility of ZFC and FC. No peak is observed at low temperature in sintered $Bi_2Fe_4O_9$. This is probably due to suppression of such anomalies because the magnetization region of the anomaly is smaller (~ 0.03 emu/g) while the range of magnetization in the sintered one is as high as (0.1 emu/g).

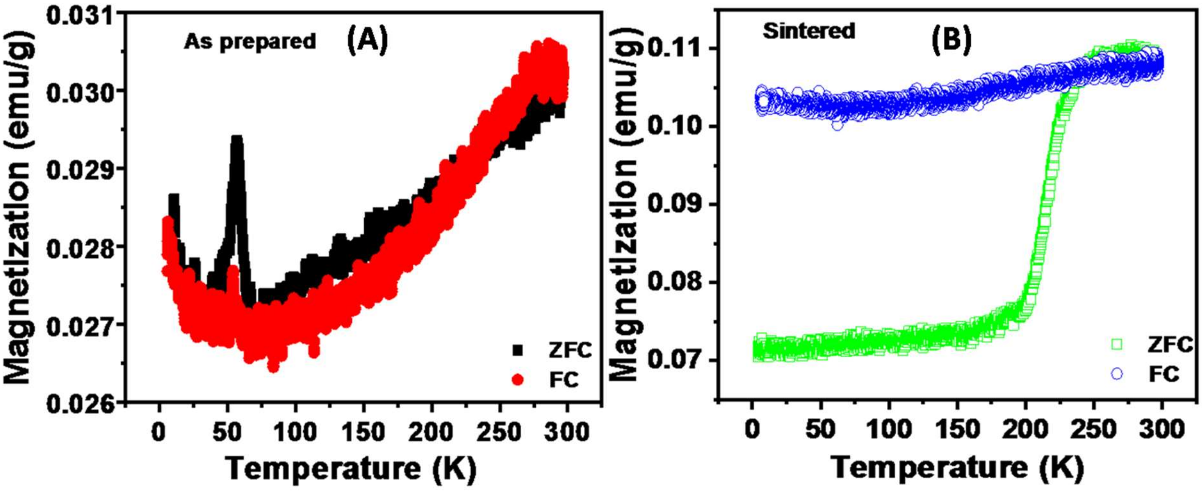

Figure 5.6 ZFC FC plot of as prepared under different applied field (A) and (B) sintered at 923 K for 24 h.

5.4.3 AC Susceptibility Studies

In order to understand the origin of bifurcation of ZFC FC as observed from dc magnetic studies and also to confirm the spin glass feature, ac susceptibility measurement is required. The in and out of phase components of magnetic susceptibility (χ) vs. temperature at different frequencies with low applied magnetic field is shown in Figure 5.7. These plots are significant in understanding the type of phase transition as well as the spin glass type variation. χ_{ac}' is the measure of degree of domain wall motion leading to spin reorientation in terms of slow dynamics of the material's magnetic properties to applied low magnetic field. This occurs due to magneto–crystalline anisotropy leading from crystal defects. χ_{ac}" implies the energy absorption corresponding to domain wall motion and more prominent below the transition temperature. The peak around 60 K in χ_{ac}' vs T where the magnetic anomaly is an indication of spin freezing temperature as per Vogel–Fulcher law observed in spin glass [187].This occurs around the anomalous temperature region in DC magnetization. Further the χ_{ac}" vs. T peak occurs around 30–40 K. The peak feature in both real and imaginary part of susceptibility show shift to low T from 34 to 30 K implies magnetic frustration at low temperature due to glassy behaviour. This confirms the spin glass behaviour. The peak feature at different temperatures for real and imaginary part of ac susceptibility signifies the relaxor type magnetic behaviour in case of $Bi_2Fe_4O_9$ [188].

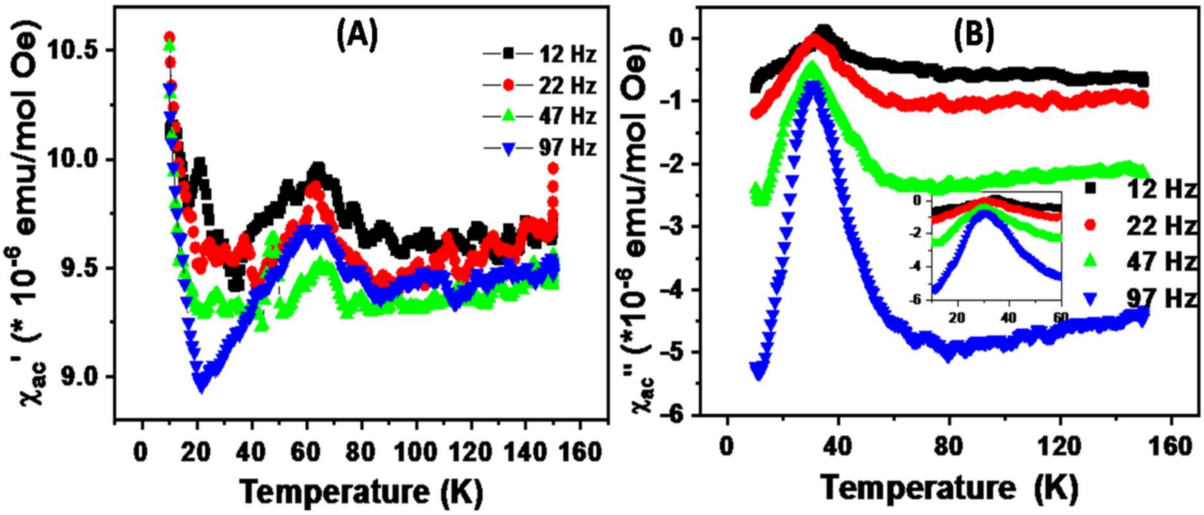

Figure 5.7 Frequency dependent real and imaginary part of ac susceptibility measurement w r t temperature for sintered $Bi_2Fe_4O_9$ showing shift of relaxation peak.

5.5 Ferroelectric Properties

Being a type II multiferroic it is essential to give an insight in to the ferroelectric properties of the prepared samples and hence the ferroelectric PE loop tracer measurements at RT were carried out for sintered sample and shown in Figure 5.8. Singh *et al.*[63] studied the loop exhibiting finite polarization at RT for $Bi_2Fe_4O_9$. In the present study the sintered $Bi_2Fe_4O_9$ shows ferroelectric behaviour at RT with order 0.2 μC/cm^2 matching well with reported values [189]. Acquiring PE loop above the reported Curie temperature 260 K indicates the strong magnetoelectric coupling effects. The dipole orientation is influenced within the magnetic ordering which is close to RT as deduced from the magnetic studies and also reported in literature. The polarization value increases upon increase in voltage symmetrically exhibiting ferroelectricity throughout the measured voltage range. This is intrinsic signature of ferroelectricity exhibited by $Bi_2Fe_4O_9$. As explained the dipole and magnetic ordering are coupled and hence in order to put more light on this coupling PE measurements are carried out under the application of magnetic field and discussed in detail subsequently.

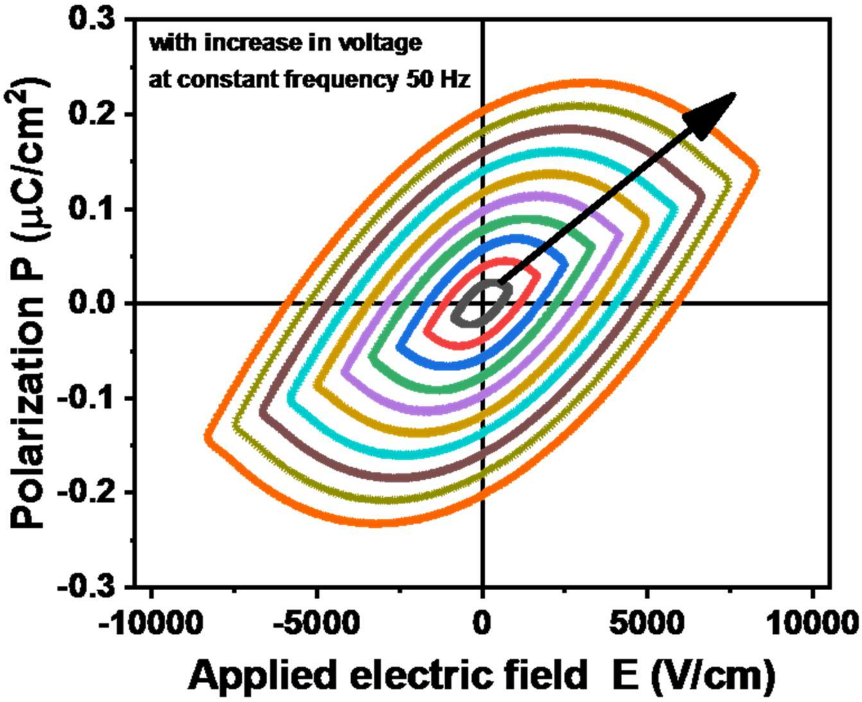

Figure 5.8 Room temperature polarization Vs electric field loop for the $Bi_2Fe_4O_9$ sintered at 923 K.

Having discussed the results of magnetic and ferroelectric properties it is important to probe the different between the magnetic behaviour between the as prepared and sintered $Bi_2Fe_4O_9$ samples. As the magnetic properties are understood to evolve based around Fe atoms in terms of Fe–O–Fe exchange interactions the results of Mössbauer studies would be helpful in understanding the observation of magnetization results in $Bi_2Fe_4O_9$ and also the observed ferroelectric behaviour in the sintered $Bi_2Fe_4O_9$.

5.6 Discussion on the Results of Mössbauer Studies

Mössbauer spectra as obtained in the as prepared and sintered $Bi_2Fe_4O_9$ samples are shown in Figure 5.9 and the resultant hyperfine parameters obtained are listed in the Table 5.4. In the case of as prepared sample the spectra could be fitted with two doublets and a six line component. The doublets obtained in both the cases with one component experiencing a high value of the quadrupole splitting (0.99 mm/s) shown in green and other component with lower quadrupole splitting (0.42 mm/s) shown in blue colour in Figure 5.9 corresponds to that of Fe atoms occupying tetrahedral and octahedral sites respectively. $Bi_2Fe_4O_9$ exhibits equally distributed Fe sites at tetrahedral and octahedral sites.

In addition to predominant doublets it is seen that as high as 5% of Fe atoms in the case of the as prepared sample experiences a six line component with the hyperfine parameters remaining almost same as that of α-Fe_2O_3. Occurrence of this component is understood to be due to the volatility of Bi in the system. This component is due to Fe atoms associated with α-Fe_2O_3 which is understood to have got formed at the surface of grains of $Bi_2Fe_4O_9$ due to prolonged annealing treatments.

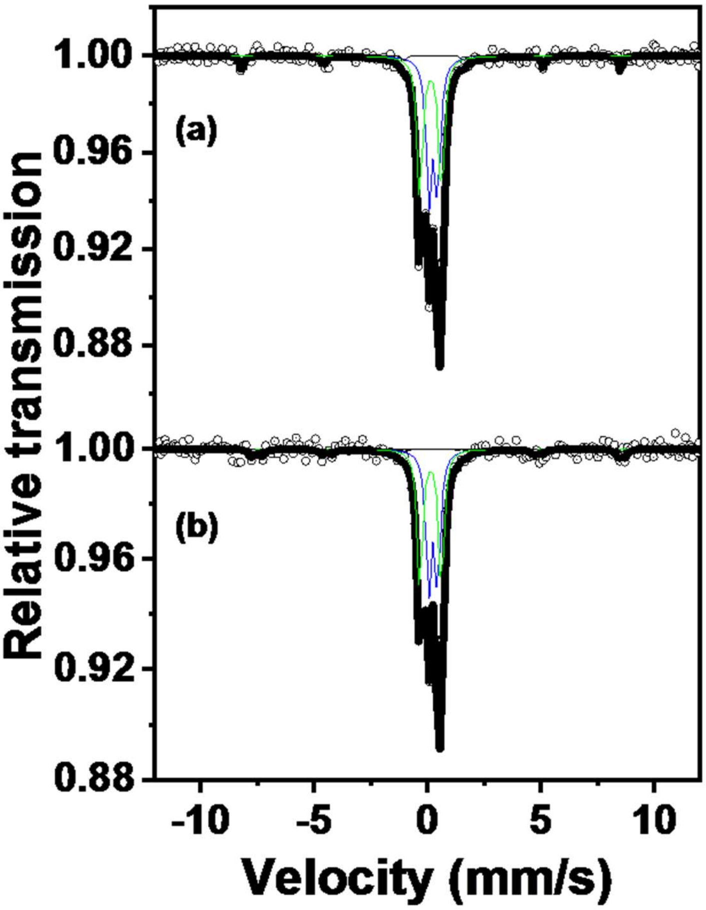

Figure 5.9 Room temperature MS of as prepared (a) and sintered at 923 K for 24 h (b) $Bi_2Fe_4O_9$.

Table 5.4 Mössbauer parameters corresponding to as prepared and sintered $Bi_2Fe_4O_9$

$Bi_2Fe_4O_9$	δ (mm/s)	Δ (mm/s)	B_{hf}(Tesla)	Rel Area(%)
As prepared	0.38±0.01	0.38±0.01	0	47
	0.26±0.01	0.96±0.01	0	48
	0.33±0.02	-0.11±0.04	51.7±0.7	5
Sintered	0.37±0.01	0.40±0.01	0	47
	0.26±0.01	0.95±0.01	0	45
	0.31±0.08	0.31±0.16	50.1±0.5	4
	0.68±0.09	0.28±0.16	46.6±0.5	4

The observed magnetization behaviour in the as prepared sample is consistent with the results of the Mössbauer studies revealing the presence of α-Fe_2O_3 along with the dominantly present $Bi_2Fe_4O_9$. Mössbauer results as obtained in the case of sintered sample shows the occurrence of two six line components with the values of isomer shifts such as 0.31 and 0.68 mm/s while the respective values of the hyperfine fields remain as 50.1 and 46.6 Tesla. Based on the values of the hyperfine components the occurrence of these two sextets could be attributed to the presence of off-stoichiometric magnetite in the sample along with the dominantly present $Bi_2Fe_4O_9$. Magnetite being a ferrimagnetic system has contributed for the weak ferromagnetic component that occurs in the sintered $Bi_2Fe_4O_9$ sample resulting in the observed magnetization and M–H behaviour as shown in Figure 5.5. Off-stoichiometric magnetite might be occurring at the surface of the grains of $Bi_2Fe_4O_9$ following the sintering treatments. Based on the Mössbauer results it could be inferred that in the case of sintered sample there occurs the distribution of magnetic phases in the form of grains of $Bi_2Fe_4O_9$ which are antiferromagnetically ordered while in the grain boundary surface there occurs magnetite which are responsible for the weak ferromagnetic interactions that are observed between the grains resulting in the observed magnetic properties in the case of sintered $Bi_2Fe_4O_9$.

5.7 Magnetoelectric Coupling

Influence of the magnetic field on the electric dipole orientation is studied based on the variation of the electric polarization with the applied magnetic field as shown in Figure 5.10. The plot shows the P–E loop as obtained in the sintered $Bi_2Fe_4O_9$ without and with the application of the external magnetic field of the value 0.5 Tesla. The value of ferroelectric parameters are $P_r = 0.1\ \mu C/cm^2$ and $E_c = 1.1$ kV/cm in the absence of magnetic field and these parameters decrease upon the applied magnetic field of 0.5 T. The polarization values vary significantly. The variation is calculated using the formula [124,125]

$$ME\ \% = \frac{P_r(H) - P_r(0)}{P_r(0)} \times 100, \qquad 5.1$$

where P_r (H) – Polarization in the presence of magnetic field

P_r (0) – Polarization in the absence of magnetic field

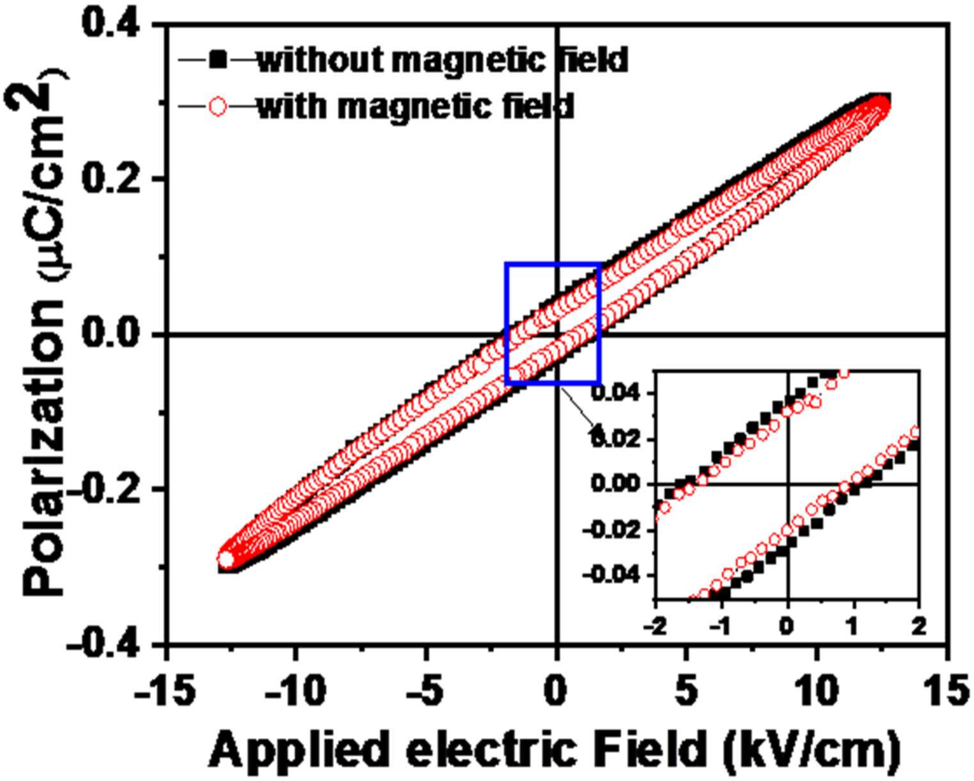

Figure 5.10 Exhibition of magnetoelectric switching in electric field in magnetic environment when magnetic field is applied. The zoomed in region (inset) implicates the change.

The change in polarization and coercive field values using the formula thus obtained are decrease in polarization by ~14 % while that of coercive field decrease by ~21 %. The observed values are well in agreement with the values obtained from MD coupling discussed subsequently. These observed results show switching behaviour and confirm the magnetoelectric coupling effects in $Bi_2Fe_4O_9$. The observed magnetodielectric coupling can be understood based on the results of Mössbauer studies indicating the formation of magnetite phase likely to have formed at the grain boundary of these particles.

5.8 Magnetodielectric Coupling

Dielectric properties of the sintered $Bi_2Fe_4O_9$ are investigated around the Néel temperature in presence of magnetic field. The dielectric properties in terms of the measurement of dielectric constant under the application of magnetic field are observed to show variation as shown in Figure 5.11. Under the influence of magnetic field, dielectric properties are observed to show anomaly around the Néel temperature and is a significant feature of coupling of magnetic and dielectric properties. Further the variation of the polarization with respect to magnetic field gives an insight to the study of magnetoelectric properties as discussed in the previous section. Variation of dielectric constant with magnetic field as measured at different frequencies shows that for all the values of the frequencies a prominent anomaly and a shift to higher temperature with frequency increasing around Néel temperature implying a strong MD coupling [190].The MD coupling as observed in this case is attributed to the strain arising within electric and magnetic domains modifying dielectric behaviour around the Néel temperature leading to strong MD coupling [186, 188, 189].The MD coupling is calculated using the formula

$$MD\ \% = \frac{\varepsilon\,(H) - \varepsilon\,(0)}{\varepsilon\,(0)} \times 100\,, \qquad \mathbf{5.2}$$

where $\varepsilon(H)$, $\varepsilon(0)$ is dielectric constant measured in presence and absence of magnetic field respectively. As discussed earlier magneto resistance effect is not likely possible hence the origin of the anomaly is most likely be ascribed to the ME behaviour [124,125].

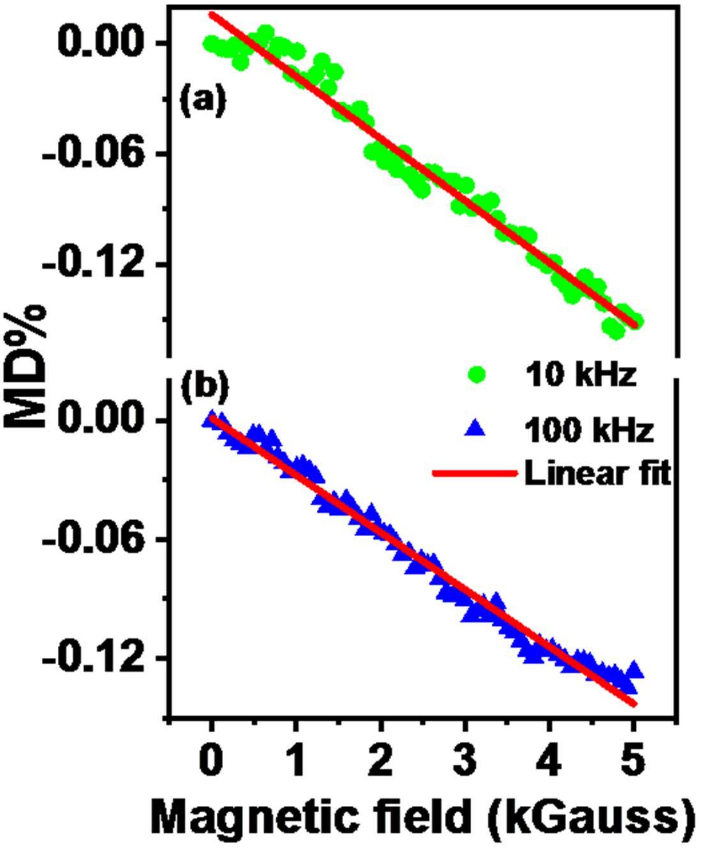

Figure 5.11 Variation of the percentage of the magneto–dielectric coupling upon the application of magnetic field at different frequencies in $Bi_2Fe_4O_9$ SSR sintered at 923 K for 24 h (a) 10 kHz and (b) 100 kHz

It is found out that the MD effect increases with respect to magnetic field from - 0.05 to 0.2 % with an increase in magnetic field. MD coupling effect can be negative or positive as discussed by Kimura *et al.*[193].The increase in MD % with magnetic field implies that the magnetodielectric coupling enhances with an increase in the value of the applied magnetic field. In addition the behaviour of dielectric constant and tan loss in presence and absence of magnetic field is studied to give an insight to the frequency dependent variation (cf. Figure 5.11) for higher frequency 10 kHz and 100 kHz to exclude maximally the contribution from dc conductivity, leakage and space charge polarization [28,191]. The plot of MD% for different frequencies i.e. 10 kHz and 100 kHz is shown in figure to explain the MD properties which shows change throughout the applied field region implying strong MD coupling [178,186,192,193]. The negative MD effect as observed in case of 10 kHz and 100 kHz is -0.16 and -0.14 respectively.

5.9 Conclusion

Magnetic properties of $Bi_2Fe_4O_9$ have been studied in a detailed manner using a detailed magnetization studies establishing the antiferromagnetic properties. Mössbauer results imply the occupation of Fe dominantly at tetrahedral and octahedral sites of $Bi_2Fe_4O_9$ experiencing pure quadrupole interaction.On the other hand the sintered $Bi_2Fe_4O_9$ sample is observed to exhibit weak ferromagnetic ordering in addition to the dominant antiferromagnetic ordering. Based on the results of the Mössbauer studies it is interpreted that the coexisting antiferromagnetic ordering and the weak ferromagnetic ordering are due to the grains of $Bi_2Fe_4O_9$ and their grain boundaries respectively. Further it is understood that at the grain boundaries of the sintered $Bi_2Fe_4O_9$ there occur off–stoichiometric magnetite particles the presence of which is confirmed based on the values of the hyperfine parameters as obtained based on the Mössbauer studies. Further the sintered $Bi_2Fe_4O_9$ is seen to exhibit ferroelectric ordering and also a strong magnetoelectric coupling effect.

6 Understanding of the Formation of Bismuth Iron Oxide Phases by Thermomechanical Route

Graphical Abstract

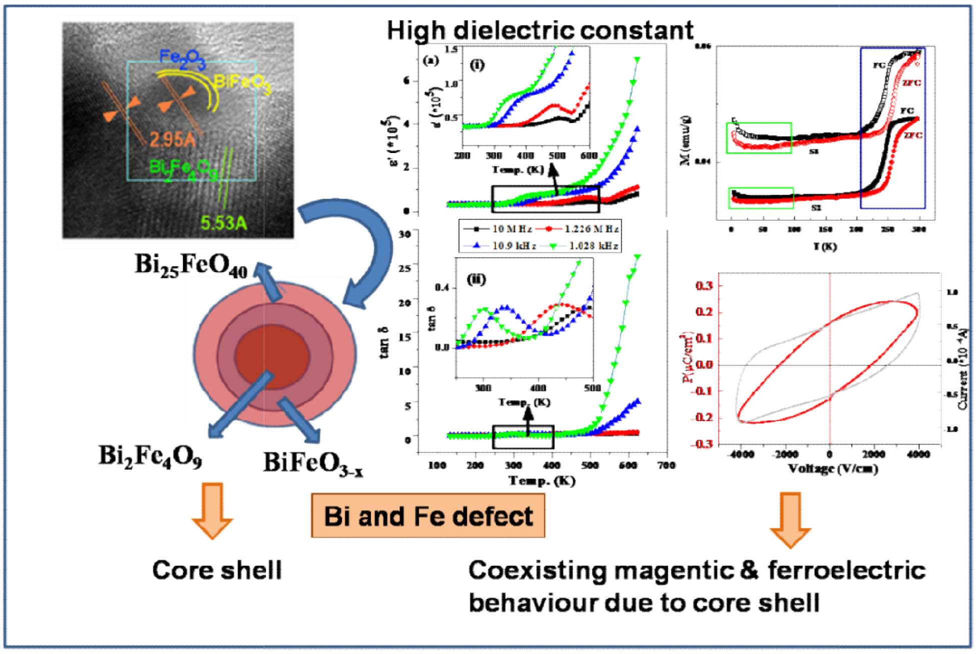

Ferromagnetic and ferroelectric properties along with the anomalies as exhibited by $Bi_2Fe_4O_9$–$BiFeO_3$core shell is shown.

Abstract:

Thermomechanical treatment on bismuth and iron oxides in a controlled manner is observed to result in the formation of radially distributed bismuth iron oxide phases in core shell formalism. The core shell formalism is elucidated using TEM studies and the mechanism of formation is proposed in this study. Mössbauer spectroscopic studies have been done to obtain an atomic scale understanding of the formation of different phases and the defects associated with these phases. Oxygen vacancies as well as defect components present in the phases are deduced from Mössbauer spectroscopic study are observed to play a crucial role in magnetic and electric properties. The resulting combinations of phases are observed to exhibit giant dielectric properties.

6.1 Introduction

$BiFeO_3$ is studied widely for its multiferroicity above RT (T_C–1103 K and T_N–643 K) while $Bi_2Fe_4O_9$ exhibits multiferroic properties at temperatures close to room temperature (T_C–260 K and T_N–250 K) [26,28,36,194].As has been studied previously, the formation of $BiFeO_3$ is always accompanied by the formation of parasitic phases as a consequence of the pseudo binary phase diagram hence suppressing the parasitic phase and enhancing the properties is a challenge in this system[34]. Several aspects related to the multiferroicity of both $BiFeO_3$ and $Bi_2Fe_4O_9$ are studied in chapter 3 and 5 respectively. These studies paved the way in the understanding the role of cationic and anionic defects on the multiferroism in these systems as deduced from the results of the detailed Mössbauer measurements. Nevertheless it is equally essential to learn the formation and properties of bismuth iron oxide phases which is the eventual outcome when the starting oxides are subjected to thermo–mechanical treatments. Multiferroicity of $BiFeO_3$ and $Bi_2Fe_4O_9$ have been separately discussed in a detailed manner with a number of magnetic and ferroelectric studies [28]. The presence of impurity phase such as $Bi_{25}FeO_{40}$ and $Bi_2Fe_4O_9$ in small concentration if any in $BiFeO_3$ is overlooked while the issues related to magnetic properties of $BiFeO_3$ are addressed since these impurity phases such as $Bi_{25}FeO_{40}$ and $Bi_2Fe_4O_9$ are paramagnetic at room temperature. Kirsch *et al.* studied the coexisting nanoparticles of $Bi_2Fe_4O_9$ and $BiFeO_3$ giving interesting optical properties and expected to exhibit enriched photocatalytic activity [65]. Bernardo *et al.* has proposed theoretically a mechanism of the reaction of Bi_2O_3 and Fe_2O_3 leading to the formation of bismuth iron oxides [198]. This chapter is aimed at studying the formation of bismuth iron oxide phases due to thermo-mechanical alloying of Bi_2O_3 and Fe_2O_3. Mössbauer spectroscopy is extensively used for addressing this problem as any evolution of iron oxides due to solid state reaction with Bi_2O_3 could be understood for its structural and magnetic properties. In addition defects related information of these phases could also be obtained elucidating the formation of bismuth iron oxide phases.

6.2 Synthesis of Bismuth Iron Oxides using Ball Milling Route

α-$Fe_2O_3$was ball milled apriori to obtain nanosized particles to interact appreciably with comparatively larger Bi_2O_3 .Hence hematite (α-Fe_2O_3) particles weresubjected to high energy ball millingfor 3 h in isopropanol medium with several steps of milling and cooling. Each step of milling and cooling period is kept at 30 minutes. Thissample will be henceforth referredasBMFe_2O_3.SubsequentlyBi_2O_3 and pre ball-milledα-Fe_2O_3 were taken in the ratio of1:3 by weight percentage respectively and again subjected to high energy ball milling for 4 h. The resulting ball-milled powders are subjected to different types of heat treatments as listed in the Table 6.1.

With respect to the initial composition of Bi_2O_3 and Fe_2O_3 and as the temperature of annealing treatment is being close to or above 1000 K, the formation of $Bi_2Fe_4O_9$ along with unreacted α-Fe_2O_3 could be predicted as guided by the phase diagram.

Therefore for a good comparison of the present results on the phases formed due to thermo mechanical alloying, $Bi_2Fe_4O_9$has also been prepared through solid-state reaction ofBi_2O_3 and α-Fe_2O_3taken in theratio of1:2 byatomicpercentage (sample S_4 inTable 6.1).The resultsofmagnetic and ferroelectric characterization studies have been compared with that of the ball-milled powder subjectedto selectiveannealing treatments in order to bring out the differences in these properties.

6.3 Identification of Phases, Local Structure and Magnetic Studies using Mössbauer Spectroscopy

Resultant phases formed due to ball milling followed by annealing treatments at different temperatures have been characterized by XRD and microstructural studies. Microstructural studies on the resultant sample would provide an understanding of different phases formed based on selective area diffraction (SAD) analysis in addition to providing an understanding of the spatial correlation if any exists between the resultant phases. There is a limitation that each of the relative phase fraction to be equal to or greater than 5% to be detected by XRD. Among other factors the scattered X–ray intensity is dependent on the atomic number Z of the atom constituting the matrix of interest. As far as the present system of the study is concerned containing Bi and Fe having atomic numbers such as 83 and 26 respectively, phases that are richer in Bi will be detected much more sensitively by XRD than that of phases which are deficient in Bi. This important constraint is overcome completely in the present studies as Mössbauer spectroscopy is extensively utilized which are selective and sensitive to identify all the phases containing iron atoms. In addition the Mössbauer spectroscopy would provide an understanding of the defects aspects and magnetic properties of these phases formed.

6.3.1 Structural Characterization

XRD patterns obtained in as ball-milled α-Fe_2O_3–Bi_2O_3 and subsequent to different annealing treatments (S_1 to S_3) along with the standard stick patterns corresponding to different bismuth iron oxide phases are shown in Figure 6.1. In the case of the as ball-milled sample (S_0), the XRD pattern (cf. Figure 6.1) essentially shows mostly the presence of α-Fe_2O_3 and α-Bi_2O_3 phases. The mean crystallite size ofα-Fe_2O_3 and Bi_2O_3 subsequent to ball milling for 4 h is evaluated to be 30 nm and 50–60 nm through Scherrer analysis. As the mean size of α-Fe_2O_3 is much smaller than that of Bi_2O_3 subsequent annealing treatments of the sample are expected to result in an enhanced interaction cross-section and reaction of these particles.As dictated by the Bi_2O_3–Fe_2O_3 phase diagram the ball-milled sample (S_0) was subjected to different annealing treatments (S_1 to S_3) to obtain bismuth iron oxide phases.

Table 6.1Details of the different treatments adopted in the study.

Sample Code	Treatment

BMFe$_2$O$_3$	α-Fe$_2$O$_3$subjected to 3h of ball milling
S$_0$	4 h ball millingofmixture of Bi$_2$O$_3$:BMFe$_2$O$_3$in the ratio 1:3 by weight percentage
S$_1$	S$_0$ annealingat1073 K /12 h +1123 K 10h
S$_2$	S$_1$ annealingat1073 K 24 h
S$_3$	S$_0$ annealingwith10 % excess Bi$_2$O$_3$at 1073 K 12 h +1123 K 10h
S$_4$	Solid-state reactionofpowdersofBi$_2$O$_3$ andα-Fe$_2$O$_3$intheratio 1:2 by atomic percentage andannealingat973 Kfor 144 h

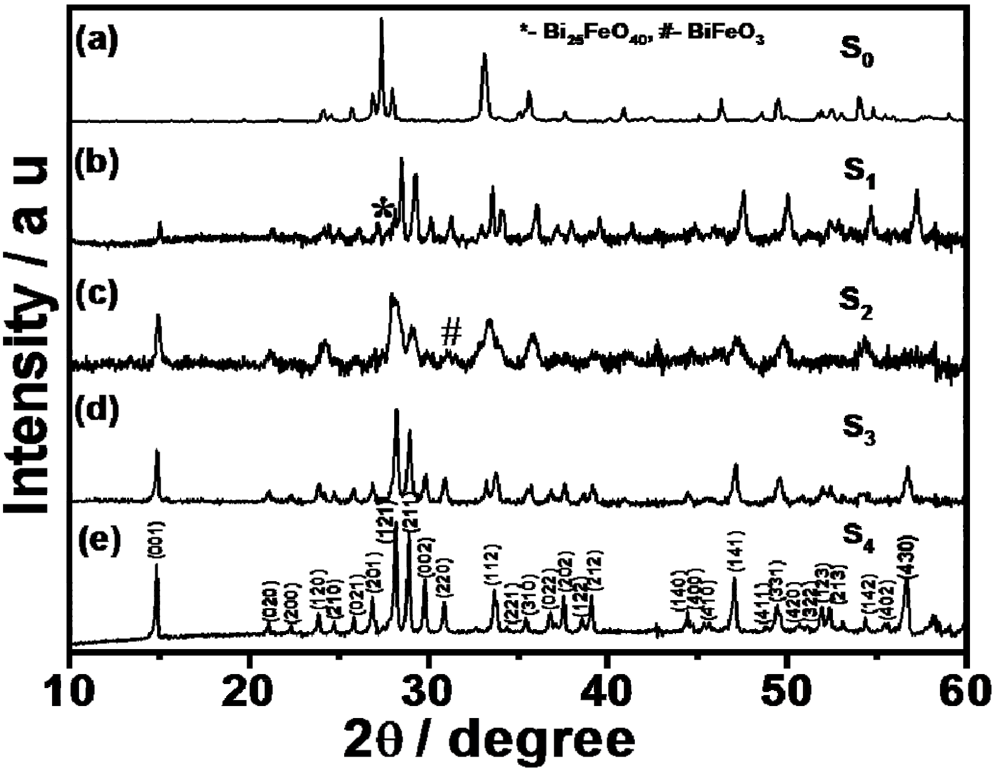

Figure 6.1 Patterns corresponding to treatment (a) S$_0$-ball-milled α-Fe$_2$O$_3$ and α Bi$_2$O$_3$ (b), (c) S$_1$ and S$_2$ while (d) S$_3$ (e) S$_4$ (* and # indicates the presence of Bi$_{25}$FeO$_{40}$ and BiFeO$_3$respectively).

Table 6.2 Phase identification through XRD analysis after different heat treatments.

Sample Code	Identified phases	Structure and space group
	Fe$_2$O$_3$	Rhombohedral (*R-3c*)

S_0	Bi_2O_3	Monoclinic ($P2_1/c$)
	Fe_2O_3	Rhombohedral (*R-3c*)
S_1	$Bi_2Fe_4O_9$	Orthorhombic (*Pbam*)
	Fe_2O_3	Rhombohedral (*R-3c*)
	$Bi_{25}FeO_{40}$	bcc (*I23*)
S_2	$Bi_2Fe_4O_9$	Orthorhombic (*Pbam*)
	Fe_2O_3	Rhombohedral (*R-3c*)
	$Bi_{25}FeO_{40}$	bcc(*I23*)
	$BiFeO_3$	Rhombohedral (*R3c*)
S_3	$Bi_2Fe_4O_9$	Orthorhombic (*Pbam*)
	Fe_2O_3	Rhombohedral (*R-3c*)
S_4	$Bi_2Fe_4O_9$	Orthorhombic (*Pbam*)

The corresponding XRD patterns are also shown in Figure 6.1 (b)–(d). Comparison of XRD patterns obtained after treatment S_1 shows that there is a drastic reduction in the intensities of most intense peaks of α-Fe_2O_3 implying an appreciable reaction and formation of bismuth iron oxides, predominantly $Bi_2Fe_4O_9$, due to the interaction between the oxides. In addition an appearance of a peak marked as * at the position corresponding to that of the most intense peak of $Bi_{25}FeO_{40}$ implies the formation of this Bi rich phase along with $Bi_2Fe_4O_9$. In order to study the temperature induced evolution of these phases, the above sample (S_1) is further subjected to annealing at 1073 K for 24 h (S_2). The XRD pattern corresponding to S_2 (cf.Figure 6.1(c))shows mainly the broadening of the peaks corresponding to $Bi_2Fe_4O_9$. It is also important to understand the effect of the concentration of bismuth oxide on the formation of phases. Towards this, the ball-milled sample (S_0) is subjected to treatment S_3, which consisted of addition of about 10 wt% Bi_2O_3 to S_0 followed by an annealing treatment similar to S_1. The XRD pattern corresponding to this sample remains almost similar to that of $Bi_2Fe_4O_9$ implying an appreciable presence of this phase. To compare the effect of the synthesis route, an attempt was made to prepare $Bi_2Fe_4O_9$ through the solid-state reaction of Bi_2O_3 and Fe_2O_3 taken in the ratio of 1: 2 by weight percentage followed by annealing at 973 K/144 h (treatment S_4). The resultant XRD pattern is shown in Figure 6.1(e), which confirms the single phase nature of the sample. Table 6.2summarizes the phases and their crystal structures identified by XRD after the different treatments.

6.3.2 Local structure and magnetic studies using Mössbauer spectroscopy

Mössbauer spectra obtained for BM α-Fe_2O_3 and ball-milled α-Fe_2O_3–Bi_2O_3 samples (S_0) are shown inFigure 6.2. Based on the analysis of the spectrum corresponding to the reference α-Fe_2O_3 it is deduced that all the absorber atoms experience a hyperfine field of 51.5 Tesla with a quadrupole splitting of -0.22 mm/s and a concomitant value of the isomer shift of 0.34 mm/s (cf. Table 6.3) consistent with the literature result[199]. An appreciable onset of interaction between α-Fe_2O_3 and Bi_2O_3 particles due to ball milling is evidenced by the occurrence of about 3% of Fe atoms associated with bismuth iron oxide phases while an appreciable size reduction of α-Fe_2O_3 is elucidated based on the hyperfine parameters [5,196,197] as have been deduced (cf. Table 6.3). The Mössbauer spectrum obtained for the sample S_1 is shown in Figure 6.2. Results of the analysis show that about 55% of the resonant Fe atoms are associated with α-Fe_2O_3. Hyperfine components corresponding to Fe atoms associated with ball-milled α-Fe_2O_3 have been labelled as 1a and 1b. Since $Bi_{25}FeO_{40}$ and $Bi_2Fe_4O_9$ are paramagnetic at room temperature, Fe atoms associated with these phases experience only quadrupole interaction and hence the spectrum should be a doublet at room temperature. Based on the Mössbauer studies it has been reported that Fe associated with $BiFeO_3$ is exposed to hyperfine fields close to 49.5 Tesla [119]which is slightly lesser than that of Fe atoms associated with α-Fe_2O_3. The much lower value of the hyperfine field as observed in the present case as compared to that of pure $BiFeO_3$ is understood to be due to local distortion at Fe sites due to defects preferably of oxygen and Bi vacancies similar to the reported result[91,195]. Hence it is observed that about a 20%

relative fraction of Fe atoms are associated with $BiFeO_3$. Values of these hyperfine fields are seen to be nearly matching with that of the nanoparticles of $BiFeO_3$ as reported [4,91,118,195,198,199]. Defects play an important role in altering the ferroelectric, and ferromagnetic properties of these systems and also their coupling [5,200– 202].

About 26% of the relative area is fitted with two doublets. This is understood to be due to the association of 6% of Fe atoms with $Bi_{25}FeO_{40}$ while the remaining 20% of iron atoms equally occupy tetrahedral sites and octahedral sites of $Bi_2Fe_4O_9$. Fe atoms associated with FeO_4 tetrahedral sites in $Bi_2Fe_4O_9$ are exposed to a high value of quadrupole splitting (± 0.94 mm/s) while Fe atoms associated with FeO_6 octahedral sites experience a lesser value of quadrupole splitting (± 0.4 mm/s). Hence Mössbauer results imply the presence of α-Fe_2O_3, $Bi_2Fe_4O_9$, $Bi_{25}FeO_{40}$ and $BiFeO_3$ in the ball-milled sample subjected to treatment S_1. For the composition of bismuth oxide and iron oxide taken in the present study the ball milling and annealing treatments are expected to have resulted mostly in $Bi_2F_4O_9$ and α-Fe_2O_3. Interestingly the occurrence of other phases such as $BiFeO_3$ and $Bi_{25}FeO_{40}$ has also been observed. This is understood to be due to the distribution in the size of fine α-Fe_2O_3 nanoparticles and their spatial distribution with respect to that of Bi_2O_3 particles. Mössbauer results corresponding to sample S_2 show that about 50% of Fe atoms are associated with α-Fe_2O_3. There is an increase in the fraction of Fe atoms associated with $Bi_2Fe_4O_9$ compared to that of S_1. About 28% of the relative area of the Mössbauer spectrum corresponding to S_2 is fitted with two doublets of equal area due to association of Fe atoms with tetrahedral and octahedral sites of $Bi_2Fe_4O_9$, while 8% of the doublet area is understood to be due to the occurrence of 1a–1c refer to Fe atoms associated with defect free and defect associated α-Fe_2O_3, while all components associated with off stoichiometric $BiFeO_3$ are numbered as 2a–2d. 3a and 3b refer to doublets corresponding mainly to $Bi_2Fe_4O_9$ along with $Bi_{25}FeO_{40}$ while the fraction associated with tetrahedral (3a) is not equal to that of octahedral sites $Bi_{25}FeO_{40}$.

The remaining 18% of the area is fitted with sextets implying magnetic interactions understood to be due to the association of a relative fraction of absorber atoms with $BiFeO_3$. Mössbauer results obtained for sample S_3 show that there is an increase in the fraction of Fe atoms associated with $Bi_2Fe_4O_9$ by about 12%. This is understood to have been caused due to a larger concentration of Bi_2O_3 nanoparticles interacting with α-Fe_2O_3 nanoparticles. The variation of the fractions of Fe atoms associated with α-Fe_2O_3, $Bi_2Fe_4O_9$ and $BiFeO_3$ is shown in Figure 6.3. This shows essentially that there is an increase in the fraction of Fe atoms associated with $Bi_2Fe_4O_9$ at the cost of α-Fe_2O_3 while that of the defect associated $BiFeO_3$ remains almost constant. Mössbauer spectra obtained for this sample could be fitted with two doublets whose quadrupole parameters are listed in the Table 6.3. Fe atoms occupying tetrahedral and octahedral sites of $Bi_2Fe_4O_9$ are observed to experience quadrupole splitting around 0.99 and 0.4 mm/s.

Summarizing, Mössbauer results show the formation of $Bi_2Fe_4O_9$, off-stoichiometric bismuth iron oxide formed mainly due to oxygen vacancy associated components, resulting in a lower value of the hyperfine field than that of iron sites corresponding to FeO_6 of $BiFeO_3$. Quadrupole splitting due to octahedral Fe sites in $Bi_2Fe_4O_9$ in the cases of S_1 and S_2 is much larger than the reported value of 0.4 mm/s. This is understood to be due to bismuth vacancies. Values of quadrupole splitting similar to those of FeO_6 and FeO_4 corresponding to $Bi_2Fe_4O_9$ are observed to be restored in the case of S_3 with the excess of Bi_2O_3 subjected to the same annealing treatment as S_1.

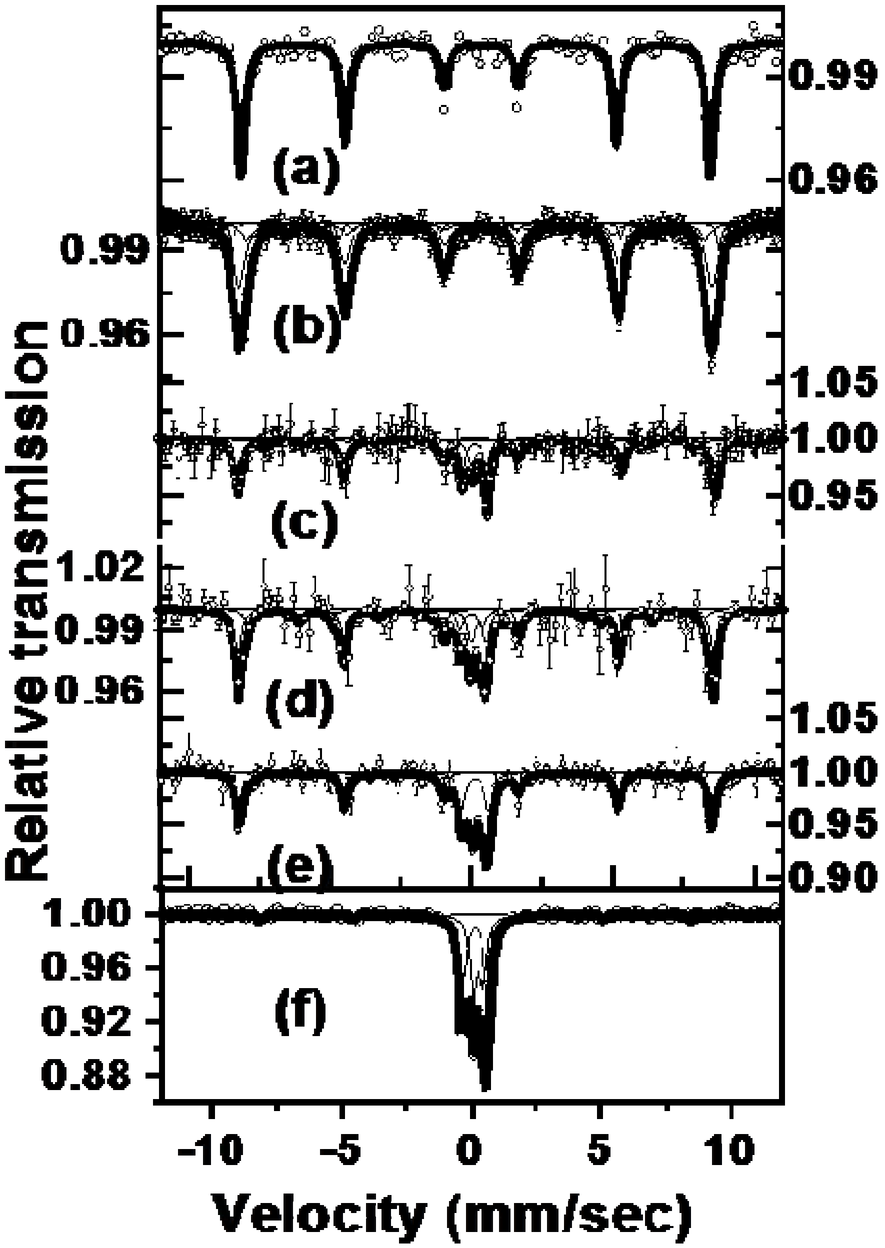

Figure 6.2 Mössbauer spectra obtained at room temperature on (a) BMFe_2O_3 (b) S_0 (as ball-milled mixture of Bi_2O_3 and Fe_2O_3), (c) and (d) corresponding to treatments S_1 and S_2 respectively, (e) treatment S_3 with addition of bismuth oxide to as ball-milled powder and subjected to annealing and (f) refers to $Bi_2Fe_4O_9$ prepared through solid-state route (S_4).

Table 6.3 Hyperfine parameters obtained through Mössbauer spectroscopy of ball milled samples subjected to different annealing treatments.

Sample details	I	δ_i mm/s	Δ_i mm/s	B_{hf} Tesla	RelArea(%) f_i	Inference
($BMFe_2O_3$)	1a	0.31	-0.21	51.5	100	α-Fe_2O_3 reference
S_0	1a	0.38	-0.21	51.8	75	α-Fe_2O_3
	1b	0.36	-0.15	50.3	18	
	1c	0.33	-0.14	53.4	04	
	2a	0.30	0.38	40.4	03	Bi–Fe oxides
S_1	1a	0.38	-0.19	51	38	α-Fe_2O_3
	1b	0.34	-0.17	52	19	
	2b	0.58	0.76	44.2	09	Bi_v&O_v $BiFeO_3$
	2c	0.55	-0.05	37.7	08	
	3a	0.24	0.94	0	10	$Bi_{25}FeO_{40}$&$Bi_2Fe_4O_9$
	3b	0.38	0.52	0	16	
S_2	1a	0.34	-0.18	51	34	α-Fe_2O_3
	1b	0.33	-0.15	52	12	
	2d	0.48	0.24	47.3	06	
	2b	0.44	1.09	46	05	$BiFeO_3$
	2c	0.50	0.23	35.5	07	
	3a	0.24	0.82	0	14	$Bi_2Fe_4O_9$ (28%) &
	3b	0.38	0.53	0	22	$Bi_{25}FeO_{40}$
S_3	1a	0.42	-0.19	51.9	22	α Fe_2O_3
	1b	0.32	-0.15	52	14	
	2d	0.44	-0.06	48.3	06	
	2c	0.24	0.32	34.1	05	$BiFeO_3$
	2b	0.37	0.15	43.3	07	
	3a	0.25	0.99	0	20	$Bi_2Fe_4O_9$&
	3b	0.38	0.4	0	26	$Bi_{25}FeO_{40}$
S_4	3a	0.38	0.38	0	47	$Bi_2Fe_4O_9$&
	3b	0.26	0.96	0	48	$Bi_{25}FeO_{40}$
		0.33	-0.11	51.7	5	

1a– defect free & 1b–1c – defect associated α-Fe_2O_3 ,2a–2d – off–stoichiometric

$BiFeO_3$, 3a,3b– $Bi_2Fe_4O_9$&$Bi_{25}FeO_{40}$

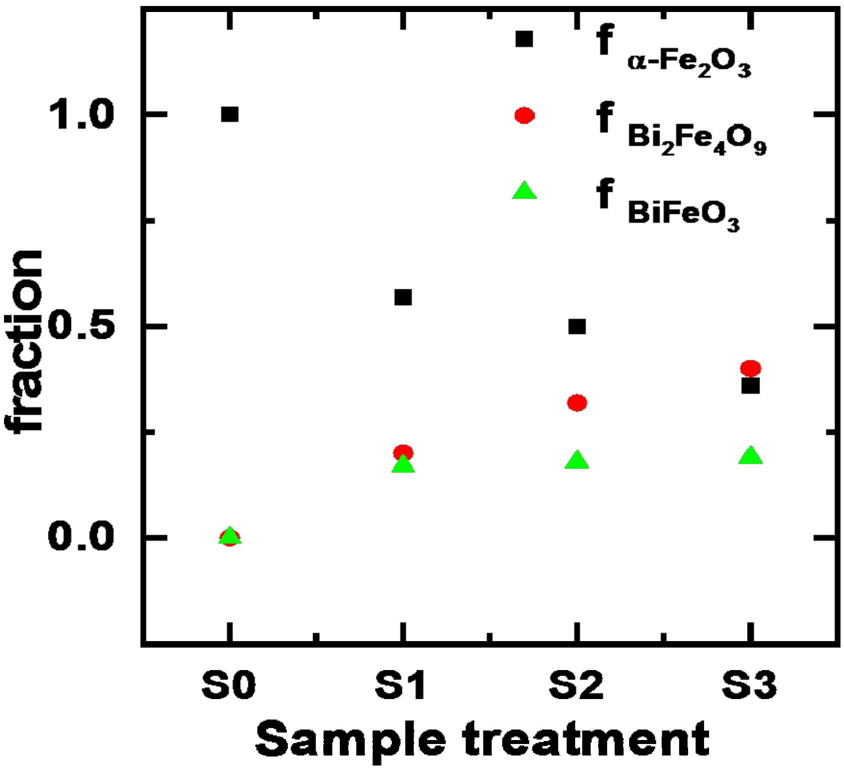

Figure 6.3 Variation of relative fractions of Fe associated with α-Fe_2O_3 (f_1), $BiFeO_3$(f_2) and $Bi_2Fe_4O_9$ (f_3) with different annealing treatments of ball-milled sample.

Figure 6.3implies a dominant increase of the fraction of Fe atoms associated with $Bi_2Fe_4O_9$ and $Bi_{25}FeO_{40}$, while that of Fe_2O_3 decreases with the fraction corresponding to that of $BiFeO_3$ remaining almost constant around 0.2. Fractions of different phases as deduced based on Mössbauer results (cf. Figure 6.3) for example for S_1 and S_2 imply that the Bi vacancies that might be occurring due to annealing treatments at elevated temperatures could partially be substituted by Fe atoms. Among other phases of bismuth iron oxide the system is understood to be predominantly of $Bi_2Fe_4O_9$ as evidenced by Mössbauer results based on distinct values of hyperfine parameters as experienced by ^{57}Fe occupying tetrahedral and octahedral sitesof $Bi_2Fe_4O_9$. Hence based on the results of XRD and Mössbauer studies the presence of $Bi_2Fe_4O_9$, $Bi_{25}FeO_{40}$, $BiFeO_3$ and mostly of amorphous like α-Fe_2O_3 could be deduced.

6.3.3 Results of Microscopy Studies

SEM images of the ball-milled sample subjected to heat treatments S_1 and S_2 are shown inFigure 6.4. Fine particles of size below 100 nm are observed after two step annealing treatment S_1, while coarser particles of different shapes i.e. spherical, cuboidal and rhombohedral varying in size from 0.2 mm to 1.50 mm are formed due to additional annealing at 1073 K for 24 h in treatment S_2. To understand the nature and microscopic features of phases formed in the sample subjected to annealing treatment S_2, detailed high resolution electron microscopy (HREM) analysis has been carried out. Figure 6.5(A)shows the HREM image of the sample, while Figure 6.5(B)and (C) show the magnified image of the region marked in Figure 6.5(A)and the Fast Fourier Transform (FFT) pattern from this region respectively. Analysis of the FFT pattern confirmed it to be $Bi_2Fe_4O_9$ as evidenced by the (110) and (211) planes with a d-spacing of 5.55 and 2.95 Å respectively. A thin inner shell around the $Bi_2Fe_4O_9$particle as indicated inFigure 6.5(B)was concluded to be amorphous as the FFT from these regions did not show any diffraction spot or ring, in contrast to the $Bi_2Fe_4O_9$ particle.

Similarly the outer shell is also observed to be amorphous. A similar observation of such core-shell structures was made in several regions. The HREM image of the same sample taken from a different region is shown in Figure 6.6(A). The FFT of the region indicated inFigure 6.6(A) is given inFigure 6.6(B). The set of reflections marked in the FFT inFigure 6.6(B)were analysed and the phases identified are given in Table 6.4. It is observed that one set of reflections indicated in Figure 6.6(B)could be matched to both $Bi_2Fe_4O_9$along the $[\bar{1}\ 3\ 0]$ zone axis and $BiFeO_3$ along the$[5\ \bar{6}\ 1]$ zone axis, due to the overlap of the d-spacings of the two phases. The inverse FFT with (002) and (310) reflections of $Bi_2Fe_4O_9$ or$(1\ 0\ \bar{4})$ and (113) reflections of $BiFeO_3$ is shown in Figure 6.6(C). This also suggests

Figure 6.6(B) could be indexed to $Bi_{25}FeO_{40}$ along the $[\bar{1}2\ 2]$ zone axis, with a clear presence of $(0\ \bar{1}\ 1)$ planes with a unique d–spacing of 7.2 Å.

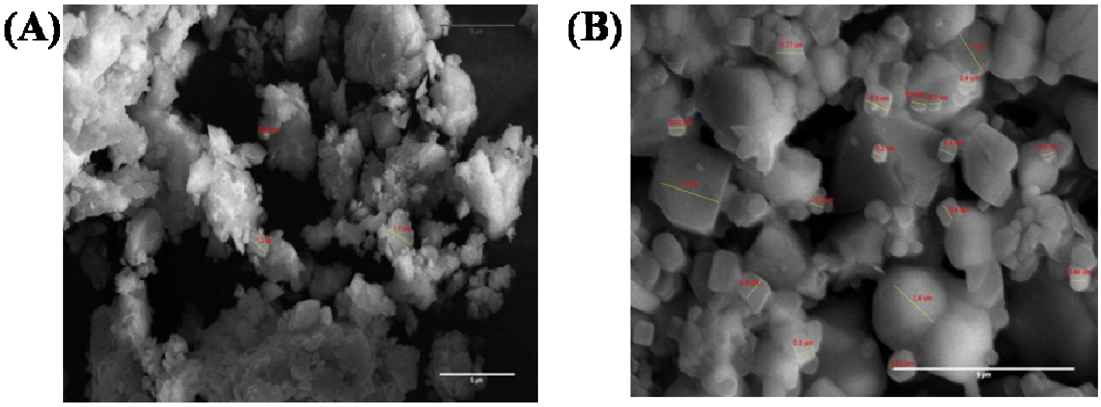

Figure 6.4 SEM images of ball milled Bi_2O_3 and Fe_2O_3 subjected to annealing treatments S_1 and S_2 showing (A) fine particles and (B) coarse particles respectively.

The inverse FFT of $(0\ \bar{1}\ 1)$and (420) reflections is shown in Figure 6.6(D). It is also interesting to note that this region of $Bi_{25}FeO_{40}$ lies at the periphery of $Bi_2Fe_4O_9$/$BiFeO_3$. This observation indicates that $Bi_{25}FeO_{40}$ is formed as an outer shell around $Bi_2Fe_4O_9$–$BiFeO_3$ particles. Combining the HREM results obtained in the sample (cf. Figure 6.5andFigure 6.6), it is understood that there are core-shell particles with $Bi_2Fe_4O_9$ as the core and an inner thin shell of crystalline or amorphous $BiFeO_3$. In some cases there are also occurrences of $Bi_{25}FeO_{40}$ particles near $BiFeO_3$. In all these cases these core-shell particles are understood to be separated by amorphous particles as evidenced by TEM. TEM results obtained for the sample thus show predominantly the occurrence of core-shell structures with $Bi_2Fe_4O_9$ as the core with a co-existing shell of $BiFeO_3$, while in a few cases also there exists a thin shell of $Bi_{25}FeO_{40}$. While the shell of $BiFeO_3$ remains amorphous or crystalline, these core-shell particles are largely surrounded by amorphous particles. Results of Mössbauer spectroscopy are discussed in the following to understand the existence of different phases based on their distinct hyperfine components and mainly regarding defects with these associated sites.

Table 6.4Analysis of FFT pattern in Figure 6.6.

	Spot 1	Spot 2	Spot3	Phase	Zone axis
Pattern 1 (pink)	0 0 2	3 1 0	3 1 2	$Bi_2Fe_4O_9$	[$\bar{1}$3 0]
Pattern 1 (pink)	1 0 $\bar{4}$	1 1 3	2 1 $\bar{1}$	$BiFeO_3$	[5 $\bar{6}$1]
Pattern 2 (Green)	0 1 $\bar{1}$	4 1 1	4 2 0	$Bi_{25}FeO_{40}$	[$\bar{1}$2 2]

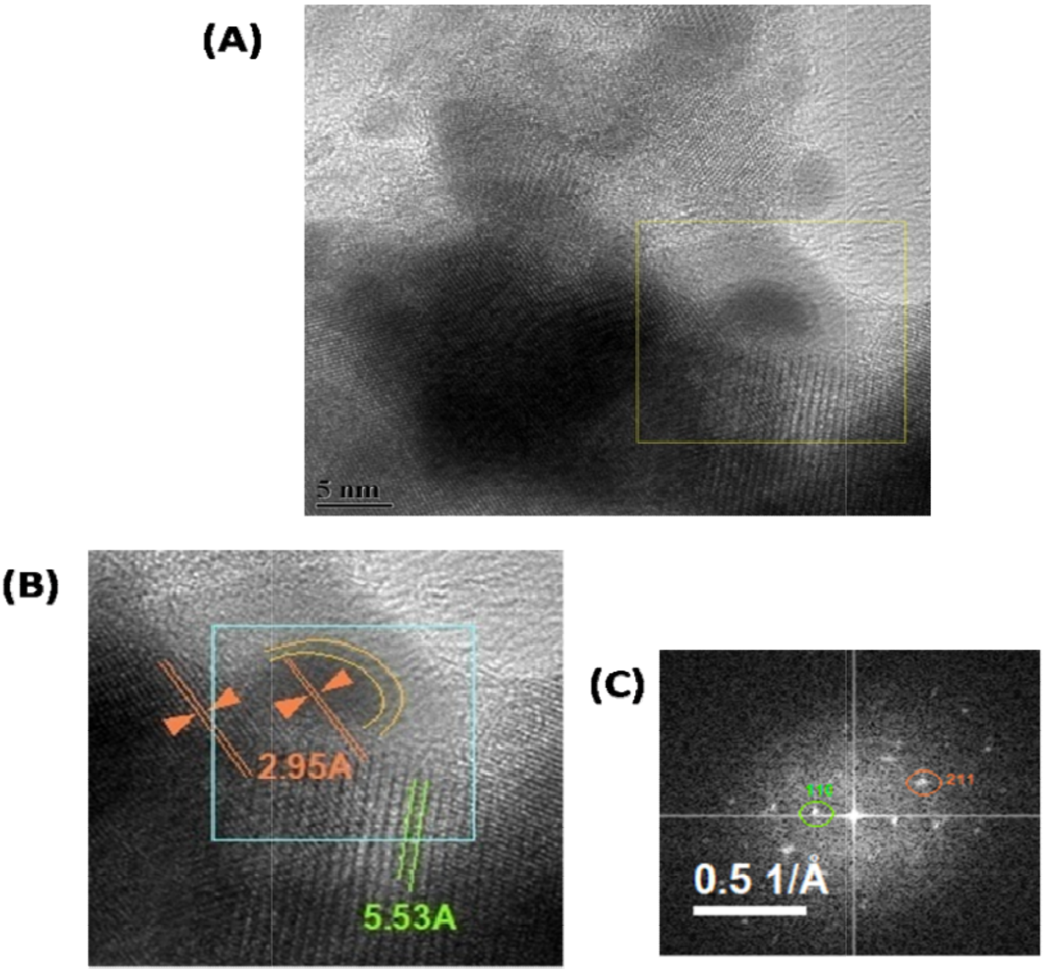

Figure 6.5 (A) TEM micrograph of S_2 , Magnified view of region marked in (B) showing the presence of core-double shell structures, where the core is identified to be $Bi_2Fe_4O_9$ as confirmed by the FFT pattern from this region in (C) and two distinct amorphous shell structures around the core.

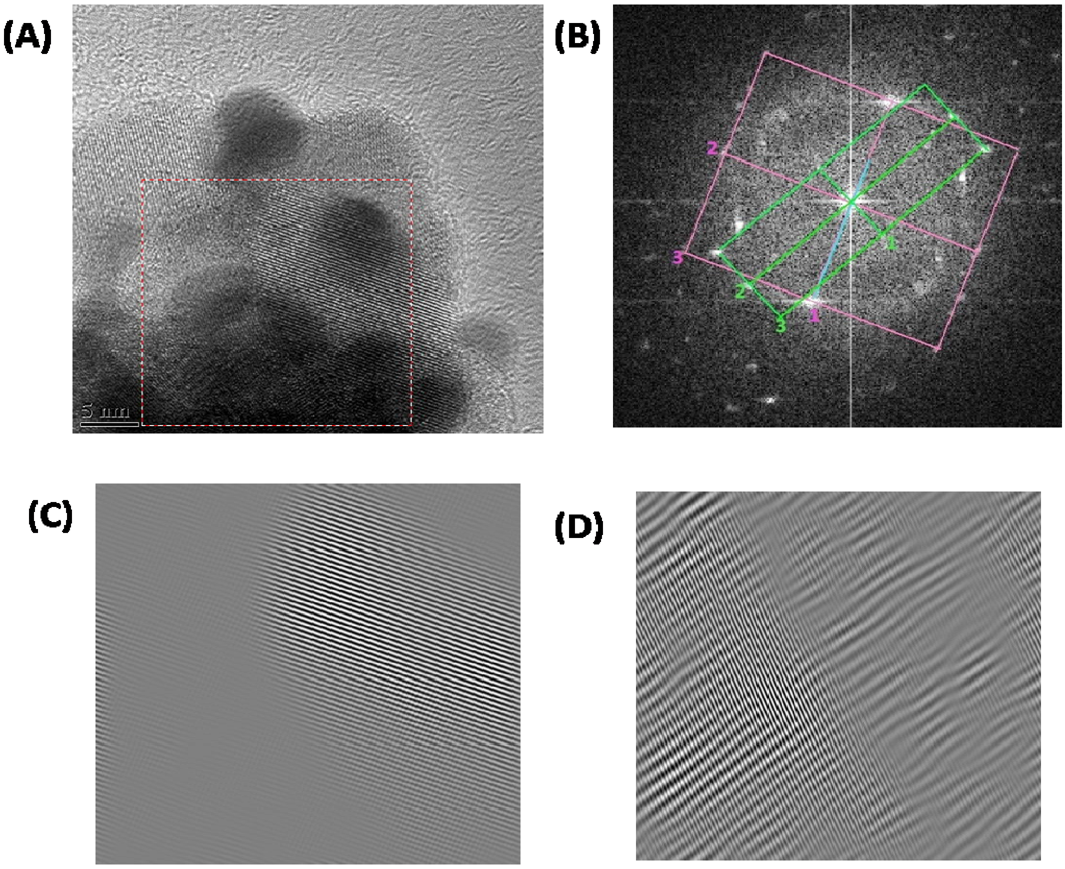

Figure 6.6 (A) HREM image of sample S_2 from another region, (B) FFT from region marked in (A) confirming the presence of $Bi_2Fe_4O_9$/ $BiFeO_3$ and $Bi_{25}FeO_{40}$, (C) Inverse FFT from reflections of $Bi_2Fe_4O_9$/ $BiFeO_3$ (D) Inverse FFT from $(0\bar{1}1)$ and (420) reflections present adjacent to $Bi_2Fe_4O_9$–$BiFeO_3$.

Based on TEM results it is understood these bismuth iron oxide phases are spatially correlated by means of the formation of a $BiFeO_3$nanoshell on a $Bi_2Fe_4O_9$ core. Some of these core-shell particles are understood to contain $Bi_{25}FeO_{40}$ at the periphery of the $BiFeO_3$ shell as evidenced by TEM. By means of correlating TEM and Mössbauer results it can be understood that the core-shell particles are separated by α-Fe_2O_3. Systems comprising such particles are expected to be structurally and chemically stable and have desired dielectric, ferroelectric and magnetic properties. A model has been proposed subsequently to discuss the formation of $Bi_2Fe_4O_9$–$BiFeO_3$/$Bi_{25}FeO_{40}$ based core-shell structures as separated by α-Fe_2O_3.

6.4 Proposed model for the formationof Bismuth Iron Oxide Core-shell Structures

TEMresults show the occurrence of $Bi_2Fe_4O_9$as core while the shelliscomposed ofcrystalline / amorphous$BiFeO_3$.In addition, in certainspots $Bi_{25}FeO_{40}$ are seen to exist closer to $BiFeO_3$while traversing away from core. Thus the occurrence of $Bi_2Fe_4O_9$–$BiFeO_3$–$Bi_{25}FeO_{40}$ based core-shellparticles implies that these phases are spatially distributed from core to shell with increasing Bi concentration.In the followingthephysical processes leading to the formation of$Bi_2Fe_4O_9$–$BiFeO_3$–$Bi_{25}FeO_{40}$particlesformedin the core-shell configurationsareexplained.

Annealingthe sample containing the mixture of ball-milled α-$Fe_2O_3$and Bi_2O_3around 1000 Kthe followingprocesses are proposed to occur.Istep of the process is thatthe Bi_2O_3 nanoparticlesdominantlycomein to contactwithα-Fe_2O_3 nanoparticleswhich are smaller sized and alsopresentin appreciableconcentration.Asthe product(s) of the reaction are dependent mainly on the temperature and time of annealing,the spatial distribution of resultant phases are understoodto be dictated by the temperature of annealing and the local concentration of the reactants and hence their spatial distributions.At a given temperature thespatial distributionofreactants aredependent upon the diffusion coefficients ofBi and Fe ions.

Istepas predictedby the model shows that Bi_2O_3 nanoparticlesreact with α-Fe_2O_3 nanoparticlesresulting mainlyin$Bi_2Fe_4O_9$particles.Duetomultiple annealingstepswithtemperatureofeachannealing steparound1000 Kthere occurs significant diffusion ofBitowards the surface of the particles.This results in the formation ofoff stoichiometric Bi_2O_3at the surface of$Bi_2Fe_4O_9$, which isschematically shown as step II in Figure 6.7.α-Fe_2O_3 particles that are presentin appreciableconcentrationcome in to contact with the outer surface of$Bi_2Fe_4O_9$ particlesin which there are segregation ofbismuth oxide.Dueto therhombohedral structureofα-Fe_2O_3theprobabilityfortheformation ofbismuth ferriteis high.Depending upon the excess concentration of surface segregated Bi_2O_3 in addition to the formation of$BiFeO_3$ in some caseseven $Bi_{25}FeO_{40}$ are observed to the formedat the outer shell. Thusleading to the formation of $Bi_2Fe_4O_9$–$BiFeO_3$–$Bi_{25}FeO_{40}$ in core-shell configuration as evidenced by TEM results.This is mainly understood to be due toenhanced diffusion ofBi^{3+}towardsgrain boundaries.Thus Bi_2O_3 which get segregated at the grain boundaries during initial period of annealing treatments act as heterogeneous nucleating centres for the formation of$BiFeO_3$ and$Bi_{25}FeO_{40}$while coming in to contact with α-Fe_2O_3. These core-shell structured particlesare understood to be surrounded by α-Fe_2O_3 whichremain mostly as amorphous.Thesethree step processes as explained abovehave been schematically explained in Figure 6.7.

Summarizing,this study mainlydiscussesthe formation ofdifferent bismuth iron oxide phases in a spatially correlated manner due to high energy ball milling ofα-Fe_2O_3 and Bi_2O_3 in the ratio of 3:1followed by certain annealing treatments.TEM results show the presence of core-shell structures having $Bi_2Fe_4O_9$ as core surrounded by thin shell ofcrystalline or amorphous $BiFeO_3$.In certain casesthe shell of$BiFeO_3$is observedto be further surroundedby $Bi_{25}FeO_{40}$.These core-shell particles are understood to be separated by amorphous α-Fe_2O_3 appreciably present in the systemMössbauer results show the presence ofdefectrelated components of $BiFeO_3$in terms ofFe atoms associatedwithoxygen vacancies thus implying the off–stoichiometric nature of $BiFeO_3$.The valuesare observed to be closely matching with that of Fe atoms associated with very finenanoparticles of$BiFeO_3$ [201]and are consistent with TEM results. Thin shell ofoff-stoichiometric $BiFeO_3$in a fewcases accompaniedby $Bi_{25}FeO_{40}$, as stabilized by $Bi_2Fe_4O_9$ core andsurrounding α-Fe_2O_3 have been obtained in this study and explained based on the above model proposed by us.

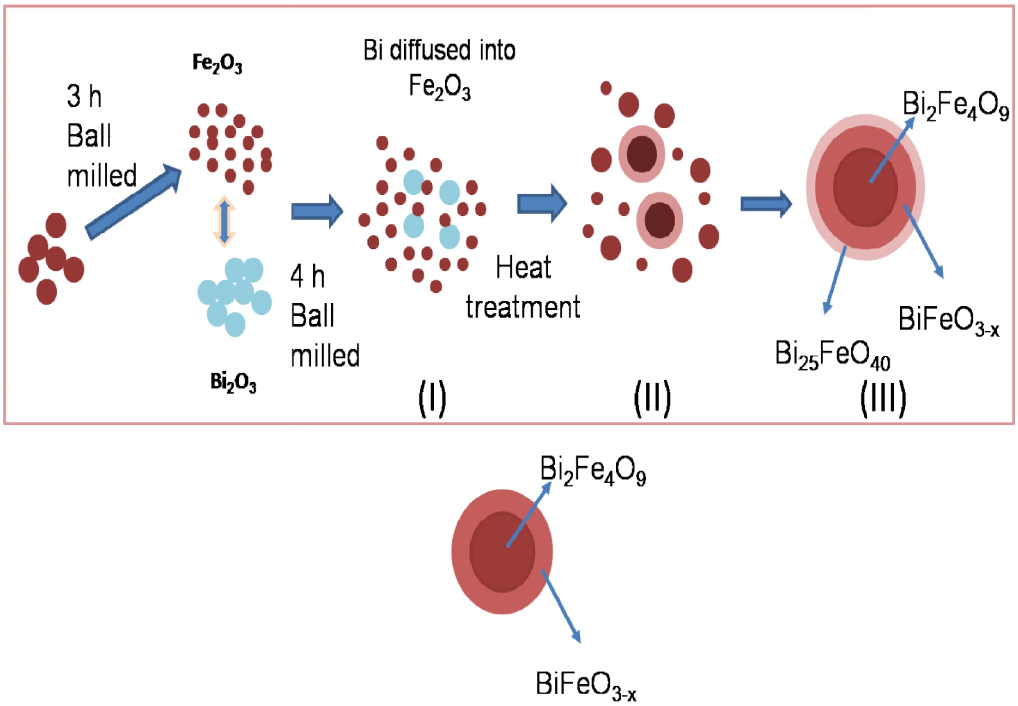

Figure 6.7 Schematic of the formation of $Bi_2Fe_4O_9$ core with shell of off stoichiometric bismuth iron oxide ($BiFeO_{3-x}$) and iron oxide (Fe_2O_3). Step I involves the occurrence of nanoparticles of α-Fe_2O_3 and Bi_2O_3. II step of reaction indicates the formation of $Bi_2Fe_4O_9$ core with a shell of bismuth oxide due to ball milling followed by annealing treatments. These particles while coming in to contact with α-Fe_2O_3 leading to the next step due to annealing. Step–III leads to the formation of $Bi_2Fe_4O_9$– $BiFeO_{3-x}$– $Bi_{25}FeO_{40}$ core-double shell structure as shown in an enlarged manner. Analogously in certain cases $Bi_2Fe_4O_9$ crystalline core is observed with shells that are of amorphous nature and could be considered as composites.

Interestingly the model formulatedin the present studybasedonthe experimentalresults is comprehendedto bematching quite well with that proposed byBernardo *et al*used to explainthemechanism of solid-state reaction between Bi_2O_3 and α-Fe_2O_3[198].This model was proposedbasedon the analysis ofSEM and EDXresults on Bi_2O_3–Fe_2O_3 diffusion coupletreatedat923 K.Dominant diffusion ofBi^{3+}in to α-Fe_2O_3 is proposed as a main mechanismand has predictedthe formation ofα-Fe_2O_3 corewith shellsof distinct phases such as$Bi_2Fe_4O_9$,$BiFeO_3$ and $Bi_{25}FeO_{40}$.It is important to observe the distribution ofbismuth iron oxide phases from core to shell with increasing concentration ofbismuthis similar to the present results as established based on TEM results.

In the present case α-Fe_2O_3 and Bi_2O_3 have been taken in the weight ratio of3:1 and subjected to high energy ball milling and differentannealing treatments as discussed.It could be observed that the solid-state reaction ofBi_2O_3:Fe_2O_3(sample S_4)at 973Khas resulted onlyin$Bi_2Fe_4O_9$ and not any other phaseas evidenced by XRDandMössbauerresults.Consideringannealing process marked as S_2 on the ball-milled sample richer in α-Fe_2O_3 with temperature ofeach annealingtreatment being higher than 973 Kthere is likely to be the formation of$Bi_2Fe_4O_9$ along with α-Fe_2O_3.In the present caseα-Fe_2O_3 particles are much finer which are also present in higher concentration as compared to that of Bi_2O_3act as heterogeneous nucleatingcentresfor the reactionto take place with Bi_2O_3 leading tothe formation of$Bi_2Fe_4O_9$in the firstannealing step. In the subsequent annealing stepsthere is an outward diffusion of$Bi^{3+}$to the grain boundary of$Bi_2Fe_4O_9$particles which inturncome in tocontact with α-Fe_2O_3 thus resulting in $BiFeO_3$ shell.Further annealing treatmentisunderstood to result inthe formation ofbismuth richer iron oxide phase suchas $Bi_{25}FeO_{40}$at the periphery of$BiFeO_3$.Thereforein the later annealing steps Bi_2O_3 formed due to outward diffusionof Bi^{3+} act as heterogeneousnucleatingcentres for the formation of$BiFeO_3$ and also $Bi_{25}FeO_{40}$.

Thusin this study a thin shell of$BiFeO_3$(in some cases accompanied with $Bi_{25}FeO_{40}$) could be formedin terms of core-shell structures which are made stable by the core of $Bi_2Fe_4O_9$which is themost stablephase ofbismuth iron oxideand α-Fe_2O_3particleswhich are in contactwith the core-shell particlesandfurther playan important role ofseparatingthe particles. In the following detailed discussions are made on the dielectric, ferroelectric and magnetic properties of this system.

6.5 Dielectric, Ferroelectric and Magnetic Properties of $Bi_2Fe_4O_9$–$BiFeO_3$Core-shell Particles

Above discussion on core-shell formalism in $Bi_2Fe_4O_9$ core and nano shell of $BiFeO_3$ in presence of other phases like $Bi_{25}FeO_{40}$ amidst the Fe_2O_3 matrix can be approximated to the composite of $Bi_2Fe_4O_9$ and $BiFeO_3$. Hence suitable technologies are administered to study these properties in detail. Overall contribution of composites to magnetic and ferroelctric properties are studiedgiving the insight to the multiferroism fo such composite.Further the core-shell interface effcts on electric properties are investigated and thus detailed dielectric studies which includes modulus, conductivity and impedance studies are carried out.

6.5.1 Bulk Magnetic and Ferroelectric Properties

The magnetic ferroelectric properties of the composites provide a bulk understanding of the overall contribution from the phases present. And thus a comparative inference can be made with respect to the solid-state $Bi_2Fe_4O_9$ consisting of single phase $Bi_2Fe_4O_9$ and that in presence of $BiFeO_3$. Hence the magnetic and ferroelectric properties are discussed in the section.

6.5.1.1 Magnetization Studies

Magnetic properties of $BiFeO_3$ havebeen widely studied and reported in the literature [32,43,47,164,165,203–207].Magnetization results correspondingto S_1 and S_2 are shown in Figure 6.8. Transition around 250 K as shown in the magnetization curves obtained in samples S_1 and S_2 is understood to be due to Morin transition which is explained based on the competition betweentwo kinds of anisotropies inα-Fe_2O_3.Spin-orbit coupling tends to make the spin due to single ion anisotropy align along (111) axis while the magnetic dipole anisotropy makes the spin alignin(111)plane. There is a tendency for superposition of ZFC and FC graphs just belowMorin transitiontemperature (T_M) while the curves are separated above T_M.Weak ferromagnetic nature above 250 Kinα-$Fe_2O_3$is interpreted to be due to slight canting which is supportedby Mössbauer results in terms of the changes in quadrupole splitting and hyperfine field values corresponding to Fe atoms associated with α-Fe_2O_3.Separation of ZFC and FC occurs below 250 K coinciding with the Néel temperature of $Bi_2Fe_4O_9$.Hence the separation is partially contributed due to spin glass behavior of $Bi_2Fe_4O_9$andmainly due to uncompensated spins of $BiFeO_3$nano-shells.M_{FC}–M_{ZFC} decreases below 250 K and reaches a minimum around 200 K and again increases below 200 K.There is an increase inM_{FC}–M_{ZFC} below 200 K.This implies that the weak ferromagnetic orderingas observedisunderstood to be mainly contributed due to $BiFeO_3$.It is important to notice that$M_{FC}$and M_{ZFC} attain minimum around 25 K and their values increase below 25 K.These results are understood due to the presence of $Bi_{25}FeO_{40}$ phase as reported elsewhere [43].

In the case of S_1 there is a more enhanced separation between ZFC and FC below 200 K than S_2. This is understood to be due to an appreciably higher magnitude of weak ferromagnetic interaction. This could be comprehended based on the Mössbauer results explained as follows.Mössbauer results in S_1 and S_2 indicate the presence of α-Fe_2O_3 and $BiFeO_3$ which are the only antiferromagnetic phases at room temperature as evidencedby thedeconvoluted six line patterns correspondingto these phases.The other two phases such as $Bi_2Fe_4O_9$ and $Bi_{25}FeO_{40}$ are paramagnetic at room temperature.In the case of S_1 the value of isomer shifts associated with sextets corresponding to off stoichiometricbismuth iron oxide lie in the range of 0.5 – 0.55 mm/s, implying the presence of higher concentration of Fe^{2+} and hence oxygen vacancies at the shell.This might mean the presence of oxygen vacancies associated with bismuth iron oxidein higher concentration in the case ofS_1 than S_2.

Presence of oxygen vacancies in $BiFeO_3$ has been reported to result in weak ferromagnetic ordering[47,165] .Alsoin a thin shell of$BiFeO_3$there would be non-cancellation ofsurface spinsresulting in a weak ferromagnetic ordering.This is understood to have manifested asseparation between ZFC and FC in S_1 and S_2.A sharp increase in magnetization below 25 K is understood to be due to Fe^{3+} moments of$Bi_{25}FeO_{40}$.A strong magnetodielectric coupling has also been reported in $BiFeO_3$ based on anomaly in dielectric constant [164].M–H curve(cf. Figure 6.8(B)) obtained in the sample S_2 at 300 K shows a loop with non-zero area implying weak ferromagnetic behavior of the sample consistent with the variation of magnetization with temperature. Surface of the anti ferromagnetically ordered off stoichiometric bismuth ferritecontributefortheweak ferromagnetic ordering due touncompensated spins thus exhibitingthe opening of the M–H loop as shownin Figure 6.8 (B).

Resultsobtained based onbulk magnetization,dielectric andMössbauer spectroscopy could be explained in a correlated manner based on the occurrence of$Bi_2Fe_4O_9$–$BiFeO_3$/ $Bi_{25}FeO_{40}$in core-shell with α-Fe_2O_3lying nearby leading to interestingweak ferromagnetic and giant dielectric response ofthe system.

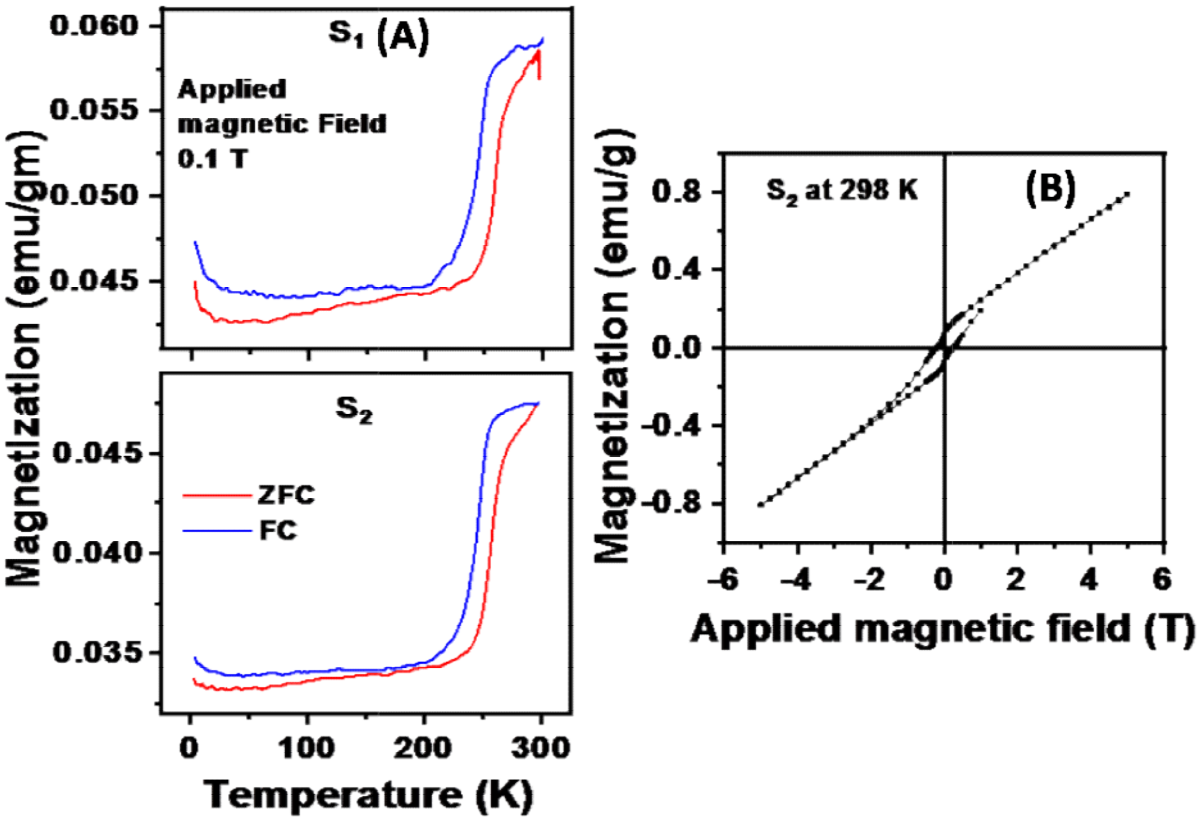

Figure 6.8 Variation of magnetization with temperature as obtained in samples S_1 and S_2 as referred to in the text (A) and M–H loop of S_2 at 298 K (B).

Oxygen vacancies associated with the thin shell of off-stoichiometric $BiFeO_3$ thus resulting instrong polarization of charges within thethin shellwhich are stabilizedby the insulating core andseparated byα-Fe_2O_3particlesis understood to result in giant dielectric response as observed in this study.This study thus elucidates the formation of core-double shell structures byusingappropriate thermo-mechanical alloying treatmentsbasicallyexploiting the most stable nature of$Bi_2Fe_4O_9$phase and compatibility of lattice parameters between α-Fe_2O_3 and $BiFeO_3$.This results in the formationofthin shell ofoff-stoichiometric $BiFeO_3$ which are associated with oxygen vacancies leading to a strong polarization of charges leading to giant dielectric response in addition to weak ferromagnetic and appreciableferroelectric properties.

6.5.1.2 Ferroelectric Studies

PEloop measured for both$Bi_2Fe_4O_9$ preparedthrough solid-state reaction andball-milled and heat treated sample (S_2)with optimized R and C values (R~ MΩ and C~ pF) and frequency range (~ Hz) are shown in Figure 6.9(A) and (B) respectively. The P_r values corresponding to SSR sample matches well with previously reported values (~ 0.2 μC/cm^2) [53]. Polarization value $P_r$ofsample $S_2$is observed to be higher than that of SSR sample which canmostprobablybe attributed to the presence of$BiFeO_3$ at the shell of the particles.

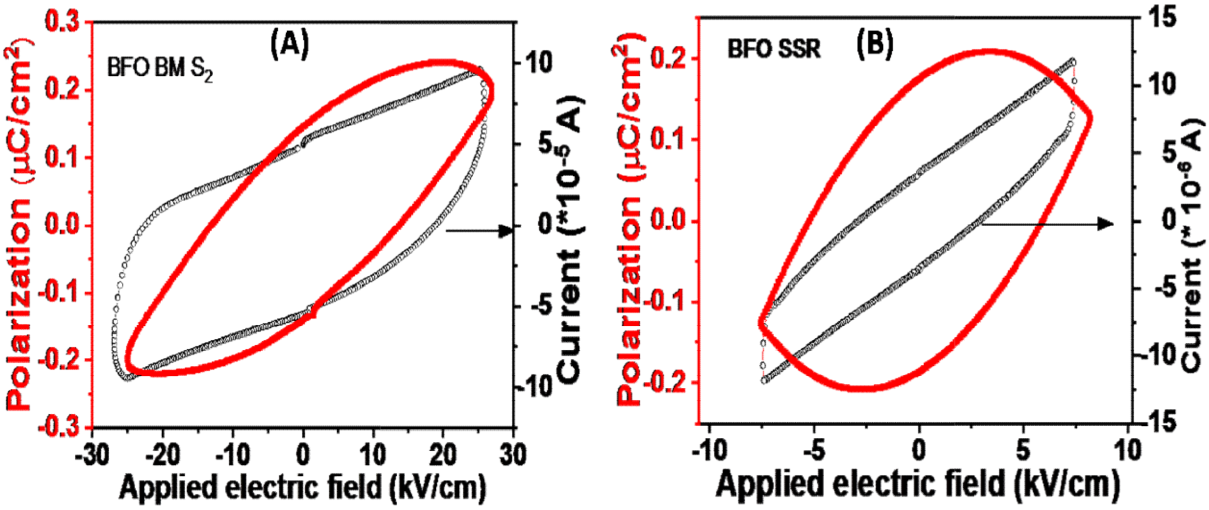

Figure 6.9 P–E loop as obtained in $Bi_2Fe_4O_9$ through solid state reaction (B) and in ball milled sample S_2 (A).

In both the cases, Ivs V curve shows hysteresis and resistive switching behavior unlike that of ohmic behavior exhibited by non-ferroelectric materials which passes through origin. The unsaturated behavior of the samples can be understood due to low value of polarization (partial reversal of polarization) and partial leakage behavior[52,191] compared to ideal ferroelectric systems. It is worth mentioning thateventhe well studied ferroelectric systems like $BaTiO_3$ system when substitution with minute fraction of Fe shows unsaturated loop [38,66,189,208–210].Further it is observed that, with increasing frequency the polarization value decreases which confirms the ferroelectricity behavior of the system and not due to leakage which is a way of confirmation as reported in literature for other multiferroic system[211, 212] .

6.5.2 Dielectric Spectroscopic Studies

The present case S_2i.e. core shell $Bi_2Fe_4O_9$–$BiFeO_3$ separated by α-Fe_2O_3 can be approximated to the composite of $Bi_2Fe_4O_9$–$BiFeO_3$ wherein the grain/grain boundary interface of phases play a significant role contributing to the net enhanced dielectric properties supported by impedance, modulus and conductivity w r t frequency is reported by us [216]. Here we presented a detailed temperature dependent dielectric property studies.

Dielectric response of a system is an impression of resistive and capacitive behavior with frequency and temperature as well which distinguishes any anomaly around the transition temperature giving information about the possible magnetodielectric, magnetocapacitive or magnetoelectric coupling.

The temperature dependence of dielectric constant (ε) and dielectric loss (tan δ) of $Bi_2Fe_4O_9$–$BiFeO_3$ composite at different frequencies is shown in Figure 6.10(A). A sharp decrease in dielectric constant with increase in frequency is observed, indicative of Maxwell-Wagner type relaxation caused due to space charge release. This scenario creates a high impedance barrier at the sample electrode interface resulting high value ofdielectric constant (ε). With increase in frequency of the applied electric field, the dipoles are unable to follow the applied field and thus dielectric constant (ε) decreases and becomes independent of temperature at high frequency region.

A close observation of the plots (cf. inset Figure 6.10(A)) show that a dielectric peak correspondingly a dielectric loss peak (cf. Figure 6.10A (i)and(ii)) is observed which shifts to high frequency with increase in temperature, indicative of conductive losses due to relaxing dipoles [217]. This occurs in a transition temperature range of $Bi_2Fe_4O_9$ (~300 K) and shifts towards the magnetic transition temperature of $BiFeO_3$ (~500 K). ε_{eff}' is expected to include ε

values from the phases in the composite that is from $Bi_2Fe_4O_9$, $BiFeO_3$ and Fe_2O_3 as well. Observation of similar anomaly in dielectric constant (ε) is previously observed and discussed for $BiFeO_3$[218]. Shifting of the loss peak indicates that it is a thermally activated process[218].

Dielectric relaxation which is a complex quantityis generally represented as

$$\varepsilon(\omega) = \varepsilon_\infty + \frac{\varepsilon_0 - \varepsilon_\infty}{1 - i\omega\tau} = \varepsilon_1(\omega) - i\varepsilon_2(\omega) \qquad 6.1$$

Hereω represents the angular frequency, ε_o andε_∞ are static dielectric constant (ω→ 0) and permanent dielectric constant (ω→∞).Where$\varepsilon_1(\omega)$ and $\varepsilon_2(\omega)$ are the real and imaginary parts of dielectric response respectively.τis the relaxation time.The dielectric loss factor tanδis given as$\frac{\varepsilon_2(\omega)}{\varepsilon_1(\omega)}$, whileδis the phase difference between applied electric field and induced current.$\varepsilon_2(\omega)$can beobtained from the above equationas$\varepsilon_2(\omega) = \frac{\omega\tau}{1+\omega^2\tau^2}$and the maximum of $\varepsilon_2(\omega)$lies around$\omega\tau \approx 1$.The dielectric relaxation timeτ, is given as,

$$\tau^{-1} = \tau_0^{-1}\, e^{\left(-\frac{E_a}{k_B T}\right)}, \qquad 6.2$$

with E_a as the activation energy required for relaxation and k_BT as the thermal energy. As the maximum of $\varepsilon_2(\omega)$lies around$\omega\tau\approx1$,from the tangent loss curve corresponding to different temperatures, the values of the dielectric relaxation time have been obtained. Plotted in Figure 6.10(C)is the variation of the naturallogarithm of dielectric relaxation time with inverse of temperature. From the slope of the linear graph,the value of the activation energy for relaxation could be obtained to be ~0.6 eV, matching well withthe thermally activated mechanism of charge carrier transport across the phase interface of the grain/grainboundary. The tangent loss peak could be fitted with the Arrhenius equation and fitted with a straightline [219]. The activation energy obtained is 0.6 eV (cf.Figure 6.10C), which is close to that of the energycorresponding to Fe^{2+}/Fe^{3+} electron hopping due to the oxygen vacancies present in the constitutingphases[220]. The insets in Figure 6.10(A) show the discontinuity around the transition temperature region ofboth the phases.

High dielectric response is mainly contributed by the shell and interfacial polarization i.e. Maxwell–Wagner polarization. In a core-shellstructure which is present in a medium with a dielectric constantε,with core having dielectric constant $\varepsilon_C$and thickness L whileifthese values corresponding to shell are $\varepsilon_S$and d, the effective dielectric constant at low frequenciesis givenωas

$$\varepsilon^* \approx \frac{\varepsilon_C}{\varepsilon} + \frac{\varepsilon_S}{\varepsilon\delta[1 + i\omega\tau]} \approx \frac{L\varepsilon_S}{d}, \qquad 6.3$$

whereδis given as d/L.In the present case taking the value ofthe dielectric constant of$BiFeO_{3-x}$ as around50 anddas typically of the order ofa few nm (≈ 1 nm)and L as afew micron, we could get the value ofε^*typically of the order of 0.5×10^5 typically matching with the results around low frequencies obtained in this study thus elucidating the giant dielectric response ofoccurrence of$Bi_2Fe_4O_9$ and bismuth iron oxide in core-shell structure. Further the presence of insulating α-Fe_2O_3 outer shell significantly enhances the effect of polarization of charges at thebismuth ferrite interface.

Thusthestrong polarization effects are understood to be betweenelectron trappedoxygen vacancies of $BiFeO_3$ and that in any other cation (Bi^{3+}) thusinducingspace charges between insulating core ($Bi_2Fe_4O_9$) and inner surface oftheshell ofα-Fe_2O_3.High values of permittivity associated with strong maximum in the dielectric losses have been reported in bismuth iron oxide based thin films and core-shell structures.

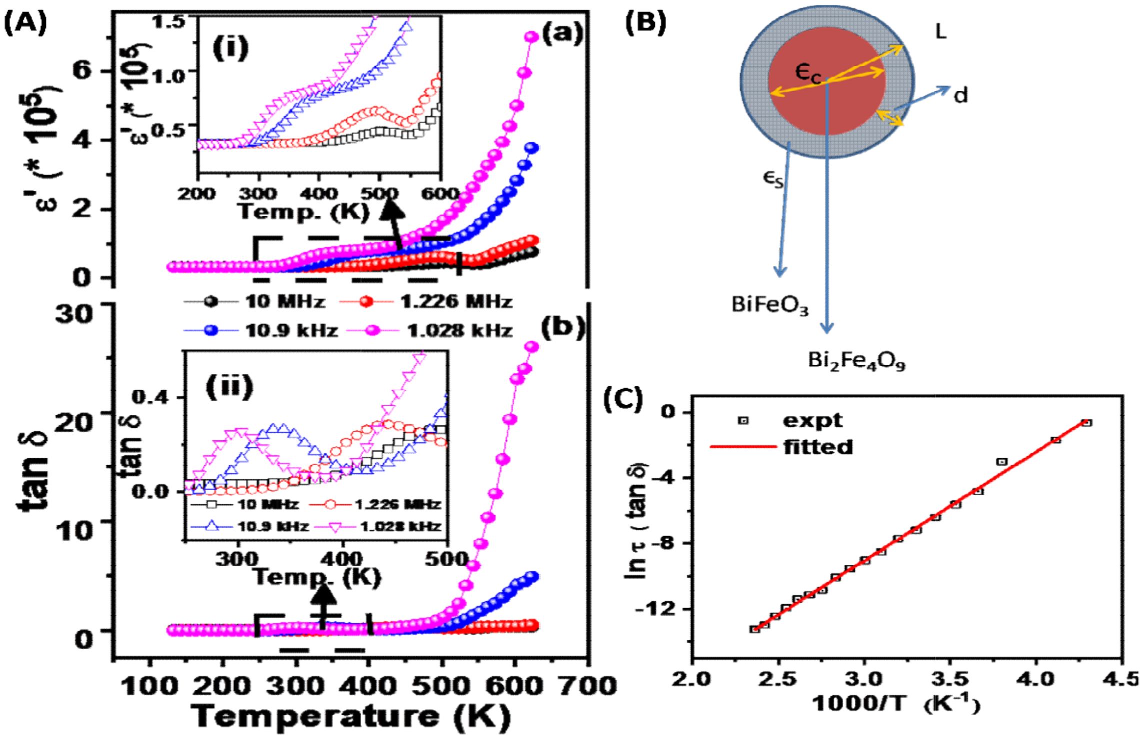

Figure 6.10 (A) Temperature dependence of (a) dielectric permittivity Corresponding variations marked inside rectangular panels are magnified and shown in insets as (i) and (ii) respectively. 6.10 (B) shows the core-shellstructured particle having dielectric constants ε_C andε_s for core and shell respectively.

6.6 Conclusions

Presence of $Bi_2Fe_4O_9$ and α-Fe_2O_3 phases could also be deduced using Mössbauer spectroscopy. Importantly Mössbauer results show the presence of defect associated components correspondingtoFe atoms associated withbismuth ferriteandareunderstood to be dueto oxygen vacancies implyingthe off–stoichiometric nature of $BiFeO_3$. This result implies that the $BiFeO_3$ formed should be occurring as a nanosized system. TEM studies carried out in this system show the presence of $Bi_2Fe_4O_9$–$BiFeO_3$ particles present in core-shell configuration. These particles are found to be separated by α-Fe_2O_3 particles as deduced using TEM. Mössbauer results pointing to the nano sized $BiFeO_3$ have been confirmed by TEM studies. Some ofthe particlesare characterized to have$Bi_{25}FeO_{40}$nearby $BiFeO_3$while directedoutwards the shell as evidenced by TEM results.Thisisachievedbasedon a well controlled annealing treatmentasguidedbythephase diagramandtheresultantphasesobtainedbased on series ofannealingtreatmentssubsequent to high energy ball millingofan appropriatecomposition ofBi_2O_3 and α-Fe_2O_3.

Amodelhas been proposed in this study to comprehend the formation ofthe above core-shell structures.These core-shell structures as separated by α-Fe_2O_3particlesare observed to be ferroelectric, weakly ferromagnetic andexhibitgiant dielectric response. Mainly oxygen vacancies associated with the thin shell of off stoichiometric $BiFeO_3$ cause strong polarization of charges in the shell and hence are understood to result in giant dielectric response as observed in this study.Hence oxygen vacancies associated with shell of off–stoichiometric $BiFeO_3$ play an important role for the observed dielectric and magnetic properties of the system. The dielectric properties of the composite systemare understood in a detailed manner.

Homi Bhabha National Institute

1. **Name of the Constituent Institution: IGCAR**
2. **Nam of the Student: Ms.Alaka Panda**
3. **Enrolment No.: PHYS 02 2014 04 003**
4. **Title of the Thesis: Mössbauer Studies on Some Fe-based Multiferroic Materials**
5. **Name of the Board of Studies : Physical Sciences**

Abstract

This thesis deals with the studies of the multiferroic properties of Bismuth iron based type I and type IIoxides such as $BiFeO_3$ and $Bi_2Fe_4O_9$. $BiFeO_3$exhibits antiferromagnetic and ferroelectricordering with the Neel and Curie temperatures at 643 K and 1103 K respectively. G-type AFM ordering due to Dzyaloshinskii-Moriya interaction is compensated by the presence of spin cycloid of wavelength 62 nm resulting in net zero magnetic moment. Further the ferroelectricity is originated from the off-centric arrangement along (111) direction resulted from stereochemically active $6s^2$ lone pair of Bi. The observed magneto electric coupling is weak as the magnetic and ferroelectric origins are different.There are challenges involved in observing multiferroicity in $BiFeO_3$ due to prevalent impurity phase presence as well as low resistance of the product. By properly controlling the synthesis parameters these shortcomings can be overcome. In order to order study the effect of size on the multiferroic properties nanoparticles of $BiFeO_3$ has been prepared using sol-gel route at low temperatures far below the temperature of formation of $BiFeO_3$through solid state route. Further suitable substitution of ions like isovalentLa^{3+}, divalent Ca^{2+} at Bi sites and Mn^{3+} at Fe sites are carried out following solid-state route aimed at enhancing multiferroic properties in addition to stabilizing $BiFeO_3$ phase. Another system of study in this thesis is $Bi_2Fe_4O_9$which is a type II multiferroic with transition temperatures close to room temperature i.e magnetic Neel transition at 250 K and ferroelectric Curie transition at 260 K. In $Bi_2Fe_4O_9$ the magnetic and ferroelectric properties are coupled by means of frustrated magnetic spin structure leading to off-centrosymmetric ferroelectric ordering with comparatively large value of magnetodielectric coupling. In addition, an attempt is made in understanding the growth of different phases in Bi_2O_3-Fe_2O_3 phase diagram by means of HRTEM and Mossbauer analysis supported by XRD results.

Suitable synthesis methods in preparing pristine phases are employed for detailed studies which is generally a challenge especially in case of $BiFeO_3$. Sol-gel auto-combustion route for nanoparticle $BiFeO_3$ preparation and solid-state route for substituted $BiFeO_3$ as well as bulk $Bi_2Fe_4O_9$ followed by heat treatment is

found to be effective towards achieving the goal. Different characterization techniques for phase identification, magnetic, ferroelectric as well as coupling are used. For structural characterization X-ray Diffraction techniques and supporting Raman spectroscopic measurements and microscopic measurements are carried out. The magnetic and ferroelectric properties are carried out using vibrating sample magnetometer (VSM) and ferroelectric PE loop tracer respectively. An arrangement is made to observed the PE under the application of magnetic to observe the coupling between magnetic and ferroelectric properties. Dielectric measurements are also carried out to look for possible magnetodielectric coupling. Mössbauer spectroscopic studies helped in understanding obtained bulk magnetic and ferroelectric properties at the atomic scale by means of probing the Fe sites in the studied systems.

Nano-particles of $BiFeO_3$ are prepared using sol gel method with different chelating agents resulting in different complex formation mechanisms hence causing size differences. Structural property studies discusses the presence of distortion and thus the consequences of these observations upon multiferroic properties are studied. These nanoparticles are deduced to be occurring in core-shell configuration with core and shell exhibiting antiferromagnetic and weak ferromagnetic ordering respectively based on the results of Mössbauer studies.Magnetic properties are found to be originated from the anioic defects and 62 nm spin cycloid anomaly causing soft ferromagnetism and leaky loop in citrate assisted $BiFeO_3$ while size effect dominated coexisting weak FM shell and AFM core with well developed PE loop for tartarate based $BiFeO_3$. An appreciable switching is observed implying exhibition of magnetoelectric coupling in the nano-$BiFeO_3$.

Isovalent La at Bi sites and co-substituted aliovalentCa in place of Bi and Mn at Fe sites are prepared via solid-state route and its structural magnetic,ferroelectric properties are studied. The structural transition is observed with respect the substitution concentration. The structural transition and distortion are found to result in complex and interesting magnetic properties. Ferroelectric properties are studied in all the cases and magnetoelectric coupling are observed. 20% La doped $BiFeO_3$ due to the presence of defects and structural transition and in 20% Ca and 5% Mn co-substituted $BiFeO_3$ due to J-T distortion ofMn and altered magnetic exchange interaction are observed to have substantial magnetoelectric electric coupling as deduced from Mössbauer spectroscopy.

The mechanism of the growth of Bismuth iron oxide phases is proposed based on the results of Mössbauer spectroscopy along with that of TEM studies. $BiFeO_3$-$Bi_2Fe_4O_9$ composite system as obtained using thermo mechanical treatment of the oxides of Bi and Fe , is found to exhibit significant magnetoelectric coupling as well giant dielectric behavior providing scope for device applications.

Thesis Highlight

Name of the Student: Alaka Panda

Name of CI: Indira Gandhi Centre for Atomic Research **Enrolment No.:** PHYS022014 04 003

Thesis Title: Mössbauer Studies on Some Fe-based Multiferroic Materials

Discipline: Physical Sciences **Sub-Area of Discipline:**Condensed Matter Experiment

Date of viva voce: 23-12-2020

This thesis is dedicated towards understanding the structural, bulk magnetic (FM/AFM), ferroelectric (FE) as well as magnetoelectric (ME) coupling in $BiFeO_3$ and $Bi_2Fe_4O_9$. An atomic level understanding of these properties is provided using Mössbauer Spectroscopic (MS)studies. Role of defects altering the magnetic properties and in turn ferroelectric and magnetoelectric coupling properties has been investigated . A mechanism is provided towards the understanding of the formation of bismuth iron oxide phases.

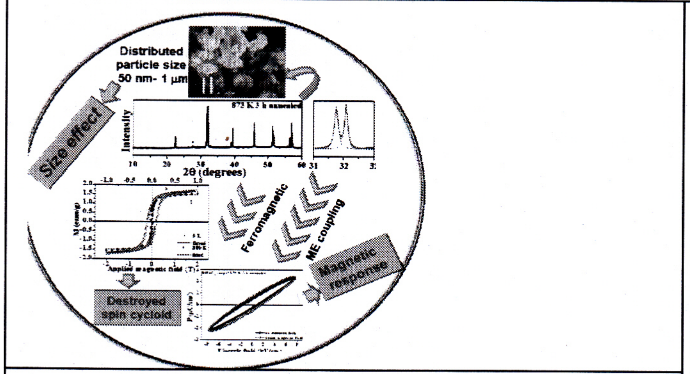

Soft FM and FE with leakage and coupling as obtained in BFO-C results from oxygen defects and distortion while coexisting AFM and FE in BFO-T is understood due to size effect

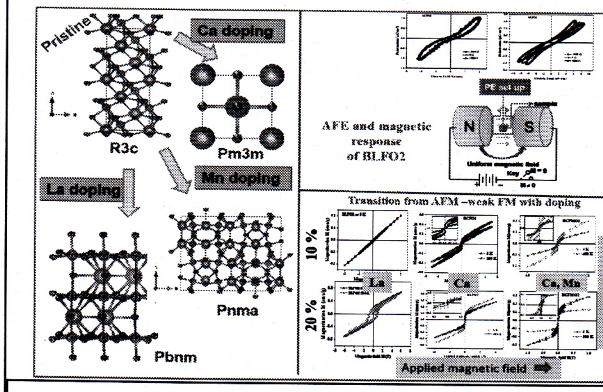

La substitution at Bi sites induces weak FM and FE as well as coupling due to partial structural transition as well as due to distortion and defects.whileCa/Mnsubstitutions at Bi/Fe sites results in enhanced muliferroic properties.

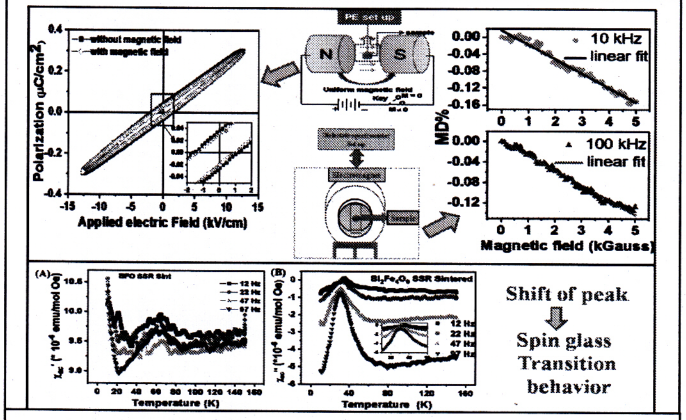

Bulk $Bi_2Fe_4O_9$ undergoes surface modification due to annealing and exhibits weak FM at low applied magnetic and Ferrroelectricity. ME and MD couplings are observed

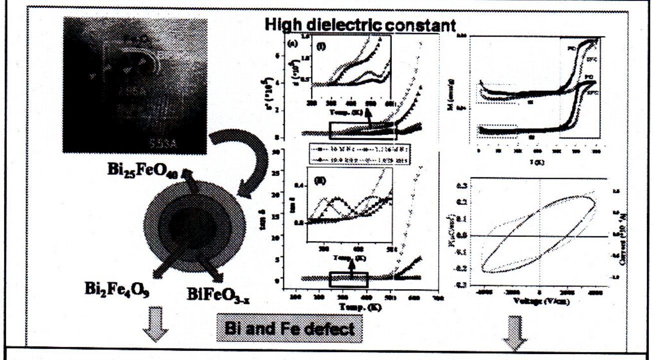

Bismuth iron oxide phases are spatially distributed in core shell structure as deduced from TEM and elucidated from MS. ME as well as giant dielectric behaviour is established.

Conclusion- A detailed understanding of the possible role of defects on the bulk Magnetic and ferroelectric of pristine and substituted $BiFeO_3$ as well as $Bi_2Fe_4O_9$is obtained using Mossbauer spectroscopy. Defects are observed to play a crucial role in controlling the magnetic properties. An atomic scale mechanism is proposed for the growth of bismuth iron oxide phases based on the results of Mossbauer studies and TEM analysis. In addition multiferroicproperties of $BiFeO_3$-$Bi_2Fe_4O_9$ composites are also studied.